UNIVERSITY OF CALIFORNIA,
IRVINE

Solid Oxide Electrolysis Cell (SOEC) and System Technology for Widespread Use with Renewable Energy

DISSERTATION

submitted in partial satisfaction of the requirements
for the degree of

DOCTOR OF PHILOSOPHY

in Mechanical & Aerospace Engineering

by

Alireza Saeedmanesh

Dissertation Committee:
Professor Jack Brouwer, Chair
Professor Yun Wang
Professor David Copp

2021

DEDICATION

To

my lovely wife, lovely family, and friends

TABLE OF CONTENTS

Page

LIST OF FIGURES vii

LIST OF TABLES xv

ACRONYMS xvi

ACKNOWLEDGEMENTS xviii

VITA xx

ABSTRACT OF THE DISSERTATION xxii

1 Introduction 1

1.1 Motivation 1

1.2 General Background 19

1.3 Research Goal 24

1.4 Objectives 24

1.5 Approach 25

1.6 Structure of this Dissertation 27

2 Background 29

3 Solid Oxide Steam Electrolysis System Design 41

3.1 SOEC Stack Model 41

3.1.1 Governing Equations 42

3.1.1.1 Electrochemical Model 42

3.1.1.2 Mass Balance 49

3.1.1.3 Energy Balance 50
3.1.1.4 Pressure Drop 51
3.2 SOEC System Design and Control Strategies 52
3.2.1 Balance of Plant Model 54
3.2.1.1 Pump 54
3.2.1.2 Electric Heater 55
3.2.1.3 Heat Exchanger 55
3.2.1.4 Hydrogen Compression Unit 56
3.2.1.5 Steam Generator 57
3.2.1.6 Ejector 57
3.2.2 Control Strategy Development 59
3.2.2.1 Temperature Control 59
3.2.2.2 Steam Flow Rate Control 61
3.2.2.3 Input Power Control 62
3.2.2.4 Cathode Oxidation Management (Cathode Recirculation Management) 62
3.2.3 System Performance Parameters 63
3.3 SOEC Stack Steady-State Results 63
3.4 SOEC System Steady-State Results 73
3.5 Summary 76
4 SOEC System Dynamic Operation 77
4.1 Sunny Day Simulation 78
4.2 Cloudy Day Simulation 87
4.3 Summary 93
5 Integration of SOEC System into the UCI Microgrid to Support High Renewable Use 94

5.1 UCI Campus Microgrid 94

5.2 UCI Microgrid Demand Profiles 95

5.3 UCI Microgrid Power Plant Model 96

5.4 UCI Microgrid Dispatch Model 99

5.5 SOE Unit Microgrid Dispatch 100

5.6 Simulation Results 101

5.6.1 Microgrid Operation 101

5.6.2 Microgrid Operation Integrated with SOE Unit Systems 103

5.6.3 Hydrogen Production 118

5.6.4 On-Site Hydrogen Utilization 120

5.7 Summary 123

6 Experimental Analysis of Solid Oxide Short Stack 125

6.1 Test Stand Set-up and Instrumentation 125

6.2 Experimental Results 133

6.2.1 Post Process of the Experimental Data 133

6.2.2 Effect of Operating Temperature 133

6.2.3 Effect of Fuel Inlet Composition 134

6.2.4 Model Calibration and Validation 136

6.2.5 Dynamic Step Profile 142

6.2.6 Dynamic Solar PV (Sunny/Cloudy) and Wind Profiles 144

6.2.7 Durability Tests under Thermal Cycles 148

6.2.8 Electrochemical Impedance Spectroscopy 152

6.3 Summary 160

7 Summary and Conclusions 161

7.1 Summary 161

7.2 Conclusions 161

7.2.1 Solid Oxide Electrolysis System Design 161

7.2.2 SOEC System Dynamic Operation 162

7.2.3 Integration of SOEC System into the UCI Microgrid to Support High Renewable Use 163

7.2.4 Experimental Analysis of Solid Oxide Short Stack 164

7.3 Future Work 165

7.3.1 Integration of SOEC System into the UCI Microgrid to Support High Renewable Use 165

7.3.2 Experimental Analysis of Solid Oxide Short Stack 165

References 167

LIST OF FIGURES

Page

Figure 1: Emissions associated with different energy sectors in the US from 1990 to 2017 [22]. 2

Figure 2: Different parts of the emissions in the US from 1990 to 2017 [22]. 2

Figure 3: Energy Sectors and their contribution in emissions in the US in 2019 [22]. 3

Figure 4: (a) Solar PV global weighted average LCOE 2010-2017, (b) Onshore wind global weighted average LCOE 2010-2017 [23]. 4

Figure 5: Renewable electricity capacity growth by technology 1994-2022 [23]. 5

Figure 6: Annual Cumulative Installed Renewable Capacity [74]. 6

Figure 7: Total Renewable Generation Serving California Load [74]. 6

Figure 8: Wind and solar curtailment in California in 2018, 2019, and 2020 [84]. 8

Figure 9: Demand and net demand in a day in February showing the duck curve [84]. 9

Figure 10: Importance of P2G in long duration of storage compared to battery energy storage [155]. 10

Figure 11: 1-year hourly simulation of the load and power generation dynamics of a 100% renewable grid in California, and the capacity of different storage technologies for (a) wind dominant case (37GW solar capacity and 80GW wind capacity installed) and (b) solar dominant case (162GW solar capacity, 5.6GW wind capacity installed) [23]. 11

Figure 12: Depiction of U.S. primary energy consumption and electricity penetration shares for different energy subsectors in 2015 [23]. 14

Figure 13: Global industrial demand for hydrogen [228]. 15

Figure 14: Global hydrogen production feedstock and global warming potential and costs associated with different pathways [229]. 16

Figure 15: Schematic of future energy network showing P2G as a heart of the system [23]. 17

Figure 16: Schematic of cost-effective Geological storage for storing hydrogen [google images]. 18

Figure 17: Comparison of SOE, Alkaline and PEM electrolyzers in terms of cost and efficiency [261]. 20

Figure 18: Total energy demand, electric demand and heat demand for electrolysis at different temperature [262]. 20

Figure 19: SOE individual cell and its compartments [263]. 21

Figure 20: Three operating modes of high temperature solid oxide electrolysis cell [264]. 22

Figure 21: Methanation process [google images]. 22

Figure 22: Fischer-Tropsch process [google images]. 23

Figure 23: Schematic of Cross-flow SOE Unit-Cell [341]. 41

Figure 24: The developed SOEC system layout [343]. 54

Figure 25: PI feedback controller loop for first control strategy. 59

Figure 26: PI feedback controller loop for second control strategy. 61

Figure 27: Steady-state spatial distribution of (a) Nernst voltage, (b) Overpotentials, (c) Current density. 64

Figure 28: Steady-state spatial distribution of molar fraction of (a) Steam, (b) Hydrogen, (c) Oxygen, (d) Nitrogen. 65

Figure 29: (a) PEN average temperature, (b) Maximum PEN temperature difference vs. stack input power. 67

Figure 30: PEN average, maximum and minimum temperatures (a) first control strategy, (b) second control strategy. 68

Figure 31: (a) Maximum PEN localized temperature gradient, (b) temperature of a node on the PEN with the highest temperature fluctuation vs. stack input power. 68

Figure 32: Spatial distribution of different operating parameters at highly exothermic condition. 71

Figure 33: Spatial distribution of different operating parameters at highly endothermic condition. 73

Figure 34: (a) System efficiency, (b) Stack efficiency vs. stack input power. 74

Figure 35: (a) Hydrogen production rate, (b) Energy consumption of the system vs. stack input power. 75

Figure 36: Contribution of system components in power consumption (a) First control strategy, (b) Second control strategy. 76

Figure 37: PV generated power for a sunny day and a cloudy day. 77

Figure 38: PV generated power vs stack consumed power for sunny day. 78

Figure 39: Cell current density and voltage for a sunny day. 79

Figure 40: PEN average temperature and maximum temperature difference along the PEN for a sunny day. 79

Figure 41: PEN minimum, average and maximum temperature for a sunny day. 81

Figure 42: Efficiencies for the sunny day scenario. 82

Figure 43: Contribution of each component in power consumption for a sunny day. 84

Figure 44: Highly endothermic spatial distribution (a) Current density, (b) Overpotentials, (c) PEN temperature, and (d) Oxygen molar fraction. 85

Figure 45: Highly exothermic spatial distribution (a) Current density, (b) Overpotentials, (c) PEN temperature, and (d) Oxygen molar fraction. 87

Figure 46: PV generated power vs stack consumed power for a cloudy day. 88

Figure 47: Cell current density and voltage for a cloudy day. 89

Figure 48: PEN average temperature and maximum temperature difference along the PEN for a cloudy day. 90

Figure 49: PEN minimum, average and maximum temperature for a cloudy day. 91

Figure 50: Efficiencies for the cloudy day scenario. 92

Figure 51: Contribution of each component in power consumption for a cloudy day. 92

Figure 52: Schematic representation of the microgrid components considered in this analysis and the SOE unit systems integration. 95

Figure 53: UCI campus (a) electricity demand, and (b) thermal demand for the year 2014. 96

Figure 54: Gas turbine regression based operating parameters: (a) efficiency, and (b) turbine exit temperature. 97

Figure 55: Annual UCI microgrid electric energy generation mix and excess electricity in future scenarios with increased PV installed capacity. 101

Figure 56: Excess power distribution in future scenarios with increased PV installed capacity. 103

Figure 57: Percentage of stored excess electric power via P2G vs. total power capacity of dispatched 300 kW SOE unit systems for different PV installed capacity. 104
Figure 58: Microgrid-SOE dispatch simulation results in a week of September (a) electric power balance, and (b) thermal power balance with the current 4 MW of PV installed capacity. 106
Figure 59: Microgrid-SOE dispatch simulation results in a week of January (a) electric power balance (b) thermal power balance with the current 4 MW of PV installed capacity. 108
Figure 60: Microgrid-SOE dispatch simulation results in a week of September (a) electric power balance, and (b) thermal power balance with 10 MW of PV installed capacity. 110
Figure 61: Microgrid-SOE dispatch simulation results in a week of January (a) electric power balance, and (b) thermal power balance with 10 MW of PV installed capacity. 112
Figure 62: Microgrid-SOE dispatch simulation results in a week of September (a) electric power balance, and (b) thermal power balance with 25 MW of PV installed capacity. 114
Figure 63: Microgrid-SOE dispatch simulation results in a week of January (a) electric power balance (b) thermal power balance with 25 MW of PV installed capacity. 115
Figure 64: Details of microgrid operation during the day January 5 (a) electric power balance, and (b) thermal power balance with 25 MW of PV installed capacity. 116
Figure 65: Statewide California electricity demand and net demand for a day in January 2019 [352]. 118
Figure 66: Annual hydrogen production for different PV installed capacity. 119

Figure 67: Hydrogen production and possible on-site consumption for different PV installed capacity. 122

Figure 68: Yearly amount of avoided natural gas consumed by the gas turbine, and (b) yearly amount of reduction in CO_2 emission from the gas turbine for different PV installed capacity. 122

Figure 69: 6-cell short stack and electric furnace to thermally manage the short stack. 125

Figure 70: Independent temperature controller (PIXSIS ATR621) to control furnace temperature. 126

Figure 71: Solenoid valves and mass flow controllers to control flow of different gases. 127

Figure 72: Electronic load and power supply. 128

Figure 73: Data acquisition system. 128

Figure 74: Deionized water supply line. 129

Figure 75: Evaporator and reformer reactor. 129

Figure 76: Evaporator and reformer reactor independent temperature controller. 130

Figure 77: Princeton applied research VersaSTAT 3F potentiostat. 130

Figure 78: Schematic of test stand set-up and instrumentation [354]. 131

Figure 79: Actual test bench and its connections. 132

Figure 80: Graphical user interface installed in the embedded computer to control the test bench. 132

Figure 81: V-j characteristic curve for electrolysis operation at three different operating temperatures. 134

Figure 82: V-j characteristic curves for three different fuel inlet compositions showing impact of H_2 inlet percentage. 135
Figure 83: Model calibration and validation at different operating temperatures. 137
Figure 84: Model calibration and validation at different operating temperatures. 140
Figure 85: Schematic of solid oxide electrolysis cell showing three regions of species concentrations that are calculated in the model. 140
Figure 86: Species concentration at different levels for 90% H_2O-10% H_2 inlet conditions case. 141
Figure 87: Species concentration at different levels for the 75% H_2O-25% H_2 inlet conditions case. 141
Figure 88: Species concentration at different levels for 50% H_2O-50% H_2 inlet conditions case. 142
Figure 89: Dynamic response of test bench and model to the input step profile. 143
Figure 90: Dynamic response of the test bench compared to model predictions for a sunny day solar PV profile. 145
Figure 91: Dynamic response of test bench compared to model predictions for a cloudy day input solar PV profile. 146
Figure 92: Dynamic response of test bench compared to model predictions for an input wind profile. 147
Figure 93: Temperature profiles during the durability test on the solid oxide test bench. 149
Figure 94: Temperature profiles during one cycle of the durability test on the solid oxide test bench. 150

Figure 95: Voltage profiles during one cycle of the durability test on the solid oxide test bench. 151

Figure 96: Voltage degradation percentage attributed to the thermal cycles imposed during the durability test. 152

Figure 97: V-j characteristics curve and its associated cell-level EIS measurements. 154

Figure 98: Stack-level and sum of the cell-level EIS measurements comparison. 155

Figure 99: Effects of operating current density on the cell-level EIS measurements. 157

Figure 100: Effects of operating temperature on the cell-level EIS measurements. 158

Figure 101: Effects of fuel inlet composition on the cell-level EIS measurements. 159

LIST OF TABLES

Page

Table 1: Summary of microgrid model parameters [345,347]. 99

Table 2: Calibrated parameters for the solid oxide test bench. 138

ACRONYMS

AC	Alternate Current
APEP	Advanced Power and Energy Program
BOP	Balance of Plant
CAISO	California Independent Service Operator
CFD	Computational Fluid Dynamics
EPA	Environmental Protection Agency
GHG	Greenhouse Gas
GT	Gas Turbine
HHV	High Heating Value
HRSG	Heat Recovery Steam Generator
HTE	High Temperature Electrolysis
LCOE	Levelized Cost of Electricity
LHV	Low Heating Value
Ni	Nickel
NREL	National Renewable Energy Laboratory
P2G	Power to Gas
PEM	Proton Exchange Membrane
PEN	Positive electrode, Electrolyte, Negative electrode
PI	Proportional-Integral
PV	Photovoltaic

RES	Renewable Energy Sources
SB	Senate Bill
SCE	SoCal Edison
SOC	Solid Oxide Cell
SOE	Solid Oxide Electrolysis
SOEC	Solid Oxide Electrolysis Cell
SOSE	Solid Oxide Steam Electrolysis
SSTB	Short Stack Test Bench
ST	Steam Turbine
T&D	Transmission and Distribution
TPB	Triple Phase Boundary
UCI	University of California Irvine
YSZ	Yttria Stabilized Zirconia

ACKNOWLEDGEMENTS

I express my sincere and genuine gratitude to my advisor and committee chair, Professor Jack Brouwer, for being much more than a great academic advisor, but a great mentor, strong advocator, true supporter, and real friend. He has always believed in me and allowed me to be involved in many academic projects and extra activities. His enthusiasm for renewable hydrogen has encouraged my positivity to follow my education in this area of my interest. His continuous guidance has made this work possible.

I thank Professor Scott Samuelsen, for establishing the Advanced Power and Energy Program, which has provided many opportunities for graduate students like me to pursue their professional goals in this amazing program on many exciting subjects.

I thank my committee members, Professor Yun Wang, and Professor David Copp, for serving on my dissertation committee and candidacy exam committee. Also, I would like to thank you for your helpful advice on this work.

I express my appreciation to Paolo Colombo, without whom this work was impossible. Paolo has been great friend, hard working person and smart colleague who had been working together with me on the novel topic of Solid Oxide Electrolysis Systems during my first six months of PhD while he was a visiting scholar at UCI. We have been collaborating after he went back to Italy graduated from Politecnico di Torino which has resulted in several conference and journal publications.

I thank Professor Dustin McLarty and his team in Washington State University for developing an open-source tool called Efficient Allocation of Grid Energy Resources including Storage (EAGERS) which has formed the basis of the modeling efforts in this work. Also, I would like to thank prof. McLarty for his guidance and advice on this work.

I thank Dr. Luca Mastropasqua and Dr. Derek Mcvay who have been great colleagues, professional mentors, and amazing friends. They have helped me in different projects, and I could not get my deep knowledge and great hands-on experience without their supports, advice, and helps.

I thank my lab mates and colleagues at the Advanced Power and Energy Program and my colleagues at Politecnico di Torino for their helps and being co-authors in the publications of this dissertation in Chapters 1, 3 and 4. Thank you to Dr. Michael McKinnon for being co-author in the “Hydrogen is Essential for Sustainability” paper. Thank you to prof. McLarty and Paolo Colombo for being co-authors in the “Dynamic Behavior of a Solid Oxide Steam Electrolyzer System Using Transient Photovoltaic Generated Power for Renewable Hydrogen Production” paper. Also, thank you to Paolo Colombo and prof. Santarelli for being co-authors in the “Dynamic dispatch of solid oxide electrolysis system for high

renewable energy penetration in a microgrid" paper. I would like to thank dr. Mastropasqua for his support and assistance with the experimental chapter of this work.

Additionally, I thank the journal of current opinion in electrochemistry and the Elsevier Ltd for permission to include portions of Chapter 1, which was originally published in the journal of current opinion in electrochemistry. I also thank European fuel cell forum for permission to include portions of Chapter 3, which was originally published in the European fuel cell forum proceedings. Also, I would like to thank the journal of electrochemical energy conversion and storage and the American Society of Mechanical Engineers (ASME) for permission to include Chapter 4, which was originally published in the journal of electrochemical energy conversion and storage. In addition, I thank the journal of energy conversion and management and the Elsevier Ltd for permission to include Chapter 5, which was originally published in the journal of energy conversion and management.

At the end, I thank my lovely wife, Maryam, who has been with me along this journey and has been supporting me regardless of the results throughout all the hard steps in my PhD. She has been a great wife and wonderful leader who has managed our life while doing her PhD at the Advanced Power and Energy Program. Also, I would like to thank my lovely parents for their love and emotional support throughout my academic journey. Also, I would like to thank my lovey brother, who has always had a great role in my life inspiring me to work hard and being strong in tackling different problems.

VITA

Alireza Saeedmanesh

2006-2010	B.Sc. in Mechanical Engineering University of Tehran, Tehran, Iran
2010-2012	M.Sc. in Mechanical Engineering University of Tehran, Tehran, Iran
2017-2021	Ph.D. in Mechanical Engineering Advanced Power and Energy Program, University of California, Irvine
Sum.2019	Internship – Renewable Hydrogen and energy Storage 174 Power Global, Irvine, CA, USA

FIELD OF STUDY

High temperature energy conversion systems focusing on solid oxide electrolysis cell and fuel cell, renewable integrated stationary systems, energy storage, and renewable hydrogen.

PUBLICATIONS

"A SOFC-based Multi-Energy System for the Efficient Production of Hydrogen and Power from Natural Gas for Hydrogen Refueling Station Applications.", American Institute of Chemical Engineers Conference, 2020
Cammarata, A., Mastropasqua, L., **Saeedmanesh, A**., Brouwer, J., and Campanari, S.

"Dynamic Modeling of a Concentrated Solar-Integrated Solid Oxide Cell System for Renewable and Zero-Carbon Hydrogen Production.", 14th European SOFC & SOE Forum, 2020
Kim, J. Y., **Saeedmanesh, A.**, Mastropasqua, L., and Brouwer, J.

"Integration of Solid Oxide Steam Electrolyzer System into the UCI Microgrid to Support High Renewable Use.", ECS Transactions, 2020
Saeedmanesh, A., Colombo, P. and Brouwer, J.

"Dynamic dispatch of solid oxide electrolysis system for high renewable energy penetration in a microgrid.", Journal of Energy Conversion and Management, 2020
Colombo, P., **Saeedmanesh, A.**, Santarelli, M. and Brouwer, J.

"Integration of Solid Oxide Fuel Cell with Liquid Desiccant Cooling for Generation of Combined Cooling and Power for a Server.", ECS Transactions, 2019
Asghari, M., Lavernia, A., **Saeedmanesh, A.**, James, S. and Brouwer, J

"Dynamic Behavior of a Solid Oxide Steam Electrolyzer System Using Transient Photovoltaic Generated Power for Renewable Hydrogen Production.", Journal of electrochemical Energy Conversion and Storage, 2019
Saeedmanesh, A., Colombo, P., McLarty, D. and Brouwer, J.

"Hydrogen is Essential for Sustainability.", Current Opinion in Electrochemistry, 2018
Saeedmanesh, A., Mac Kinnon, M. and Brouwer, J.

"Dynamic Behavior of a Solid Oxide Steam Electrolyzer System Using Transient Photovoltaic Generated Power for Renewable Hydrogen Production.", ASME - International Mechanical Engineering Congress and Exposition, 2018
Saeedmanesh, A., Colombo, P., McLarty, D. and Brouwer, J.

"Dynamic Modeling of a Solid Oxide Electrolyzer System under Two Different Thermal Control Strategies.", 2018
Saeedmanesh, A., and Brouwer, J.

ABSTRACT OF THE DISSERTATION

Solid Oxide Electrolysis Cell (SOEC) and System Technology for Widespread Use with Renewable Energy

by

Alireza Saeedmanesh

Doctor of Philosophy in Mechanical & Aerospace Engineering

University of California, Irvine, 2021

Professor Jack Brouwer, Chair

Sustainable energy conversion requires zero emissions of greenhouse gases and criteria pollutants using primary energy sources that the earth naturally replenishes quickly, like renewable resources. Solar and wind power conversion technologies have become cost effective recently, but challenges remain to manage electrical grid dynamics and to meet end-use requirements for energy dense fuels and chemicals. Renewable hydrogen can be made at very high efficiency using electrolysis systems that are dynamically operated to complement renewable wind and solar power dynamics and to provide feedstocks for chemicals and energy-dense fuels.

A solid oxide electrolysis system is a highly efficient high temperature system that is suitable for large-scale hydrogen production. It has shown inherently high energetic and exergetic efficiencies for production of both hydrogen and other synthetic gases (e.g., methane synthesized from renewable hydrogen and captured CO_2) via electrolysis and co-

electrolysis processes. The high operating temperature of these systems eliminates the need for expensive catalysts and increases conversion efficiency and system integration opportunities.

In this dissertation, first, a quasi-3D spatially and temporally resolved solid oxide electrolysis cell model is developed. A solid oxide electrolysis system including stack and balance of plant components, and its required control strategies is designed, modeled, and developed. A comparative analysis of an SOEC system for a stepwise dynamic operation under two different thermal control strategies is performed, by analyzing the overall system performance at different stack power loads. Moreover, the dynamic behavior of a SOE system which uses transient PV generated power as an input to produce compressed renewable hydrogen to be stored or injected directly into the natural gas network is analyzed under sunny and cloudy days scenarios.

Next, a dynamic model is developed to evaluate the dynamic dispatch of solid oxide electrolysis system into the UCI microgrid to support high renewable use in the UCI microgrid. Also, an optimization model is developed to minimize imported electricity and natural gas consumption for different PV installed capacity scenarios in the UCI microgrid.

Finally, a solid oxide short stack is experimentally evaluated in electrolysis mode in steady state and dynamic perspectives. Effects of different operating parameters i.e., operating temperature and fuel composition on the performance of the short stack are investigated. The capability of the short stack to operate dynamically under different input profiles is explored. Electrochemical impedance spectroscopy technique is employed to characterize the short stack in both cell and stack levels.

1 Introduction

1.1 Motivation

The world population is steadily increasing, expected to reach 9.7 billion by 2050 [1]. Additionally, modern societal living standards, the industrialization and urbanization of developing nations, long-distance travel, shipping, and freight transport are experiencing rapid growth [2–6]. Hence, global demands for energy services, including transportation, residential and commercial buildings, electricity generation, and industrial applications, will increase substantially over this century [7–14].

Since the Industrial Revolution, the vast majority of energy converted in society has been obtained from fossil fuels -coal, natural gas, and petroleum- which require tremendously long times for earth and the power of the sun to produce. This trend is widely expected to continue in coming decades [15–18]. Although the available global quantity of these fuels is extremely large, they are nevertheless finite and so will inevitably 'run out' at some near future time as we consume them much faster than the earth produces them [19]. A primary reason for their continued use is economics – energy from fossil fuels has been more cost effective than most other sustainable forms of energy, including renewable resources.

In addition, the continued use of fossil fuels is associated with increased criteria pollutant and greenhouse gas (GHG) emissions [20]. Emissions from fossil fuel combustion degrade air quality, pose human health risks, and drive global climate change. In 2017, global energy-related CO_2 emissions reached an historic high of 32.5Gt as a result of global economic growth, reduced fossil-fuel prices and weaker energy efficiency efforts [21]. Figure 1 shows the emissions associated with different energy sector for the whole US. According to Environmental Protection Agency (EPA) [22], although the US emissions have increased about 1.3% from 1990 to 2017, emissions associated with some of the energy sectors have increased e.g., transportation and agriculture sectors. However, emissions associated with other energy sector have decreased e.g., electricity generation, industry, residential and commercial sectors.

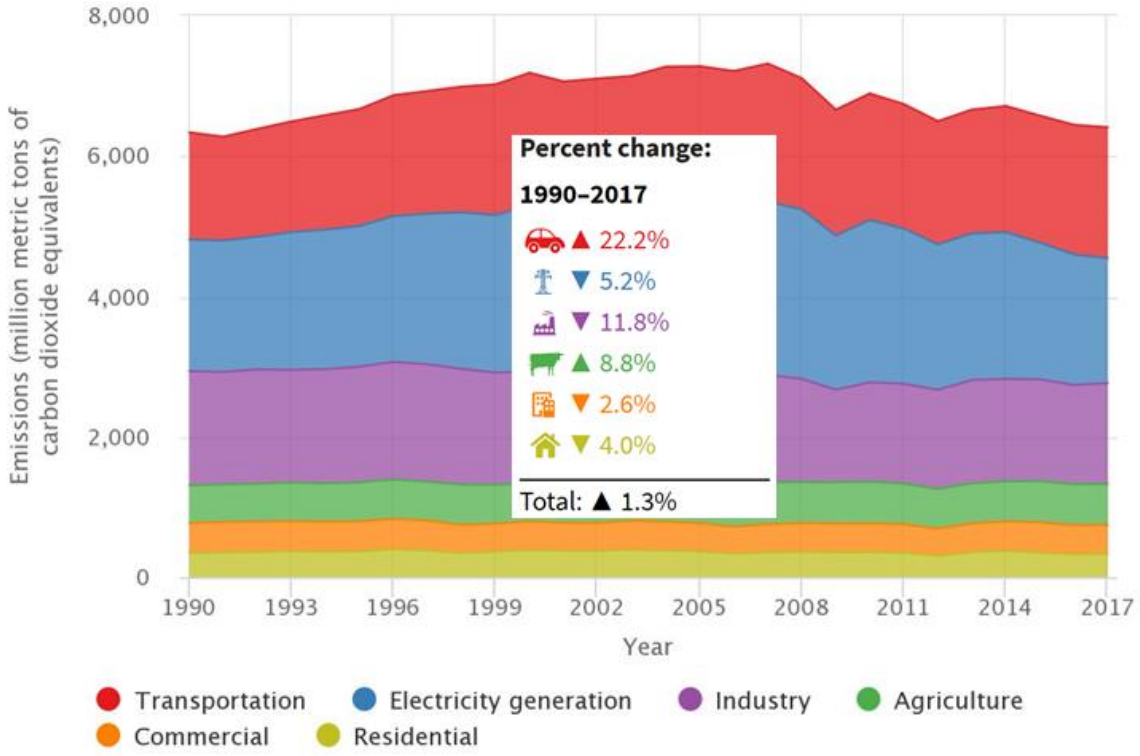

Figure 1: Emissions associated with different energy sectors in the US from 1990 to 2017 [22].

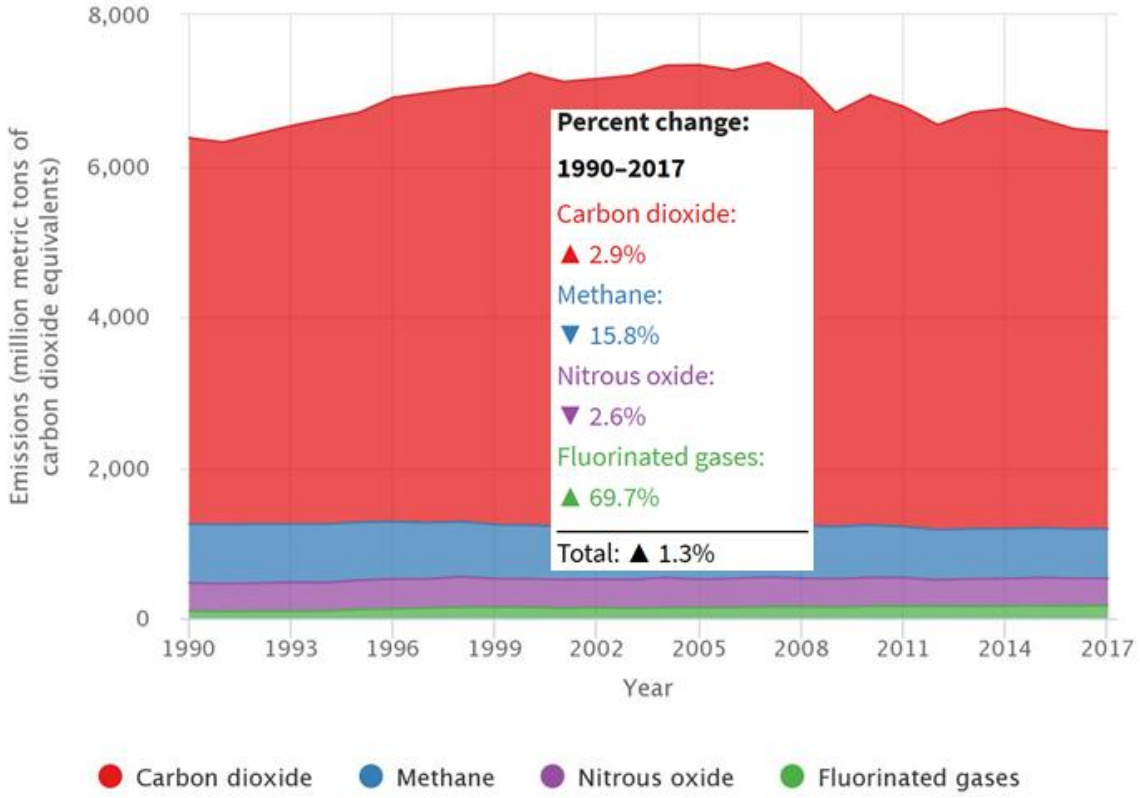

Figure 2: Different parts of the emissions in the US from 1990 to 2017 [22].

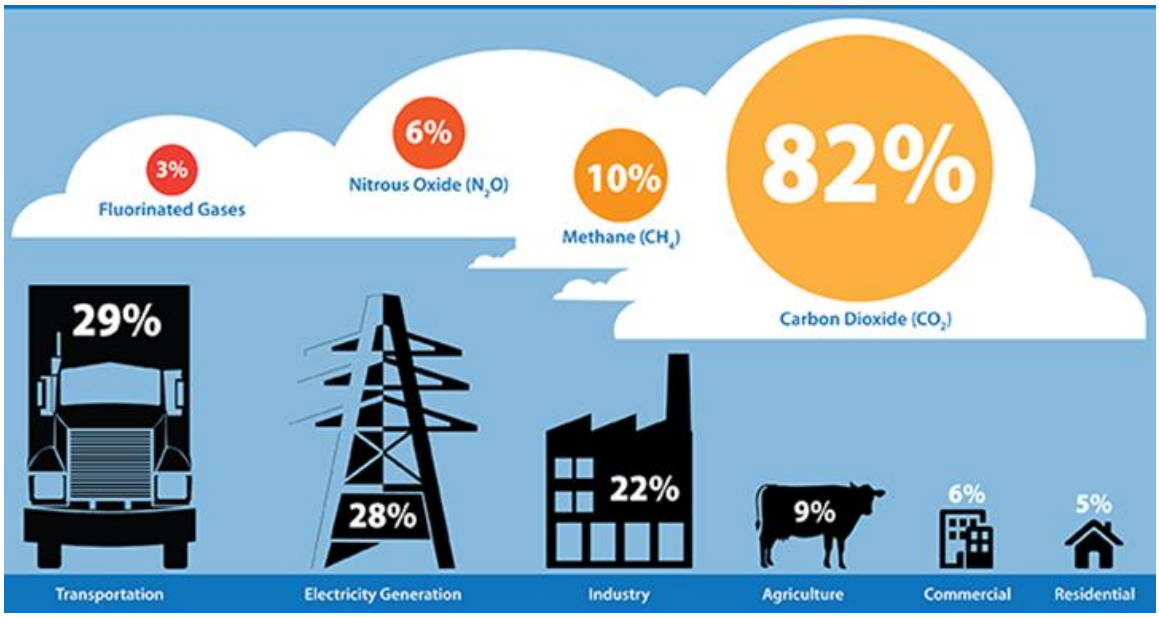

Figure 3: Energy Sectors and their contribution in emissions in the US in 2019 [22].

Figure 2 shows different species of the emissions from 1990 to 2017. According to figure 2, CO_2 is responsible for most of the emissions in the US. Other emissions that build a small portion of the whole US emissions include methane, nitrous oxide, and fluorinated gas.

According to Figure 3, in 2019, in the US, transportation is responsible for 29% of emissions, followed by electricity generation with 28% contribution. The industry, agriculture, commercial and residential sectors are responsible for 22%, 9%, 6% and 5% respectively.

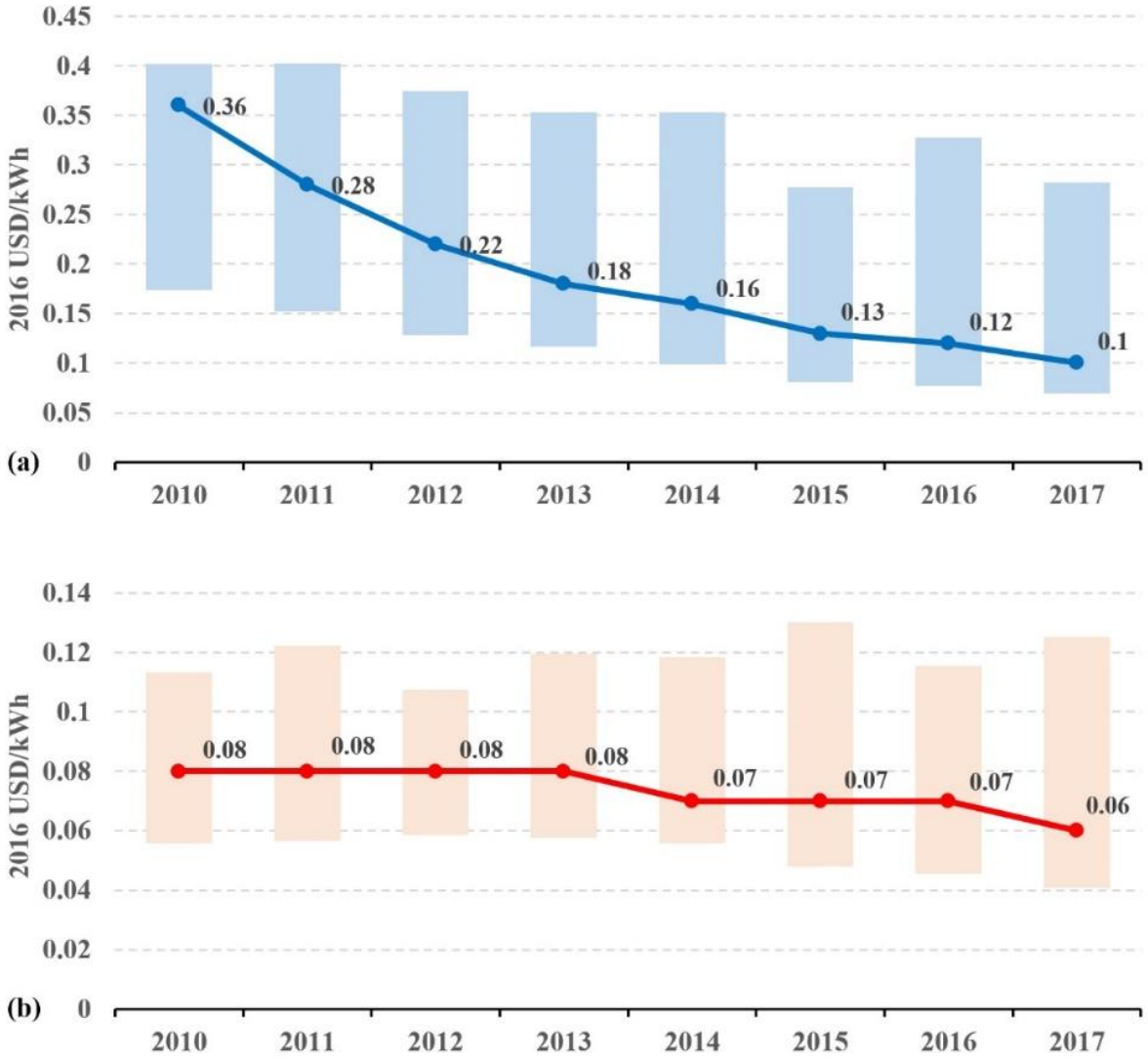

Figure 4: (a) Solar PV global weighted average LCOE 2010-2017, (b) Onshore wind global weighted average LCOE 2010-2017 [23].

Additionally, the uneven geographic distribution of energy resources is associated with conflicts between nations. Given these issues, it is clear that eventually societies across the world must accomplish all energy conversion from renewable resources [24,25,34–43,26,44–53,27–33].

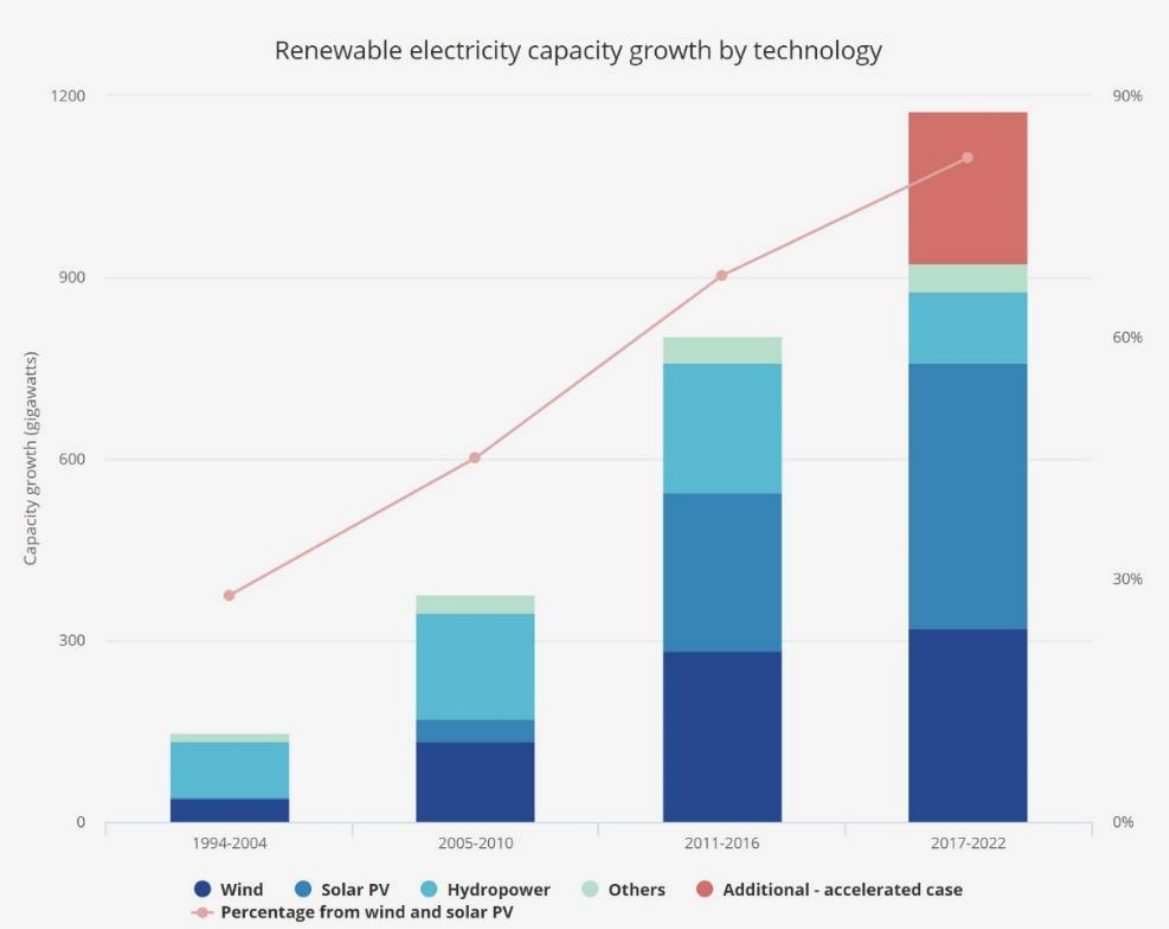

Figure 5: Renewable electricity capacity growth by technology 1994-2022 [23].

While the earth rapidly and naturally replenishes many forms of primary energy (solar, wind, geothermal, hydropower, biomass, biogas, and wave and tidal energy), this study will focus upon photovoltaic (PV) and wind power as they have become increasingly competitive in the power generation market [54,55,64–69,56–63]. The global weighted average Levelized Cost of Electricity (LCOE) from both solar PV and an onshore wind turbines in 2017 were in the middle of fossil fuel cost ranges, and will be close to the lower end of this range by 2022 (Figure 4) [70]. Reductions in LCOE are making renewable energy from solar PV panels and wind turbines more desirable than other renewable resources, and even preferred over fossil resources [71,72]. As a result, renewable electricity capacity growth has largely been associated with solar PV and wind (Figure 5) [73].

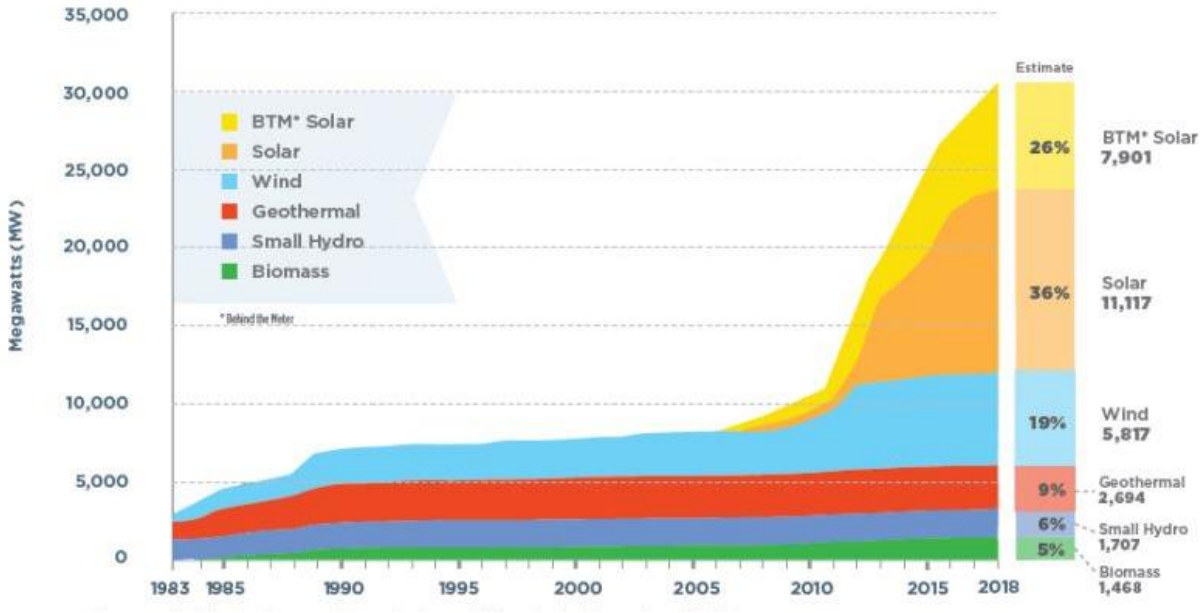

Figure 6: Annual Cumulative Installed Renewable Capacity [74].

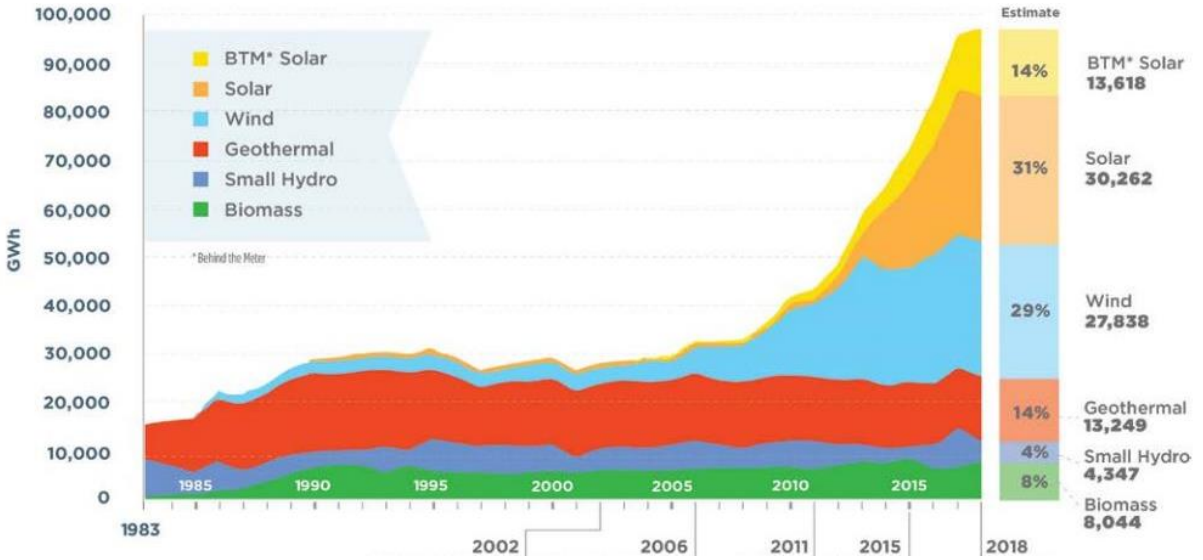

Figure 7: Total Renewable Generation Serving California Load [74].

California has been installing a huge amount of renewable resources, specifically solar and wind, since 2000. According to Figure 6, California had 30 GW of renewable installed capacity [74]. Also, according to Figure 7, about 100 TWh of California's electricity was generated by renewable resources in 2018 [74].

In 2018, the California governor signed SB100 billed through which California is mandated to produce 50% of its electricity with renewable resources by 2025 and 605 of it by 2030.

Also, it mandates California to have zero-carbon electricity generation by 2045. Moving towards SB100, California will have much more of renewable installation in the near future. While integrating wind and solar power into electric grids at low levels has been accomplished throughout the world, integrating increasing amounts is challenging. First, the intermittent and uncontrollable nature of some renewable resources (particularly solar and wind) increases the dynamics of electrical grid operation, which can have major impacts on the performance of the system [75–78]. Moreover, the integration of renewable energy sources into existing electric power systems increases the interdependence between natural gas and electricity transmission networks, and as a result the required dynamic operation of the gas grid increases [79,80]. Integrating high levels of solar and wind power into electric grids requires various types of technologies that can provide instantaneous, hourly, daily, weekly and seasonal storage, power generation, and ancillary services to ensure the stability of the grid [81]. Moreover, characterizing resource variability and implementing different balancing strategies in different regions with different resources requires detailed planning by utility providers and other stakeholders [82]. The potential use of and interactions between firm low-carbon resources (e.g., natural gas with carbon capture and sequestration), variable renewable resources, and highly dynamic electric resources (short-duration battery energy storage and demand-side flexibility) must likely all contribute to a highly renewable electric grid [83]. However, due to lack of energy storage facility and rapid increase in renewable installation, California has curtailed a huge amount of solar and wind generated electricity in 2018, 2019, and 2020 according to the California Independent System Operator (CAISO) [84]. According to Figure 8, 500 GWh of energy was curtailed in 2018 in California while this number almost doubled in 2019 by having 950 GWh of curtailed renewable energy and tripled in 2020 by having 1500 GWh curtailment (Figure 8). Finding a promising solution to store inexpensive and otherwise curtailed, large-scale renewable energy produced during peak generation times and seasons, followed by use in later demand periods is an increasingly important issue.

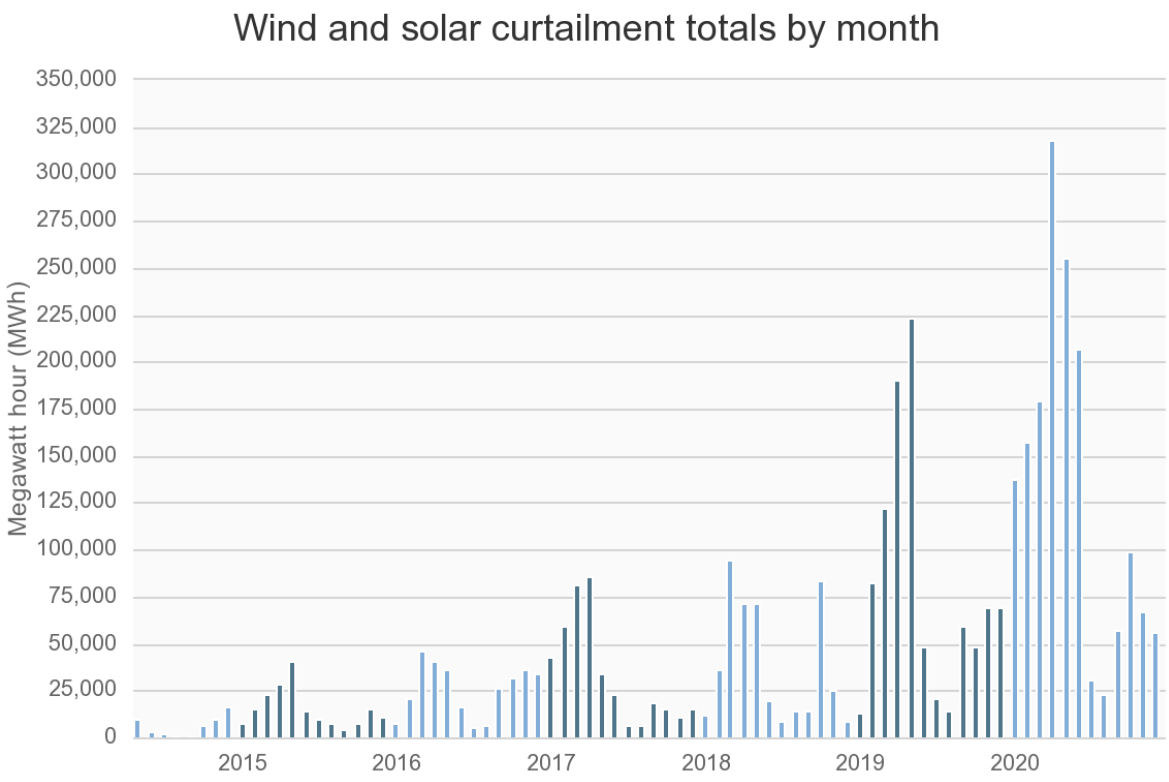

Figure 8: Wind and solar curtailment in California in 2018, 2019, and 2020 [84].

On the other hand, in many energy markets the peak demand occurs after sunset, when solar power is no longer available. In locations where a substantial amount of solar electric capacity has been installed, the amount of power that must be generated from sources other than solar or wind displays a rapid increase around sunset and peaks in the mid-evening hours, producing a graph that resembles the silhouette of a duck. The duck curve operation makes different challenges for operation of dispatchable conventional electricity generation resources since they were not designed to operate high ramp up and ramp down rates. Figure 9, depicts the duck curve in California electric grid during a day in February 2020.

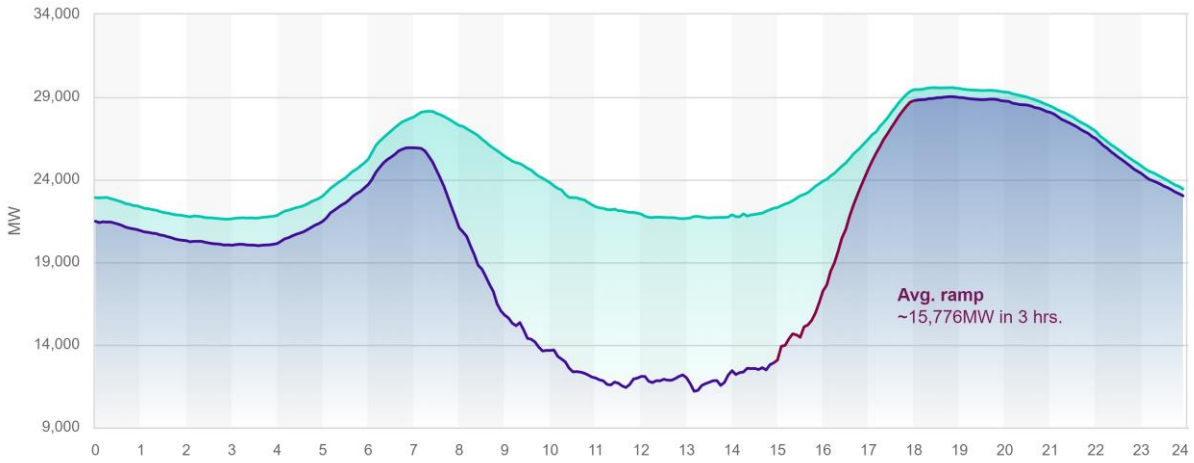

Figure 9: Demand and net demand in a day in February showing the duck curve [84].

California needs a mature technology to enable storing inexpensive and otherwise curtailed renewable electricity. Different forms of energy storage can be used in various levels and for various purposes in the electric grid to ensure that the supply of power generation matches power demand at every instant. Energy storage technologies include thermal storage, compressed air, pumped hydroelectric storage, flywheels, batteries, flow batteries, capacitors, and hydrogen [85,86,95–100,87–94].

Battery energy storage is a good candidate for small, isolated power systems to store small amounts of excess renewable electricity for short durations (hours to days). [101–103]. However, for large-scale and long duration storage, it must be considered that lithium-ion battery systems will be limited due to immutable features of: (1) insufficient global reserves of lithium and cobalt to produce enough batteries to meet all of the storage required [104–107], (2) challenges with self-discharge that preclude seasonal storage [108–115], (3) challenges with recycling and waste [113,116], and (4) lithium-ion battery energy density may not become sufficient to meet some end-uses [117–119].

P2G technology, which involves the conversion of electrical power into a gaseous energy carrier, is a promising prospect for future energy systems seeking sustainability, as it can address many of the challenges associated with 100% renewable systems [120,121]. Integrating high levels of solar and wind requires a large storage capacity which can be provided by hydrogen production via a P2G approach [122–128]. Hydrogen can be supplied completely from excess renewable energy using P2G, which benefits both balancing the

electrical grid with high use of variable, unpredictable renewable power, and providing high capacity, long-term energy storage for seasonal shifting [129–137]. Hydrogen production via P2G has also been shown to be the most cost-effective approach for long-term energy storage [138]. Newly developed smart energy systems provide more efficient, more cost-effective, and more sustainable solutions by combining both renewable energy sources and hydrogen energy systems [139]. Energy management strategies, as well as predictive controllers, are important components of combined renewable energy sources and hydrogen energy systems because they allow hydrogen production using surplus renewable energy and power production from hydrogen when renewable energy is insufficient [140–143].

P2G has shown considerable potential in transitions to 100% renewable energy systems in different countries [144–153]. While the emergence of hydrogen over other low-carbon technologies will require reductions in cost [154], these reductions can be facilitated with appropriate policies that support development of infrastructure to transition to a hydrogen economy.

A recent study that has been done by NREL proves that when the duration of storage goes higher than around 13 hours, then fuel cell + hydrogen tank storage and fuel cell + geological storage would be financially more reasonable and suitable compared to li-ion batteries. Figure 10 shows the mentioned study from NREL for comparing P2G and battery energy storage performance for long duration of storage [155].

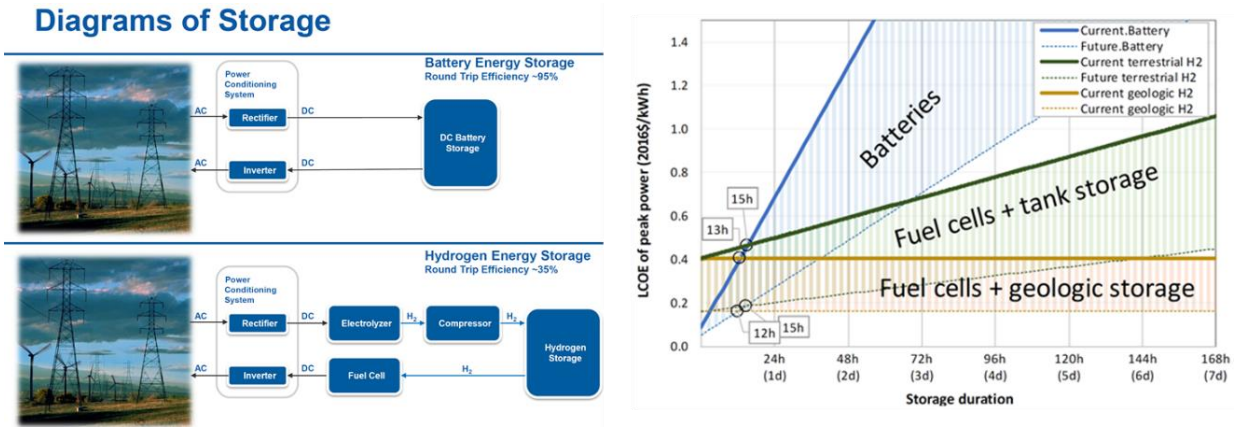

Figure 10: Importance of P2G in long duration of storage compared to battery energy storage [155].

According to [23], there is a long duration of storage required for the California electricity grid to reach to 100% renewable grid. Figure 4 shows residual load resulting from simulations of a 100% renewable California electric grid, hourly matching demand with available solar and wind resources. Two cases are considered: (1) wind dominant, and (2) solar dominant. While the amount of electric energy produced is slightly greater than the demand, it is clear that massive and seasonal energy storage is required.

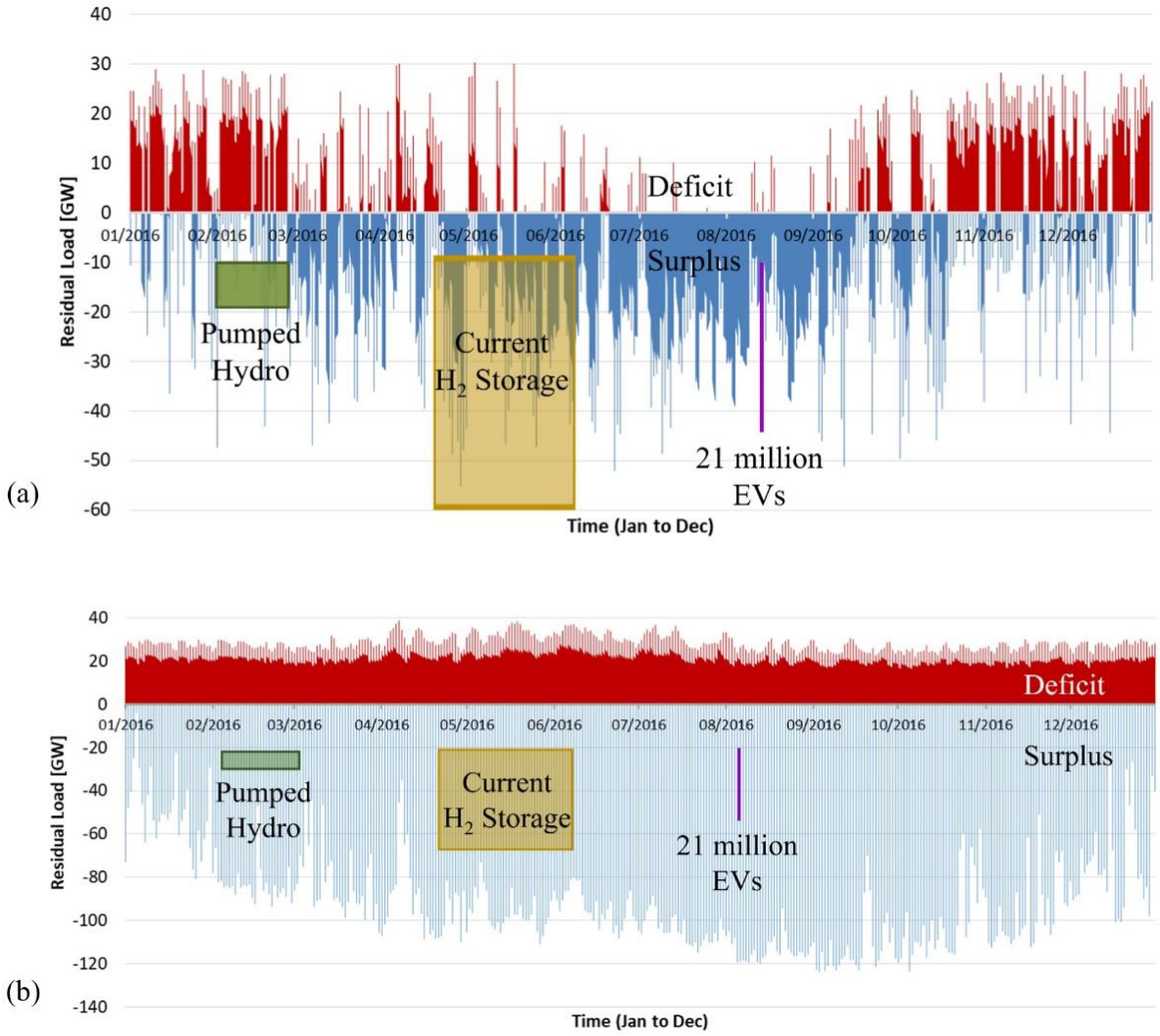

Figure 11: 1-year hourly simulation of the load and power generation dynamics of a 100% renewable grid in California, and the capacity of different storage technologies for (a) wind dominant case (37GW solar capacity and 80GW wind capacity installed) and (b) solar dominant case (162GW solar capacity, 5.6GW wind capacity installed) [23].

Options for storage technologies are also presented in Figure 11 showing that both the power and energy capacity of hydrogen energy storage in current gas infrastructure (pipelines and storage facilities) is the only option that can technically balance renewable power and energy with load on an annual basis. The magnitude of hydrogen energy storage compared to existing pumped hydro and to lithium-ion batteries (from complete electrification of the light and medium duty fleet of 21 million vehicles) is the only one sufficient to hourly and seasonally balance load and generation. This fact, together with the lack of self-discharge or evaporation, and separate power and energy scaling that enables cost effective seasonal storage, make hydrogen essential for achieving our zero-emission goals. While seasonal storage appears more clearly required for the wind dominant case, similar amounts of seasonal storage and more daily storage are required for the solar dominant case.

Many research efforts have suggested that the bulk of future energy conversion could be generated by renewables (largely wind and solar power) in combination with energy storage (including large-scale battery energy storage) and the electrification of end-use sectors, e.g., transportation, residential and commercial buildings, and industry [156–158]. Indeed, a significant body of research exists regarding technologies, costs and performance analysis of electrification options, with technology projections in the various sectors [159,160,169,161–168].

Figure 12 presents the U.S. subsector primary energy conversion shares in 2015 [170]. While in the transportation sector, initial electrification of light duty vehicles is occurring now, complete electrification of the light duty fleet and electrification of heavy duty transportation face challenges including upfront costs, range limitations, payload requirements, and infrastructure development [171–173]. The residential and commercial building sectors are widely amenable to electrification and should be electrified as much as possible using various, potentially cost effective technologies [174–178]. For the industrial sector, studies examining the potential electrification of its subsectors, including cost and performance analysis, are limited due to the complexity and challenges associated with the industrial sector [178–182].

It must be considered that electrification of all end-use sectors will be potentially more expensive and less resilient than transforming both electricity and fuel production to zero emissions technologies [163,183]. In addition, some end-uses such as aviation, long-haul trucking, shipping, heavy industry (e.g., cement, steel production) and the fertilizer industry, which account for roughly 30% of global carbon emissions, are difficult to electrify [184–187]. Furthermore, demands for these sectors are expected to grow substantially in the coming decades. Hence, it is essential to find a solution for these difficult-to-electrify energy services [5,188–190]. It is required to find a zero carbon and zero emissions fuel that could be used for difficult-to-electrify end-users seeking for sustainability. The mentioned fuel could be renewable hydrogen that produced from renewable generated electricity via P2G.

Renewable hydrogen provides the best opportunity for a zero carbon and zero criteria pollutant emissions fuel across its life cycle, from production to end-use [191–198]. P2G enables the production of a clean feedstock that can be used in difficult to electrify applications [199,200]. P2G can also support the utilization of intermittent renewables in decarbonizing the industrial sector [201–203].

P2G is also a means of coupling renewable electricity and the transportation sector by producing a renewable fuel that can be used in state-of-art fuel cell vehicles with considerable environmental benefits [204–209]. Also, renewable hydrogen can be methanated with CO_2 to produce synthetic fuels like methane and methanol as alternative fuels for heavy duty transport [210–214]. In addition, P2G provides a path to store large-scale excess renewable electricity in the form of methane by using CO_2 capture process, which can be used in different applications e.g., combine cycle gas turbine power plants [215–221].

Although electrification is a good option for residential and commercial sectors, hydrogen as an energy carrier appears to be feasible in residential and commercial applications, as well as in microgrids and for cases when long duration or large magnitude storage is required [222–226]. Hydrogen can be used in different residential and commercial applications e.g., as an environmentally sustainable cooking fuel relative to conventional cooking fuels typically used in developing countries, such as liquefied petroleum gas, charcoal, and

firewood. The use of produced renewable hydrogen via P2G can reduce carbon emissions between 2.5-14 times (0.04kg CO_2eq/MJ) compared to firewood (0.1kg CO_2eq/MJ) and liquefied petroleum gas (0.57kg CO_2eq/MJ) [227].

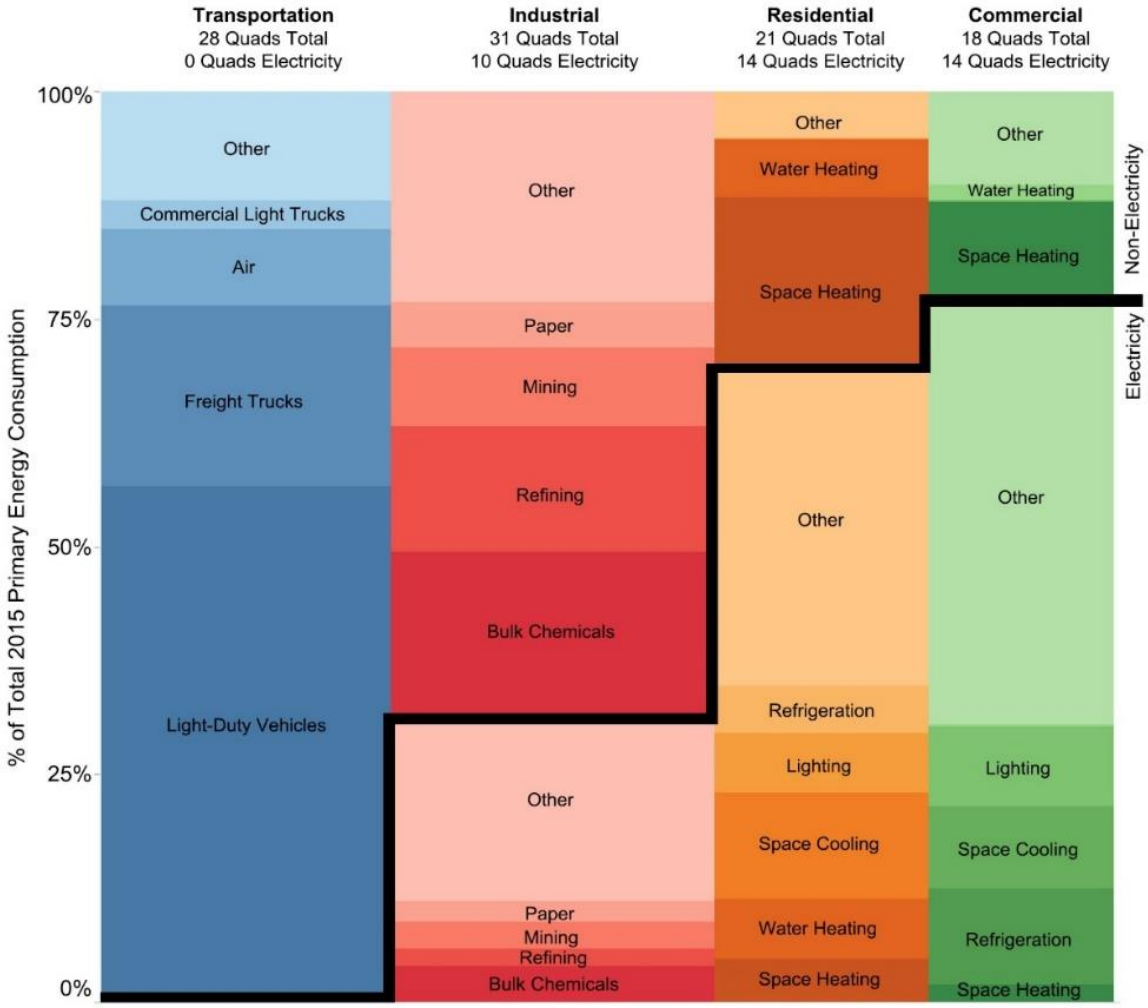

Figure 12: Depiction of U.S. primary energy consumption and electricity penetration shares for different energy subsectors in 2015 [23].

The global industrial demand for hydrogen has been increasing a lot since 1980 as shown in Figure 13 [228]. Hydrogen is used as feedstock for different industries including chemical (ammonia, polymers and resins), refining (hydrocracking and hydrotreating), iron & steel (annealing, blanketing gas and forming gas), and general industry (semiconductor, propellant fuel, glass production, hydrogenation of fats and cooling of generators). According to [229], most of the industrial hydrogen demand is produced with natural gas and coal via

steam methane reformation and coal gasification as shown in Figure 14. However, there are cleaner and more sustainable ways to produce hydrogen e.g., biomass gasification, nuclear based Cu-Cl cycle, electrolysis using solar and wind, and photo-electrochemical water split. According to [229], the cost associated with the mentioned sustainable ways are higher than cost associated with the conventional method. But the global warming potential of conventional hydrogen production methods are much higher than sustainable ones. In order to move towards having sustainable society, the hydrogen production industry should be also decarbonized. So, the policy makers and stakeholders should focus more on sustainable hydrogen production ways to decarbonize this sector of energy economy. The cost of hydrogen production using electrolysis technology is mainly associated with electrolyzer price which can be decreased when there is a huge demand for electrolyzers. Electrolyzer price would decrease when the electrolyzer manufacturing rate increases.

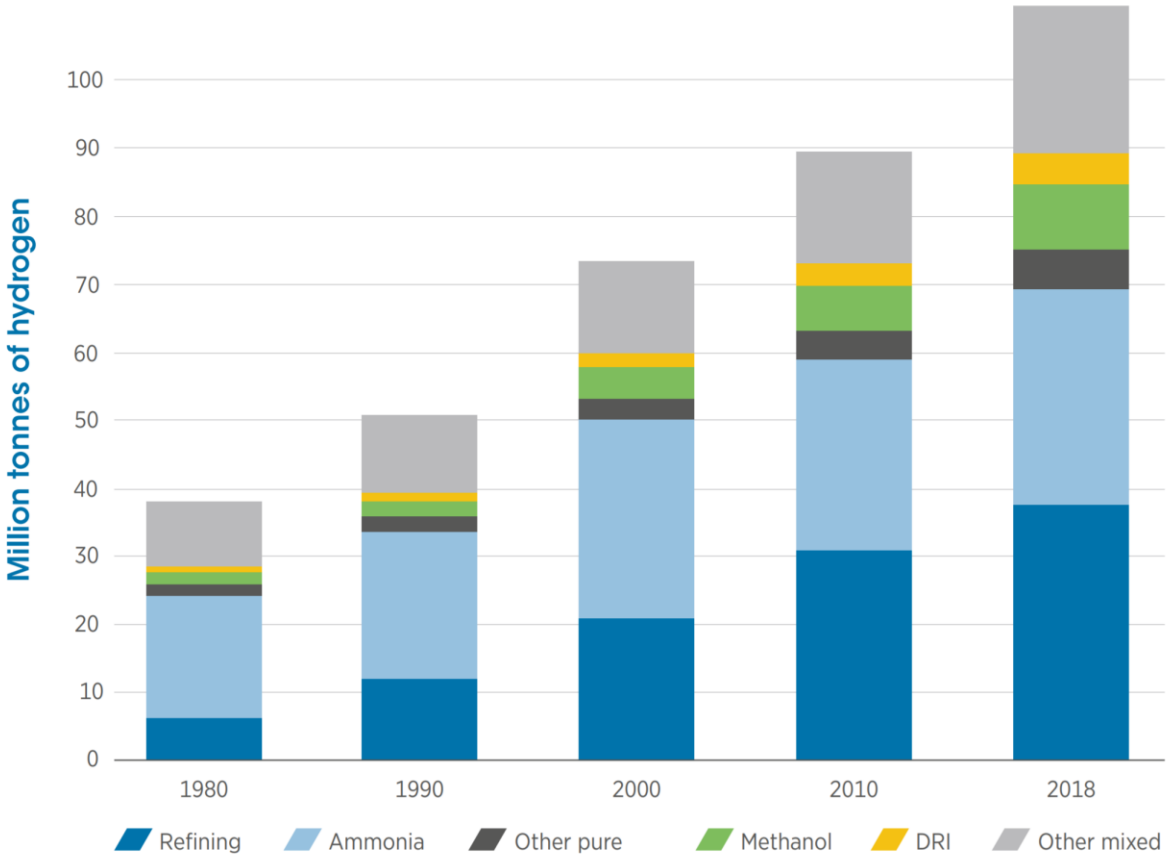

Figure 13: Global industrial demand for hydrogen [228].

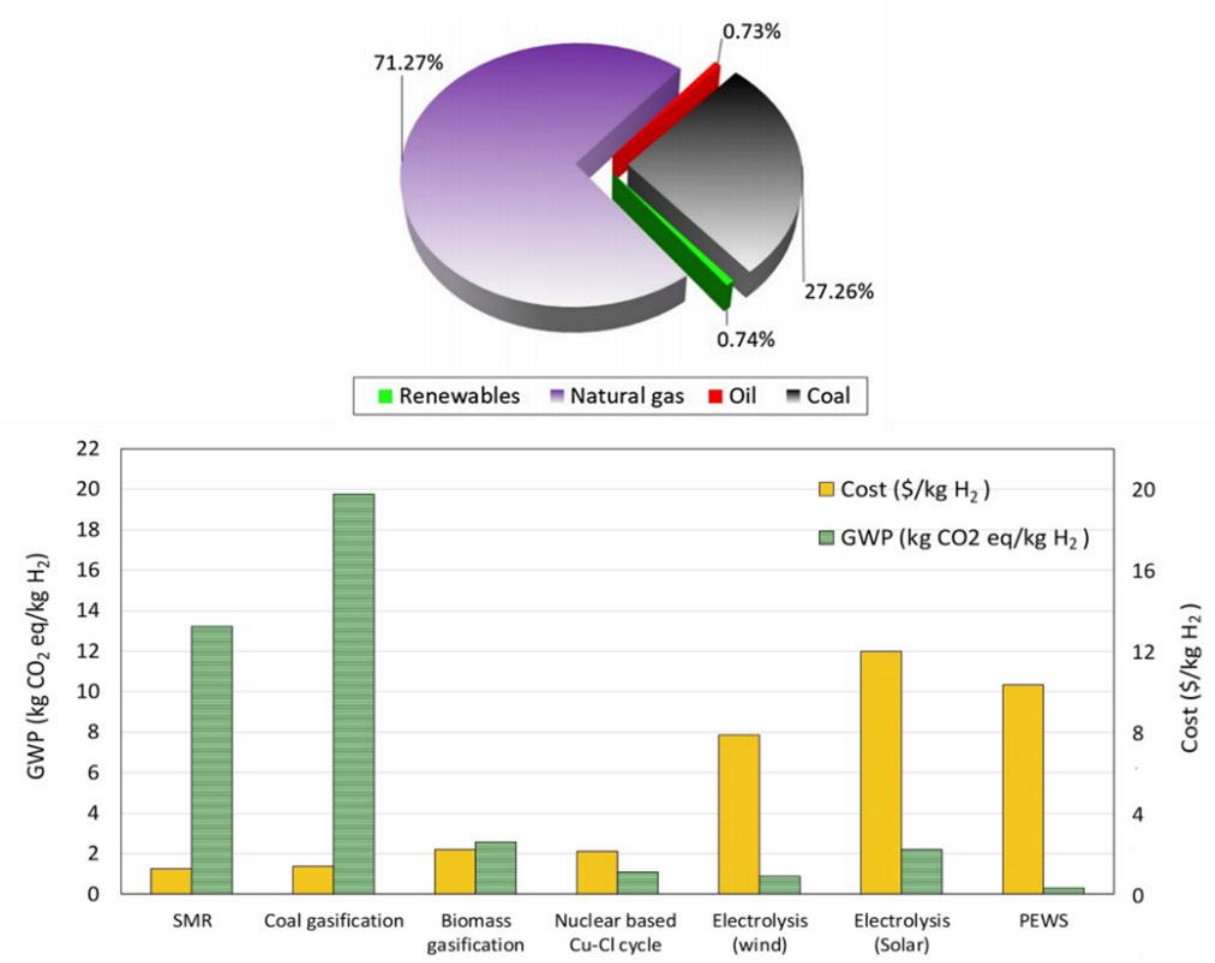

Figure 14: Global hydrogen production feedstock and global warming potential and costs associated with different pathways [229].

Due to all of the reasons that have been discussed so far in this Chapter, it could be concluded that P2G will be the heart of the future energy system as shown in Figure 15. P2G provides different benefits to the energy sector. First, it transfers renewable electricity into other energy sectors (difficult-to-electrify sectors). For example, in transportation sector, the hydrogen-driven fuel cell vehicle, buses, trucks, and trains have been already developed and commercialized. Second, it provides flexibility for the electricity grid to accommodate more renewable resources. Third, it provides usage of natural gas infrastructure for large-scale long-term energy storage. Forth, it provides large-distance energy transmission when the electricity grid is inadequate.

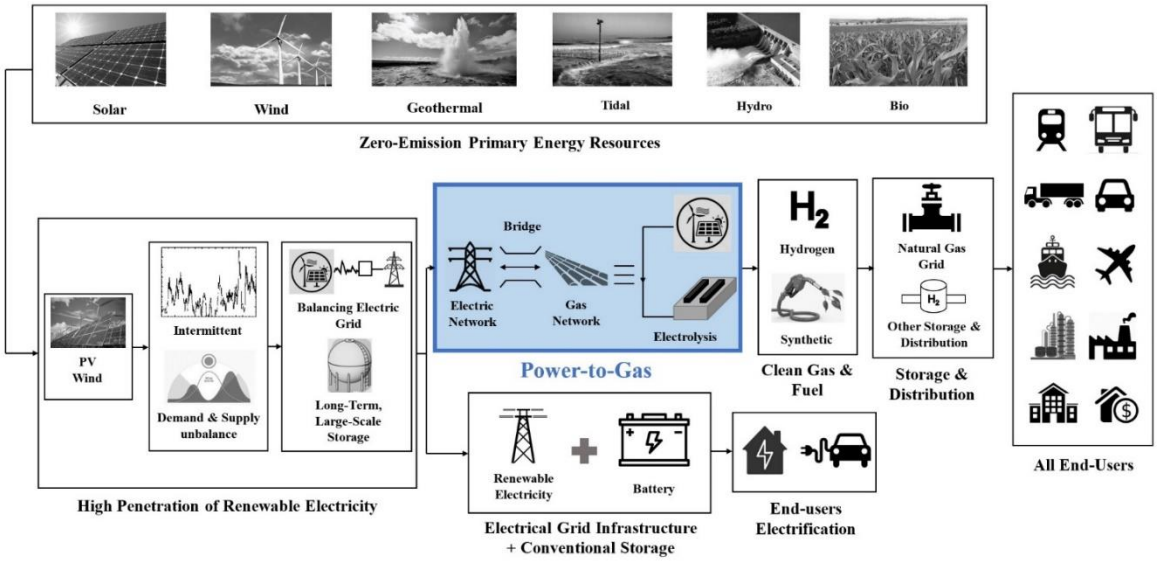

Figure 15: Schematic of future energy network showing P2G as a heart of the system [23].

Hydrogen storage, transmission and distribution are regarded as critical issues that must be solved before a technically and economically viable hydrogen economy can be established. Various hydrogen storage-delivery scenarios have been evaluated in terms of cost, performance and environmental impacts for both large-scale and small-scale hydrogen production [230–234]. Blending increasing amounts of hydrogen into the existing natural gas pipeline network has been proposed as a low cost means of handling renewable hydrogen, which makes large-scale hydrogen storage and distribution possible [235,236]. Hydrogen also enables Transmission and Distribution (T&D) of energy over long distances, which is simpler to manage and less costly than electric grid T&D.

P2G is the only energy storage concept that addresses massive energy storage in a range of more than 100GWh [237] in addition to T&D by using the existing natural gas system, which should provide the lowest cost solution for massive storage capacity. Using the gas network in this manner avoids unwanted installation of electric T&D infrastructure to manage the electric grid [238]. This strategy of storing and delivering renewable energy to markets appears to be viable without significantly increasing risks associated with gas end-uses (such as household appliances), overall public safety, or the durability and integrity of the existing natural gas pipeline network [239–242].

Over time, as hydrogen concentrations increase there may be some required alterations to current natural gas pipelines, including replacement of some pipelines, and adding new compressor stations and pressure management equipment to assure safety [243]. This should be followed by piecewise conversion of some pipelines to 100% hydrogen over time, until the entire gas network is converted to a zero-emissions hydrogen storage and delivery system. The dynamics for transferring hydrogen through a long natural gas transmission pipeline appear to be viable without significantly increasing risks in the gas system [244].

More studies and long-term measurements and demonstrations are required to further understand and address the impacts of increased hydrogen injection on existing natural gas infrastructure and to evaluate the required changes for metering systems and other components [245]. However, it is clear from historical use of town gas (containing primarily hydrogen and carbon monoxide) [246], from the safe operation of existing hydrogen storage and T&D infrastructure throughout Europe, the south-eastern US (from Texas to Florida), and in California [247], and from the current standards for hydrogen injection into the natural gas system that have already been set in Germany, Japan, Canada, England and other jurisdictions [135,248,249], that this evolution of the gas system is possible.

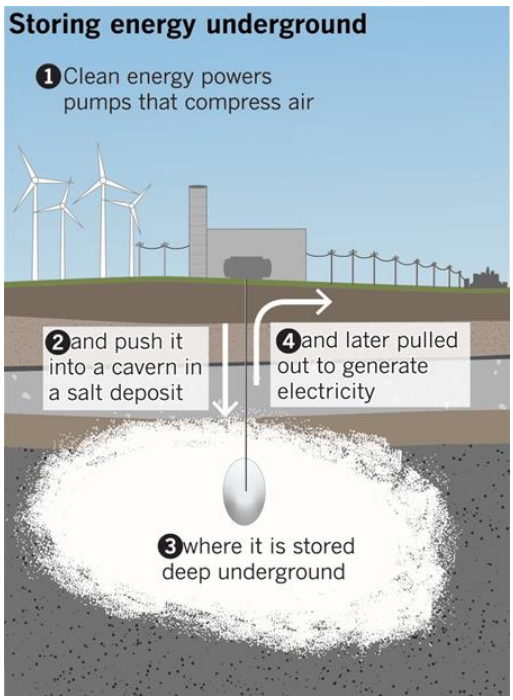

Figure 16: Schematic of cost-effective Geological storage for storing hydrogen [google images].

Geological storage such as salt caverns, on the other hand, is the one of the most cost-effective approach for storing large amounts of energy (Figure 16) because of the separate scaling of power and energy and massive size (each cavern can be individually sized to store between 2 million and 40 million cubic feet of natural gas, compressed air, liquid energy product, or hydrogen). Geological storage has a very low cost per unit of stored energy in comparison to other forms of energy storage. And unlike battery storage systems, geological storage systems incur a cost to provide a given rate of charge or discharge (rate) but incur very little additional cost for storing more energy (quantity). Long-term storage of hydrogen in geological formations is fully proven. Two large salt-cavern hydrogen storage facilities in Texas, operated by Praxair and Air Liquide, are interconnected with a vast hydrogen pipeline network. Beyond its storage function, hydrogen can also be transported to demand areas for use as a zero-emission vehicle fuel. This "sector coupling" allows hydrogen to be optimally dispatched for use as fuel for electricity generation or as vehicle fuel based on demand and price dynamics.

1.2 General Background

One of the ways to implement P2G is high-temperature highly efficient Solid oxide Electrolysis (SOE) technology. SOE technology has attracted considerable attention as an efficient large-scale hydrogen production system that can create a sustainable pathway to hydrogen production [250]. A vast body of research has been aimed at developing electrochemical, thermodynamic, and fluid mechanics models to investigate the effects of operating conditions, component materials, as well as cell geometry on the performance of SOE cells. They showed inherently high energetic and exergetic efficiencies for using SOE systems for both hydrogen and other synthetic gases (e.g., methane synthesized from renewable hydrogen and captured CO_2) via electrolysis and co-electrolysis processes [251–254]. The high operating temperature of SOE cells, i.e., 800–1300 K, eliminates the need for expensive catalysts and increases conversion efficiency (Figure 17) and system integration opportunities. The high operating temperature also allows use of thermal inputs to reduce the electrical power demand of the SOE system (Figure 18) and enhance the hydrogen production by using thermal energy for water to steam conversion [255,256]. These electrolysis systems can be operated dynamically to well complement renewable wind and

solar power dynamics [257,258]. One of the main challenges associated with operating at high-temperature is degradation of materials, but, recent studies have shown that the mixed conductor and proton conductor SOE cells are more stable and showing lower degradation rate [259,260].

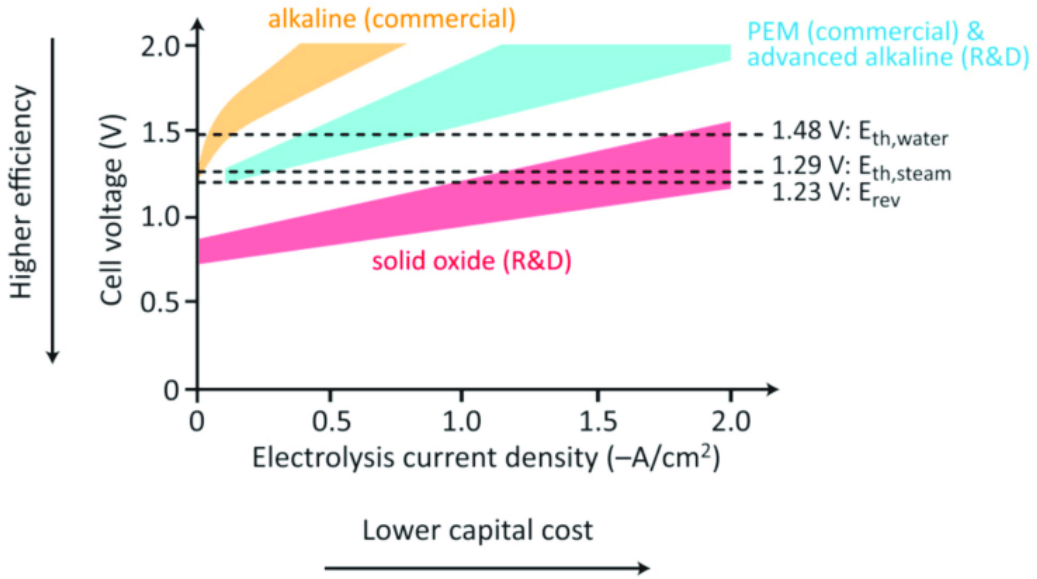

Figure 17: Comparison of SOE, Alkaline and PEM electrolyzers in terms of cost and efficiency [261].

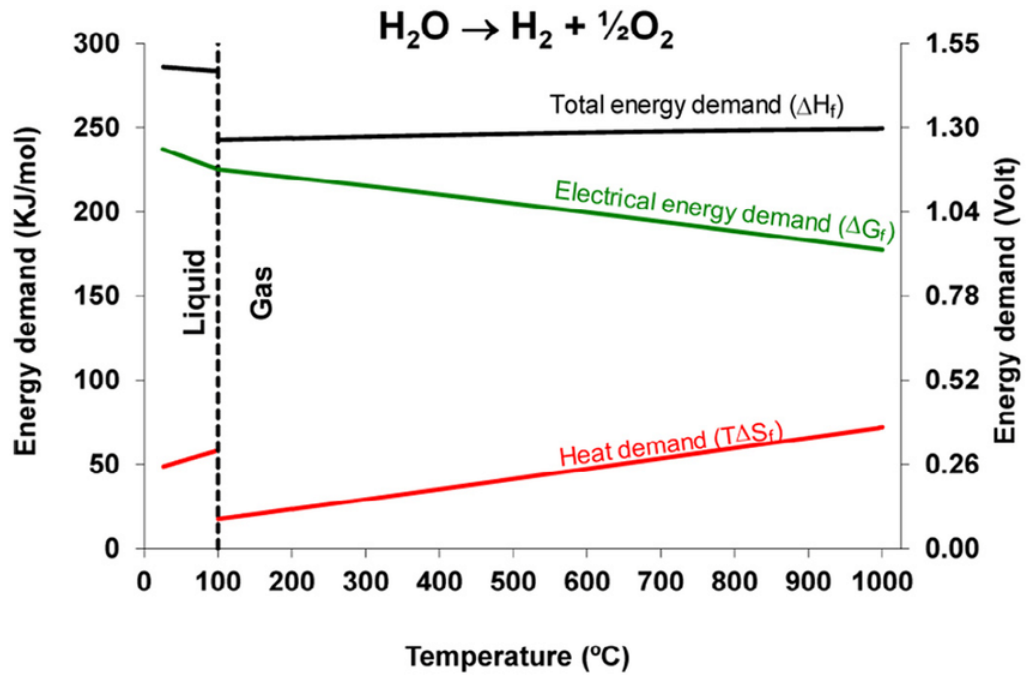

Figure 18: Total energy demand, electric demand and heat demand for electrolysis at different temperature [262].

The electrochemical reaction is achieved in an SOE cell by flowing superheated high temperature steam over a cathode and applying a voltage high enough across the cathode and anode to drive the reaction forward. Oxygen ions separate from the water at triple phase boundary on cathode side and travel across the electrolyte and combine at triple phase boundary on the anode side to create oxygen gas. Meanwhile in the cathode, hydrogen is created and remains mixed with steam (Figure 19). In a cell of given length, the concentration of hydrogen increases along the length of the flow direction of steam while the water concentration decreases.

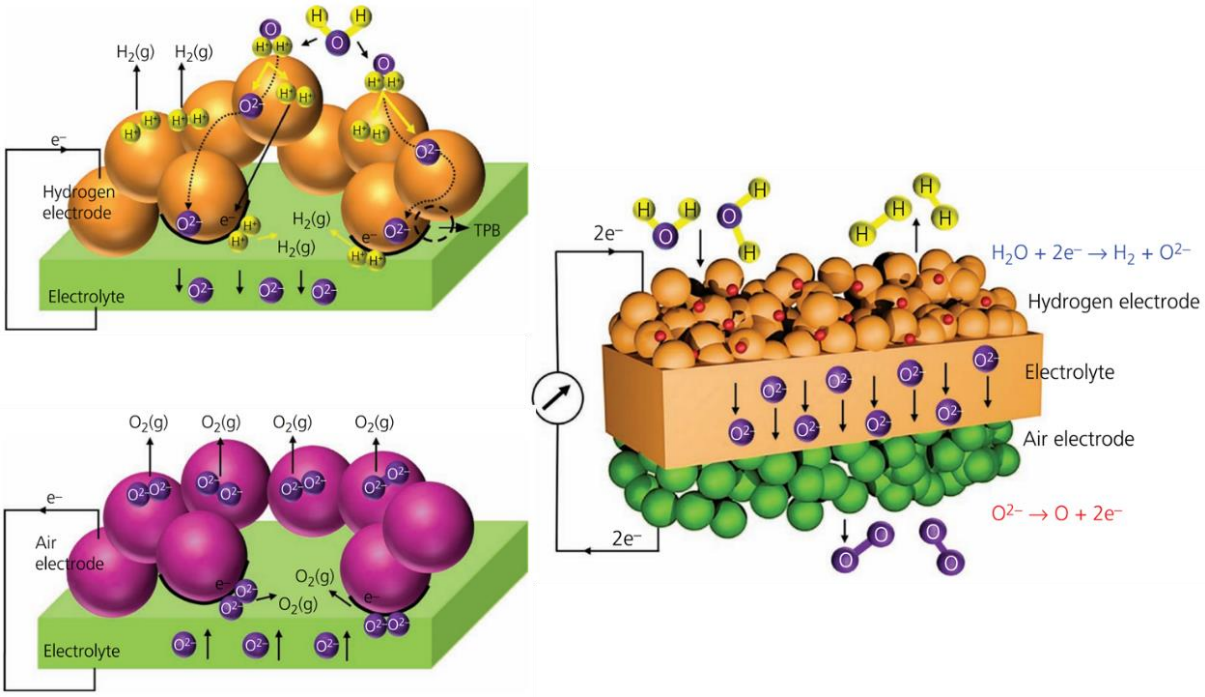

Figure 19: SOE individual cell and its compartments [263].

Three operating modes can be distinguished for a high temperature electrolysis (HTE) system: thermoneutral, endothermal, and exothermal. The HTE operates at thermal equilibrium (1.286V at 800°C) when the electrical energy input equals the total energy demand, and the electrical-to-hydrogen conversion efficiency is 100%. In the thermoneutral mode, the heat demand $Q=T\Delta S$ necessary to sustain the endothermic water splitting equals the heat released by the joule heating (ohmic losses) within the cell. In the exothermal mode, the electric energy input exceeds the enthalpy of reaction, corresponding to an electrical efficiency below 100%. In this mode, heat is generated from the cell and can be reused in the

system to preheat the inlet gases. This mode has also the advantage to operate at higher current density allowing decreasing the size of the system. However, it could be a source of prematurely ageing of the system components. Finally, in the endothermal mode the electric energy input stays below the enthalpy of reaction which means a cell voltage below the thermoneutral one (<1.286V at 800°C). Therefore, heat must be supplied to the system to maintain the temperature. This mode means electrical-to-hydrogen conversion efficiencies of the SOEC above 100%. This operation mode also allows minimal long-term degradation rates since it is achieved at the lowest power densities. Figure 20 shows these three operating modes for steam high temperature electrolysis at 800°C.

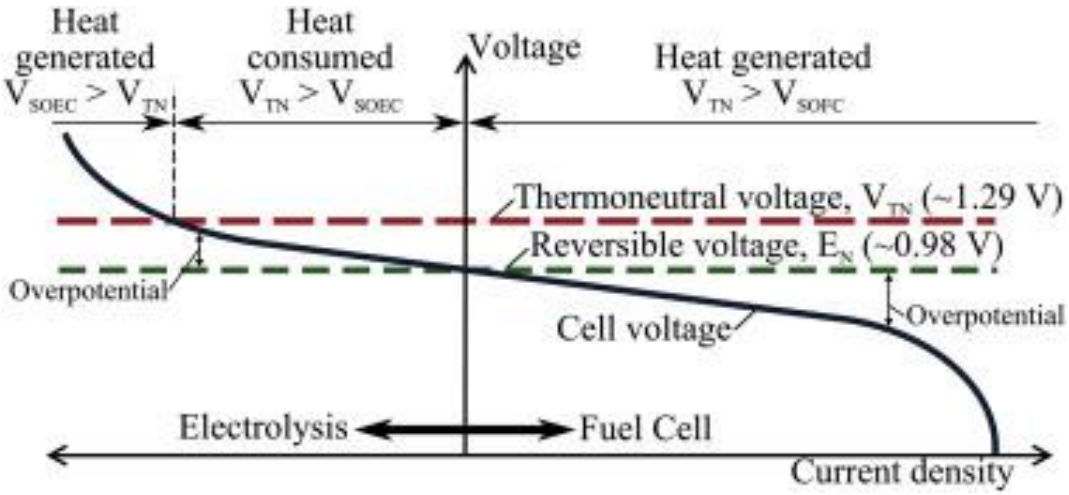

Figure 20: Three operating modes of high temperature solid oxide electrolysis cell [264].

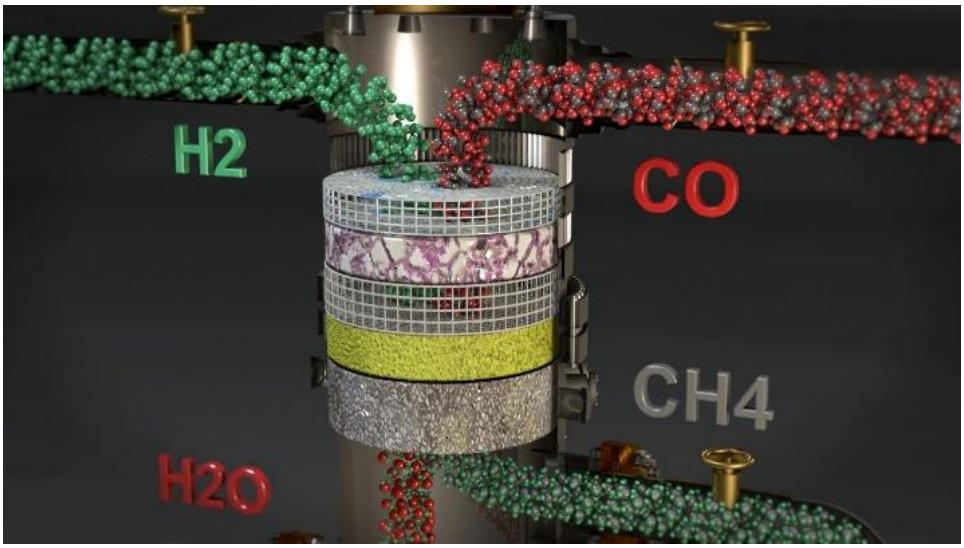

Figure 21: Methanation process [google images].

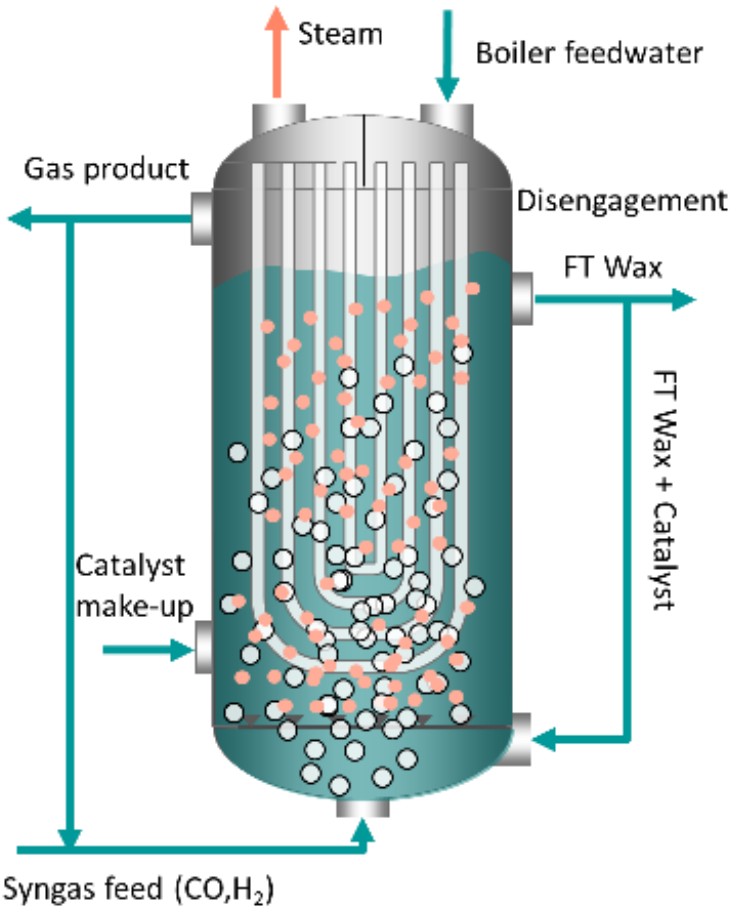

Figure 22: Fischer-Tropsch process [google images].

Because high operating temperature, solid oxide electrolyzer is also liable to electrolyze different compounds, and not only steam. For instance, carbon dioxide can also be electrolyzed, as well as a mixture of H_2O and CO_2 which produces syngas, that is to say H_2+CO [265–267]. The produced H_2+CO can be utilized for production of synthetic natural gas through methanation process (Figure 21). The synthetic natural gas can then be injected to natural gas grid network for later use. The other possible way of using H_2+CO is to produce liquid fuels through Fischer-Tropsch processes (Figure 22). Fischer-Tropsch processes convert synthesis gas with a given hydrogen to carbon monoxide ratio into hydrocarbon liquids with water as a coproduct via a stepwise polymerization process. The process is carried out in the presence of an iron or cobalt catalyst at moderate temperature (200–350°C) and pressure (20–50 bar). The sequential addition of carbon, followed by hydrogen to form hydrocarbon groups, allows the nascent hydrocarbon chain to grow. Selective

production by the FT process is dependent on the ability of the catalyst to promote chain elongation and to prevent termination reactions. In addition to the hydrocarbon products, very small quantities of oxygen-containing hydrocarbons and some light gases (methane, ethane, etc.) are formed. The produced synthetic liquid fuel can then be used in difficult-to-electrify end users seeking for sustainability.

1.3 Research Goal

The goal of this dissertation is to theoretically and experimentally develop and evaluate the advanced high-temperature solid oxide electrolysis cell (SOEC) system technology for widespread use with renewable energies. SOEC systems could be dynamically dispatched on the electric grid or microgrids (as a P2G technology) to store inexpensive or otherwise curtailed renewable electricity in the form of hydrogen. Moreover, advanced SOEC systems could be integrated with renewable resources to produce a zero carbon and zero emissions fuel like hydrogen for difficult-to-electrify end-users.

1.4 Objectives

To meet this dissertation goal, the following objectives will be completed:

1. Conduct an extensive continuous literature review on SOEC technology in both modeling and experimental perspectives.
2. Develop stack-level and system-level dynamic models and control strategies of SOEC system that simulates physical operation of the SOEC system.
3. Evaluate dynamic operation of SOEC system in different input conditions.
4. Perform theoretical analysis for integration of SOEC system into microgrids to support high renewable use.
5. Develop and operate an experimental setup to evaluate the steady state and dynamic performance characteristics of an SOEC short stack and analyze experimental results to validate the developed model.

1.5 Approach

This dissertation encompassed five key tasks, one established for each of the objectives described previously. This section describes how each task, and specific activities, maps to the Chapters constituting this dissertation.

Task 1: Background (Chapter 2)

An extensive, continuous literature review on the topics below was made throughout this research.

- Solid oxide electrolysis cell/stack level analytical and numerical simulation models including 0-D, 1-D, 2-D, and 3-D spatially and temporally resolved models.
- Steady state and dynamic analytical and numerical simulation of solid oxide steam electrolysis and steam + carbon dioxide co-electrolysis system.
- Dynamic simulation and control strategies of integrated solid oxide electrolysis system with intermittent renewable resources like solar and wind.
- Integrated solid oxide electrolysis system with microgrids to support high renewable penetration.
- Steady state and dynamic experimental analysis of solid oxide electrolysis cell/stack.
- Electrochemical impedance spectroscopy and other characterization methods on both cell and stack level.

Task 2: Develop stack-level and system-level dynamic models and control strategies of SOEC system that simulates physical operation of the SOEC system (Chapter 3)

- Develop a quasi-3D dynamic model of solid oxide steam electrolysis and steam + carbon dioxide co-electrolysis.
- Design a 300-kW solid oxide electrolysis system.
- Develop dynamic model of balance of plant components.
- Develop various control strategy to control dynamic operation of solid oxide electrolysis system.
- Evaluate steady-state and dynamic behavior of solid oxide electrolysis system under different developed control strategies (stack level and system level).

Task 3: Evaluate dynamic operation of the developed solid oxide electrolysis system model and control strategies integrated with renewable electricity from solar PV for two different scenarios (Chapter 4)

- Process solar PV annual data from the UCI microgrid.
- Determine sunny and cloudy profiles with 15-min time resolution to be given to the model as a power input.
- Evaluate the dynamic operation of the developed solid oxide electrolysis system and the performance of the developed control strategies both in stack and system levels.
- Compare performance characteristics of solid oxide electrolysis system under two different scenarios.

Task 4: Perform theoretical analysis on dynamic dispatch of solid oxide electrolysis system into the UCI microgrid to support high renewable use (Chapter 5)

- Collect thermal load, electric load, solar PV profile, gas turbine and steam turbine characteristics profiles of the UCI microgrid
- Develop representative model of different components in the UCI microgrid e.g., gas turbine, steam turbine, and heat recovery steam generator model.
- Implement governing equations for conservation of electrical and thermal energy in the UCI microgrid.
- Develop dynamic dispatch strategies for dispatching solid oxide electrolysis system to support high renewable use in the UCI microgrid.
- Develop optimization model to minimize imported electricity and natural gas consumption based on linear programming optimization tool in Matlab software.
- Analyze the outcomes of the optimization model e.g., gas turbine generation, steam turbine generation, PV generation, solid oxide electrolysis system capacity, and its dynamic operation for different renewable installed capacity scenarios.
- Calculate CO_2 emissions reduction and natural gas consumption reduction by feeding mixed renewable hydrogen and natural gas to the gas turbine.
- Analyze the possibility of using the produced renewable hydrogen in the local hydrogen refueling station.

Task 5: Develop and operate an experimental setup to evaluate the steady state and dynamic performance characteristics of an SOEC short stack and analyze experimental results to validate the developed model (Chapter 6)

- Develop and install all the components and connections of a six-cell short stack solid oxide system which can operate in both fuel cell and electrolyzer modes.
- Develop test matrices for both steady state and dynamic characterization of the system.
- Develop post processing tool to post process and analyze the experimental measurements during different tests.
- Investigate the effect of operating temperature on V-j characteristics curve.
- Investigate the effect of fuel composition on V-j characteristics curve.
- Investigate the dynamic behavior of the system under step, PV sunny, PV cloudy and wind profiles.
- Investigate the durability performance of the system under thermal cycles.
- Analyze the degradation of the system under the durability test.
- Calibrate the develop model in previous task with one set of steady-state experimental data and validate the model with all other sets of data including steady-state and dynamic ones.
- Install and deploy a potentiostat and booster to evaluate characteristics of the system in both cell and stack levels for a wide range of operating current densities.
- Characterize cell and stack performances using different state of the art techniques e.g., electrochemical impedance spectroscopy.

1.6 Structure of this Dissertation

Chapter two intends to provide an extensive literature review on all the subparts of the literature review conducted during the course of this dissertation.

Chapters three to six map directly to the second task to fifth task. A summary section at the end of each chapter identifies the major points and insights from the results. Lastly, Chapter seven consolidates all the most relevant findings and provides the main conclusions of this work.

It should be mentioned that the results and analysis of most chapters of this dissertation were submitted to prestigious peer-reviewed journals and conferences, as mapped below.

- Chapter 1:
    - Hydrogen is Essential for Sustainability, Saeedmanesh, A., McKinnon, M., Brouwer, J. Current Opinion in Electrochemistry, 2018.
- Chapter 3:
    - Dynamic Modeling of a Solid Oxide Electrolyzer System under Two Different Thermal Control Strategies, Saeedmanesh, A., Brouwer, J. European Fuel Cell Forum, 2018.
- Chapter 4:
    - Dynamic Behavior of a Solid Oxide Steam Electrolyzer System Using Transient Photovoltaic Generated Power for Renewable Hydrogen Production, Saeedmanesh, A., Colombo, P., McLarty, D., Brouwer, J. Journal of Electrochemical Energy Conversion and Storage, 2019.
- Chapter 5:
    - Dynamic dispatch of solid oxide electrolysis system for high renewable energy penetration in a microgrid, Colombo, P., Saeedmanesh, A., Santarelli, M., Brouwer, J. Journal of Energy Conversion and Management, 2020

2 Background

High temperature electrolysis of steam via a solid oxide steam electrolysis (SOSE) system is a promising technology due to its potential higher efficiency compared to current electrolysis technologies. Much research has been carried out focusing upon the steady state and dynamic operation of SOEC in cell/stack level. Ni et al. successfully developed a theoretical model to investigate the overpotentials of a reversible solid oxide cell, which can perform dual functions as a SOSE for hydrogen production and as a SOFC for power generation using hydrogen fuel [268]. An electrochemical model was developed by Ni et al. to simulate the J-V characteristics of an SOSE used for hydrogen production. They considered activation, concentration, and ohmic overpotentials as the main factors for voltage loss [269]. A theoretical model was developed by Ni et al. to study the electrical characteristics of a solid oxide steam electrolyzer (SOSE) for hydrogen production. The activation and concentration overpotentials at the electrodes as well as the ohmic overpotential at the electrolyte were considered as the main sources of voltage loss. They performed a parametric analyses to study the effects of material properties and operating conditions on the anode-supported SOSE cell performance [270]. Zahadat et al. applied artificial neural network to model the electrical behavior of SOEC. They used experimental data from different available sources for making the model [271]. Udagawa et al. developed a model, which consists of an electrochemical model, a mass balance, and four energy balances, and employed to study the steady state behavior of an SOEC stack at different current densities and temperatures [272]. Udagawa et al. reported the development of a one-dimensional dynamic model of a cathode-supported planar intermediate temperature SOEC stack with air flow introduced through the cells. Their model, which consists of an electrochemical model, two mass balances, and four energy balances, was employed to study the prospect of the stack temperature control through the variation of the air flow rate [273]. Nieminen et al. present a comprehensive overview of comparative performance characteristics of Proton Exchange Membrane (PEM) and SOSE based on a thermodynamic analysis. They found that the main factors which influence electrolyzer energy and exergy efficiencies were temperature, summation of overpotentials, applied voltage, and to a lesser extent pressure. Also, they found that anodic overpotentials make up a majority of the total overpotentials in

both electrolyser types studied and therefore further development of catalysts to reduce the overpotentials was recommended [274]. Ni et al. developed two models to investigate the performance of a solid oxide electrolysis cell (SOEC) for CO_2 electrolysis at different levels. The first model is a one-dimensional model which is basing on a previously developed electrochemical model for steam electrolysis and considered all overpotentials in the SOEC. The second model is a two-dimensional thermal-fluid model consisting of the 1D model and a Computational Fluid Dynamics (CFD) model [275]. Xie et al. developed a solid oxide electrolysis cell model for syngas generation using a button cell test system as a physical base. Their model coherently bridged the multi transport processes of charge, mass, momentum, and energy with detailed surface chemistry. They validated their model using experimental polarization curves [276]. Luo et al. developed one-dimensional elementary reaction kinetic model for solid oxide fuel-assisted steam electrolysis cell, which is coupling heterogeneous elementary reactions, electrochemical reaction kinetics, electrode microstructure and transport processes of charge and mass. Their model was calibrated and validated by experimental data from a button cell [277]. Kazempour et al. developed a dynamic cell model that coupled the reversible electrochemistry, reactant chemistry, and the thermo-fluidic phenomena inside a cell channel. Their model was calibrated and validated using available experimental and numerical data for button cells, single cells, and multi-cell stacks supplied with either steam or syngas [278]. Menon et al. investigated the performance of a SOEC during co-electrolysis by focusing on the interactions between transport processes and electrochemical parameters. They modeled electrochemistry at the three-phase boundary by a modified Butler–Volmer approach that considers H_2O electrolysis and CO_2 electrolysis, individually, as electrochemically active charge transfer pathways [279]. Luo et al. developed a dynamic model to predict the dynamic response of H_2O/ CO_2 co-electrolysis in tubular SOEC. Their developed dynamic model comprehensively considered the macroscopic fluid flow, microscopic diffusion, heat transfer and electrochemical/chemical reactions in the tubular SOEC [280]. Duhn et al. optimized design of a gas distributor to distribute gas flow into parallel channels for SOEC, with respect to flow distribution, using CFD modelling. They found out that a temperature gradient along the parallel channels does not affect the flow uniformity, whereas a temperature difference between the channels does [281]. Tanaka et al. developed a quasi-1D simulation model to estimate total area-specific

resistance for overvoltages and cell voltage by separating gas conversion impedance from overall real-part impedance in high temperature steam electrolysis with a solid oxide cell [282]. Xu et al. studied the effects of fuel-assisting on CO_2/H_2O co-electrolysis numerically using a 2D model. Their model was validated with the experimental data for CO_2/H_2O co-electrolysis [283]. Ni developed a 2D computational fluid dynamics model to study the performance of a planar SOEC for hydrogen production. The governing equations for mass continuity, momentum conservation, energy conservation and species conservation were discretized with the finite volume method [284]. Grondin et al. proposed a multi-physics model to predict the SOEC behavior, based on similar charge, mass, and heat transport phenomena as for SOFC [285]. Jin et al. developed a 2D CFD SOEC model and utilized it to investigate the sensitivity of electrolysis performance to delamination occurred at oxygen electrode/electrolyte interface. Their results indicated that delamination significantly influence local charge current density distributions since the charge transport path is cutoff. In both parallel flow and counter flow settings, electrolysis performance is more sensitive to the delamination occurred at the center of the cell than those occurred at the edges of the cell [286]. Laurencin et al. developed a 2D multi-physic in-house-model to analyze the performances of SOEC stack. Their model encompassed a combined electrochemical and thermal description of the electrolyzer. They implemented an analytical solution for multi-species diffusion across the porous cathode in their model [287]. Ni developed a 2D thermal model to study the heat/mass transfer and chemical/electrochemical reactions in SOEC for H_2O/CO_2 co-electrolysis. The developed model was based on 3 sub-models: a CFD model describing the fluid flow and heat/mass transfer; an electrochemical model relating the current density and operating potential; and a chemical model describing the reversible water gas shift reaction and reversible methanation reaction [288]. Hawkes et al. created a three-dimensional computational fluid dynamics electrochemical model to model high-temperature electrolysis stack performance and steam electrolysis in the Idaho National Laboratory Integrated Lab Scale experiment. Their model was made of 60 planar cells stacked on top of each other operated as SOEC [289].

According to the literature, much research has been carried out focusing upon the steady state operation of SOEC in system level. Ni et al. conducted energy and exergy analysis to

investigate the thermodynamic–electrochemical characteristics of hydrogen production by a solid oxide steam electrolyzer plant. All overpotentials involved in the SOEC cell have been included in their thermodynamic model. The waste heat in the gas stream of the SOSE outlet was recovered to preheat the H_2O stream by a heat exchanger. The heat production by the SOEC cell due to irreversible losses has been investigated and compared with the SOSE cell's thermal energy demand [290]. Sigurvinsson et al. developed a techno-economic optimization model for a high-temperature electrolysis process which includes SOEC stack as well as a high temperature heat exchanger network. They investigated the integration of geothermal energy with SOEC to reduce the electrical energy consumption by using geothermal available heat [291]. Jensen et al. indicated that the SOEC technology has a promising potential to produce hydrogen from renewable energy sources. However, they mentioned that before this potential can be realized more R&D is required. Their ongoing research and development was addressing stability of the SOEC in order to assure sufficient long life time of a high performance SOEC system [262]. Gopalan et al. showed through modeling and simulation that the efficiency of hydrogen production can be further increased by operating the SOEC at the optimum combination of operating conditions. Specifically, their analysis of a recuperative SOEC that utilizes the thermal energy from the exhaust gases revealed that operating the electrolysis cell above the thermoneutral voltage increased the efficiency of hydrogen production [292]. Stoots et al. performed CO_2/H_2O electrolysis experiments using button cells and three different 10-cell planar solid oxide stacks. Their results included electrolysis performance at various temperatures, gas mixtures, and electrical settings [293]. O'Brien et al. developed a process model to evaluate the potential performance of a large-scale high-temperature co-electrolysis plant to produce syngas from steam and carbon dioxide. The process model was developed using the UniSim system-analysis code. Using this code, a detailed process flow sheet was defined that included all the components that are present in an actual plant such as pumps, compressors, heat exchangers, turbines, and the electrolyzer [294]. Wang et al. measured the steam electrolysis performance of an SOEC at various steam concentrations. They showed that the system efficiency reached a higher heating value of 98% due to the effective recovery of thermal energy from exhaust gas [295]. Stoots et al. assessed the feasibility of using solid oxide-based electrolysis cell technology for high temperature electrolysis of steam for large-scale

hydrogen production. In parallel, they studied simultaneous electrolysis of steam and carbon dioxide for syngas (hydrogen/carbon monoxide mixture) production. They mentioned when SOEC linked to a nuclear power source, this technology provides a carbon neutral means of producing syngas while consuming CO_2 [296]. Jensen et al. presented results of a cell test with pressures ranging from 0.4 bar to 10 bar. The cell was tested both as an SOEC and as an SOFC. They showed that the SOFC performance increases with pressure. The SOEC performance, at 750 °C, was found to be weakly affected by the pressure range in their study, however the internal resistance decreased significantly with increasing pressure [297]. Zhang et al. with the help of the typical model of a water electrolysis hydrogen production system, which mainly includes the electrolysis cell, separator, and heat exchangers, compared and evaluated three expressions of the system efficiency in literature [298]. Graves et al. examined the initial performance and durability of a solid oxide cell applied for co-electrolysis of CO_2 and H_2O. Their study introduced the use of the distribution of relaxation times to study cell degradation without relying on a model. The durability was tested at consecutively higher current densities [265]. Graves et al. reviewed the many possible technological pathways for recycling CO_2 into fuels using renewable or nuclear energy, considering three stages— CO_2 capture, H_2O and CO_2 dissociation, and fuel synthesis. One of the dissociation methods they considered is high temperature SOEC co-electrolysis of CO_2 and H_2O [261]. Ebbesen et al. studied electrolysis of steam and co-electrolysis of steam and carbon dioxide SOEC stacks composed of Ni/YSZ electrode supported SOECs. Their result showed that long-term electrolysis is feasible without notable degradation in the SOEC stacks. The degradation of the electrolysis cells was found to be influenced by the adsorption of impurities from the applied inlet gases, whereas the application of chromium containing interconnect plates and glass sealing do not seem to influence the durability [299]. Mougin et al. described their recent promising results obtained in terms of performance and durability in stack environment, because the use of protective coatings on one hand, and of advanced cells on the other hand. They demonstrated that the integration of protective coatings was mandatory to decrease the degradation rate in high-temperature steam electrolysis stacks [300]. Brisse et al. presented a summary of the experimental results with a focus on the observation of cell and stack degradation [301]. Dillig et al. analyzed the thermal balance of a solid oxide electrolyzer cell to enable highly transient operation at high

temperatures and high storage efficiencies. Furthermore, they proposed a thermal balancing, heat supply and removal mechanism via high temperature heat pipes integrated into the solid oxide cell stacks [302]. Kim et al. investigated effects of the operating temperature and the humidity on the performance of high-temperature electrolysis. They manufactured flat-tubular solid oxide electrolysis cells with a ceramic interconnector in a body to minimize the stack volume and eliminate metallic components [303]. Kim et al. presented degradation mechanism of the electrolyte and air electrode for solid oxide electrolysis cells. Degradation behavior in the impedance spectra was characterized as growth of mid-frequency arc at the initial stage, gradual increase of ohmic resistance throughout the operation, and sharp rise of low frequency resistance at the final stage, followed by catastrophic cell failure [304]. Petipas et al. described the steady-state behavior of a SOEC system operated at different power loads without an external heat source and producing compressed hydrogen (3 MPa) [305]. Diethelm et al. characterized two short SOEC stacks (6-cells) in steam-electrolysis mode. The first was based on Ni-YSZ supported cells with LSCF-based air electrodes. The second included LSC-based air electrodes. The stacks were fed with a 90% steam, 10% hydrogen mixture, and characterized between 600 and 700°C [306]. Ferrero et al. designed and modeled a hydrogen production system based on SOEC and compared to the performance of a more mature system based on PEM technology. Their SOEC system mainly consisted of an SOEC stack, a heat recovery system, and a hydrogen compression section. They utilized experimental data measured in steam electrolysis tests performed on single solid oxide cells into the model to characterize the stack performance. Their model carried out a thermodynamic analysis in order to calculate the energy efficiency and the exergetic consumption of the system [307]. Petipas et al. investigated the performance of a solid oxide electrolysis cell, by performing tests on a single SOEC for 600 hours. Tests were performed at the reference current of 20A, corresponding to the thermoneutral voltage (1.28V) [308]. Momma et al. electrochemically investigated the effect of operating pressure on the performance of SOEC under pressurized and depressurized conditions (0.01-1.0 MPa) using practical size single cells [309]. Zhang et al. did an experimental investigation on the performance and durability of single solid oxide cells. They noticed that degradation is a more significant issue when operating SOCs in the electrolysis mode. In order to understand and mitigate the degradation issues in high

temperature electrolysis, single SOCs with different configurations from several manufacturers were evaluated for initial performance and long-term durability by them [310]. Li et al. tested H_2O– CO_2 co-electrolysis performance and mechanisms in solid oxide electrolysis button cells at different operating temperature (550–750°C) [311]. Li et al. developed a one-dimensional elementary reaction model of CO_2/H_2O co-electrolysis in SOEC coupled with heterogeneous elementary reactions, electrochemical reactions, electrode microstructure, and the transport of mass and charge. Their model validated with the experimental performance of H_2O electrolysis, CO_2 electrolysis and CO_2/H_2O co-electrolysis at 700°C, showing to be a useful tool for understanding the intricate reaction and transport processes within SOEC electrode and the electrode structure design and optimization [312]. Dasari et al. evaluated electrochemical performance of Ni–YSZ electrode, which is widely used as the anode for solid oxide cells, is evaluated for hydrogen production in SOEC [313]. Lay-Grindler et al. built an in-house micro model to describe the electrochemical mechanisms governing both H_2 and O_2 electrodes operating in SOEC mode. A special attention was paid to take into account the microstructure properties of the ionic, electronic and gas phases as well as the processes occurring therein [314]. Ozturk et al. conducted thermodynamic analysis of a renewable-based multi-generation energy production system which produces several outputs, such as power, heating, cooling, hot water, hydrogen, and oxygen. Their solar-based multi-generation system consisted of four main sub-systems: Rankine cycle, organic Rankine cycle, absorption cooling and heating, and hydrogen production and utilization. Exergy destruction ratios and rates, power or heat transfer rates, energy and exergy efficiencies of the system components were carried out in their study [315]. Klotz et al. presented the combination of two established models: (i) a physically motivated zero-dimensional model that described the static behavior of planar anode supported SOECs with high precision in the whole range of technically relevant operating conditions and (ii) a performance model for large area SOEC which expands the behavior of a small cell to a large cell by a discretization of the gas channel. They mentioned that the combination yields the possibility to make predictions of performance and efficiency of an SOEC stack operated in technically relevant operating conditions [316]. Sanz-Bermejo et al. analyzed an integrated SOEC and a linear Fresnel reflector field for grid management. They considered thermal oil to be retained as heat transfer fluid avoiding phase change through

the solar receiver. Also they considered the heat is stored during the day for later use by the SOECs [317]. Stempien et al. reported a thermodynamic analysis and simple optimization of a combined SOEC and Fisher–Tropsch synthesis processes for sustainable hydrocarbons fuel production is reported. They employed their model to describe effects of temperature, pressure, reactant composition and molar flux and flow on the system efficiency and final production distribution [318]. Stempien et al. proposed and analyzed a possible pathway for renewable and sustainable methane production from captured carbon dioxide, water (or seawater) and renewable electricity. Their proposed system included SOEC combined with ex-situ methane synthesis reactor comprising Sabatier, Methanation and Water-Gas Shift reactions. They used A well validated electrochemical model to describe the behavior of the electrolyzer for steam/carbon dioxide co-electrolysis [319]. Reytier et al. carried out experiments at stack level in both electrolysis and co-electrolysis modes. They tested a 10-cell stack and a 25-cell stack in electrolysis mode [320]. Bernadet et al. with a goal of improving the electrolysis efficiency, adopted an experimental and modeling approach to better understand the basic underlying mechanisms of pressurized electrolysis operation. Experiments were carried on two different single commercial solid oxide cells at 800 °C in the pressure range of 1–10 bar [321]. Aicart et al. highlighted an experimental and modeling approach devoted to a better understanding of H_2O and CO_2 co-electrolysis mechanisms at 800°C. A standard Cathode Supported Cell was used in their study. Through numerical adjustments on experimental polarization curves, the cathode microstructural parameters and exchange current densities for H_2O and CO_2 reductions were determined and subsequently implemented in an in-house co-electrolysis model [322]. Pozzo et al. proposed and analyzed a novel process design of a plant integrating a dimethyl ether (DME) synthesis unit with a woody biomass gasifier and a high-temperature co-electrolysis unit. The plant foresees a two-stage gasifier that produces a CO_2-rich syngas, which is further upgraded to a product gas with a higher energy content through a high temperature co-electrolysis section consisting of a SOEC module. The energy system analysis of the whole process was developed by them, also taking into account the kinetic mechanisms for the syngas conversion to DME in a catalytic reactor [323]. Peters et al. investigated different system configurations and operating conditions to study the efficiencies of producing hydrogen by solid oxide electrolysis. They mentioned that important factors for system efficiencies are the voltage at

which the stack is operated, the source of heat for the water evaporation, the pressure level of the hydrogen storage, and the system configuration. Based on these factors, they defined four efficiencies taking into account the different conditions and configurations [324]. Cacciuttolo et al. analyzed the pressure influence on the electrochemical reactions occurring in high temperature steam electrolyzer. The behavior of half-cells constituted by YSZ electrolytes and Ni/YSZ cathodes or LSCF anodes was simulated by COMSOL multiphysics®. Their model highlighted that the limiting current density due to the lack of steam is shifted towards higher steam conversion rates by increasing the operating pressure, without negative thermodynamic effect at high current density [325]. Zhang et al, presented the results of 4 kW high temperature steam electrolyzer long-term test completed in a multi-kW test facility recently developed at the Idaho National Laboratory. Their 4-kW steam electrolyzer unit consisted of two solid oxide electrolysis stacks electrically connected in parallel, each of which included 40 electrode-supported planar cells. A current density of 0.41 $A.cm^{-2}$ was used for their long-term operating at a constant current mode, resulting in a theoretical hydrogen production rate about 23 standard liter per minute. A demonstration of 830-hour stable operation was achieved with a degradation rate of 3.1% per 1000 h [326]. Sanz-Bermejo et al. implemented a complete model of a solid-oxide electrolysis process has been developed to optimize the design of the process and its operation at part load. Different thermodynamic cell operational modes (constant cell inlet temperature vs. thermoneutral following point) and operational strategies (constant steam conversion vs. constant flow rate) were analyzed by them. Additionally, three different temperature-dependent area specific resistance equations were implemented in order to analyze the influence of the dependency of the ionic conductivity of the electrolyte on temperature over the performance of the process [327]. Shariatzadeh et al. proposed a new power plant plan which simultaneously generates heat and electricity using a solar chimney with solid oxide fuel cells and solid oxide electrolysis cells. In one hand, in their proposed system, the solar chimney generates electricity by sunlight and supplies a part of demand. Then, additional electricity is generated through the high temperature electrolysis which produces hydrogen that is stored in tanks and converted into electricity by solid oxide fuel cells [328]. Buttler et al. investigated the effect of high temperature heat utilization in solid oxide electrolysis on efficiency and hydrogen specific cell area based on a detailed 1D electrochemical model

validated with literature data. Their first feasibility analysis indicated that the mean heat transfer required to maintain isothermal conditions as a function of heat integration shows a maximum with 1426 W/m^2 at a heat utilization of 0.34 kWh/Nm^3 H_2, which seemed to be technically achievable [329]. Visitdumrongkul et al. studied the effect of operating parameters of non-catalytic partial oxidation reaction (i.e., the oxygen to carbon ratio, operating temperature, and pressure) on SOEC performance, including exergy analysis of the process. Their study indicated that non-catalytic partial oxidation could enhance the hydrogen production rate and efficiency of the system. In terms of exergy analysis, the non-catalytic partial oxidation reactor was demonstrated to be the highest exergy destruction unit due to irreversible chemical reactions taking place, whereas SOEC is a low exergy destruction unit [330]. Cinti et al. described and analyzed the results of experiments on a SOEC with and without the supply of a fuel to the oxygen producing electrode. In their experiments a 5 × 5 cm^2 SOFC was used operating in electrolyzer mode. They tested the influence of varying reactant utilization (i.e., steam utilization) and fuel utilization in fuel assisted electrolysis. In particular the effect of insufficient fuel supply was studied experimentally as well as theoretically [331]. Zhang et al. calculated the overall efficiency of the high temperature co-electrolysis system through electrochemical and thermodynamic analysis. A thermodynamic model in regards to the efficiency of the HTCE system was established by them and the effects of five key parameters, electricity generation efficiency of high temperature gas-cooled reactor, electrolysis efficiency of CO_2, electrolysis efficiency of H_2O, thermal efficiency and co-electrolysis temperature on the overall efficiency were investigated in detail [332]. Seitz et al. designed an electrolysis system with solid oxide electrolyzer stacks. They used a solar thermal receiver to produce the steam supplied to the electrolyzer stacks. On the other hand, a thermal energy storage, using a phase change material, was considered for the extension of the operational hours during the nighttime. The system was optimized to minimize the levelized costs of hydrogen and compared to a system without a thermal energy storage [333]. AlZahrani et al. reported the design and thermodynamic performance of an SOEC system at a capacity of 1 MW, from which various renewable electricity resources can be utilized to produce hydrogen and oxygen from water. To investigate the standalone operation and eliminate they examined the need for external heat, the SOE while operating in an exothermic mode, where heat is internally generated,

and in an endothermic mode, where heat is provided by electric heaters. Additionally, a network of heat exchangers was optimized to increase the system efficiencies and enable an efficient standalone operation. Thus, the SOE system can be adapted for renewable hydrogen production applications, such as wind and Photovoltaic (PV) farms. The influences of operating conditions on efficiencies, power demand, and exergy destruction rates of the SOE system were also assessed, including a case of 15 MPa hydrogen storage [252]. For both steam- and co-electrolysis, Wang et al. comprehensively and comparatively investigated several critical design issues of a solid-oxide electrolyzer based power-to-methane system with fixed-bed methanation reactor and membrane-based methane upgrading: (1) system-level heat integration, (2) the impacts of operating variables (e.g., operating voltage, reactant utilization, anode/cathode feed ratio, and operating pressure of the methanation reactor and membrane) on system performances, (3) the competitiveness of the electrolyzer operation with pure oxygen production, and (4) the possibility of avoiding electrical heating, which is necessary for thermoneutral operation to heat up the electrolyzer feeds to the required temperature. To achieve this target, they employed a multi-objective optimization platform with integrated heat cascade calculation with experimentally-calibrated component models [214]. Kupecki et al. presented a conceptual power-to-gas system based on a high temperature electrolysis unit. They presented a 10 kW-class power-to-gas system and the efficiency of the system assessed and discussed from an energy point of view. Accepting the current assumptions related to the performance of cells making up the electrolysis unit, they reported that the system can achieve efficiency in excess of 74% [334]. Schiller et al. reported on the successful integration of solar heat into a solid oxide electrolyzer. Their experimental setup of the prototype system consisting of a solar simulator, a solar steam generator, a steam accumulator and a solid oxide electrolyzer as well as first results with regard to solar steam generation and electrochemical performance of the electrolyzer were presented [335]. Mastropasqua et al. proposed a plant which is conceived to supply hydrogen for a small refueling station. Their proposed plant was based on solid oxide electrolyzer cell technology, which performs water electrochemical reduction, to produce a target of 150 kg per day of hydrogen. The plant was integrated with a parabolic dish solar field designed to provide both electricity and thermal energy, necessary for the electrolysis reaction to take place. Specifically, a modular multi-dish configuration was selected, in which electric power

is produced by 30kW solarized micro-gas turbines placed in the dishes focus [336]. Chen et al. developed a numerical model for a novel reactor combining a SOEC section with a Fischer Tropsch like section for methane production under pressurized & temperature-gradient condition. Governing equations for mass, momentum, charge transport were solved with finite element method. The chemical reaction kinetics of reversible water gas shift reaction and reversible methanation reaction in Ni/YSZ cathode were also fully considered. Their model was validated by comparing simulation results with experimental data. Parametric simulations were also conducted to understand the physical-chemical processes in the reactor with a focus on the pressure effect [337]. Posdziech et al. summarized Sunfire's recent developments in the fields of reversible solid oxide cells and pressurized SOEC. Sunfire could demonstrate large technology steps towards a marketable product. The durability and robustness at cell and stack level were proven with long-term stationary and ambitious cycling tests. Within the last 3 years, Sunfire has developed two largescale reversible solid oxide cell generators in cooperation with Boeing and other partners. The world-first reversible SOC system was demonstrated in the Boeing/US Navy facilities in California. The system was designed as an electrochemical electricity storage using pressurized hydrogen. They mentioned that in contrast to batteries, the hydrogen storage capacity is more or less infinite due to low costs of storage vessels [338]. Roeb et al. analyzed the coupling of solar central receiver systems and the nuclear pressurized water reactor with an SOEC unit as well as the solar tower technology with ambient air as heat transfer fluid. They also investigated central receiver systems with direct steam generation [339].

3 Solid Oxide Steam Electrolysis System Design

A Solid Oxide Steam Electrolyzer (SOSE) system model has been developed in Matlab software based upon a previously developed model in Matlab/Simulink software at National Fuel Cell Research Center (NFCRC) [340]. The developed model is comprised of a temporally and spatially resolved quasi-3D sub-model for an SOSE stack and Balance of Plant (BoP) dynamic sub-models for different BoP components, such as heat exchangers, compressors, electric heaters, valves, and air blower.

3.1 SOEC Stack Model

The stack is comprised of 2500 cathode-supported crossflow planar SOE unit-cells that are assumed to be assembled into identically operating stacks, creating a 300kW electrolyzer stack module. In the developed Matlab model of a single repeating unit-cell is assumed to be representative of the behavior of all cells in each of the stacks. Therefore, the input and output flows and power are multiplied by the number of cells in the stack to obtain the stack values. The cell is modelled considering 5 different layers i.e., steam side interconnect, steam flow channels, Positive Electrode-Electrolyte-Negative Electrode (PEN), air flow channels and air interconnect.

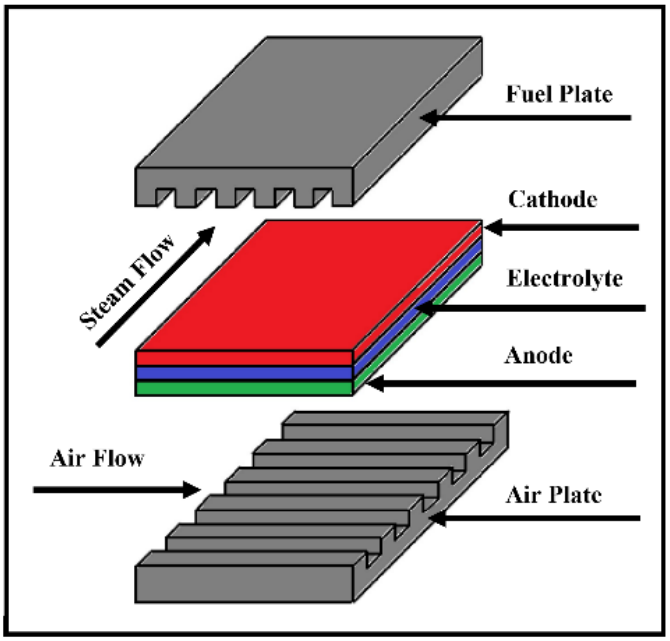

Figure 23: Schematic of Cross-flow SOE Unit-Cell [341].

To capture temporal and spatial behavior properties, various spatially distributed states are calculated at each time in time span using MATLAB ODE solver. To implement material and energy balances as well as polarization model, each layer is discretized into an 8×8 nodes and control volumes. In this study, the following assumptions are made on SOSE stack modeling:

- Electrochemical reactions occur instantaneously, due to fast kinetics of electrochemical reactions compared to thermal time scales.
- Electrical current only flows in one direction (from one electrode to the other along the PEN), due to the iso-potential electrode surfaces.
- Gases behave as an ideal gas, due to high operating temperature and atmospheric pressure operating conditions.
- For each discrete gaseous nodal control volume, temperature and species concentrations are averaged between inlet and outlet and assumed constant in the node for calculation purposes.
- Both cathode and anode streams are in a laminar flow regime based upon the low Reynolds number in the flow channels, due to the low gas flow rate and the small cross-sectional area of the channels on both sides.
- Stack heat losses to the environment are neglected.

Figure 23 shows a schematic of a 10cm×10cm crossflow planar SOE unit-cell.

3.1.1 Governing Equations

To solve the operating parameters of the SOEC stack, governing equations need to be solved. The governing equations can be expressed as follows:

3.1.1.1 Electrochemical Model

The Nernst potential is the minimum electrical potential required to split steam which accounts for species concentration, operating temperature and pressure, and extent of reaction as well at each node (Equation 1).

$$V_{Nernst}|_{Node} = E^0|_{Node} + \frac{R\,T_{PEN}|_{Node}}{n_e\,F} \times Ln\left(\frac{X_{H_2,b}\big|_{Node}\,X_{O_2,b}^{0.5}\big|_{Node}}{X_{H_2O,b}\big|_{Node}}\right) + \frac{R\,T_{PEN}|_{Node}}{2\,n_e\,F} \times Ln(P_A|_{Node})$$

Equation 1

Where $E^0|_{Node}$ (V) is a standard reversible voltage of each node, R is a universal gas constant equal to 8.314 $(J/mole.K)$, $T_{PEN}|_{Node}$ (K) is temperature of each node on the PEN, n_e (mole of electron/moles of steam) is number of moles of electron transferred per unit mole of steam equal to 2, F $(C/mole)$ is Faraday constant equal to 96485, X_i is species molar fraction and $P_A|_{Node}$ (atm) is pressure of each node along the anode stream.

The standard reversible voltage ($E^0|_{Node}$) of each node is calculated based upon the Gibbs energy change of reaction at the node temperature and standard pressure ($\Delta G|_{T_{PEN|_{Node}},P_{Amb}}(J/\,mole)$) according to Equation 2:

$$E^0|_{Node} = \frac{\Delta G\left(H_2O \rightarrow H_2 + \frac{1}{2}O_2\right)\Big|_{T_{PEN|_{Node}},P_{Amb}}}{n_e\,F}$$

Equation 2

Where $\Delta G\ (H_2O \rightarrow H_2 + ½\ O_2)$ is the Gibbs free energy change for steam splitting at the nodal temperature ($T_{PEN,Node}$) and pressure (P_{Amb}), n_e (mole of electron/moles of steam) is number of moles of electron transferred per unit mole of steam equal to 2, F $(C/mole)$ is Faraday constant equal to 96485. When the current is non-zero in the electrolyzer, the cell operating voltage is greater than the Nernst voltage due to the overpotentials. These overpotentials can be described as follows: ohmic overpotentials governed by ohm's law, activation overpotential governed by Butler-Volmer equation and concentration overpotential.

The Butler-Volmer equation is typically employed to characterize electrochemical activation overpotential associated with charge transfer reactions at the operating conditions of the cell.

$$J|_{Node} = -J_{0,Ca}\big|_{Node} \times \left\{exp\left(\frac{\alpha\,n_e\,F\,\eta_{act,Ca}\big|_{Node}}{R\,T_{PEN}|_{Node}}\right) - exp\left(-\frac{(1-\alpha)\,n_e\,F\,\eta_{act,Ca}\big|_{Node}}{R\,T_{PEN}|_{Node}}\right)\right\}$$

Equation 3

$$J|_{Node} = -J_{0An}|_{Node} \times \left\{ exp\left(\frac{\alpha\, n_e\, F\, \eta_{act,An}\big|_{Node}}{R\, T_{PEN}|_{Node}} \right) - exp\left(-\frac{(1-\alpha)\, n_e\, F\, \eta_{act,An}\big|_{Node}}{R\, T_{PEN}|_{Node}} \right) \right\}$$ Equation 4

Where $J_{0An}|_{Node}$ is the exchange current density, α is the transfer coefficient, $T_{PEN}|_{Node}$ is the nodal temperature, F is the Faraday constant, R is the universal gas constant, n_e is number of moles of electron transferred per unit mole of steam equal, and $\eta_{act}|_{Node}$ is the nodal activation overpotential.

The exchange current density is a kinetic parameter measuring the local electrode current density at open circuit conditions i.e., at equilibrium conditions when no net current density is consumed or produced within the cell. Equations (5) and (6) are employed to calculate the exchange current density.

$$J_{0,Ca}\big|_{Node} = (1.344 \times 10^{10}) \times exp(-\frac{1 \times 10^5}{R\, T_{PEN}|_{Node}})$$ Equation 5

$$J_{0,An}\big|_{Node} = (2.051 \times 10^{9}) \times exp(-\frac{1.2 \times 10^5}{R\, T_{PEN}|_{Node}})$$ Equation 6

Where $T_{PEN}|_{Node}$ is the nodal temperature, F is the Faraday constant, and R is the universal gas constant.

The value of transfer coefficient is usually 0.5 for fuel cell and electrolyzer applications. With $\alpha = 0.5$, Equation 3 and Equation 4 can be expressed as:

$$\eta_{act,Ca}\big|_{Node} = \frac{R\, T_{PEN}|_{Node}}{F} \times sinh^{-1}(\frac{-J|_{Node}}{2\, J_{0,Ca}\big|_{Node}})$$ Equation 7

$$\eta_{act,An}\big|_{Node} = \frac{R\, T_{PEN}|_{Node}}{F} \times sinh^{-1}(\frac{-J|_{Node}}{2\, J_{0,An}\big|_{Node}})$$ Equation 8

Where $J_{0An}|_{Node}$ is the exchange current density, $T_{PEN}|_{Node}$ is the nodal temperature, F is the Faraday constant, and R is the universal gas constant.

Ohm's law is employed to evaluate the cell ohmic overpotential. Ohmic overpotential consists of cathode, anode, and electrolyte ohmic overpotentials as well as interconnect ohmic overpotentials and contact ohmic overpotential which has the effect of ohmic resistance in the contact region between electrodes and interconnect plates. Equation 9 to Equation 13 describe the ohmic overpotential different components:

$$\eta_{ohm,Ca}\big|_{Node} = (1.05 \times 10^{-8}) \times T_{PEN}|_{Node} \times exp(\frac{1150}{T_{PEN}|_{Node}}) \times \delta_{Ca} \times (-J|_{Node}) \quad \text{Equation 9}$$

$$\eta_{ohm,An}\big|_{Node} = (2.38 \times 10^{-8}) \times T_{PEN}|_{Node} \times exp(\frac{1200}{T_{PEN}|_{Node}}) \times \delta_{An} \times (-J|_{Node}) \quad \text{Equation 10}$$

$$\eta_{ohm,El}\big|_{Node} = (2.99 \times 10^{-5}) \times exp(\frac{10300}{T_{PEN}|_{Node}}) \times \delta_{El} \times (-J|_{Node}) \quad \text{Equation 11}$$

$$\eta_{ohm,Ic}\big|_{Node} = (1.075 \times 10^{-7}) \times T_{IC}|_{Node} \times exp(\frac{1100}{T_{IC}|_{Node}}) \times \delta_{Ic} \times (-J|_{Node}) \quad \text{Equation 12}$$

$$\eta_{ohm,Cont}\big|_{Node} = 0.1 \times 10^{-4} \times (-J|_{Node}) \quad \text{Equation 13}$$

Where $T_{PEN}|_{Node}$ is the nodal temperature, F is the Faraday constant, δ is the thickness of different compartments, $T_{IC}|_{Node}$ is the nodal temperature of interconnect.

Due to diffusion resistance in porous electrodes, the concentration of reactant and product species changes between three phase boundary, electrode surface and bulk flow in both anode and cathode channels. Diffusion overpotential at anode and cathode side channels can be calculated as:

$$\eta_{conc,Ca}\big|_{Node} = \frac{R\ T_{PEN}|_{Node}}{2\ F} \times ln(\frac{X_{H_2O,b}\big|_{Node}\ X_{H_2,TPB}\big|_{Node}}{X_{H_2,b}\big|_{Node}\ X_{H_2O,TPB}\big|_{Node}})$$ Equation 14

$$\eta_{conc,An}\big|_{Node} = \frac{R\ T_{PEN}|_{Node}}{4\ F} \times ln(\frac{X_{O_2,TPB}\big|_{Node}}{X_{O_2,b}\big|_{Node}})$$ Equation 15

Where $T_{PEN}|_{Node}$ is the nodal temperature, F is the Faraday constant, R is the universal gas constant, X_b is molar fraction of different species at bulk level, and X_{TPB} is molar fraction of different species at triple phase boundary level.

The mole fractions employed in these equations are at both the Triple Phase Boundary (TPB) and bulk fluid locations. Hence, to evaluate the cell concentration overpotential, it is necessary to estimate the concentration of the reactant and product gas species in the bulk flow and at the TPB for each computational element. Fick's law is implemented to calculate the mole fraction differences between the bulk flow and electrode surfaces:

$$X_{O_2,s}\big|_{Node} = 1 + \left(1 - X_{O_2,b}\big|_{Node}\right) \times exp(\frac{R\ T_A|_{Node}\ J|_{Node}}{4\ F\ P_A|_{Node}\ D_{O_2}\big|_{Node}} \times \frac{H_{CH,A}}{2})$$ Equation 16

$$X_{H_2,s}\big|_{Node} = X_{H_2,b}\big|_{Node} - \frac{R\ T_F|_{Node}\ J|_{Node}}{2\ F\ P_F|_{Node}\ D_{H_2}\big|_{Node}} \times \frac{H_{CH,F}}{2}$$ Equation 17

$$X_{H_2O,s}\big|_{Node} = X_{H_2O,b}\big|_{Node} + \frac{R\ T_F|_{Node}\ J|_{Node}}{2\ F\ P_F|_{Node}\ D_{H_2O}\big|_{Node}} \times \frac{H_{CH,F}}{2}$$ Equation 18

Where $T_A|_{Node}$ is the nodal temperature of air stream, $T_F|_{Node}$ is the nodal temperature of fuel stream, H_{CH} is height of the channel, R is the universal gas constant, F is the Faraday constant, X_b is molar fraction of different species at bulk level, $P|_{Node}$ is pressure of air/fuel stream side, and is $D|_{Node}$ diffusion coefficient of different species.

The air and fuel temperatures are considered in the above equations since the processes occur in flow channels. As the cathode and anode gas flows consists of different components, each cathode and anode gas species diffusivity are calculated.

$$D_{O_2}\big|_{Node} = \frac{1 - X_{O_2,b}\big|_{Node}}{\frac{X_{N_2,b}\big|_{Node}}{D_{O_2,N_2}\big|_{Node}}} = D_{O_2,N_2}\big|_{Node} \qquad \text{Equation 19}$$

$$D_i|_{Node} = \frac{1 - X_{i,b}\big|_{Node}}{\sum_j \frac{X_{j,b}\big|_{Node}}{D_{i,j}\big|_{Node}}} \qquad \begin{pmatrix} if\ i = H_2 \ \rightarrow j \in \{H_2O, CH_4, CO, CO_2\} \\ if\ i = H_2O \ \rightarrow j \in \{H_2, CH_4, CO, CO_2\} \end{pmatrix} \qquad \text{Equation 20}$$

Where $D|_{Node}$ diffusion coefficient of different species, $D_{i,j}\big|_{Node}$ is binary diffusion coefficient of different species, and $X_{i,b}\big|_{Node}$ is the molar fraction of different species at bulk level.

These diffusivities are calculated based upon the binary diffusion coefficients that are also calculated based upon Fuller equation:

$$D_{O_2,N_2}\big|_{Node} = (1 \times 10^{-4}) \times \frac{(1 \times 10^{-3}) \times (T_{PEN}|_{Node})^{1.75} \times \left(\frac{1}{M_{O_2}} + \frac{1}{M_{N_2}}\right)^{0.5}}{P_A|_{Node} \times \left[V_{O_2}^{\frac{1}{3}} + V_{N_2}^{\frac{1}{3}}\right]^2} \qquad \text{Equation 21}$$

$$D_{i,j}\big|_{Node} = (1 \times 10^{-4}) \times \frac{(1 \times 10^{-3}) \times (T_{PEN}|_{Node})^{1.75} \times \left(\frac{1}{M_i} + \frac{1}{M_j}\right)^{0.5}}{P_F|_{Node} \times \left[V_i^{\frac{1}{3}} + V_j^{\frac{1}{3}}\right]^2} \qquad \text{Equation 22}$$

$(i, j \in \{H_2, H_2O, CH_4, CO, CO_2\})$

Where $D_{i,j}\big|_{Node}$ is binary diffusion coefficient of different species, $T_{PEN}|_{Node}$ is the nodal PEN temperature, $P|_{Node}$ is pressure of air/fuel stream side and M is the molar mass of different species.

Calculation of gaseous mole fractions at the TPB is complicated by the presence of multi-component species transfer, as well as the porous electrode microstructure. Fick's model can be used to within a good approximation as follow:

$$X_{O_2,TPB}\big|_{Node} = 1 + \left(1 - X_{O_2,s}\big|_{Node}\right) \times exp\left(\frac{R\ T_{PEN}|_{Node}\ J|_{Node}}{4\ F\ P_A|_{Node}\ D_{O_2}^{eff}\big|_{Node}} \times \delta_{An}\right)$$ Equation 23

$$X_{H_2,TPB}\big|_{Node} = X_{H_2,s}\big|_{Node} - \frac{R\ T_{PEN}|_{Node}\ J|_{Node}}{2\ F\ P_F|_{Node}\ D_{H_2}^{eff}\big|_{Node}} \times \delta_{Ca}$$ Equation 24

$$X_{H_2O,TPB}\big|_{Node} = X_{H_2O,s}\big|_{Node} + \frac{R\ T_{PEN}|_{Node}\ J|_{Node}}{2\ F\ P_F|_{Node}\ D_{H_2O}^{eff}\big|_{Node}} \times \delta_{Ca}$$ Equation 25

Where $D_i^{eff}\big|_{Node}$ is effective diffusion coefficient of different species, $T_{PEN}|_{Node}$ is the nodal PEN temperature, $P|_{Node}$ is pressure of air/fuel stream side, R is the universal gas constant, δ is the thickness of different compartments, F is the Faraday constant, and $X_{H_2O,s}\big|_{Node}$is different species concentration at electrode surface.

Knudsen diffusion occurs when the mean free path is relatively long compared to the pore size, so the molecules collide frequently with the pore wall. Knudsen diffusion is dominant for the pores that range in diameter between 2 and 50nm. Molecular diffusion occurs when the mean free path is relatively short compared to the pore size and is described by Fick's law. Both ordinary diffusion and Knudsen diffusion may occur simultaneously in the porous media and the effect of these can be considered with the effective diffusion coefficient which is used in the above equations. The effective diffusion coefficient can be expressed as:

$$D_i^{eff}\big|_{Node} = \frac{\epsilon}{\tau} \times \left(\frac{1}{D_i|_{Node}} + \frac{1}{D_{i,Kn}\big|_{Node}}\right)^{-1}$$ Equation 26

Where $D_i^{eff}\big|_{Node}$ is effective diffusion coefficient of different species, $D_i|_{Node}$ is the diffusion coefficient of different species, $D_{i,Kn}\big|_{Node}$ is the Knudson diffusion coefficient of different species, ϵ is electrode porosity, and τ is electrode tortuosity.

The Knudsen coefficient can be calculated based upon the average molecular speed of each species as follows:

$$D_{i,Kn}\big|_{Node} = \frac{d_p}{3} \times \sqrt{\frac{8\,R\,T_{PEN}|_{Node}}{\pi\,M_i}} \quad \text{Equation 27}$$

Where $T_{PEN}|_{Node}$ is the nodal PEN temperature, M is the molar mass of different species, $D_{i,Kn}\big|_{Node}$ is the Knudson diffusion coefficient of different species, and d_p is pore diameter of electrodes.

3.1.1.2 Mass Balance

The mass balance equation for each node for different species are presented below.

$$\frac{dX_{H_2O}\big|_{Node}}{dt} = \frac{\dot{n}_{H_2O,In}\big|_{Node} - \dot{n}_{H_2O,Out}\big|_{Node} + \frac{I|_{Node}}{n_e \times F} - r_{SR}|_{Node} \times V_C|_{Node} - r_{WGS}|_{Node} \times V_C|_{Node}}{\frac{P_C|_{Node} \times V_C|_{Node}}{R \times T_C|_{Node}}} \quad \text{Equation 28}$$

$$\frac{dX_{H_2}\big|_{Node}}{dt} = \frac{\dot{n}_{H_2,In}\big|_{Node} - \dot{n}_{H_2,Out}\big|_{Node} - \frac{I|_{Node}}{n_e \times F} + 3 \times r_{SR}|_{Node} \times V_C|_{Node} + r_{WGS}|_{Node} \times V_C|_{Node}}{\frac{P_C|_{Node} \times V_C|_{Node}}{R \times T_C|_{Node}}} \quad \text{Equation 29}$$

$$\frac{dX_{CO}|_{Node}}{dt} = \frac{\dot{n}_{CO,In}\big|_{Node} - \dot{n}_{CO,Out}\big|_{Node} + r_{SR}|_{Node} \times V_C|_{Node} - r_{WGS}|_{Node} \times V_C|_{Node}}{\frac{P_C|_{Node} \times V_C|_{Node}}{R \times T_C|_{Node}}} \quad \text{Equation 30}$$

$$\frac{dX_{CO_2}\big|_{Node}}{dt} = \frac{\dot{n}_{CO_2,In}\big|_{Node} - \dot{n}_{CO_2,Out}\big|_{Node} + r_{WGS}|_{Node} \times V_C|_{Node}}{\frac{P_C|_{Node} \times V_C|_{Node}}{R \times T_C|_{Node}}} \quad \text{Equation 31}$$

$$\frac{dX_{CH_4}\big|_{Node}}{dt} = \frac{\dot{n}_{CH_4,In}\big|_{Node} - \dot{n}_{CH_4,Out}\big|_{Node} - r_{SR}|_{Node} \times V_C|_{Node}}{\frac{P_C|_{Node} \times V_C|_{Node}}{R \times T_C|_{Node}}} \quad \text{Equation 32}$$

$$\frac{dX_{O_2}\big|_{Node}}{dt} = \frac{\dot{n}_{O_2,In}\big|_{Node} - \dot{n}_{O_2,Out}\big|_{Node} - \frac{I|_{Node}}{2 \times n_e \times F}}{\frac{P_A|_{Node} \times V_A|_{Node}}{R \times T_A|_{Node}}} \quad \text{Equation 33}$$

$$\frac{dX_{N_2}\big|_{Node}}{dt} = \frac{\dot{n}_{N_2,In}\big|_{Node} - \dot{n}_{N_2,Out}\big|_{Node}}{\frac{P_A|_{Node} \times V_A|_{Node}}{R \times T_A|_{Node}}} \quad \text{Equation 34}$$

Where $\dot{n}$ $(mole/s)$ is the species molar flow rate, $I|_{Node}$ (A) is current of each node (negative for electrolysis process), $T_{A/C}\big|_{Node}$ (K) is temperature of each node along the anode/cathode stream, $P_{A/C}\big|_{Node}$ (Pa) is pressure of each node along the anode/cathode stream and $V_{A/C}\big|_{Node}$ (m^3) is volume of each node along the anode/cathode stream. The negative current leads to production of hydrogen and oxygen at cathode and anode sides as well as depletion of steam at cathode side.

3.1.1.3 Energy Balance

The energy balance equations for cathode and anode streams, PEN and bipolar plate are presented:

$$\left(\frac{P_C|_{Node} \times V_C|_{Node}}{R \times T_C|_{Node}} \times \bar{C}_{P_C}\big|_{Node}\right) \times \left.\frac{dT_C}{dt}\right|_{Node} = \sum_{Species} \dot{H}_{In}\big|_{Node} - \sum_{Species} \dot{H}_{Out}\big|_{Node} + \sum \dot{Q}_{conv_{C,PEN}}\big|_{Node} + \sum \dot{Q}_{conv_{C,BP}}\big|_{Node} - \frac{I|_{Node}}{n_e \times F}\left(h_{H_2}\big|_{Node} - h_{H_2O}\big|_{Node}\right) \quad \text{Equation 35}$$

$$\left(\frac{P_A|_{Node} \times V_A|_{Node}}{R \times T_A|_{Node}} \times \bar{C}_{P_A}\big|_{Node}\right) \times \left.\frac{dT_A}{dt}\right|_{Node} = \sum_{Species} \dot{H}_{In}\big|_{Node} - \sum_{Species} \dot{H}_{Out}\big|_{Node} + \sum \dot{Q}_{conv_{A,PEN}}\big|_{Node} + \sum \dot{Q}_{conv_{A,BP}}\big|_{Node} - \frac{I|_{Node}}{2 \times n_e \times F}\left(h_{O_2}\big|_{Node}\right) \quad \text{Equation 36}$$

$$(\rho_{PEN} \times V_{PEN} \times C_{PEN})|_{Node} \times \left.\frac{dT_{PEN}}{dt}\right|_{Node} = \sum \dot{Q}_{conv_{PEN,A,C}}\big|_{Node} + \sum \dot{Q}_{,cond_{PEN,BP}}\big|_{Node} + \sum \dot{Q}_{,cond_{PEN,PEN}}\big|_{Node} + I|_{Node} \times V_{op}\big|_{Node} - \frac{I|_{Node}}{n_e \times F}\left(h_{H_2O}\big|_{Node} - h_{H_2}\big|_{Node} - \frac{1}{2} \times h_{O_2}\big|_{Node}\right) \quad \text{Equation 37}$$

$$(\rho_{BP} \times V_{BP} \times C_{BP})|_{Node} \times \left.\frac{dT_{BP}}{dt}\right|_{Node} = \sum \dot{Q}_{conv_{BP,A,C}}\big|_{Node} + \sum \dot{Q}_{,cond_{BP,PEN}}\big|_{Node} + \sum \dot{Q}_{,cond_{BP,BP}}\big|_{Node} \quad \text{Equation 38}$$

Where $\dot{H}_{In}\big|_{Node}$ (J/s) and $\dot{H}_{Out}\big|_{Node}(J/s)$ are the total enthalpy of inlet and outlet stream of each node along anode/cathode stream, $\bar{C}_{P_{A/C}}\big|_{Node}$ $(J/mole.K)$ is an average specific heat capacity of species in each node along anode/cathode stream, $C_{PEN}|_{Node}$ $(J/kg.K)$ and

$C_{BP}|_{Node}$ $(J/kg.K)$ are specific heat capacities of each node on the PEN and interconnect plate, $\rho_{PEN}|_{Node}$ (kg/m^3) and $\rho_{BP}|_{Node}$ (kg/m^3) are densities of each node on the PEN and interconnect plate, $V_{PEN}|_{Node}$ (m^3) and $V_{BP}|_{Node}$ (m^3) are volume of each node on the PEN and interconnect plate and $T_{PEN}|_{Node}$ (K), $T_{BP}|_{Node}$ (K) are temperature of each node on the PEN and interconnect plate and $\dot{Q}\big|_{Node}$ (J/s) is composed of convection and conduction heat transfer to each node on each of different layers.

To calculate convection heat transfer between flows and solid walls, a local convective heat transfer coefficient is required. Reynolds numbers of steam and air flows in channels are much lower than critical Reynolds number because not only the steam and air channels' cross-sectional area are typically small, but also mean velocities of steam and air flow are not too high. In these conditions, a fully developed laminar flow and uniform surface temperature exist almost within all control volumes. Based upon engineering tables, in this study, a constant Nusselt number of four was used to calculate local convection heat transfer coefficient as below:

$$h = \frac{Nu_D \times k}{D_h} \qquad \text{Equation 39}$$

Where h is convection heat transfer coefficient, D_h is hydraulic diameter of channels, k is conduction coefficient of streams, and Nu_D is the Nusselt number.

3.1.1.4 Pressure Drop

Pressure difference between cathode/anode inlet and outlet flow conditions along the channel is calculated based upon the molar flow rate of cathode/anode flow as shown below:

$$P_{In,i} - P_{Out,i} = K_P \times \dot{n}_{In,i} \qquad i = Cathode\ Flow, Anode\ Flow \qquad \text{Equation 40}$$

Where P is pressure of different streams, and $\dot{n}_{In,i}$ is molar flow rate of different streams.

The constant K_P is:

$$K_P = Re_i \times f_i \times \frac{2 \times L_{CH,i}}{D_{h,i}^2 \times A_{CH,i}} \times \frac{\mu_i}{\rho_i} \times M_i \qquad i = Cathode\ Flow, Anode\ Flow$$

Equation 41

Where Re_i is Reynolds number of different streams, f_i is friction factor, $L_{CH,i}$ is length of channel, $D_{h,i}$ is hydraulic diameter of channel, $A_{CH,i}$ is cross sectional area of channel, μ_i is dynamic viscosity of different streams, ρ_i is density of different streams, and M_i is molar mass of different streams.

The friction factor f_i for cathode/anode flow which is considered as a fully developed laminar flow is calculated as:

$$f_i = \frac{16}{Re_i} \qquad i = Cathode\ Flow, Anode\ Flow$$

Equation 42

Where Re_i is Reynolds number of different streams, and f_i is friction factor.

The variation of cathode and anode flow inlet pressures (cathode/anode inlet pressures are considered as a state) can be obtained during the dynamic operating condition as below:

$$\frac{dP_{In,i}}{dt} = \frac{dP_{Out,i}}{dt} + K_P \times \frac{d\dot{n}_{In,i}}{dt} \qquad i = Cathode\ Flow, Anode\ Flow$$

Equation 43

Where P is pressure of different streams, and $\dot{n}_{In,i}$ is molar flow rate of different streams.

The change in outlet pressure in each time step comes from the change in inlet pressure of the next component in steam/air side. To obtain nodal pressure of streams, it is assumed that the pressure of anode and cathode flows drop linearly along the channels, so having inlet and outlet pressures as described above, all the nodal pressures can be calculated.

3.2 SOEC System Design and Control Strategies

Various system configurations can be designed for enabling safe and controllable SOEC operation. A particular system configuration has been developed to realize a stand-alone electrolysis system where the only energy input needed is electrical energy. Two inlet streams are present, the water stream and the ambient air stream. The system layout is

shown in Figure 24. Water is fed to the system by a pump to provide sufficient head to overcome system pressure drops and is assumed to enter the system at 15 °C. Feed water is pre-heated to 100 °C by the two intercooling stages of the hydrogen compression section. Evaporation is then carried out recovering heat from both stack outlet flows and completed by an electric steam generator. The steam is further pre-heated in a counter-flow heat exchanger with the outlet hydrogen-rich flow and then mixed with the hydrogen-rich recirculated flow entrained by the recirculation ejector in order to obtain the required cathode inlet composition with 10% hydrogen molar concentration [342]. The final super-heating necessary to bring the steam to the required stack inlet temperature is performed by the steam side electric heater. After the passage through the stack channels, where the electrochemical conversion of steam into hydrogen takes place, a recirculation valve allows a split of the outlet hydrogen-rich mixture for partial recirculation. The main stream is then cooled down by the counter-flow heat exchanger and steam generator in order to recover its thermal energy. Additional cooling below 60 °C is performed in the water separator and the water is recirculated into the feed water flow. The pure hydrogen flow is then sent to the two-stage compression section with intercooling to reach a final outlet pressure of 30 bar adequate for natural gas pipeline injection.

On the sweep-gas side, ambient air is fed to the system by a blower, pre-heated by a counter-flow plate heat exchanger with the stack anode outlet and further heated to the required stack inlet temperature by an electric heater. Crossing the stack, the flow is enriched by oxygen coming from the cathode side and then is used to pre-heat the entering air and contribute to the steam generation before being discharged to the environment.

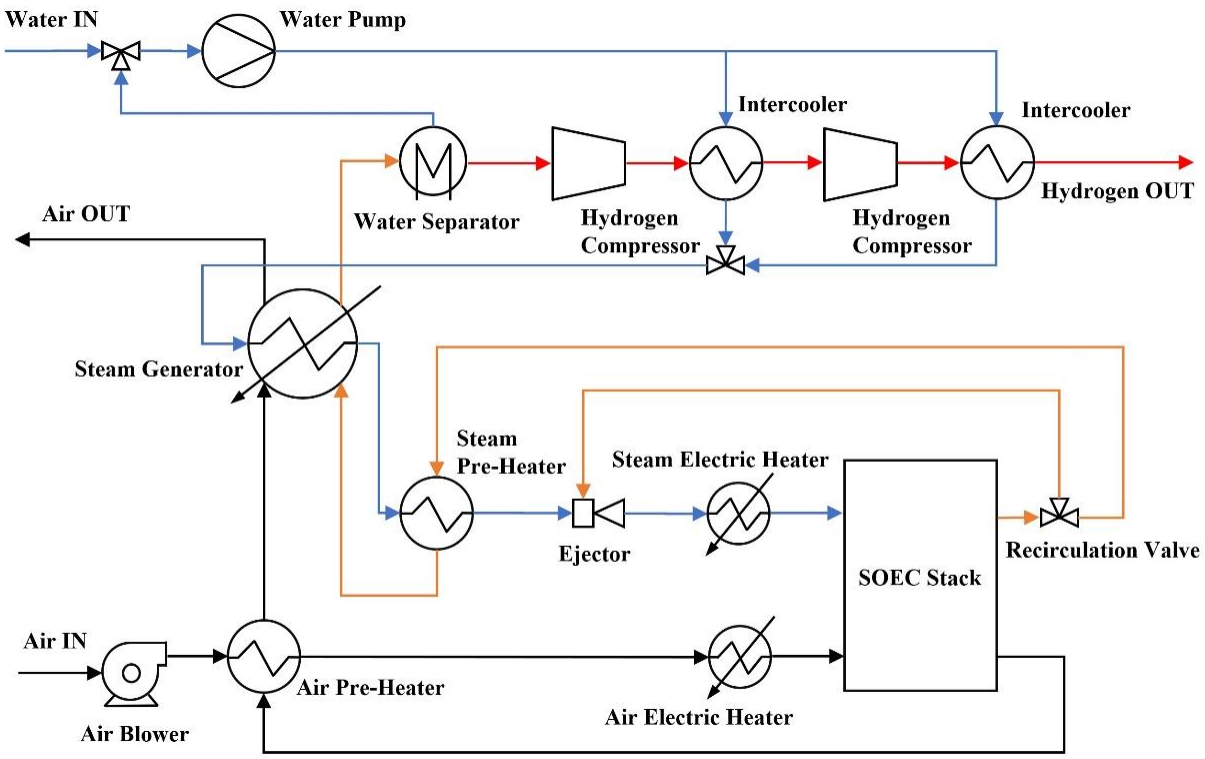

Figure 24: The developed SOEC system layout [343].

3.2.1 Balance of Plant Model

The BoP includes all the necessary components that are required to deliver both steam (fuel) and air (sweep gas) with a desired temperature at the electrolyzer inlet. It is composed of different components e.g., pump, blower, compressors, recuperator, ejector, electric heaters, intercoolers, and recirculation valve. Total steam and air flow rates are calculated based on the required steam and air at the electrolysis cell multiplied by the number of cells (N_{Cell}) in a unit stack. It is assumed that incoming steam and air are uniformly distributed between the cells. The balance of plant sub models are described below.

3.2.1.1 Pump

The pump sub-model as a component of BOP calculates the electric power of pump as below:

$$P_{Pump} = \frac{\dot{V}_{Feed\ Water} \times \Delta P_{Cathode\ Side}}{\eta_{Isentropic_{Pump}}}$$ Equation 44

Where $\dot{V}_{Feed\ Water}$ is volumetric flow rate of feed water, $\Delta P_{Cathode\ Side}$ is the pressure drop in cathode flow side, which is composed of pressure drop in electrolyzer, heat exchangers and mixing volume (ejector) and η_{iso} is isentropic efficiency of pump. Time constant for the pump is considered negligible.

3.2.1.2 Electric Heater

The electric heater sub-model is a component of BOP in both cathode and anode flow sides. This model calculates the power of electric heater based on inlet and outlet flow enthalpy as below.

$$P_{Electric\ Heater} = \frac{\dot{H}_{Out} - \dot{H}_{In}}{\eta_{Electric\ Heater}} \quad \text{Equation 45}$$

Where $\dot{H}$ is enthalpy of stream, and $\eta_{Electric\ Heater}$ is efficiency of the electric heater.

3.2.1.3 Heat Exchanger

A spatially and temporally resolved heat exchanger model has been developed for steam and air heat exchangers (recuperator) because thermal inertia (thermal time constant) is considerable and because bulk heat exchanger models ineffectively capture dynamic or off-design operating condition. In this study, the steam and air heat exchangers are assumed to be plate heat exchangers. This is a type of heat exchanger that uses metals to conduct heat from hot flow to cold flow. A main advantage of plate heat exchangers over a conventional heat exchanger is that the fluids have a much larger heat transfer surface area because the fluids spread out over the plates. This not only facilitates the transfer of heat but also greatly increases the speed of the temperature change. The spatially and temporally resolved model uses different states to calculate parameters at different nodes of a cell. These nodal states are calculated at each time among set of points in time vector with Matlab ODE solver. These states are composed of nodal temperature of hot flow, nodal temperature of metal plates, nodal temperature of cold flow and inlet pressure of both hot and cold streams. Nodal energy balance equation for the hot/cold stream includes convective heat transferred to the plate nodes and inlet/outlet enthalpy flux of the bulk flow from/to adjacent nodes. It is assumed that temperature in each control volume decreases/increases linearly along the control

volume of each node (for cold/hot streams). The nodal energy balance for the solid plates includes convective heat transferred to the solid plates from hot and cold streams and conductive heat transferred to adjacent nodes in plates. The inlet pressure for hot and cold streams are calculated at each time step completely the same as what was described for anode and cathode flows in electrolyzer model.

$$\left(\frac{P_{Cold} \times V_{Cold}}{R \times T_{Cold}} \times \bar{C}_{P_{Cold}}\right)\Big|_{Node} \times \frac{\partial T_{Cold}}{\partial t}\Big|_{node} = \sum_{Species} \dot{H}_{In}|_{node} - \sum_{Species} \dot{H}_{Out}|_{node} + \sum \dot{Q}_{conv_{Cold,Plate}}|_{node} \quad \text{Equation 46}$$

$\bar{C}_{P_{Cold}}$: Mean specific heat capacity of species (Cold Stream)

$$\left(\frac{P_{Hot} \times V_{Hot}}{R \times T_{Hot}} \times \bar{C}_{P_{Hot}}\right)\Big|_{Node} \times \frac{\partial T_{Hot}}{\partial t}\Big|_{node} = \sum_{Species} \dot{H}_{In}|_{node} - \sum_{Species} \dot{H}_{Out}|_{node} + \sum \dot{Q}_{conv_{Hot,Plate}}|_{node} \quad \text{Equation 47}$$

$\bar{C}_{P_{Hot}}$: mean specific heat capacity of species (Hot Stream)

$$(\rho_{Plate} \times V_{Plate} \times C_{Plate})|_{Node} \times \frac{\partial T_{Plate}}{\partial t}\Big|_{node} = \sum \dot{Q}_{conv_{Plate,Cold,Hot}}|_{node} + \sum \dot{Q}_{,cond_{Plate,Plate}}|_{node} \quad \text{Equation 48}$$

Where $\dot{H}_{In}|_{Node}$ (J/s) and $\dot{H}_{Out}|_{Node}(J/s)$ are the total enthalpy of inlet and outlet stream of each node, $\bar{C}_P|_{Node}$ $(J/mole.K)$ is an average specific heat capacity of species/plate in each node, $\rho_{Plate}|_{Node}$ (kg/m^3) is density of each node on the plate, V (m^3) is volume of each node on T (K) is temperature of each node, and $\dot{Q}|_{Node}$ (J/s) is composed of convection and conduction heat transfer to each node on each of different layers.

3.2.1.4 Hydrogen Compression Unit

In this study, a mixture of generated hydrogen and remained steam is separated at water separator (condenser) to inject generated hydrogen into the gas grid. The separation of hydrogen and steam occurs at the saturated temperature of steam at its partial pressure in the mixture (obtained based upon the system steam utilization and working pressure) which is about 333K. Then, the separated hydrogen compressed to the gas grid pressure which is 3MPa. In this study, two compression stage are performed to compress generated hydrogen

from 0.1MPa up to 3MPa. After each compression stage, an intercooler is performed to decrease the temperature to 333K. Required power of each compression stage and the outlet temperature of hydrogen at each compression stage are obtained as below:

$$T_{Out} = T_{In} \times (1 + \frac{\left(\frac{P_{Out}}{P_{In}}\right)^{\frac{\gamma-1}{\gamma}} - 1}{\eta_{Isentropic_{Compressor}}})$$

Equation 49

$$P_{Compressor} = \dot{n}_{H_2\ Produced} \times (T_{Out} - T_{In}) \times \frac{R}{\eta_{mechanical_{Compressor}}} \times \sum_{\#\ of\ Stage} Z \times \frac{\gamma}{\gamma - 1}$$

Equation 50

$$P_{Compressor,Total} = \sum_{\#\ of\ Stage} P_{Compressor}$$

Where T is temperature of hydrogen stream, R is the universal gas constant, P is pressure of hydrogen stream, $\eta_{Isentropic_{Compressor}}$ is isentropic efficiency of compressor, $\eta_{mechanical_{Compressor}}$ is mechanical efficiency of compressor, and γ is ratio of specific heats.

3.2.1.5 Steam Generator

Feed water should be evaporated to be used as a steam in high temperature SOEC. Steam generator is converting water to steam using two heat exchangers to recover the energy of both discharged air and mixture of hydrogen/steam. During dynamic operating condition, it is probable that the recovered energy is not enough to provide all the required steam. Therefore, an electric heater is considered to provide the required energy to completely convert fresh water to steam. Pinch point temperature of heat exchangers in which the energy of discharged air and hydrogen/steam mixture are recovered, are considered 20K in this study.

3.2.1.6 Ejector

As it was mentioned earlier, to prevent from the oxidation of materials at high operating temperatures, a portion of cathode outlet flow is recirculated (high hydrogen low steam mixture). The recirculated flow and fresh inlet steam are mixed in ejector. The ejector model uses states e.g., species concentration at the ejector outlet, outlet flow temperature and main

flow inlet pressure to simulate mixing of two flows. Simulating mixing of streams requires solving material balance equation for each species as well as energy balance equation.

In this study, the blower model uses blower rotational velocity as a state to consider the inertia of the blower. The blower rotational velocity is calculated at each time among set of points in time vector with Matlab ODE solver. The governing equation for blower calculates changes in blower rotational velocity based upon the difference between motor power supplied to the blower and power loss associated with the impeller. In this study, the minimum of the motor power supplied to the blower is set to be 0.5kW to avoid concentration losses in anode electrode as well as having nitrogen at the anode outlet flow to limit the corrosion of metallic components.

Equation 51

$$J \times w \times \frac{dw}{dt} = P_{Blower} - P_{Impeller}$$

Where J is momentum inertia of the blower, w is rotational speed of blower, and P is either blower power or impeller power.

Where the power loss associated with the impeller loss is calculated as below:

Equation 52

$$P_{Impeller} = \frac{1}{\eta_{Isentropic_{Blower}}} \times \frac{\gamma R T_{Amb}}{\gamma - 1} [\left(\frac{P_{Out}}{P_{Amb}}\right)^{\frac{\gamma-1}{\gamma}} - 1]$$

Where T_{Amb} is ambient temperature of air, R is the universal gas constant, P is pressure of air stream, $\eta_{Isentropic_{Blower}}$ is isentropic efficiency of blower, and γ is ratio of specific heats.

The blower outlet temperature is dependent on the pressure ratio of blower (based upon ideal gas assumption) is calculated as below:

Equation 53

$$T_{Out} = T_{In} \times \left(\frac{P_{Out}}{P_{Amb}}\right)^{\frac{\gamma-1}{\gamma}}$$

Where T is temperature of air, P is pressure of air stream, and γ is ratio of specific heats.

3.2.2 Control Strategy Development

3.2.2.1 Temperature Control

The primary challenge in designing an appropriate control scenario is to implement and control various components in the BoP, e.g., 3-way valve, air electric heater, steam electric heater and blower for different control purposes to support the dynamic operation of the SOEC for different operating conditions, while minimizing stack degradation and maximizing system efficiency. At different operating conditions, depending upon operating voltage, heating, or cooling of the stack may be required. In this study, to thermally manage the SOEC stack in a standalone SOEC system, two different thermal control strategies are investigated.

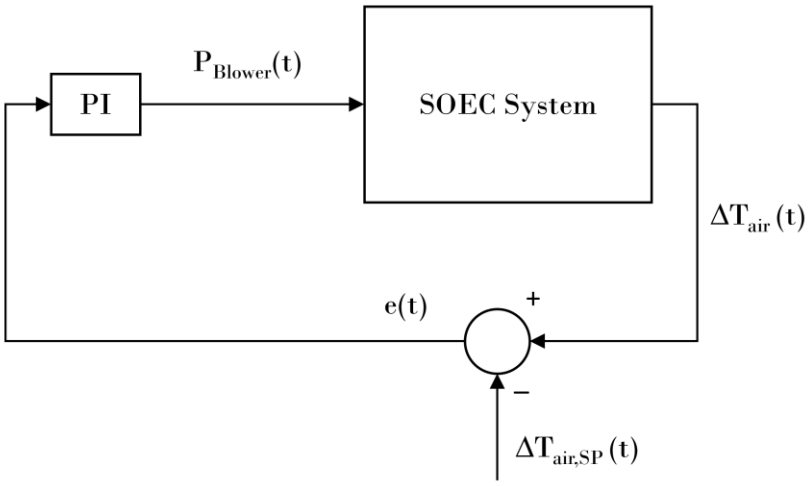

Figure 25: PI feedback controller loop for first control strategy.

In the first control strategy (Strategy I), the stack temperature is controlled by manipulating only one control variable which is blower power, manipulated with a PI controller in a feedback loop. Two sensors are applied to calculate the temperature difference between anode inlet flow and outlet flow. A variable speed blower physical model is used, such that the airflow can be increased/decreased by increasing/decreasing blower power to thermally manage the stack. The PI controller increases blower power to increase airflow rate when the magnitude of anode flow temperature difference becomes higher than the set-point which is 40K in this study. 0.5kW is a minimum motor power supplied to the blower to have sweep gas flow, which permits the convective transport of the produced oxygen to

avoid concentration overpotential in the anode electrode. Also, it introduces nitrogen at the anode side to limit the corrosion of metallic components. This control strategy keeps the cell operating temperature within a viable safe range. In this control strategy, the inlet temperature of both cathode and anode flows are fixed at 1023K, which is the nominal operating temperature of the stack.

In the second control strategy (Strategy II), the stack temperature is controlled by manipulating two control variables which are blower power and anode inlet temperature (sweep gas) manipulated with PI controllers in two independent feedback loops. Four sensors are applied to measure the temperature of the PEN corners in this control strategy besides the two sensors that mentioned for the first control strategy. The average of these four temperatures is an accurate representation of the PEN average temperature called "measured PEN average temperature" later in this article. When the measured PEN average temperature changes from the nominal operating temperature which is 1023K (controller set-point), the blower power and the anode inlet temperature begin changing in a way leading the measured PEN average temperature to get back into the controller set-point as well as temperature difference along the air side to be set in the desired one. In this control strategy, these two manipulated variables work in a way that simultaneously increase or decrease the cooling or heating potential of the anode stream. The main challenge in developing this control strategy is to accurately calibrate two manipulated actuators to be changed in a way that, for all the possible thermal scenarios, keeps the PEN measured average temperature at controller set point which is the nominal operating temperature. In this control strategy, the cathode flow inlet temperature is fixed at 1023K which is the nominal operating temperature of the stack. The schematic of PI controller is shown in Figure 26.

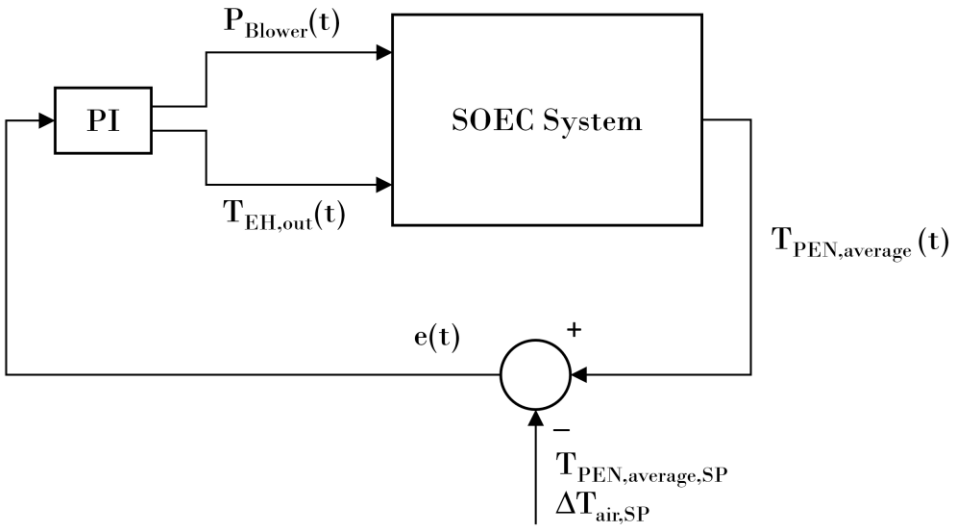

Figure 26: PI feedback controller loop for second control strategy.

3.2.2.2 Steam Flow Rate Control

The required feed water to the SOSE system is determined based upon Faraday's Law of electrolysis and specified steam utilization as indicated below.

$$\dot{n}_{H_2O} = \frac{I}{2\,.\,F} \cdot \frac{N_{Cell}}{SU} \qquad \text{Equation 54}$$

Where I is operating current, N_{Cell} is number of cells, F is Faraday constant, and SU is steam utilization.

The stack and system steam (fuel) utilizations in the cathode can be expressed in terms of the consumption of steam as:

$$SU|_{Stack} = \frac{\dot{n}_{H_2O,In}\big|_{Stack} - \dot{n}_{H_2O,Out}\big|_{Stack}}{\dot{n}_{H_2O,In}\big|_{Stack}} \qquad \text{Equation 55}$$

$$SU|_{System} = \frac{\dot{n}_{H_2O,In}\big|_{System} - \dot{n}_{H_2O,Out}\big|_{System}}{\dot{n}_{H_2O,In}\big|_{System}} \qquad \text{Equation 56}$$

In the proposed system, there is a little difference between stack steam utilization and system steam utilization, because there is a recirculation of produced hydrogen (a mixture

of hydrogen and steam) immediately after stack (cathode outlet) to satisfy having 10 percent mole of hydrogen at the cathode inlet. The addition of 10 percent mole of hydrogen in the cathode inlet flow is assumed to avoid the oxidation of the materials at elevated temperatures. For a given amount of steam flow rate, the higher the steam utilization, the higher the amount of hydrogen production is. It should be considered that the steam utilization should not be too high not only to avoid significant increasing in concentration overpotentials caused by steam starvation at the cathode flow outlet.

3.2.2.3 Input Power Control

The SOSE system is controlled by the electric power supplied to the stack. It is assumed that the power controller immediately adjusts the current for any change in stack input power (current controller).

$$I = \frac{P_S}{V_{cell}.N_{cell}} \qquad \text{Equation 57}$$

Where I is operating current, N_{Cell} is number of cells, and V_{cell} is cell voltage.

3.2.2.4 Cathode Oxidation Management (Cathode Recirculation Management)

Having hydrogen at the cathode inlet is assumed to prevent oxidation of materials which is probable in high temperatures. In this study the desired (set point) molar percentage of hydrogen at cathode inlet is considered 10 percent. The molar percentage of hydrogen is controlled by manipulating the opening percentage of a 3-way valve (considered as a state) in proportional-integral controller. The controller takes the percentage of hydrogen at the cathode inlet and calculate the difference between the actual percentage and the set point called hydrogen percentage error. Based on this error, controller begins opening the 3-way valve more (means that the portion of recirculated flow to passed flow is increased) whenever the error value is negative (molar percentage of hydrogen is less than the desired percentage) and vice versa.

3.2.3 System Performance Parameters

Once the system configuration was defined, the system performance can be evaluated considering system efficiency, stack efficiency and voltage efficiency.

$$\eta_{Sys} = \frac{\dot{n}_{H_2} \,.\, LHV_{H_2}}{P_S + P_{EH,An} + P_{EH,Ca} + P_{SG} + P_P + P_B + P_{Comp}} \quad \text{Equation 58}$$

$$\eta_S = \frac{\dot{n}_{H_2} \,.\, LHV_{H_2}}{P_S} \quad \text{Equation 59}$$

$$\eta_V = \frac{V_{Tn}}{V_{cell}} \quad \text{Equation 60}$$

where η is efficiency, $\dot{n}_{H_2}$ is the molar flow rate of produced hydrogen, LHV_{H_2} is the lower heating value of the hydrogen, P is power consumption of different components, and V_{Tn} is thermoneutral voltage at the stack operating temperature.

3.3 SOEC Stack Steady-State Results

First, the developed SOSE system model is used to carry out a steady state simulation on both stack level and system level to obtain not only the spatial distribution of different variables e.g., Nernst voltage, overpotential, current density and species concentration, but also the performance of the system at steady-state operating condition. The SOSE system is designed to operate at 1023K temperature and thermoneutral voltage, which is 1.285V at the design temperature. It should be noticed that the spatial distribution of both PEN operating temperature and operating voltage are obtained uniform with constant value of 1023K and 1.285V respectively.

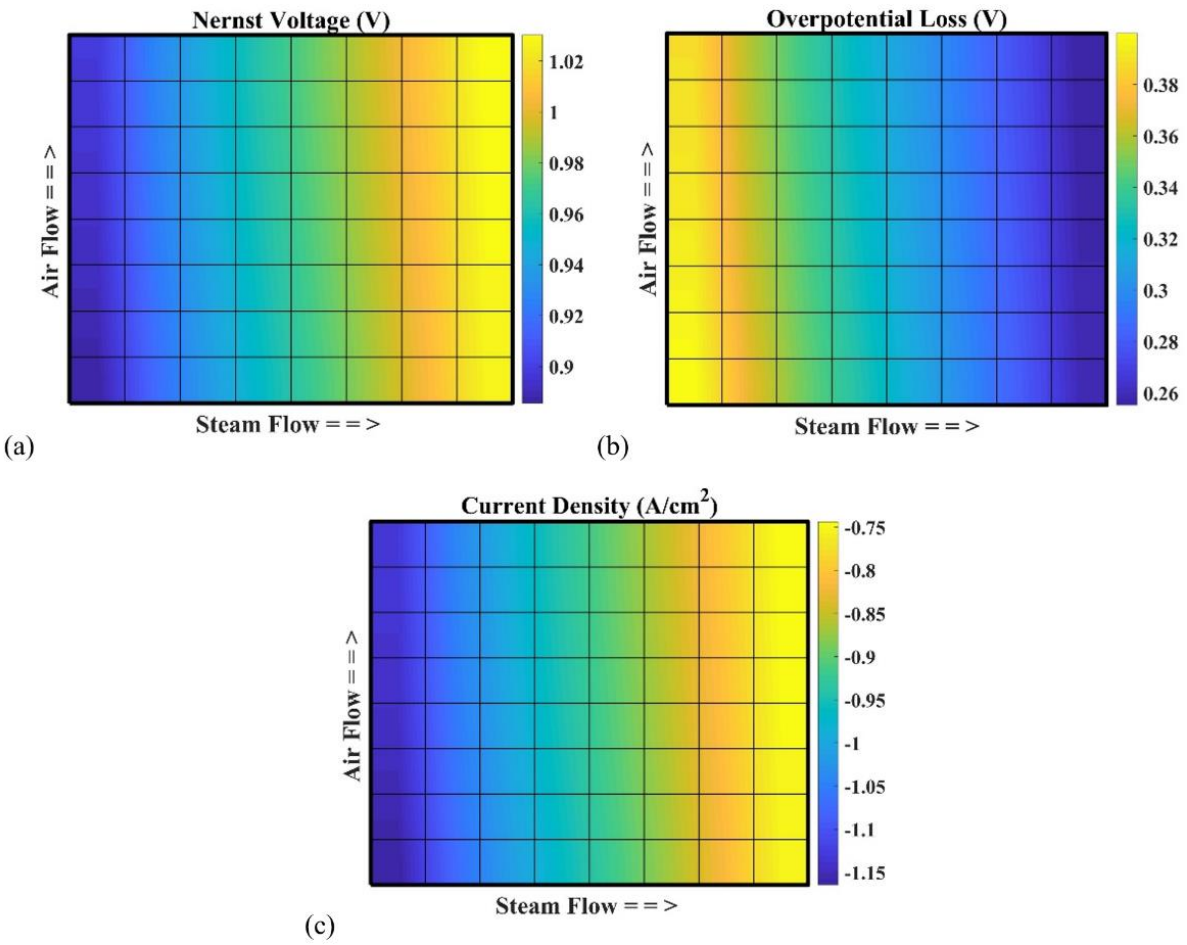

Figure 27: Steady-state spatial distribution of (a) Nernst voltage, (b) Overpotentials, (c) Current density.

Figure 27 shows the spatial distribution of Nernst voltage, overpotentials and current density in a unit SOE cell. The Nernst voltages are in the range of 0.89V-1.03V. The Nernst voltage has its highest amount at the corner close to the cathode and anode streams outlet and its lowest amount at the corner close to the cathode and anode streams inlet where both steam and air are fresh. The lowest amount of overpotentials is 0.26V captured where the current density has its lowest absolute value (0.76A/cm^2) and the Nernst voltage has its highest value. On the other hand, the highest amount of overpotentials is 0.39V which corresponds to the highest absolute value of current density (1.15A/cm^2) and lowest Nernst voltage value.

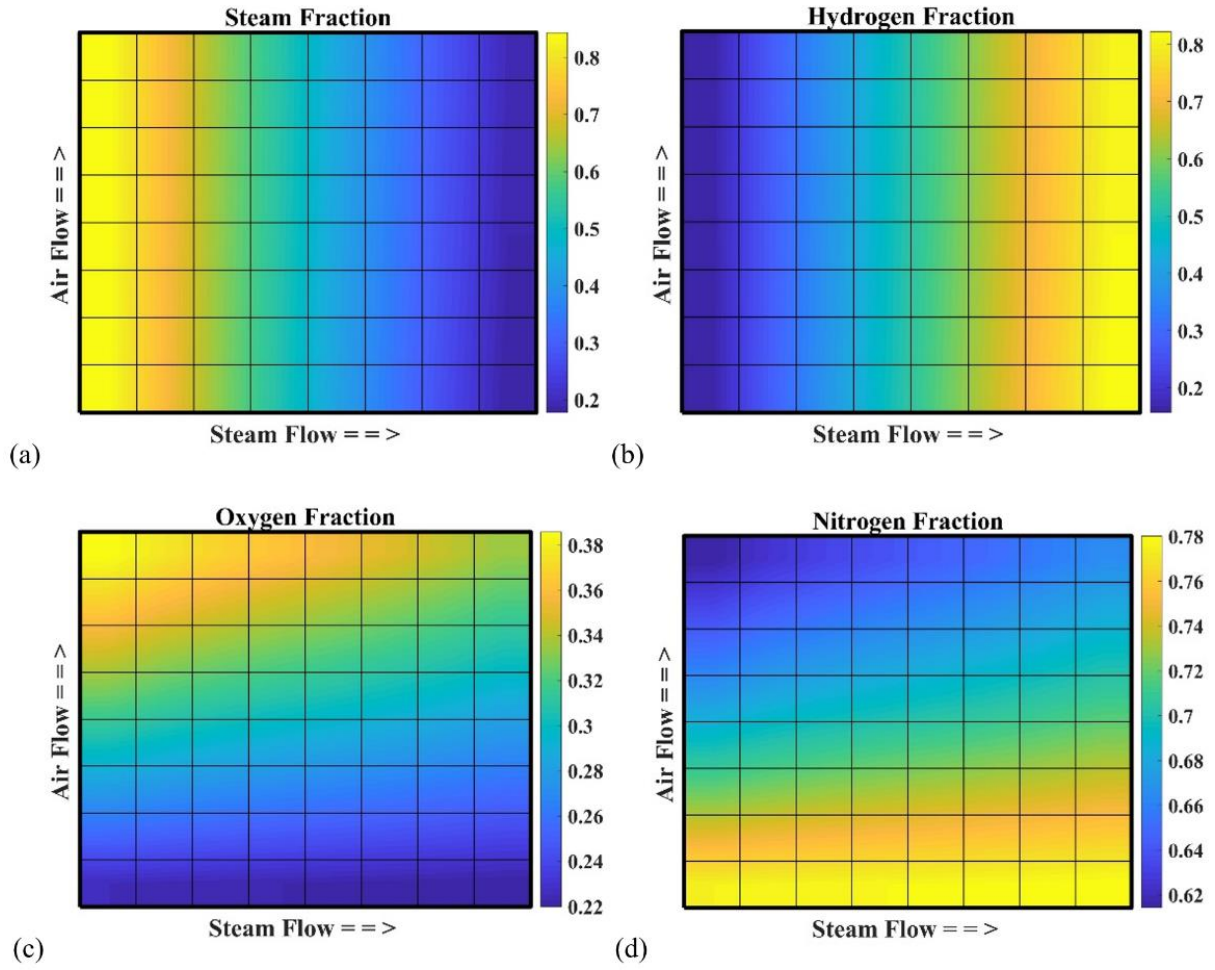

Figure 28: Steady-state spatial distribution of molar fraction of (a) Steam, (b) Hydrogen, (c) Oxygen, (d) Nitrogen.

Figure 28 shows the spatial distribution of different species' molar fractions. As shown, along the steam flow direction, the steam is consumed in the electrochemical reactions while the hydrogen is produced as a product of electrochemical reactions leading to lower steam and higher hydrogen molar fractions in the flow direction. The hydrogen concentration at the beginning of the cell is 10% which is imposed by a controller so that hydrogen present at the cathode inlet may prevent oxidation of stack materials at the high operating temperatures of an SOEC. At the cathode stream outlet, the hydrogen concentration is 80% which results from the inlet composition and steam utilization to produce hydrogen. Along the anode stream flow direction, oxygen molar fraction increases due to oxygen production by the electrochemical reactions, also resulting in a decrease in nitrogen molar fraction. The oxygen concentration varies from 22% to 38%. This relatively high change in oxygen concentration

along the anode flow direction is due to conditions of air flow rate that is at its minimum value associated with thermoneutral conditions. It should be noted that if the endothermicity or exothermicity of the electrochemical reactions is great enough, more air will be introduced to the SOEC stack (to cool or warm the stack), so that lower final oxygen concentrations will be achieved.

The developed model is also used to carry out a step-wise dynamic simulation for a wide range of stack input powers of 60kW to 450kW (20% to 150% of nominal power) with 15kW step size to evaluate and compare the effects of two thermal control strategies on the performance of the stack and BoP, particularly on the temperature distribution and the overall performance of the system.

Figure 29(a) shows that under the first strategy, increasing the stack input power from 300kW to higher powers moves the stack operating voltage from thermoneutral voltage to exothermic voltage conditions. The exothermicity of the electrochemical reactions increases the PEN average temperature since the blower does not act (push more air) for anode flow temperature differences lower than the set-point (40K). At a stack input power of about 420kW, the anode flow temperature difference becomes larger than 40K, and the blower begins pushing more air to decrease the anode flow temperature difference, leading to a small drop in PEN average temperature. Reducing the stack input power from 300kW to lower power makes the electrochemical reactions endothermic, which leads to a drop in the PEN average temperature since the blower does not act again for anode flow temperature differences lower than the controller set-point. At the stack input power of about 195kW, the magnitude of the anode flow temperature difference goes higher than 40K, and the blower begins increasing the introduced air to decrease the anode flow temperature difference leading to a small rise in the PEN average temperature. While, under the second control strategy, as shown in Figure 29(a), the controller acts in a way that it keeps the PEN average temperature quite constant at its nominal operating temperature (1023K). The PEN average temperatures change between 985-1061K and 1022.9-1023.1K under the first and the second control strategies, respectively.

As shown in Figure 29(b), maximum temperature difference along the PEN is always higher under the first strategy compared to the second one for all the evaluated stack loads. The maximum PEN temperature difference varies between 0.5K-16.5K and 0.5K-41.3K under the control strategies 'I' and 'II', respectively. As a result, the second strategy keeps the PEN average temperature quite constant while increases the PEN temperature difference. On the other hand, the first control strategy changes the PEN average temperature more while keeps the PEN temperature difference lower compared to the Second strategy. It is clearly shown in Figure 29(b), that both control strategies keep the PEN temperature difference within a safe operating range (lower than 100K).

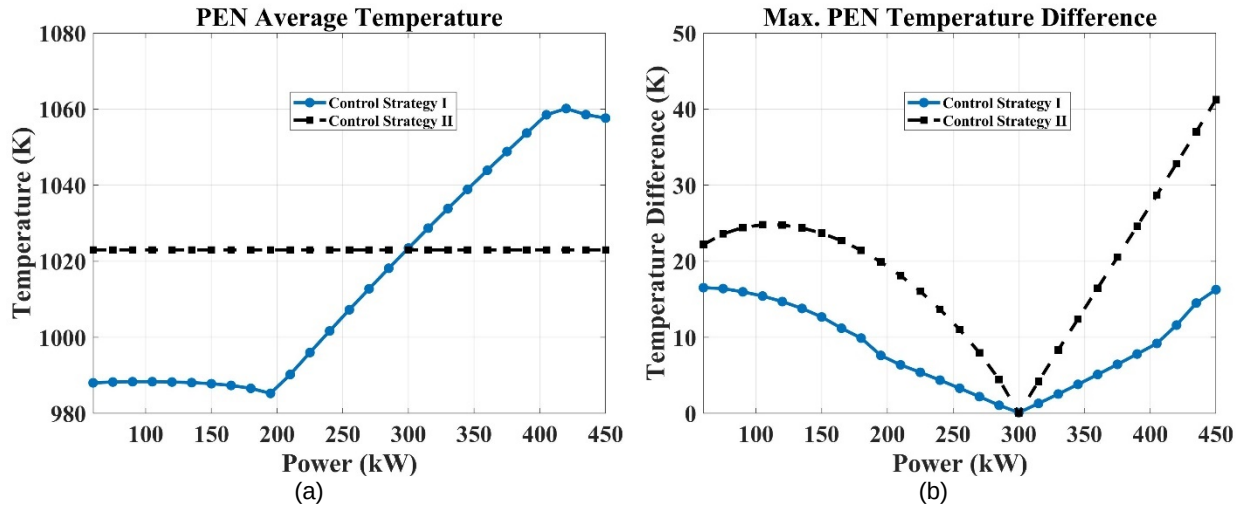

Figure 29: (a) PEN average temperature, (b) Maximum PEN temperature difference vs. stack input power.

Figure 30(a) and Figure 30(b) show the variation of minimum, average and maximum PEN temperature at different stack loads under the two developed control strategies. As clearly shown, all these temperatures change in quite a similar pattern as the stack operates under the first control strategy. However, when the stack operates under the second control strategy, as stack power goes higher than 300kW or lower than 300kW, the maximum and minimum temperatures change in the opposite direction leading to a constant PEN average temperature. It should be noted that the maximum or minimum temperatures shown in Figure 30 are not related to one specific node on the PEN, meaning that one node might have maximum temperature at one stack load and another node might have the maximum temperature at a different stack load.

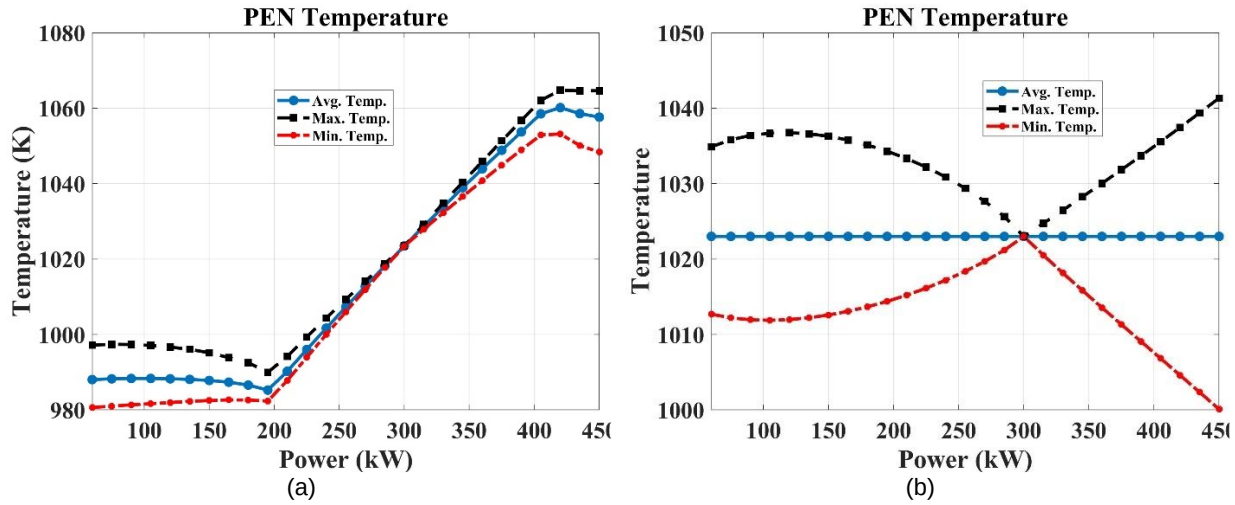

Figure 30: PEN average, maximum and minimum temperatures (a) first control strategy, (b) second control strategy.

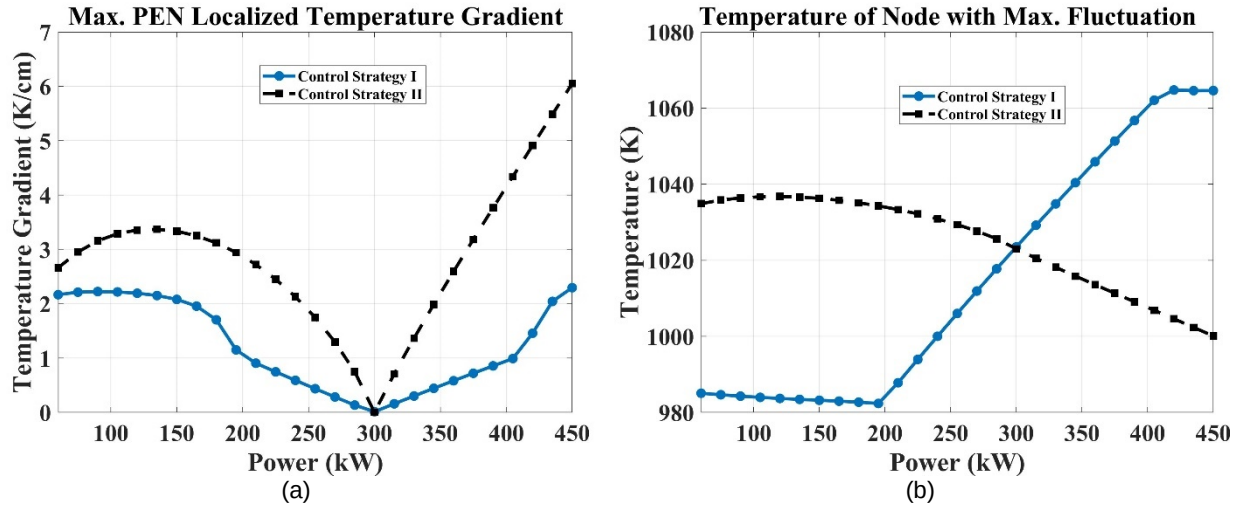

Figure 31: (a) Maximum PEN localized temperature gradient, (b) temperature of a node on the PEN with the highest temperature fluctuation vs. stack input power.

The maximum PEN localized temperature gradient changes between 0.01-2.3K/cm and 0-6.1K/cm, operating under first and second strategies, respectively, as represented by Figure 31(a). Both control strategies keep the PEN localized temperature gradient inside a safe operating range (lower than 10K/cm). Figure 31(b) depicts the temperature of a specific node which experiences the highest temperature fluctuations and varies between 982-1065K and 1000-1037K under first and second strategies, respectively. These nodes are

located at one corner of the PEN for control strategy I, and at the opposite corner of the PEN for control strategy II.

Figure 32 shows the spatial distribution of different operating parameters in a highly exothermic condition in which the operating voltage is higher than thermoneutral voltage for the two developed control strategies. As expected, the PEN average temperature is above 1023K under first control strategy while it is equal to 1023K under second control strategy.

Control Strategy I	Control Strategy II
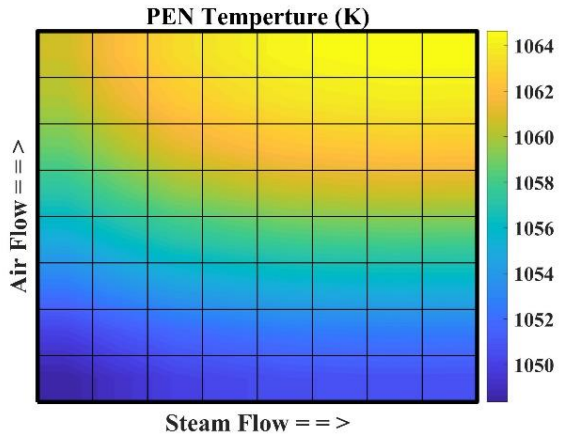	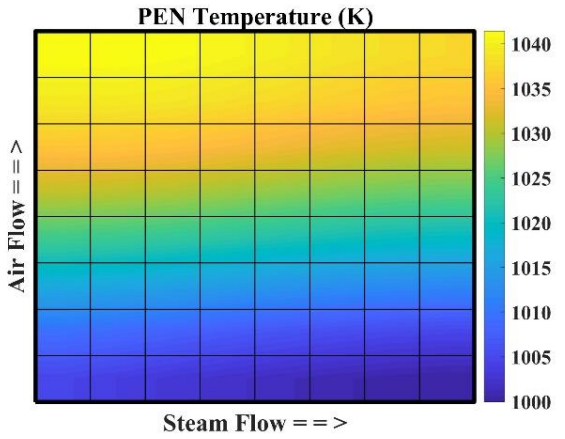
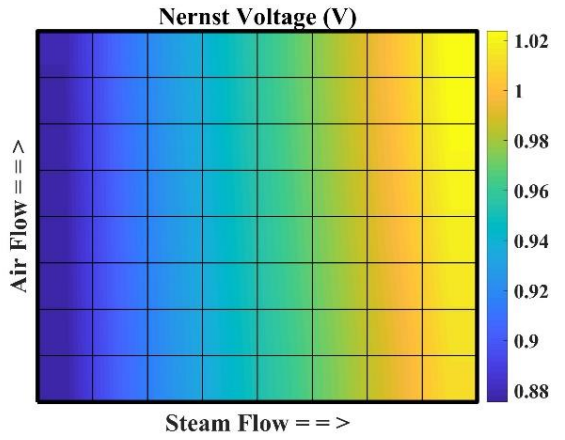	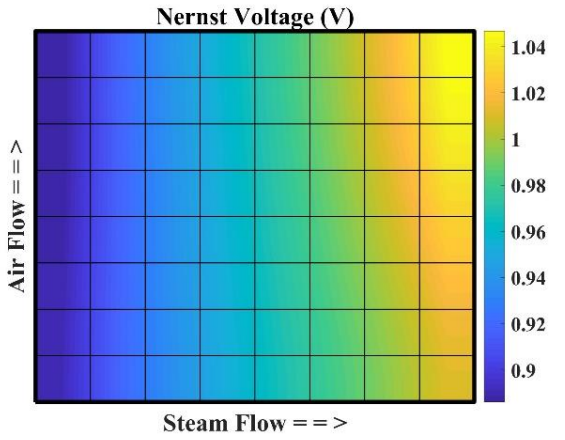
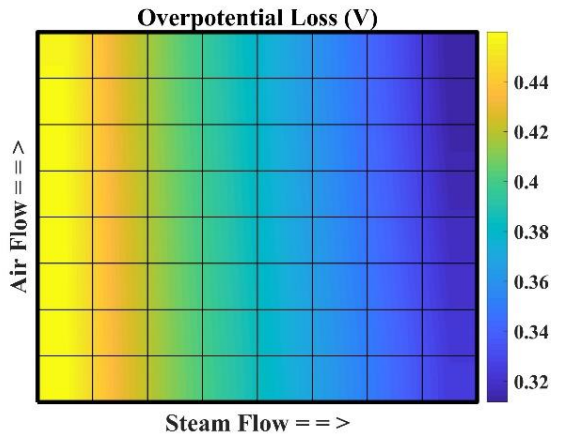	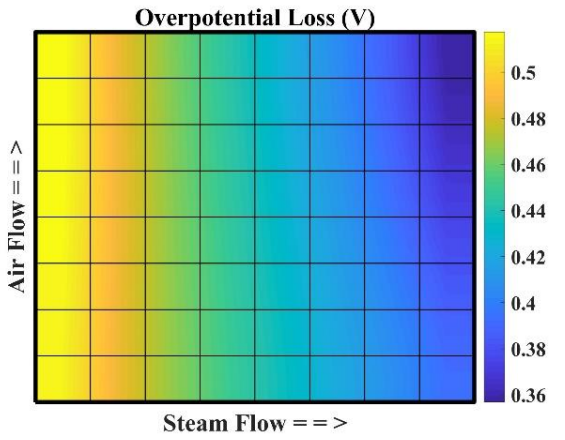

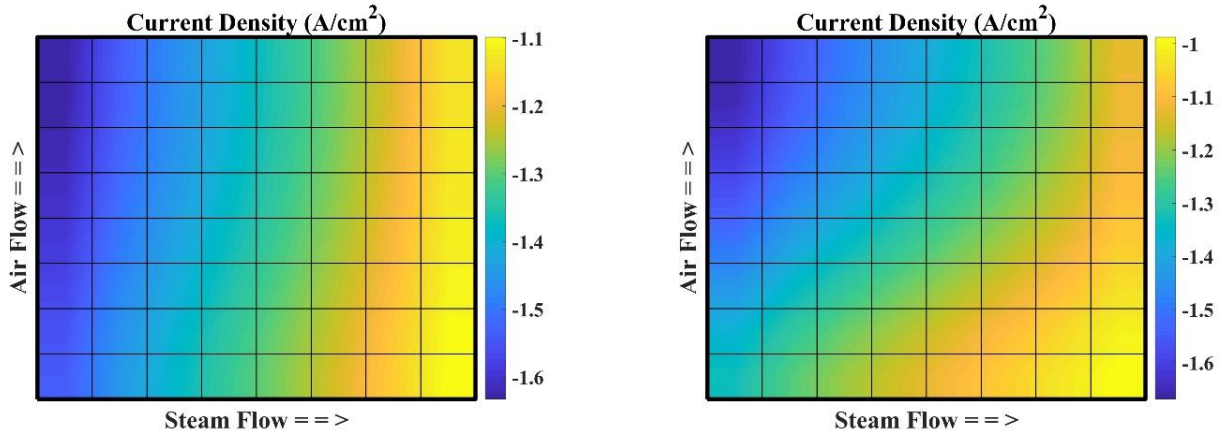

Figure 32: Spatial distribution of different operating parameters at highly exothermic condition.

Figure 33 shows the spatial distribution of different operating parameters in a highly endothermic condition in which the operating voltage is lower than thermoneutral voltage for the two developed control strategies. As expected, the PEN average temperature is below 1023K under first control strategy while it is equal to 1023K under second control strategy.

Control Strategy I | **Control Strategy II**

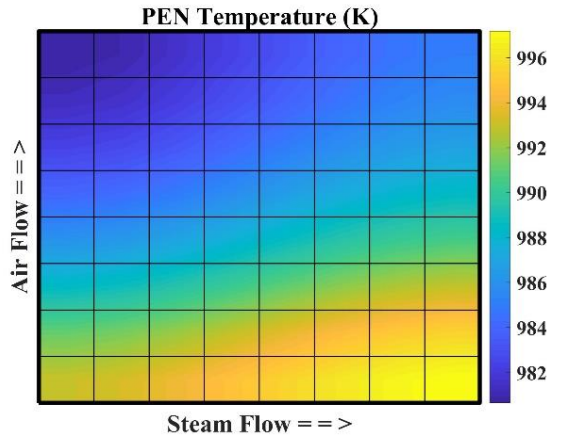

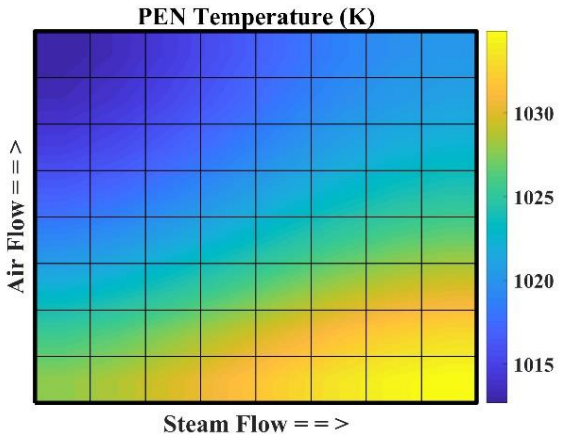

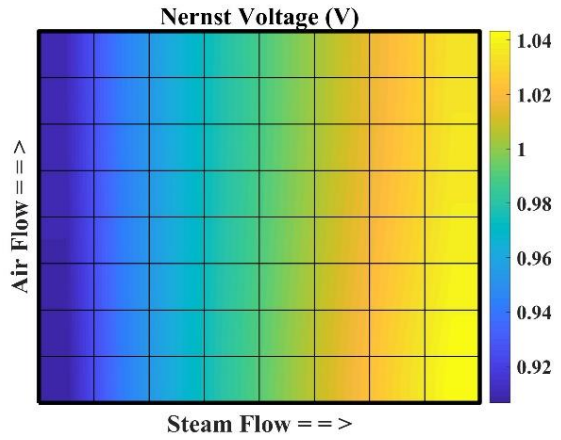

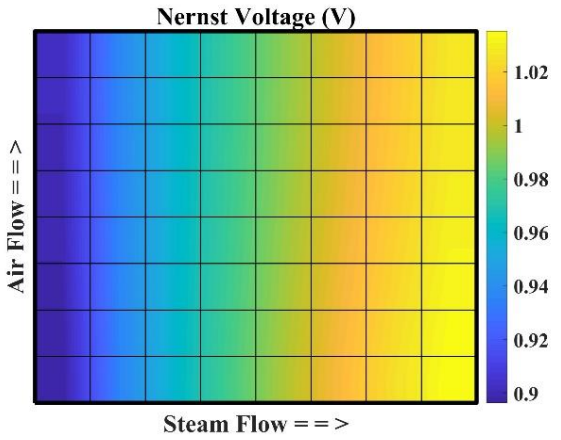

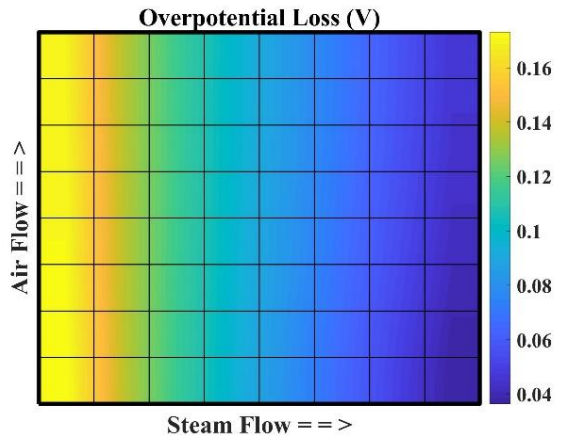

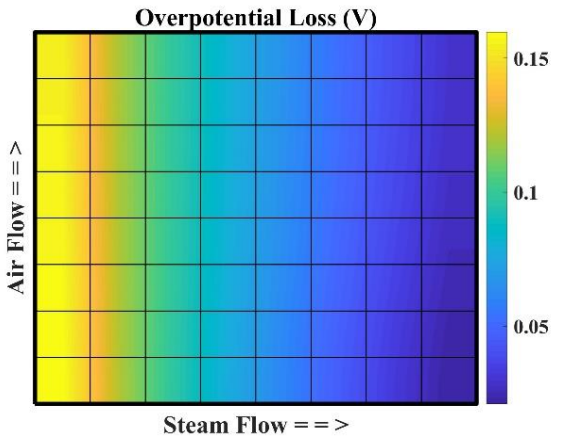

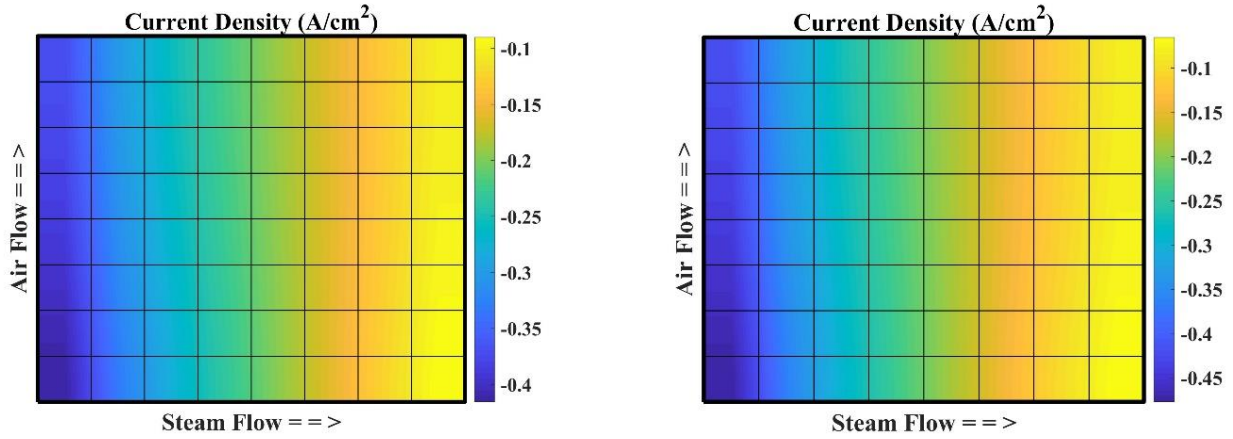

Figure 33: Spatial distribution of different operating parameters at highly endothermic condition.

3.4 SOEC System Steady-State Results

The system and stack efficiencies are presented in Figure 34(a) and Figure 34(b). For both control strategies, the system efficiency varies between 45% and 75%. Under the first control strategy, the system efficiency is almost constant between stack input powers of 195kW to 420kW results from having the blower working at its minimum power since anode flow temperature difference is below the controller set-point. However, for the second control strategy, the system efficiency is at its highest value at the nominal power (300kW) since at greater and lesser stack input powers, both the blower power and the air electric heater power change to keep the PEN average temperature fixed at its nominal value. For stack input powers higher than 300kW, the stack efficiency is higher for the first control strategy compared to the second one since current, and as a result hydrogen production rate, is higher due to the lower ASR, and as a consequence, lower overpotential associated with higher PEN average temperature is achieved. In opposition, for stack powers lower than 300kW, the stack efficiency is lower for the first strategy due to the higher ASR, and as a result, higher overpotential results from lower PEN average temperature.

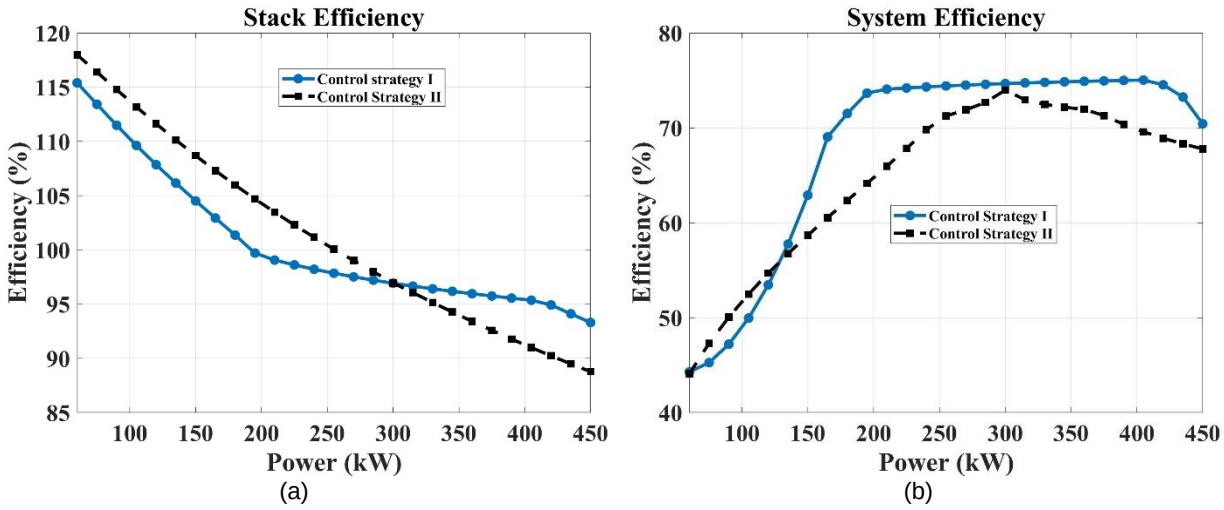

Figure 34: (a) System efficiency, (b) Stack efficiency vs. stack input power.

Figure 35(a) demonstrates the hydrogen production rate at different stack input powers. Under the two control strategies investigated, the hydrogen production rate is similar. The operating current and so the hydrogen production rate are higher when the system operates under the second control strategy for stack loads lower than 300kW, while these parameters are higher for stack loads higher than 300kW under the first control strategy. The captured difference under the two control strategies is due to the difference in operating voltage at a given current level that results from a difference in the PEN temperature and resulting ASR. Figure 35(b) shows the system energy consumption per mass of produced hydrogen at different stack input powers. Note that these range from 45-75 kWh/kg, which is better than low temperature electrolysis at the low end, and comparable to those of low temperature electrolysis in the middle and high end of this range. Note that all the required energy is supplied in the form of electrical energy without using an external heat source on the system, which would improve the SOEC electrical efficiency.

According to Figure 36(a), the stack accounts for the largest part of electricity consumption, higher than 70% in wide range of operating conditions. Only in strong endothermic conditions, does the required energy for stack heating reduce the stack power contribution to below 50%. The required energy for steam generation contributes about 10-14% of the total consumption for stack loads between 195-420kW. This is the range in which the air flow is at its minimum, meaning that a small amount of heat can be recovered in the steam

generator section and the evaporation heat must be provided via electric heating. As shown in Figure 36(b), when the system operates under the second control strategy, the main electricity consuming components are the stack and air electric heater, which together account for more than 80% of the system electricity consumption. When the stack loads are lower than 300kW and the stack works below the thermoneutral voltage, and the BoP contribution in power consumption increases noticeably. Especially the blower and the air electric heater power consumption increase due to the need to increase both air flow and stack inlet air temperature to maintain the constant cell temperature. However, for stack loads higher than 300kW, the air flow increases while the stack inlet air temperature decreases to cool the stack to keep its temperature constant. For most stack load conditions, the electric steam generator contributes only around 1% of total system consumption because of a high mass flow rate of air involved in thermally managing the stack and therefore effective heat recovery can be used in the steam generator. However, when the system operates near the thermoneutral voltage, where cooling or heating decrease consistently, less heat can be recovered at the evaporation temperature and therefore the steam generator consumption reaches up to about 10% of the total power consumption. The hydrogen compressor contribution is about 3-7% which is only dependent on the hydrogen production rate. It can be concluded that when the electrolysis system does not use an external heat source, it is better in terms of efficiency and performance to work at or above the thermoneutral voltage.

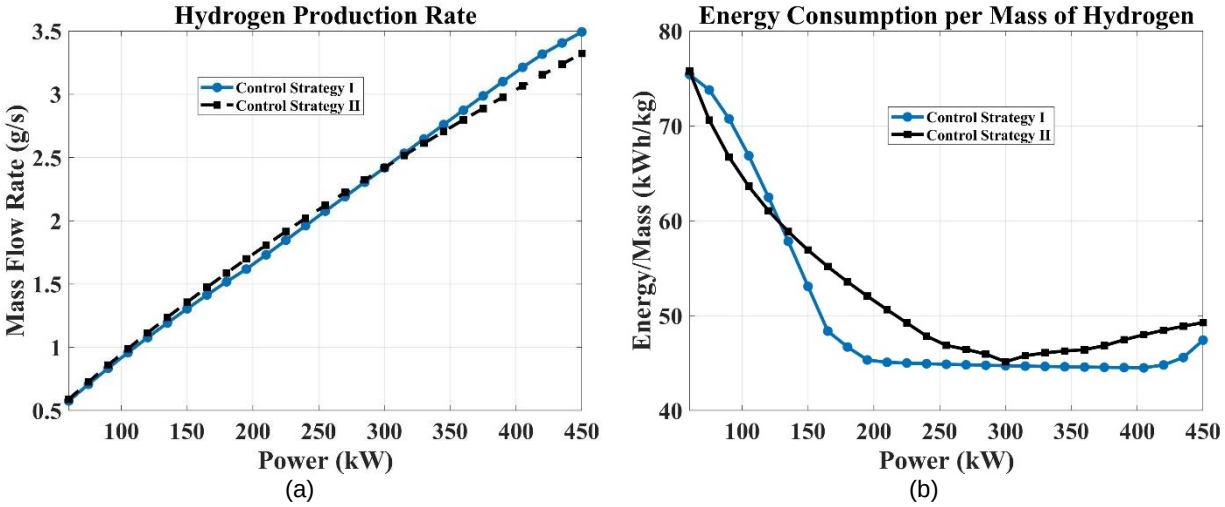

Figure 35: (a) Hydrogen production rate, (b) Energy consumption of the system vs. stack input power.

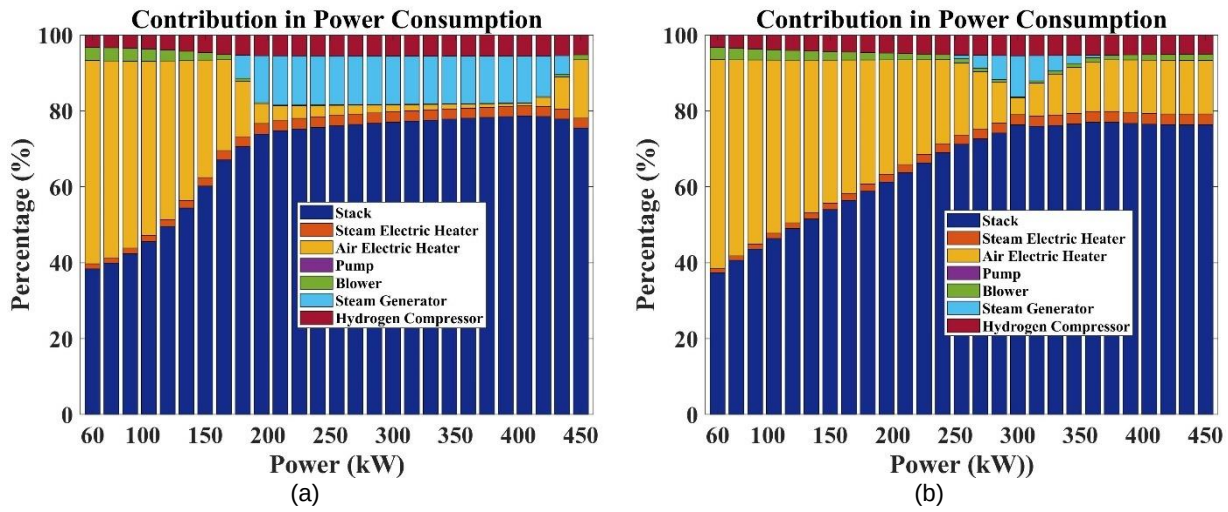

Figure 36: Contribution of system components in power consumption (a) First control strategy, (b) Second control strategy.

3.5 Summary

This Chapter has focused on developing a spatially and temporally resolved solid oxide electrolysis cell model. It has also focused on designing solid oxide electrolysis system and its required control strategies and developing dynamic model of different balance of plant components. Additionally, it has focused on a comparative analysis of an SOEC system for a stepwise dynamic operation under two different thermal control strategies, by analyzing the overall system performance at different stack power loads. System simulation results show that the PEN average temperature can be well maintained by both control strategies while operating dynamically. PEN average temperature is quite constant and invariant under the second control strategy while it varies considerably more under the first one. Operation under both control strategies, the PEN localized temperature gradient is always maintained below the maximum tolerable temperature gradient. The overall efficiency of the system is higher for the first control strategy compared to the second one while the temporal temperature variation of the PEN is lower for the second control strategy compared to the first one.

4 SOEC System Dynamic Operation

The University of California, Irvine (UCI) campus microgrid incorporates about 4MW of solar PV. A 15-minute resolution dataset for operation of PV generation was obtained from a database that archives PV power dynamics of systems on the UCI campus. The dataset was scaled to a maximum of 450kW of PV generation to consider the case where about 10% excess generated electricity is to be utilized by the SOSE system for renewable hydrogen production.

The PV generation dataset was analyzed to obtain a day in which the PV generated power has its highest dynamic behavior (a cloudy day) and another day in which the PV generated power is maximum (a sunny day). Figure 37 shows PV generated power for both the sunny day and the cloudy day.

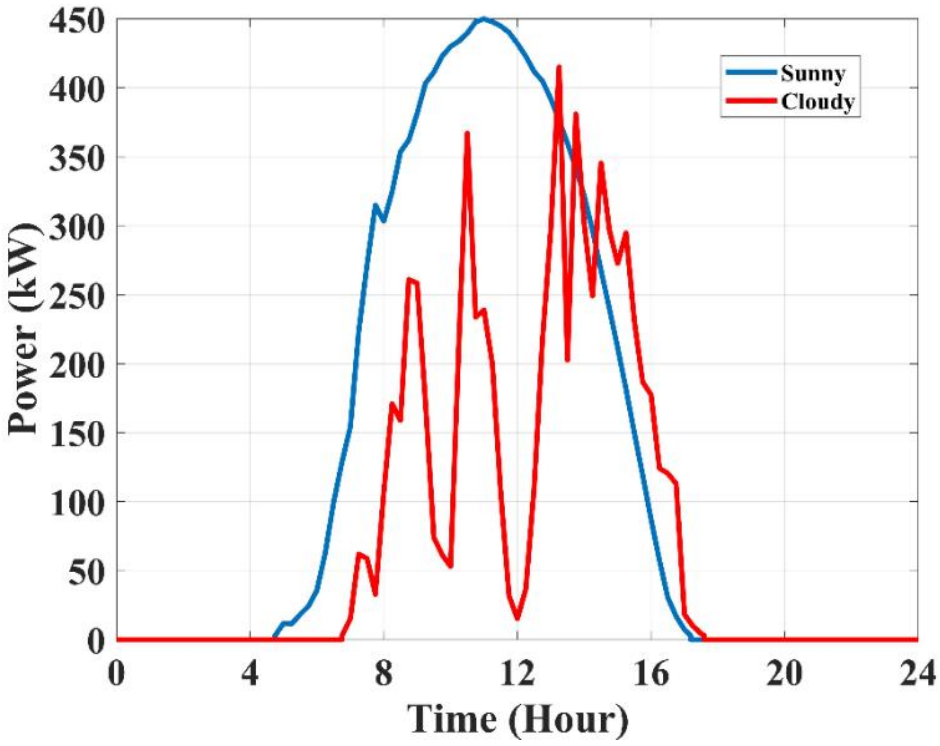

Figure 37: PV generated power for a sunny day and a cloudy day.

The purpose of this section is to evaluate the capability of the SOSE system to effectively convert renewable electrical power into hydrogen and to dynamically follow input power variations while maintaining all system variables within acceptable limits. The obtained PV

generated powers (Figure 37) are given directly to the SOSE system to evaluate the performance of the SOSE system as it might be integrated with over-generated renewable PV power. The dynamic simulation of the SOSE system using measured dynamic power generation profiles for sunny and cloudy days as input to the system are exactly expected for a real-world application.

4.1 Sunny Day Simulation

The PV generated power for a sunny day between 4:45 and 17:15 is directly given to the stack as an input power to capture the dynamic performance of the SOSE system. Figure 38 shows both the PV generated power in the sunny day which is directly given to the stack and the SOE stack consumed power which is obtained by multiplying the operating voltage by the current and number of the cells. It shows that how closely the SOE system captures the transient behavior of the given power.

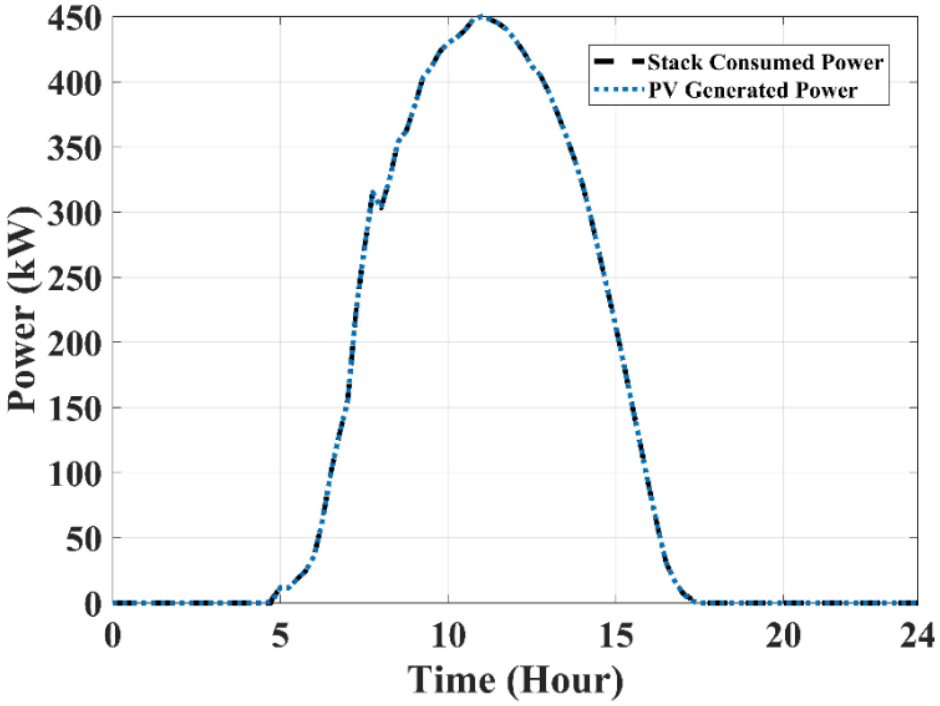

Figure 38: PV generated power vs stack consumed power for sunny day.

Figure 39 shows that the cell current density varies in the range of 0-1.35A/cm^2 and reaches its maximum value at about 11 exactly when the PV Generated Power has its maximum amount (Figure 38). As displayed in Figure 39, the cell operating voltage varies between the

0.87-1.33V. The operating voltage begins in endothermic region crossing the thermoneutral voltage at about 7:30 going to exothermal operating condition, and it goes back to endothermal operating condition at 14:30. These 7 hours of operation include conditions in which stack input power is higher than nominal 300kW stack power.

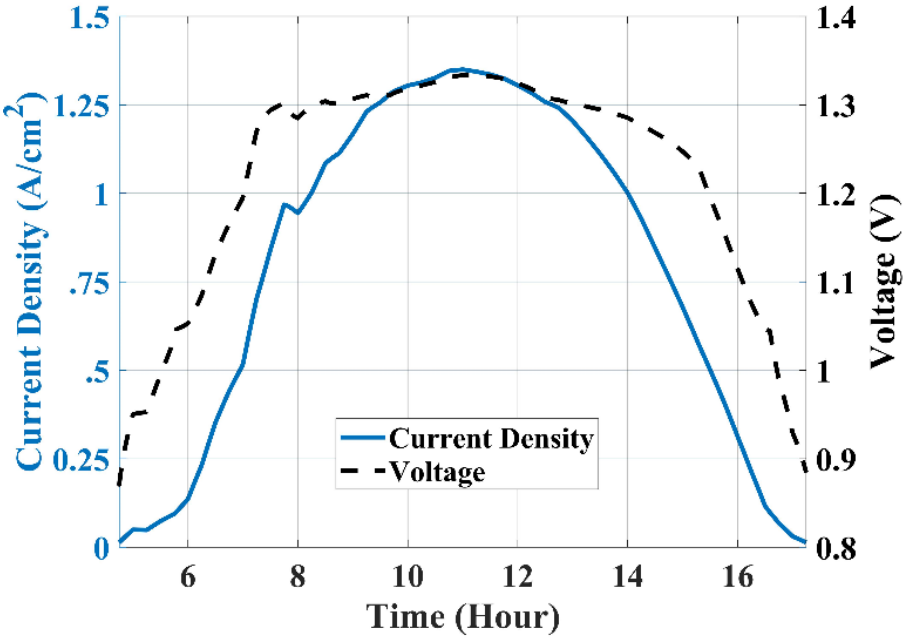

Figure 39: Cell current density and voltage for a sunny day.

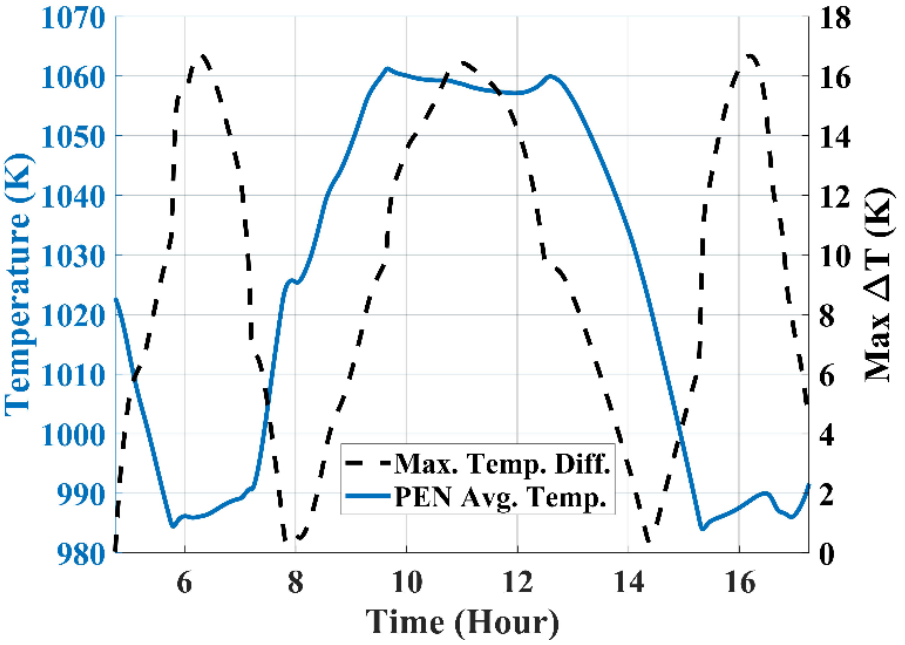

Figure 40: PEN average temperature and maximum temperature difference along the PEN for a sunny day.

Figure 40 illustrates that the PEN average temperature varies between 985-1062K. It is assumed that at the beginning of system operation, the stack has uniform temperature of 1023K, which is the steady-state nominal operating condition at thermoneutral conditions so that the temperature difference along the PEN is zero. Early in the morning, during the startup, the PEN average temperature drops because of the endothermicity of the reactions below the thermoneutral point. At about 6:00, the PEN average temperature reaches its minimum level due to a period of operation in the high endothermicity region of the electrochemical reaction. Due to the large and continuous endothermicity at this moment, the anode stream temperature difference reaches to 40K (the controller set-point). The thermal controller begins introducing more air flow to the SOE stack by manipulating the blower power. As a result, the cell average temperature is maintained between maximum and minimum set-point values (1023K±40K). The minimum cell average temperature is 985K which is about 40K (controller set-point) lower than the nominal operating temperature. However, increasing the air mass flow rate to maintain average cell temperature in the acceptable region, causes a temperature gradient along the cell as shown in Figure 40. The maximum temperature difference along the cell is 18K which is acceptable for SOEC dynamic operation in terms of resulting thermal stress. Figure 40 clearly shows how the temperature controller perfectly acts to maintain the cell average temperature between maximum and minimum set-point values (1023K±40K) by manipulating the blower power. At about 7:30, when the operating voltage approaches the thermoneutral voltage, the PEN average temperature returns to 1023K (the steady state nominal operating temperature). Around 11:00, the SOEC is working in the highly exothermic operating condition, in which the temperature controller increases the blower power to maintain the temperature below 1062K, which is about 40K higher than the nominal operating point. At 11:00, the PEN average temperature and temperature difference along the PEN are close to their maximum value. As shown in Figure 40, the thermal controller maintains the temperature in the range of ±40K of the nominal operating temperature. The closer the voltage gets to the thermoneutral point, the more the PEN average temperature approaches the nominal operating point and the more uniform the temperature distribution becomes. Note also that the temperature difference along the PEN is zero when the stack is not operating and whenever the cell operating voltage is close to thermoneutral point. Note that

both Figure 39 and Figure 40 provide evidence of the SOEC stack thermal inertia at around 7:30 when the cell operating voltage crosses the thermoneutral voltage. At this moment, the stack average temperature is about 997K which is about 25K lower than what is expected under thermoneutral operating conditions. Also, according to Figure 40, there is a 6K temperature difference along the stack at this moment (versus the uniform temperature that occurs under thermoneutral conditions at steady state). At around 7:45, the stack average temperature becomes 1023K. It shows that although the operating voltage crosses thermoneutral voltage at 7:30, there is a 15-minute delay for the stack, due to its thermal inertia, to reach 1023K which is associated with thermoneutral operating point.

Figure 41 shows minimum, average, and maximum PEN temperature versus time. When the operating voltage is close to the thermoneutral point, all three temperatures are close to each other and equal to the nominal operating temperature. However, at highly endothermic and exothermic operating conditions, the deviation of minimum and maximum temperature from the average temperature increases which causes temperature gradient along the cell (as discussed regarding Figure 40).

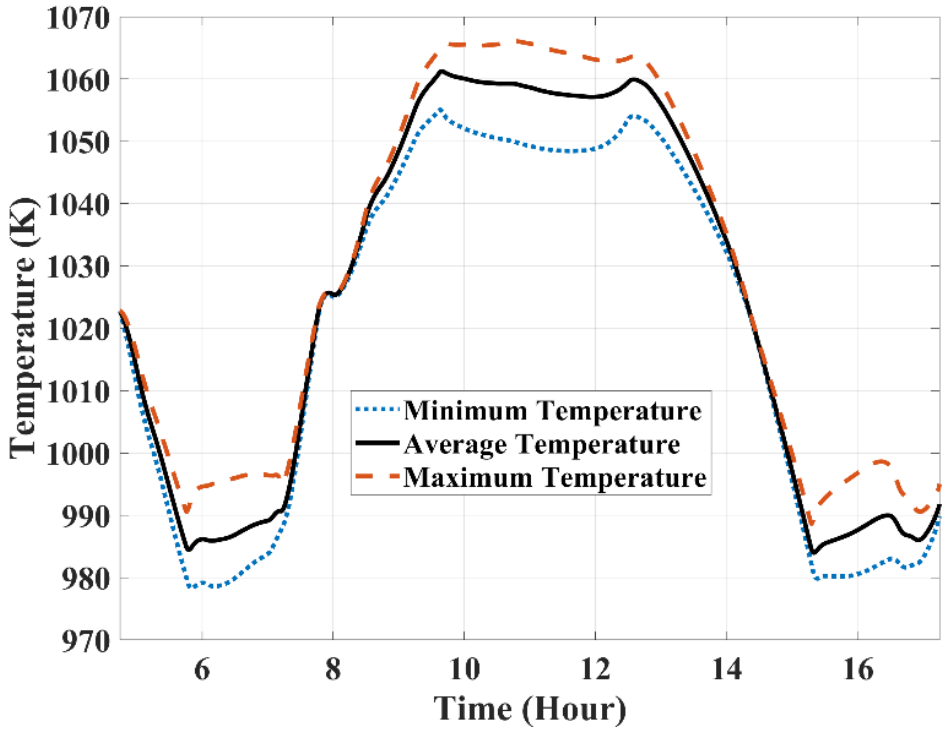

Figure 41: PEN minimum, average and maximum temperature for a sunny day.

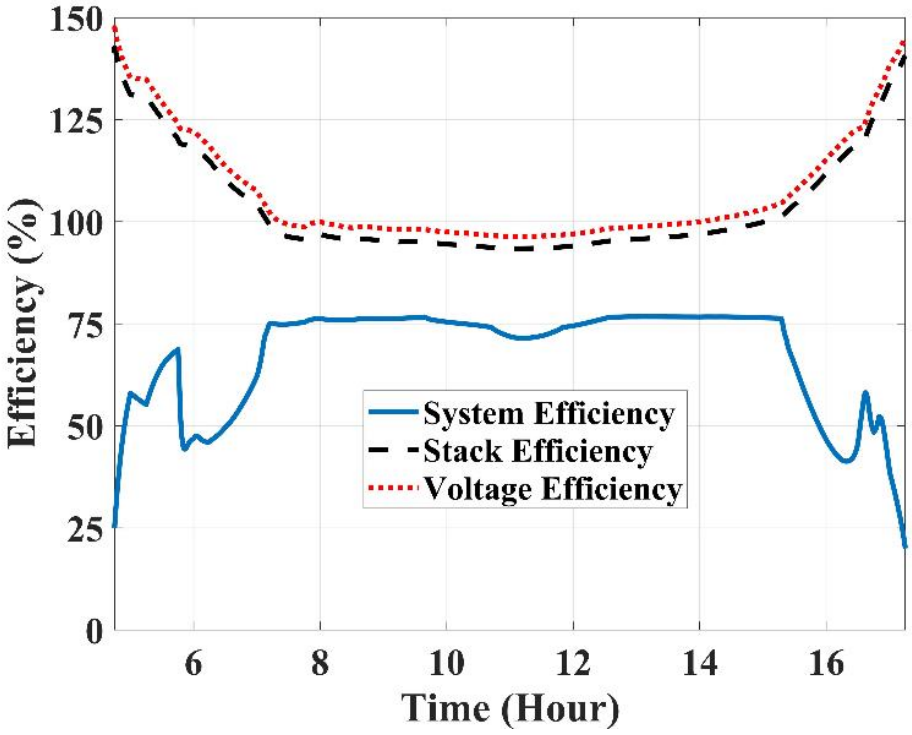

Figure 42: Efficiencies for the sunny day scenario.

The good performance of the SOSE system is highlighted in Figure 42, which indicates that the system efficiency throughout the majority of the operating time remains at values higher than 70% LHV. High efficiency is even achieved during the periods in which the current is high leading to high hydrogen production rate. The average efficiency of the SOSE system over the entire 12.5 hours of operation is 68%. It should be noted that between 7:30 and 15:30, the average system efficiency is 74%. According to Figure 42, when the SOE system begins working, between 4:45 and 6:00, the system efficiency increases up to around 70%. Since the cell operating voltage is very low from 4:45 to 6:00, the endothermicity of the electrochemical reaction is very low, and as a result, the absolute change in both the average temperature of the cell and the anode stream temperature difference along the cell is less than 40K (the controller set-point). Hence, the system requires minimum amount of air flow rate and as a result the blower power works at its minimum power. Also, low air flow rate needs low air electric heater power consumption. As a result, an increase in efficiency due to increase in the amount of hydrogen produced can be observed. However, at around 6:00, the endothermicity of the cell causes an increase in anode stream temperature difference which is greater than the controller set-point. So, the blower begins introducing more air into the

system. This results in an increase in both blower power consumption and air electric heater power consumption. Hence, a slight dip in the SOE system efficiency occurs at around 6:00. Between 7:00 and 10:00, the SOE system is working close to its thermoneutral voltage and as a result the endothermicity (for times the cell operating voltage is lower than the thermoneutral voltage) and exothermicity (for times the cell operating voltage is higher than the thermoneutral voltage) are not too much which causes the blower to be working around its minimum power setting and so minimal amounts of air are introduced to the anode side. Around 11:00, there is a slight drop in efficiency which is due to the high operating voltage and high exothermicity operation of the cell. The high operating voltage pushes the controller to manipulate the blower power to increase the air flow rate to the anode side to maintain the anode stream temperature difference at the controller set-point. After 15:00, when the PV generated power decreases, a drop in efficiency is obtained, which is due to the thermal controller function for highly endothermic conditions (like what happened at around 6:00). The controller pushes more air to the stack which increases both blower and air electric heater power consumption. The voltage and stack efficiencies have quite similar trends where the former varies between 96-148% while the latter varies between 93%-142%. They are above 100% when the cell operating voltage is lower than thermoneutral voltage and vice versa. It should be noticed that for the hours in which the stack efficiency is above 100% (the operating voltage is below the thermoneutral voltage (thermoneutral voltage is a voltage at which hydrogen and oxygen are produced with 100% thermal efficiency (i.e., no waste heat produced from the reaction))), the electric power given to the stack is lower than the energy of the produced hydrogen (based on LHV), since the electrolysis reaction is endothermic reaction and the stack gets a portion of its required energy in a form of heat provided by electric heaters. Stack efficiency above 100% is significantly valuable in case of having available external heat sources that can be utilized to provide a portion of the required energy for electrochemical reaction. This results in stack efficiency above 100% by utilizing the external heat source to produce hydrogen by consuming less electric energy. In a sunny day, during the 12.5 hours of operation, the SOSE system consumes 4322kWh, produces 94 kg of hydrogen.

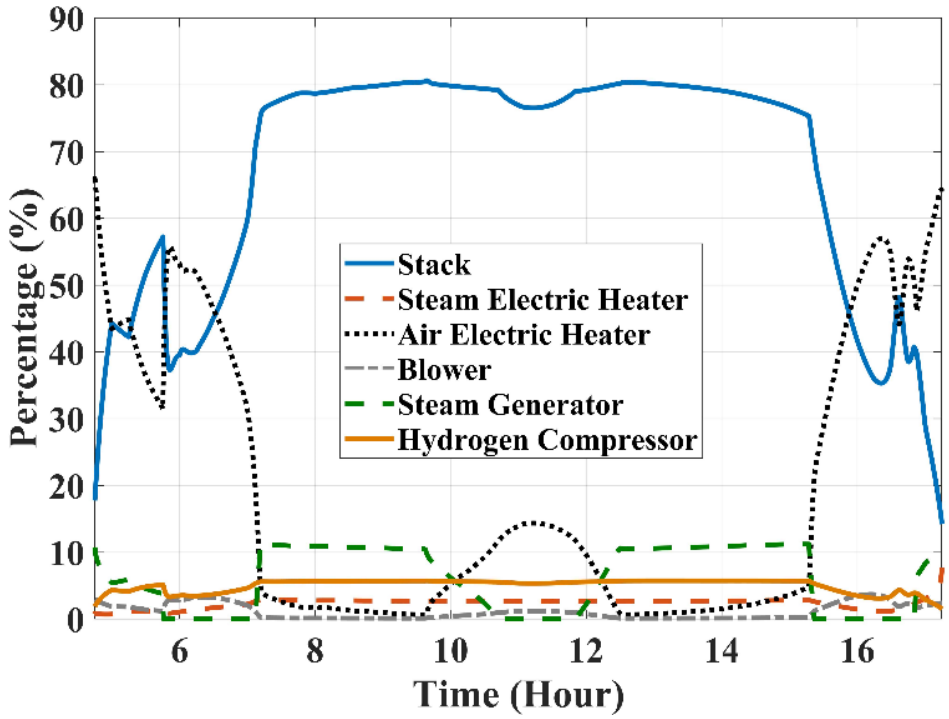

Figure 43: Contribution of each component in power consumption for a sunny day.

Figure 43 shows the contribution of each SOSE component to the system power consumption. For most of the operating time, the stack power accounts for the highest consumed power. For 2.5 hours at the beginning and at the end of the system operating time, the contribution of the air side electric heater increases not only due to the increased air flow rate for heating purposes, but also due to the higher required temperature rise via air electric heater that results from lower heat recovered in the air side heat exchanger from lower temperature air leaving the stack. When the air electric heater consumed power increases, the steam generator power consumption decreases because of increased air heat recovery in the steam generator. In the middle of the day, when the stack is operating in the highly exothermic region, the air electric heater power consumption increases (non-intuitively) to maintain air inlet temperature while increasing air flow to provide adequate cooling to the stack.

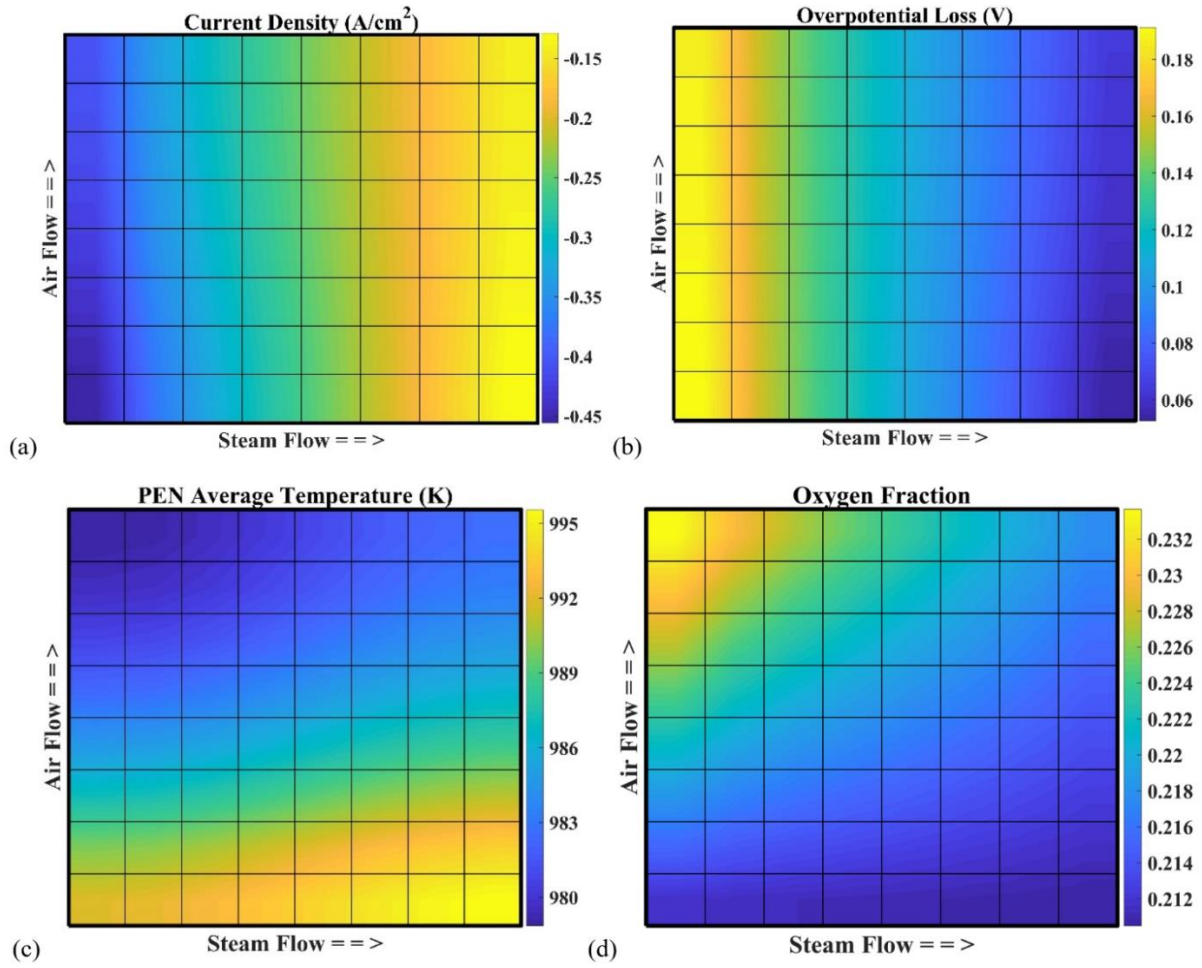

Figure 44: Highly endothermic spatial distribution (a) Current density, (b) Overpotentials, (c) PEN temperature, and (d) Oxygen molar fraction.

Figure 44 shows the spatial distribution of current density, overpotential voltage, temperature, and oxygen concentration at around 6:00, in which the SOEC exhibits its minimum average temperature and maximum temperature difference along the cell. This operating condition is the highly endothermic condition in which the operating voltage is between the open circuit voltage and the thermoneutral voltage. The operating voltage at this most endothermic operating condition is 1.1V. According to Figure 44, the spatial overpotential loss varies from 0.06V to 0.18V which is lower than that of steady state operating conditions and results from operating in this regime at lower current density. Moreover, the spatial temperature at this case varies from 979K to 995K while the highest and lowest spatial temperature are located at the cell corners. As shown in Figure 44, the

oxygen concentration changes only slightly due to controller action to introduce large amounts of air to warm the cell. Since in this case, the endothermicity is high, the blower pushes more air to keep the anode stream temperature difference at the controller set-point. As a result, the amount of oxygen produced in electrochemical reaction is almost negligible compared to the amount of oxygen entering the anode.

Figure 45 shows the spatial distribution of operating parameters at around 11:00, in which the system is working at its maximum average temperature. This operating condition is the highly exothermic condition in which the operating voltage is greater than the thermoneutral voltage. The operating voltage at this endothermic operating condition is 1.33V. According to Figure 45, the spatial overpotential loss varies from 0.31V to 0.45V which is higher than that of steady state conditions, resulting from high current density. Moreover, the spatial temperature at this case varies from 1050K to 1066K which is greater than nominal operating temperature conditions. As shown in Figure 45, the oxygen concentration changes more compared to the endothermic condition shown in Figure 44. This small change results from controller that introduces more air to cool the stack because endothermicity is high. The small, but larger, change in oxygen concentration in anode compartment compared to the endothermic condition is due to the higher current density and higher oxygen production by the electrochemical reactions. However, the variation of oxygen concentration is lower compared to the steady-state operating condition (thermoneutral condition) since in the exothermic condition, the blower introduces more air to the anode to control the temperature of the stack.

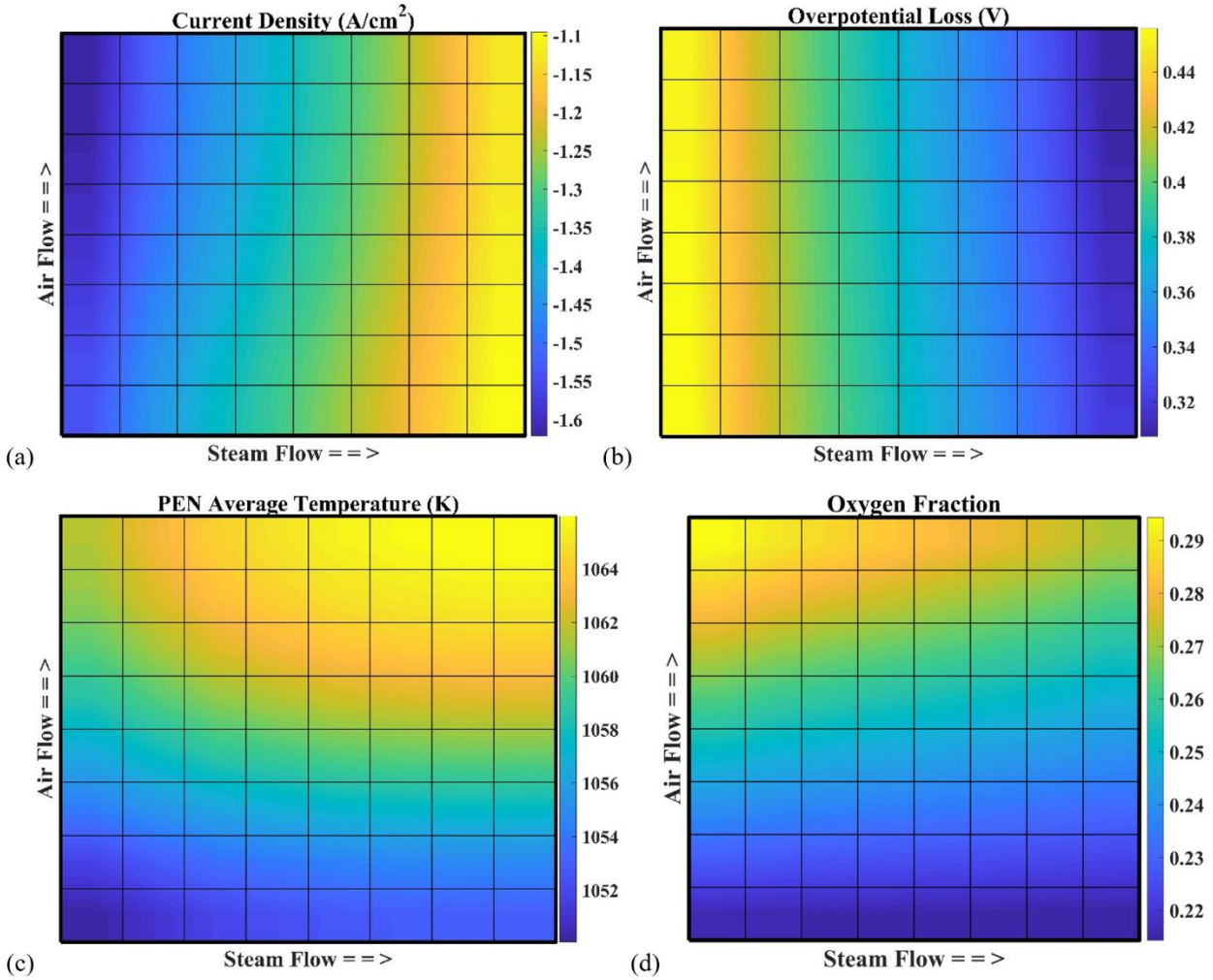

Figure 45: Highly exothermic spatial distribution (a) Current density, (b) Overpotentials, (c) PEN temperature, and (d) Oxygen molar fraction.

4.2 Cloudy Day Simulation

The PV generated power for a cloudy day between 6:45 and 17:45 is directly given to the stack as an input power to capture the dynamic performance of the SOSE system. During the cloudy day, several strong dynamic conditions are present but nevertheless the system is able to modulate its operating condition following the highly dynamic renewable excess power. The transients related to the passing clouds cause multiple fluctuations of the cell operating voltage during the day rapidly switching between exothermic and endothermic modes of operation 10 times.

Figure 46 shows both the PV generated power in the cloudy day which is directly given to the stack and the SOE stack consumed power which is obtained by multiplying the operating voltage by the current and number of the cells. It shows that how closely the SOE system captures the transient behavior of the given power.

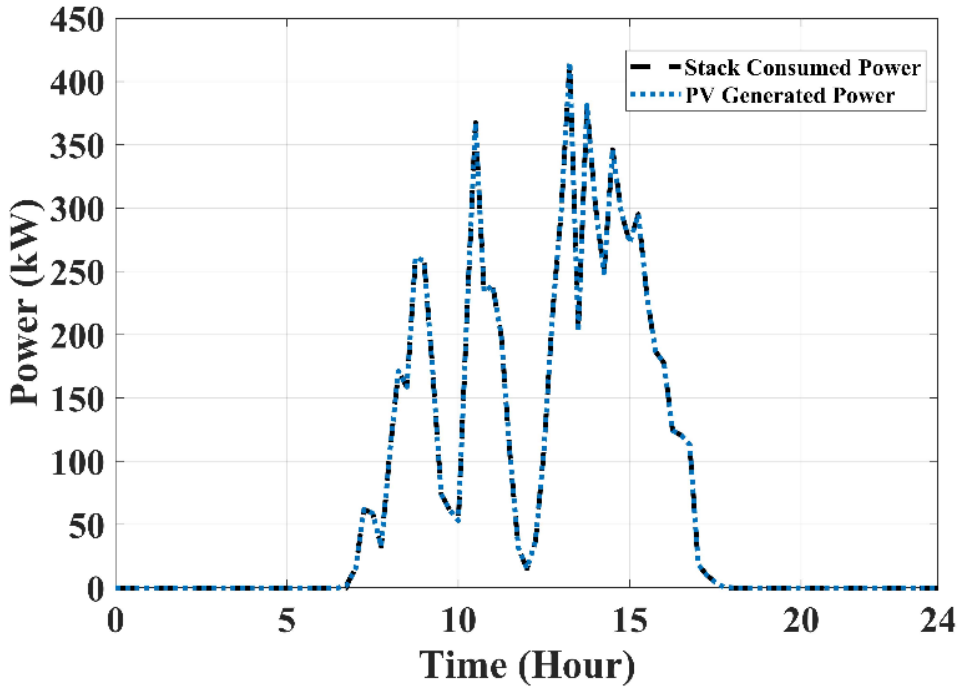

Figure 46: PV generated power vs stack consumed power for a cloudy day.

As presented in Figure 47, the cell operating voltage varies between the 0.87-1.33V while the cell current density varies between 0-1.25A/cm^2 and reaches its maximum value at about 13:25 exactly when the PV Generated Power has its maximum amount (Figure 46). It should be noticed that due to the lower amount of PV generated power in this cloudy day scenario compared to the sunny day scenario, the SOEC is working mostly in endothermic and endothermal operating conditions.

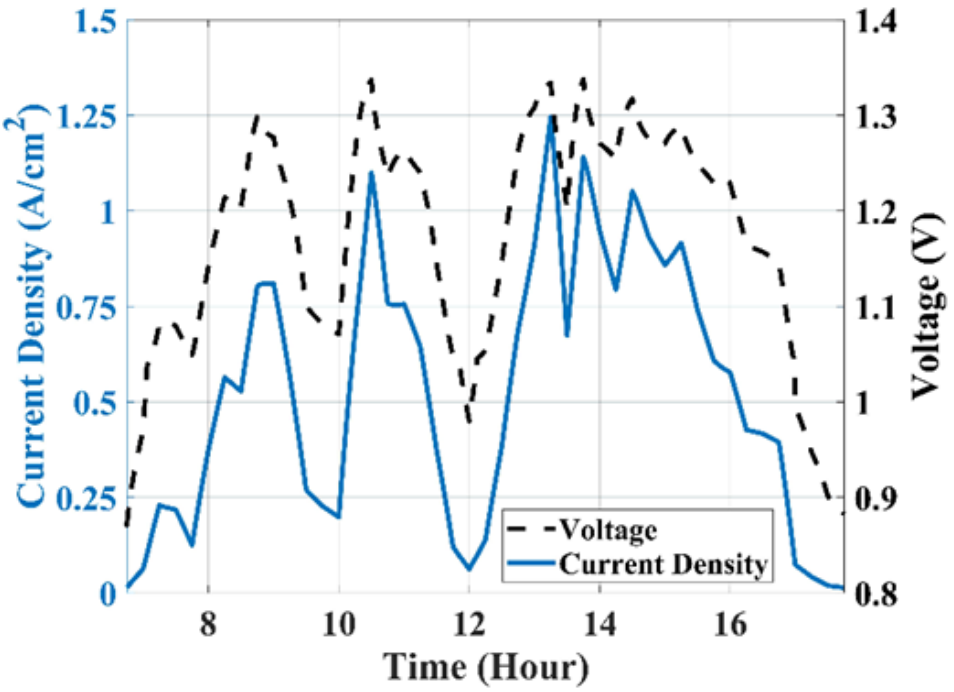

Figure 47: Cell current density and voltage for a cloudy day.

Figure 48 shows multiple dynamic fluctuations in both PEN average temperature and maximum temperature difference along the PEN. These variations are within safe operating limits, confirming the appropriate system configuration and appropriate applied temperature control strategy that can keep the stack operating temperature inside the 80K safe range during realistic and highly dynamic operating conditions. The maximum temperature difference across the PEN is lower than 18K. It is shown that the maximum PEN temperature difference increases when the PEN average temperature reaches its lower limit value. According to Figure 48, for the cloudy day scenario, the PEN average temperature reaches its lower limit (40K below 1023K) during endothermic operating conditions since it stays in endothermic condition for a considerable time. However, it does not reach to its upper limit (40K higher than 1023K) because the SOE system does not stay in exothermic operating condition for a very long time. Thus, the SOEC stack does not have enough time to heat up to the upper limit due to its thermal inertia. It should be noted that when the operating voltage is switched between endothermic and exothermic conditions, the SOEC stack takes time to experience dynamic changes in its temperature. In the cloudy day scenario even though at several moments the operating voltage crosses the thermoneutral

condition toward exothermic conditions, the short duration of stay in exothermic mode does not allow the temperature of the stack to reach the upper safe limit. According to Figure 49, the maximum and minimum temperature of PEN have their highest deviation from the average temperature under highly endothermic operating conditions, while there is a small deviation obtained in moderate exothermic operating conditions.

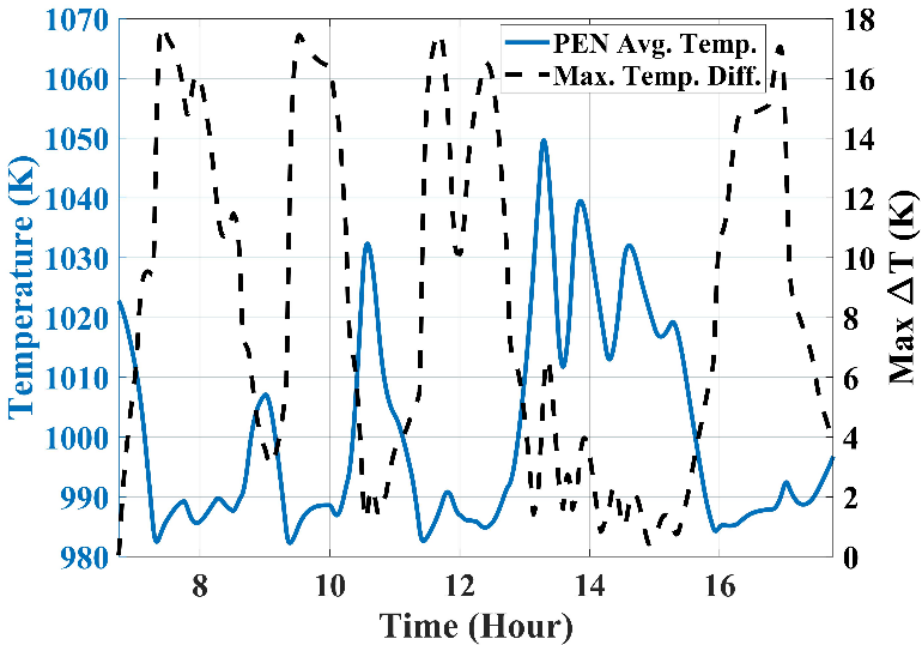

Figure 48: PEN average temperature and maximum temperature difference along the PEN for a cloudy day.

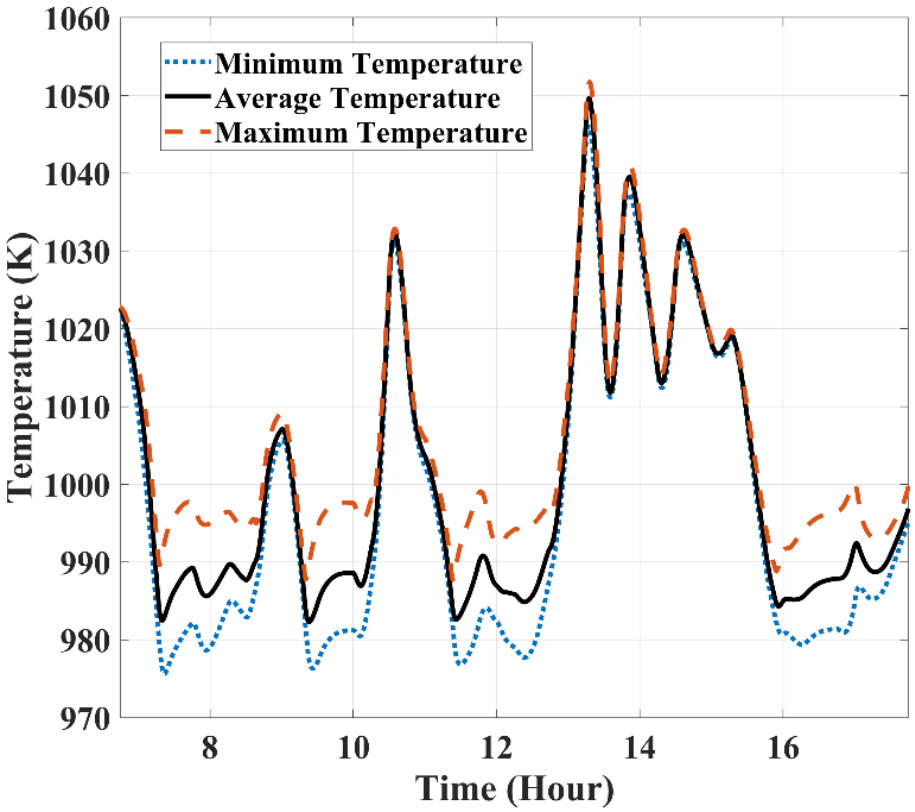

Figure 49: PEN minimum, average and maximum temperature for a cloudy day.

The system efficiency for the cloudy day fluctuates a lot due to the fluctuations in stack input power (Figure 50). The average efficiency of the SOSE system for the 11 hours of operation in 63%. The voltage and stack efficiencies have quite similar trends where the former varies between 96-148% while the latter varies between 93%-142%. Both stack and voltage efficiencies are above 100% for majority of the time due to the operating voltage which is lower than the thermoneutral voltage most of the time. During the 11 hours of operation, the SOSE system consumes 2663kWh and produces 55 kg of hydrogen.

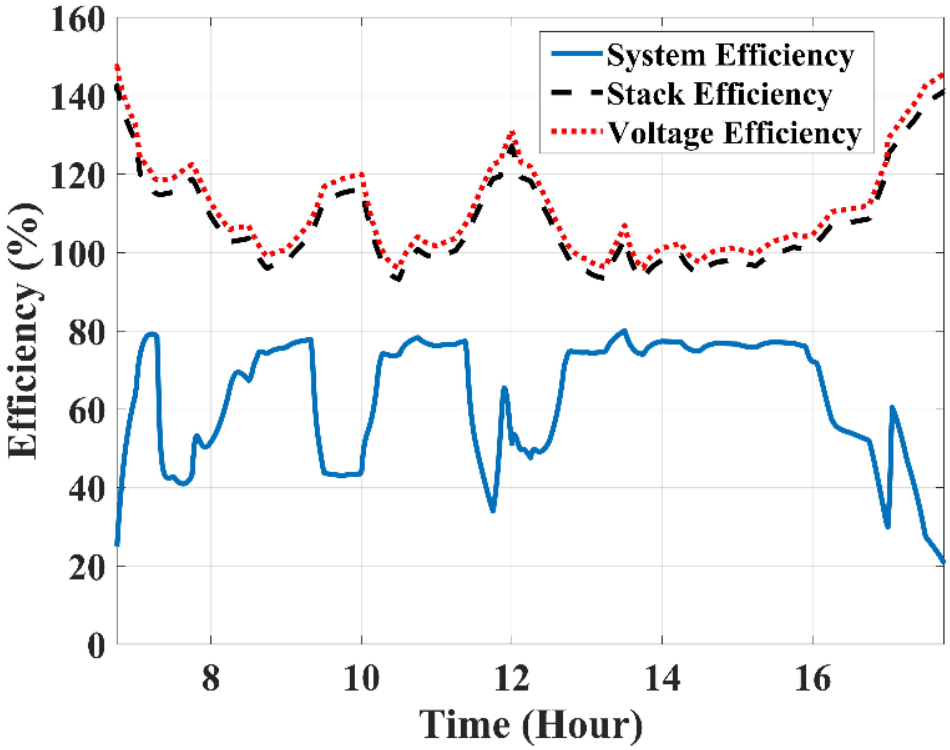

Figure 50: Efficiencies for the cloudy day scenario.

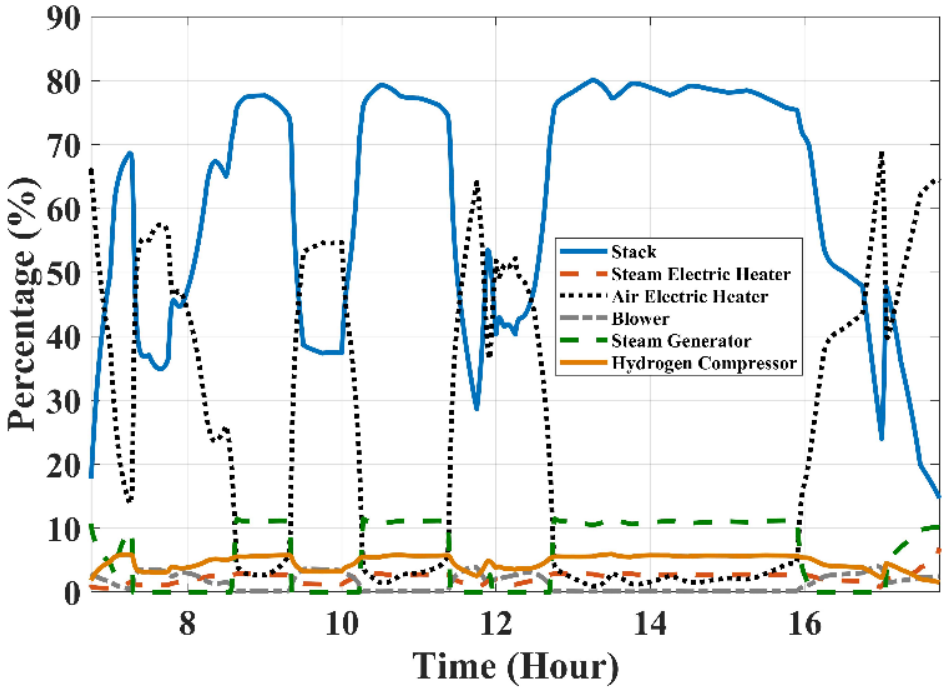

Figure 51: Contribution of each component in power consumption for a cloudy day.

Figure 51 shows the contribution of each SOSE component in the total system power consumption. As clearly shown in Figure 51, the blower power and therefore the air electric heater power contributions increase four times throughout the day, corresponding to hours in which the cell operating temperature reaches its lower limit, and the controller forces the blower to blow more air toward the SOSE stack to heat the stack. For most of the hours that correspond to increased contribution of the air electric heater to overall power consumption, the contribution of the steam generator drops due to the higher air heat recovered in the steam generator. The highest stack power contribution happens between 13:00 and 15:00 where the PV generated power given to the stack, has its maximum amount (Figure 46), and the blower power is at its minimum power.

4.3 Summary

This chapter has focused on evaluating the dynamic behavior of a SOSE system without an external heat source which uses transient PV generated power as an input to produce compressed (to 3 MPa) renewable hydrogen to be stored or injected directly into the natural gas network. The study developed an SOSE system design and control strategy and demonstrated that the proposed SOSE system can operate dynamically to directly convert solar power to hydrogen for both sunny and cloudy days. For the entire operating periods of both days, the stack temperature and temperature difference along the stack were maintained in a safe operating range. The 12.5 h operation of the SOSE system on a sunny day resulted in the production of 94 kg hydrogen by using an average of 46 kWh/kg of the produced hydrogen. The SOSE system operated 11 h on a cloudy day and produced 55 kg hydrogen at average system power consumption per kilogram of produced hydrogen of 48.4 kWh/kg. The temperature distribution and dynamics of temperature gradients (spatial and temporal) that our dynamic model has produced, as demonstrated in this Chapter, will have a significant impact on degradation and other performance characteristics.

5 Integration of SOEC System into the UCI Microgrid to Support High Renewable Use

5.1 UCI Campus Microgrid

The University of California, Irvine campus offers a unique opportunity to investigate the management and performance of a microgrid. The microgrid presents a variety of building types such as classrooms, laboratory facilities and offices and also some features that are going to become part of future energy systems such as electric vehicle and bus fleets and their charging stations, chemical batteries for grid balance, and a large set of renewable distributed energy generation resources (mostly solar PV) [344]. The campus microgrid is connected to the external Southern California Edison (SCE) grid through a single substation where the voltage is decreased from 66 to 12 kV. The campus power plant can provide more than 90% of campus electricity consumption via ten 12 kV circuits and district heating and cooling network. The power plant consists of a 19 MW natural gas-fired combined cycle formed by a 14 MW gas turbine and a 5 MW steam turbine, 7 electrically driven chillers and 1 steam driven chiller. One of the main characteristics of the UCI central plant is the presence of a 175 MWh cold water storage tank and cold water distribution to all major campus buildings that allows the microgrid management to produce campus air conditioning via the chillers during at any time of day or night (e.g., at off-peak hours or when solar is available in excess) [345]. On the UCI campus, following the plan of the University of California to achieve carbon neutrality in 2025, there are already in operation three large PV installations over parking structures and many other distributed rooftop installations for a total installed capacity of about 4 MW and two two-axis tracking concentrated solar-PV systems of 113 kW installed capacity. These solar installations, coupled with deep energy efficiency measures deployed throughout the campus, are already introducing challenges to the microgrid operation when the power plant output has to adjust to very low power levels to allow renewable energy utilization in the microgrid. Given the future goal of UCI administration to increase the renewable share of the energy mix, the implementation of energy storage will become a fundamental requirement of the campus energy infrastructure.

In this section, the implementation of a P2G system based upon dispatching SOE unit systems is investigated. Figure 52 shows the existing microgrid components in addition to current proposed use of the SOE unit systems (dashed lines).

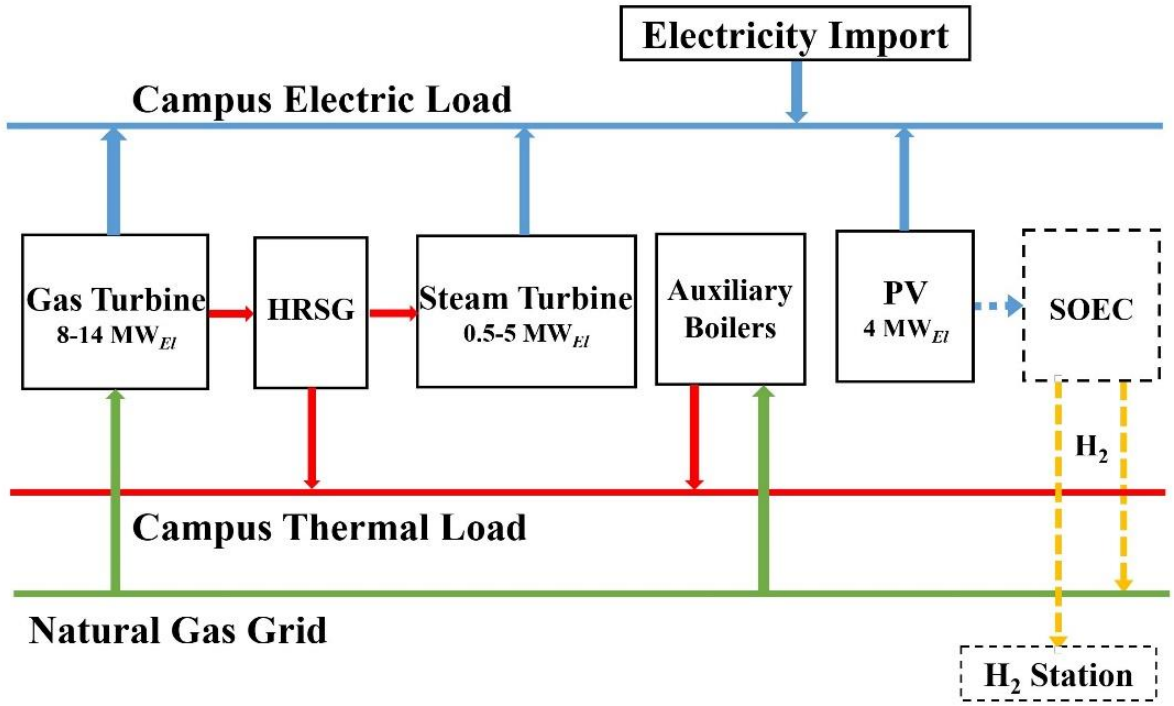

Figure 52: Schematic representation of the microgrid components considered in this analysis and the SOE unit systems integration.

5.2 UCI Microgrid Demand Profiles

Historical data regarding the campus demand and PV production from the year 2014 have been provided by UCI facilities management and used as inputs in this study. The data come with a 15 min-resolution and include both electricity and thermal demand. The campus electric and thermal loads are presented in Figure 53. The campus annual electric demand was around 126 GWh in 2014 with an average load of 14.32 MW, a maximum load of 27.7 MW and a minimum load of 9.2 MW. Electricity demand is quite uniform (primarily because of careful control of the chillers and thermal energy storage system) during the year presenting daily peaks in workdays and decreasing over the weekends. The highest electrical consumption days usually coincide with the hottest days when the electrical demand for campus air conditioning is highest. Campus thermal demand varies between 5 and 27 MW

and shows a significant seasonal variation rising during the winter and generally decreasing over the summer. The PV installed capacity in 2014 represented by the data was 893 kW and PV power demand dynamics have been scaled up for all of the future simulation scenarios using a scaling factor, in order to simulate the grid response to increasing renewable installed capacity.

Previous work at the Advanced Power and Energy Program (APEP) at UCI estimated that a maximum of 15 MW of fixed PV installations (mainly on building rooftops, parking structure terraces, and above parking lots) and up to 22 MW of ground mounted 2-axis tracking PV systems (37 MW in total) could be installed in and/or nearby the UCI campus [344].

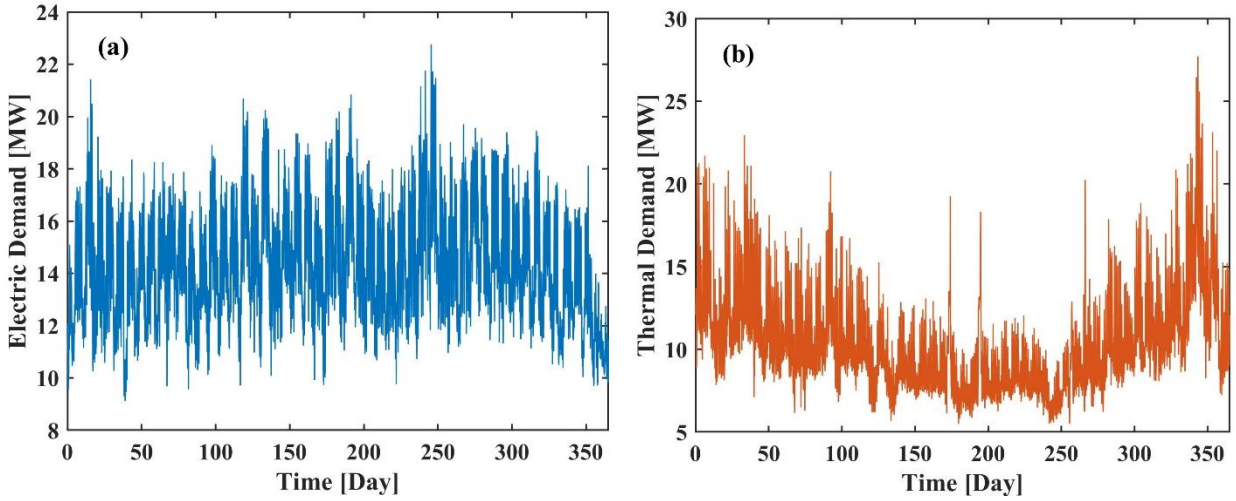

Figure 53: UCI campus (a) electricity demand, and (b) thermal demand for the year 2014.

5.3 UCI Microgrid Power Plant Model

The Gas Turbine is the main component of the campus power plant. The maximum electrical power output is 14 MW and the turbine can be turned down to a minimum power output of 8 MW; the minimum operating point is a consequence of necessary compliance with the strict criteria pollutant emissions laws of the state of California. Moreover, in this study, the gas turbine is constrained not to ramp faster than 6 MW/h [345]. A simplified regression based gas turbine model has been previously developed [346], and has been implemented to simulate the operation of the campus power plant. The gas turbine electrical efficiency ($\eta_{GT,El}$) and turbine exit temperature ($T_{GT,Out}$) are correlated to the electrical power output

($P_{GT,El}$) according to the following equations, represented in Figure 54 for a range of the gas turbine electrical power outputs.

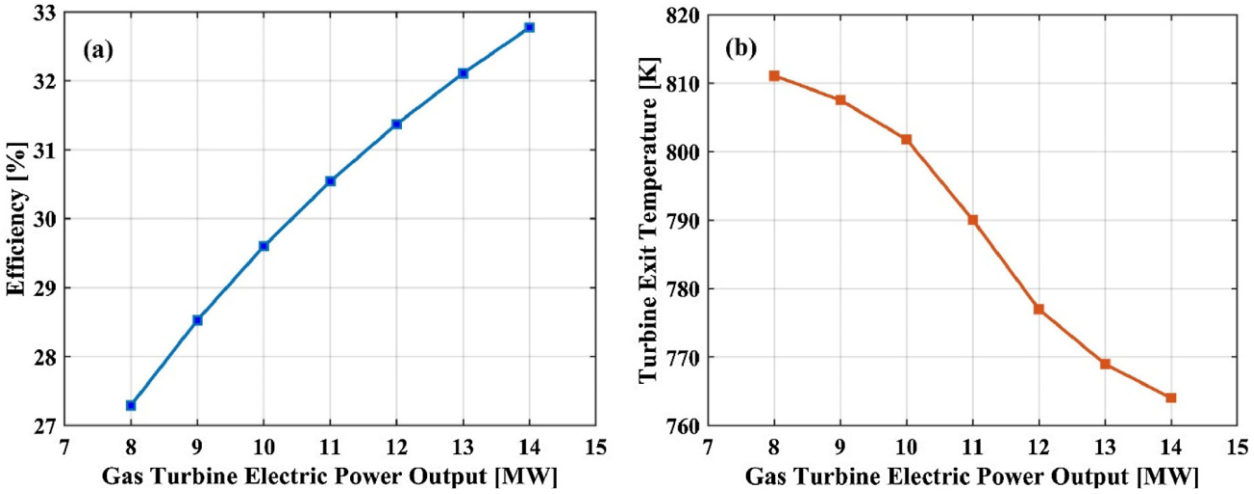

Figure 54: Gas turbine regression based operating parameters: (a) efficiency, and (b) turbine exit temperature.

$$\eta_{GT,El} = f(P_{GT,El}) = -8.9 \times 10^{-4} \times P_{GT,El}^2 + 0.0299 \times P_{GT,El} + 0.0833 \quad \text{Equation 61}$$

$$T_{GT,Out} = g(P_{GT,El}) = 0.069 \times P_{GT,El}^4 - 2.12 \times P_{GT,El}^3 + 19.14 \times P_{GT,El}^2 - 31.57 \times P_{GT,El} + 636.27 \quad \text{Equation 62}$$

where $P_{GT,El}$ is the electric power produced by the gas turbine, $\eta_{GT,El}$ the electrical efficiency of the gas turbine, and $T_{GT,Out}$ is the gas turbine outlet temperature.

According to Figure 54, the electrical efficiency of the turbine decreases from 33% at the maximum operating load to 26% when the turbine operates at the minimum electric power output of 8 MW. On the other hand, the temperature of the turbine outlet increases form 764 K (at maximum load) to 811 K when the turbine is turned down to the minimum load.

The thermal power available from the turbine exhaust for the heat recovery steam generator is evaluated using the following equation which takes into account the ratio between the difference between $T_{GT,Out}$ and temperature of gases leaving the steam generator (450 K) and the difference between $T_{GT,Out}$ and the reference temperature (273 K) at which heating values are evaluated.

$$P_{GT,Th,Waste} = P_{GT,El} \times \frac{(1-\eta_{GT,El})}{\eta_{GT,El}} \times \frac{T_{GT,Out} - 450}{T_{GT,Out} - 273}$$ Equation 63

where $P_{GT,El}$ is the electric power produced by the gas turbine, $\eta_{GT,El}$ the electrical efficiency of the gas turbine, $P_{GT,Th,Waste}$ is the waste heat of gas turbine associated with exhaust gas, and $T_{GT,Out}$ is the gas turbine outlet temperature.

This thermal energy in the form of steam is then used in the cogeneration plant to feed the steam turbine and to cover the campus heat demand via steam/pressurized water heat exchangers.

The 5 MW Steam Turbine never operates at full load since it is oversized for the application. Also, the minimum operating power is 0.5 MW to avoid the risk of an electrical trip if the campus were to suddenly draw additional steam for heating. Moreover, it can be turned on and off depending upon electric demand and steam availability [347]. During emergencies the turbine can respond to transients as fast as 1 MW/min, though standard operation limits manipulation to a rate of approximately 4 MW/h [345]. In every moment the maximum possible electrical output that can be delivered by the recuperative steam turbine is then related to the available waste heat by the electrical efficiency $\eta_{ST,El}$ according to the following equation.

$$P_{ST,El} = P_{GT,Th,Waste} \times \eta_{ST,El}$$ Equation 64

where $P_{GT,Th,Waste}$ is the waste heat of gas turbine associated with exhaust gas, $P_{ST,El}$ is steam turbine power, and $\eta_{ST,El}$ is the steam turbine efficiency.

Steam turbine will operate when excess steam is available to minimize the import power level to the campus, as long the minimum import restriction will not be violated. During periods in which the waste heat from the gas turbine is not sufficient to cover the campus heat demand, additional natural gas can be burned with the use of duct burners to raise the temperature of the exhaust gas [348]. The operational parameters and assumptions of the microgrid model are summarized in Table 1. It should be noted that a minimum import of

100 kW (from external grid) is considered as a constraint in the model because, in real life, it is extremely inefficient and unavailable to turn on and off the import of power when desired [349].

Table 1: Summary of microgrid model parameters [345,347].

Microgrid model parameters			
Gas Turbine	Electric Output Range	8 – 14	MW
	Electrical Efficiency, $\eta_{GT,El}$	$f(P_{GT,El})$	-
	Turbine Exit Temperature, $T_{GT,Out}$	$g(P_{GT,El})$	K
	Ramp Rate	6	MW/h
Steam Turbine	Electric Output Range	0.5 – 5, off	MW
	Electrical Efficiency, $\eta_{ST,El}$	0.25	-
	Ramp Rate	4	MW/h

5.4 UCI Microgrid Dispatch Model

The dispatch of the microgrid energy resources has been simulated as a linear programming problem implemented in Matlab®. In the linear programming, variables are linked together with linear constraints and upper and lower boundaries must be set. The problem variables include the electrical power output of the gas turbine ($P_{GT,El}$), the amount of waste thermal power in the form of steam fed to the steam turbine ($P_{ST,Th}$), the extra natural gas power needed to satisfy thermal demand ($P_{EXTRA,Th}$), the electrical power import from external grid ($P_{IMPORT,El}$), the possible electric power excess ($P_{EXCESS,El}$) and the waste thermal power still available from the gas turbine outlet that is not being recovered ($P_{EXCESS,Th}$).

The electrical and thermal power balances, shown in following equations, are constraints that must be satisfied at every time step:

$$P_{GT,El} + P_{ST,El} + P_{IMPORT,El} - P_{EXCESS,El} = LOAD_{El} - P_{PV,El,SCALED} \quad \text{Equation 65}$$

$$P_{GT,Th,Waste} - P_{ST,Th} + P_{EXTRA,Th} - P_{EXCESS,Th} = 1.1 \times LOAD_{Th}$$ Equation 66

where P_{El} are electric powers for different components of the microgrid, andP_{Th} are thermal powers for different components of the microgrid.

It should be noted that a coefficient of 1.1 is considered in the thermal load energy balance to take into account all the heat losses to the environment (distribution/piping heat losses) [350].

The objective function reflects the current dispatch strategy of the UCI microgrid, oriented to maximize the utilization of the solar PV and combined cycle plant thus minimizing imports of electrical power from Southern California Edison grid and using additional natural gas to cover thermal demands.

5.5 SOE Unit Microgrid Dispatch

The integration of SOE unit systems into the campus microgrid has been simulated as the deployment of multiple identical SOE unit systems as described previously. The annual excess electricity profile of the UCI microgrid obtained from the microgrid dispatch model is the SOE input parameter. The otherwise curtailed electricity available at every time step is supposed to be delivered to the SOE unit systems which supplies both the SOE stack and BoP components. In this study, the SOE units are designed to stay in a hot idle state when not in operation: energy consumption during the idle periods has not be taken into account, but it has been estimated for a similar system that a 30 cm insulation layer is enough to keep overnight temperature decrease negligible without additional active heating [351]. A sequential dispatch strategy has been developed and described in this study. When excess electricity from PV production is available on the microgrid, the SOE units are turned on sequentially one after the other. The units are turned on when the amount of excess electrical power is higher than the power consumption of the single SOE unit system at its minimum operating power of 120 kW. When the maximum load of the single SOE unit system is reached, the optimization allows some curtailment until enough power is available to turn on the next unit. With this dispatch strategy every unit works at full load except the last one

that has been turned on, which works at part load. In the case of decreases of excess electrical power, the switch off procedure follows the opposite symmetrical sequence.

5.6 Simulation Results

5.6.1 Microgrid Operation

The microgrid dispatch results are summarized in Figure 55, highlighting the contribution of the available electrical energy sources to the annual electricity demand of the campus, from the current situation of 4 MW of PV installed capacity to the maximum local estimated capacity of 35 MW. The dashed line represents the percentage of the energy produced by the future PV installations that cannot be absorbed by the microgrid and that which would have to be curtailed or stored in the form of hydrogen using P2G technology. According to Figure 55, currently the campus combined cycle plant provides around 94% of the campus electrical needs, 83% of electricity production comes from the gas turbine and 11% from the steam turbine. The PV production can be fully absorbed by the microgrid and covers 5% of the annual campus electricity demand in a low PV installed capacity scenario. The imported electricity from the external grid is needed to supply only 1% of the electrical demand.

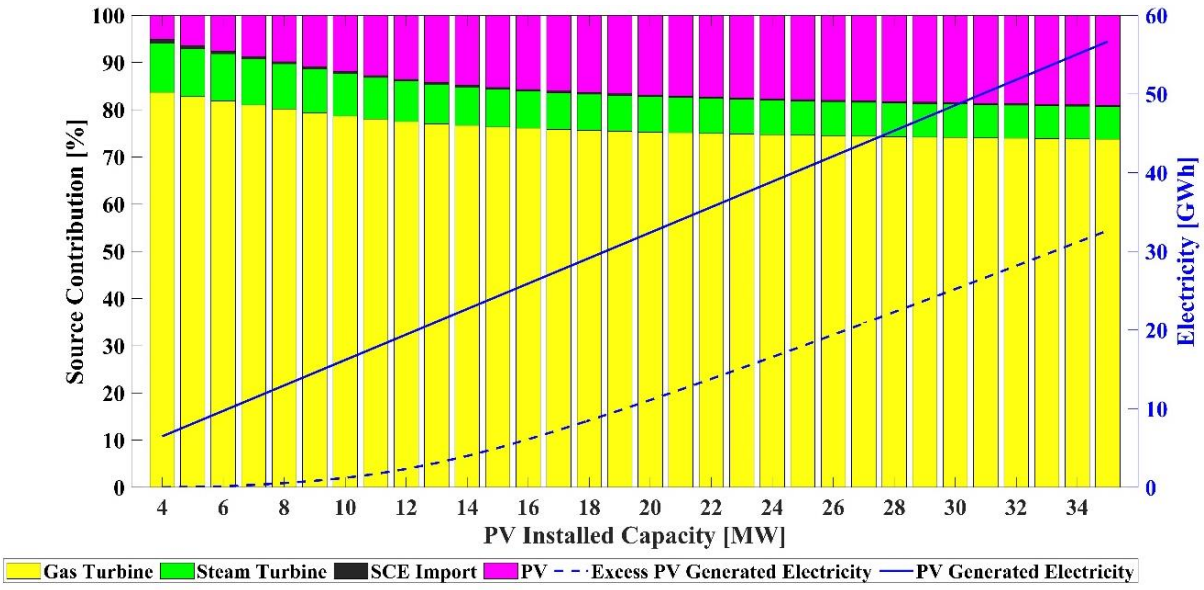

Figure 55: Annual UCI microgrid electric energy generation mix and excess electricity in future scenarios with increased PV installed capacity.

The general trend is obviously the increase of RES penetration as the installed PV capacity increases with consequent decrease of gas turbine and steam turbine contributions. The electricity import from the external grid shows a slight decrease but stays around 1% because of the current interconnection agreement that imposes a continuous minimum import.

The intrinsic limits of the microgrid structure, due to the power plant operation constraints, start to show as the amount of solar energy that would have to be curtailed or stored immediately starts to increase as the PV installed capacity increases (shown as excess percent of PV power). Installing new capacity up to 15 MW would result in sensible increasing in RES contribution from 5 to 15%, keeping solar excess around 20% of the production. Scenarios with further increasing of PV capacity show that only a 4% increase of RES is achieved up to 19% if the installed capacity increase from 15 MW to 35 MW. In the same range the percentage of excessive PV production that would have to be curtailed or stored increases from 20% to 58%.

Figure 56 shows the distribution of excess of PV power in terms of entity and frequency. On the y-axis there is an indication of the number of hours of the year during which the excess power is at least the value that can be read on the x-axis. The six lines correspond to scenarios with increasing PV capacity. The intercept points with the y-axis are the total number of hours with curtailment while the intercept points with the x-axis represent the annual maximum value of excess power. It can be highlighted that the peak power evolves linearly with the increase of installed capacity while the number of excess hours increase rapidly for scenarios up to 15 MW and then the growth slows down converging to the total number of hours of PV production meaning that the additional capacity cannot be handled by the grid in most of the hours with solar irradiation. The massive excess power can be noticed as the general trend of how the curvature of the curves changes moving toward higher PV capacity scenarios and much more hours have excess power closer to the maximum than to the minimum value.

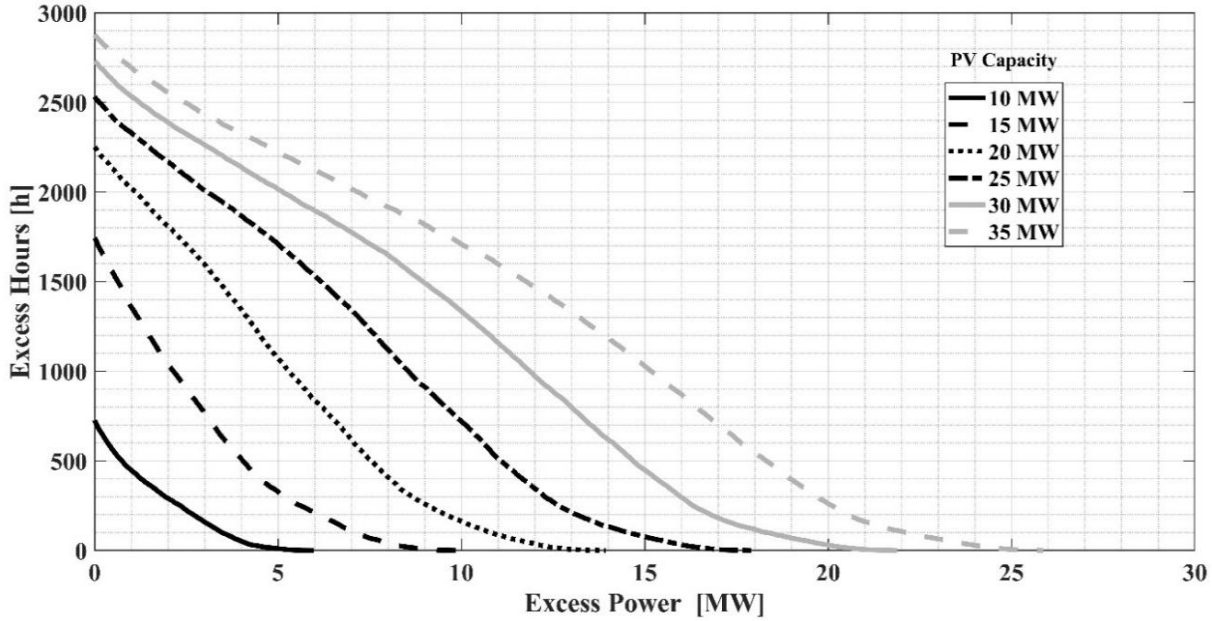

Figure 56: Excess power distribution in future scenarios with increased PV installed capacity.

5.6.2 Microgrid Operation Integrated with SOE Unit Systems

Simulations of microgrid operation integrated with SOE unit systems have been performed for the current situation and for future scenarios with increasing PV capacity installed, to investigate the microgrid and P2G system behaviors to accommodate additional solar energy production and its limits. In this study, annual simulations have been performed to calculate the annual percentage of otherwise curtailed excess electricity which is stored in the form of hydrogen. Figure 57 shows the percentage of stored excess electricity versus the total power capacity of dispatched 300 kW SOE systems for different PV capacity scenarios. The percentage of stored excess electrical energy increases with an increase in the aggregated power capacity of dispatched SOE systems. For each PV capacity scenario, the aggregated power capacity of 300 kW SOE unit systems deployed varies between 300kW (one SOE system) to a maximum aggregated power capacity required to store nearly 100% of the excess electric energy during the analyzed year. According to Figure 57, the percentage of stored excess electricity increases nearly linearly with the combined power capacity of dispatched 300 kW SOE systems up to 80% of total electric energy stored. For 35 MW of solar PV capacity, 6 MW of SOE systems are required to store about 80% of annual excess electricity while more than twice that power (12.3 MW of SOE systems) is required to store

all the excess electrical energy. This non-linear behavior results from the fact that to store nearly 100% of the annual surplus of renewable electricity, the storage system needs to cover the very highest peaks of otherwise curtailed renewable electricity, which occurs infrequently. That is, these later added SOE systems have low capacity factor. In this study, the minimum aggregated SOE systems power capacity (minimum number of dispatched 300 kW SOE systems) that is simulated for each PV capacity scenario is the minimum total power required to store at least 80% of otherwise curtailed excess electricity. Only scenarios with installed PV capacity higher than 10 MW are reported here because lower capacities resulted in electricity excess that does not occur on a daily basis.

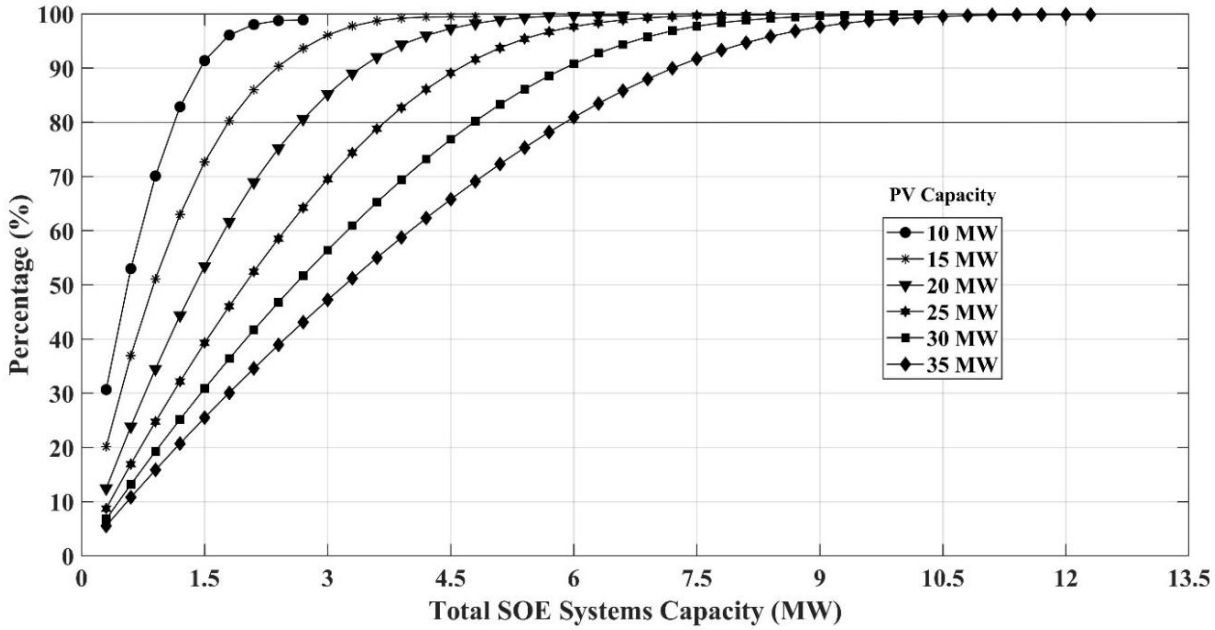

Figure 57: Percentage of stored excess electric power via P2G vs. total power capacity of dispatched 300 kW SOE unit systems for different PV installed capacity.

Two representative weeks of operation for the current installed PV capacity of 4 MW are explained and shown in Figure 58 and Figure 59. Figure 58 shows a week in September characterized by high electric demand and relatively low thermal demand. It can be clearly noticed that the weekly electric demand behavior with daily peaks during workdays and a general decrease over the weekend when most of campus work activities are suspended. This week shows the ideal operation of the combined cycle plant, the gas turbine works at maximum load (and highest thermal efficiency) most of the time and, since the campus heat

demand is low, the steam turbine is also able to be employed to cover electric load. The fluctuation of the steam turbine output, even when full electricity production would be requested, is complementary to the fluctuation of heat demand since priority on heat recovery is given to the campus thermal load. The daily PV production can be clearly identified with its peak in the middle of every day close to the maximum nameplate capacity of the current situation. September five shows an irregular shape of the PV production probably due to temporary cloud cover. During this chosen week the electrical demand is particularly high overcoming the electricity production of both the campus power plant and PV installations and, as a consequence, electricity import from the external grid is present during the first four days and reaches values around 2 MW. Substantial turn down of the combined cycle plant can be noticed during September 6 and 7 as a consequence of low electricity demand and high PV production forcing the power plant to reach close to the minimum operating condition of the gas turbine (8 MW) during September 7; in this case the fast ramps are provided mainly by the steam turbine, given the availability of recovered heat. It can be clearly noticed that during this week the PV production is beneficial because it mainly reduced the otherwise high electricity demand from grid imports. Also, in the represented week, there is no excess PV power to be stored or curtailed and as a result the amount of both P2G power and curtailment are zero. According to the Figure 58(b), most of the time in the represented week, the steam turbine consumes most of the available heat recovered from the gas turbine exhaust gas in the heat recovery steam generator. On September 7, when the gas turbine reaches its minimum operating condition in the middle of the day, we have excess thermal power since the steam turbine steam consumption begins decreasing as a result of an increase in solar PV power. Also, according to Figure 58(b), there is no need for the extra thermal heat in the represented September week since thermal demand is relatively low and can be supplied completely with heat recovered from gas turbine exhaust gases in the heat recovery steam generator.

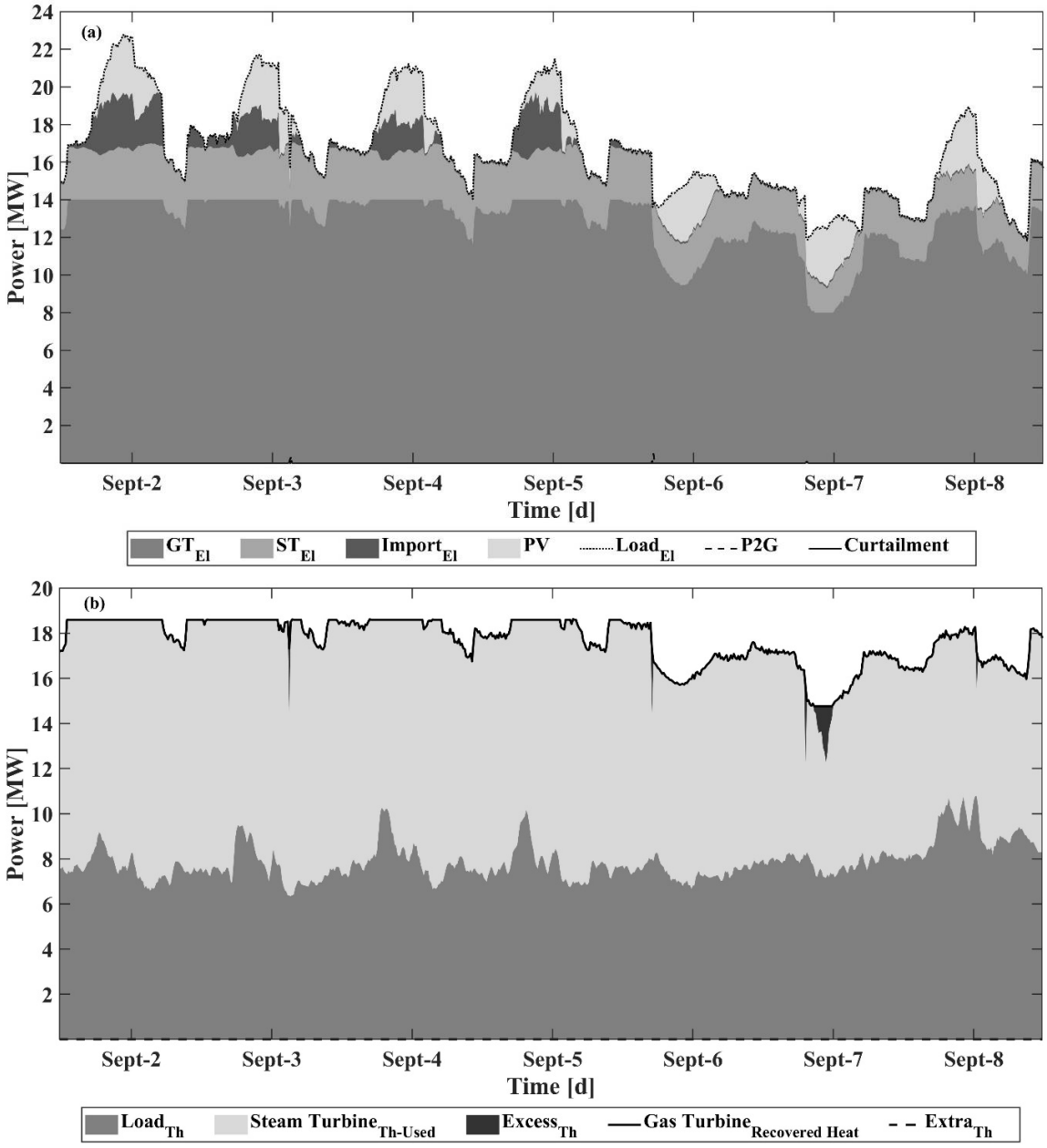

Figure 58: Microgrid-SOE dispatch simulation results in a week of September (a) electric power balance, and (b) thermal power balance with the current 4 MW of PV installed capacity.

A week in January is presented in Figure 59 showing a relatively lower electrical demand while the campus thermal demand is much higher and presents large peaks at the beginning of every day. During the first four days these peaks reach 20 MW making it impossible to be satisfied completely by heat recovery from the gas turbine even if it works at maximum load and the steam turbine is turned off. Additional natural gas must be burned in the auxiliary

boilers present in the power plant every morning, as can be noticed in the lower portion of the Figure 59(b). Moreover, since the steam turbine is not covering its part of electrical load because of the unavailability of steam for power generation, electricity import is also present during those mornings. Nevertheless, even during this week the PV production is well matched with the campus electrical demand, reducing considerably the electricity that would need to be imported since the heat recovery into the steam turbine is not possible as a consequence of relatively high heat demand. Similarly, to the represented week in September, in the represented January week, PV power is not in excess and does not need to be stored via P2G or curtailed. Due to the priority given to the thermal demand of the campus, high for most of the time in January, the steam turbine consumes a small portion of the heat recovered in the form of steam in the heat recovery steam generator. In Figure 59(a), at the end of January 8, we can see a moment in which the steam turbine is turned off because of decreasing electrical demand and as a result it does not consume any steam provided by heat recovered from the gas turbine. Consequently, since the thermal load is not high at that moment, we see an excess of thermal energy available.

According to Figure 59(b), this represented week needs more heat compared to the available excess heat. Also, in comparison to the analyzed September week which has lower thermal demand, the steam turbine works at lower power output since the priority of the microgrid is to provide the thermal demand of the campus with the recovered gas turbine heat which is higher in January.

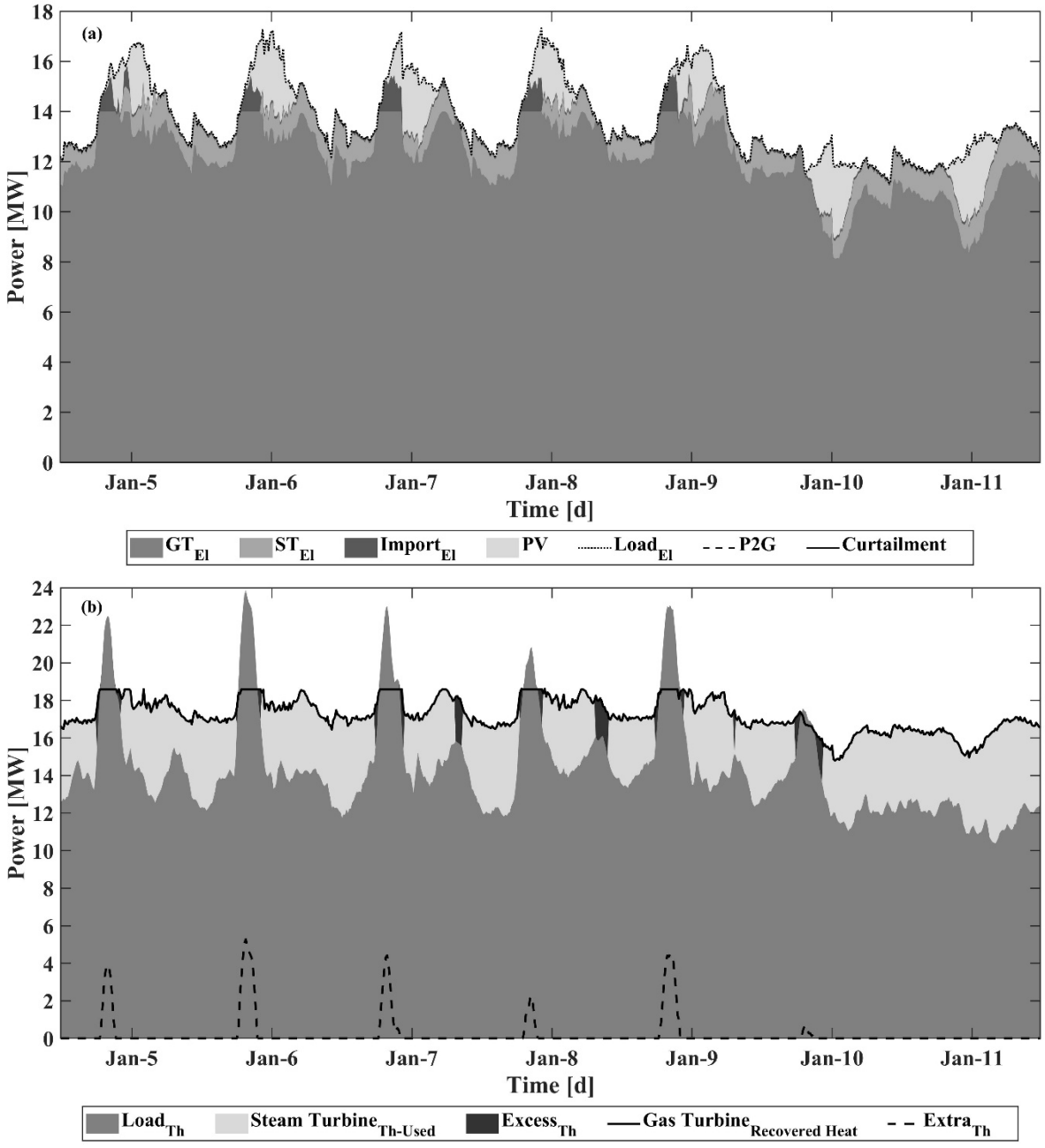

Figure 59: Microgrid-SOE dispatch simulation results in a week of January (a) electric power balance (b) thermal power balance with the current 4 MW of PV installed capacity.

The second scenario presented is the case in which 10 MW of peak PV capacity is installed on the UCI campus, which is more than double the amount currently installed. The same two weeks of demand and solar availability used in previous analyses (Figure 58 and Figure 59) are reported in Figure 60 and Figure 61 to analyze the differences in microgrid response with the added PV. In Figure 60, it can be noticed that now the peak power output from the

PV is around 8 MW. More flexibility is requested of the gas turbine since every day the turbine has to ramp down as the PV output rises in the morning and ramp up as it decreases later in the afternoon. During the days with high electricity demand these fluctuations are still inside the microgrid limits and the additional PV capacity leads to reduced electricity import and reduced natural gas consumption in the gas turbine plant compared to the 4 MW of peak PV case. As the electrical demand drops during the weekend, the first episodes of important excess power occur on September 7 in which the steam turbine is turned off and the gas turbine works at the minimum power output of 8 MW but up to 4 MW of excess PV electric power is produced during the day since the power production exceeds the microgrid demand. Since the aggregated power capacity of dispatched 300 kW SOE units was determined to store around 80% of the excess PV power, it can be seen that in the middle of the day on September 7, the P2G consumed power reaches its maximum design capacity and as a result a portion of excess power cannot be delivered to the SOE units and stored as a hydrogen fuel and has to be curtailed. Also, on that same day, we have up to 8 MW of excess heat during the day since the steam turbine is turned off and the recovered heat is much larger than the campus thermal load.

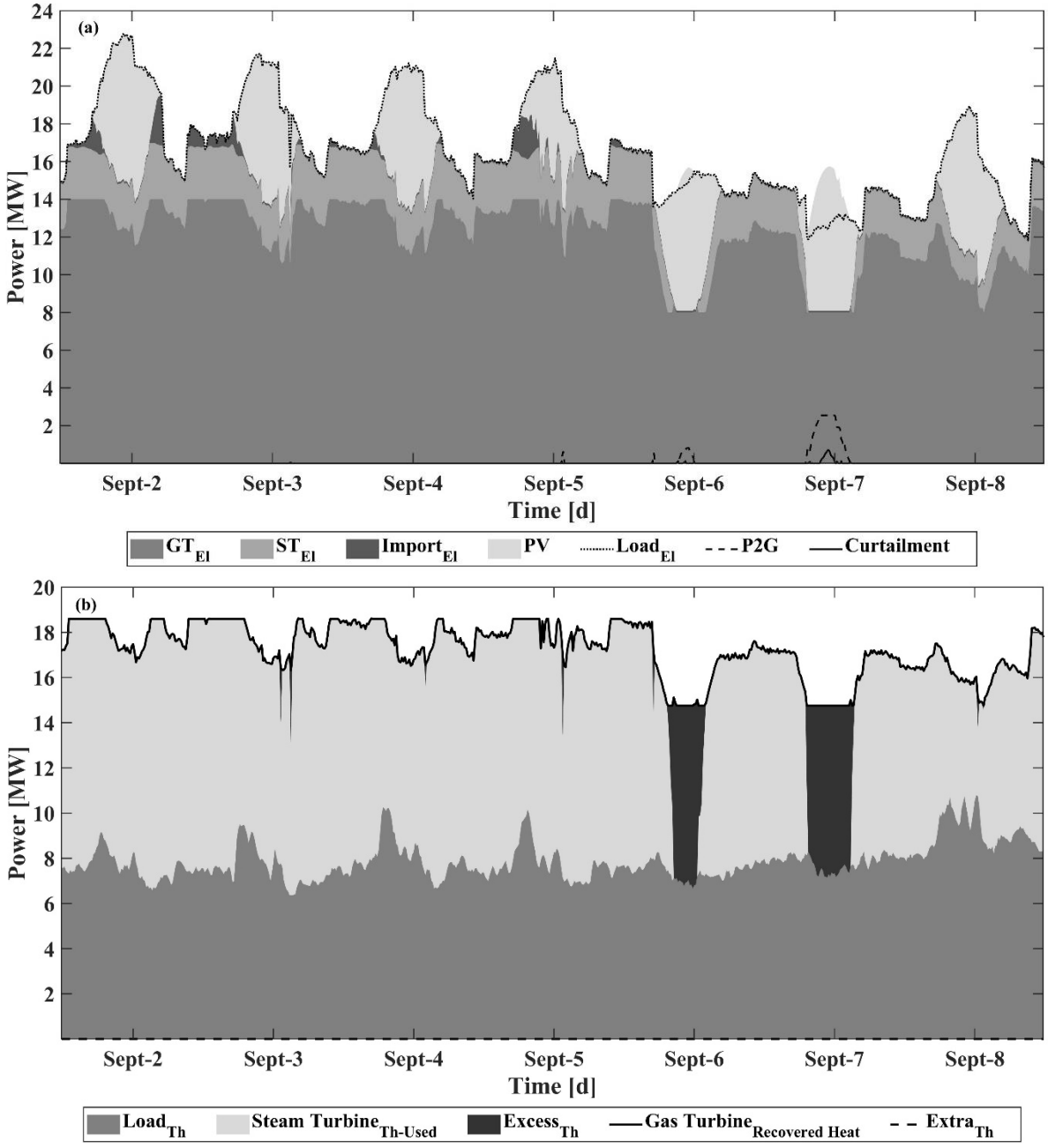

Figure 60: Microgrid-SOE dispatch simulation results in a week of September (a) electric power balance, and (b) thermal power balance with 10 MW of PV installed capacity.

Regarding the week in January shown in Figure 61, the same response of the power plant to incoming PV production can be noticed throughout the week and again during workdays the electrical demand is high enough to avoid complete gas turbine turn down while during the weekend excess PV power would occur. It can be also noticed that during days with cloudy weather, as on January 5 and 9, strong dynamics have to be imposed to the campus power

plant to compensate for the loss of PV production. The resulting ramp rates are still achievable by the gas turbine alone in this scenario since the high thermal demand prevents the utilization of the steam to drive the steam turbine. Moreover, in both the weeks reported it can be highlighted that, as the power output of the campus power plant decreases to accept PV production, the fact that the steam turbine is turned off leaves large amounts of heat available to recovery from the gas turbine exhaust when the campus thermal demand is not particularly high: in particular, during the days of January 10 and 11 the excess of electricity and heat are simultaneous.

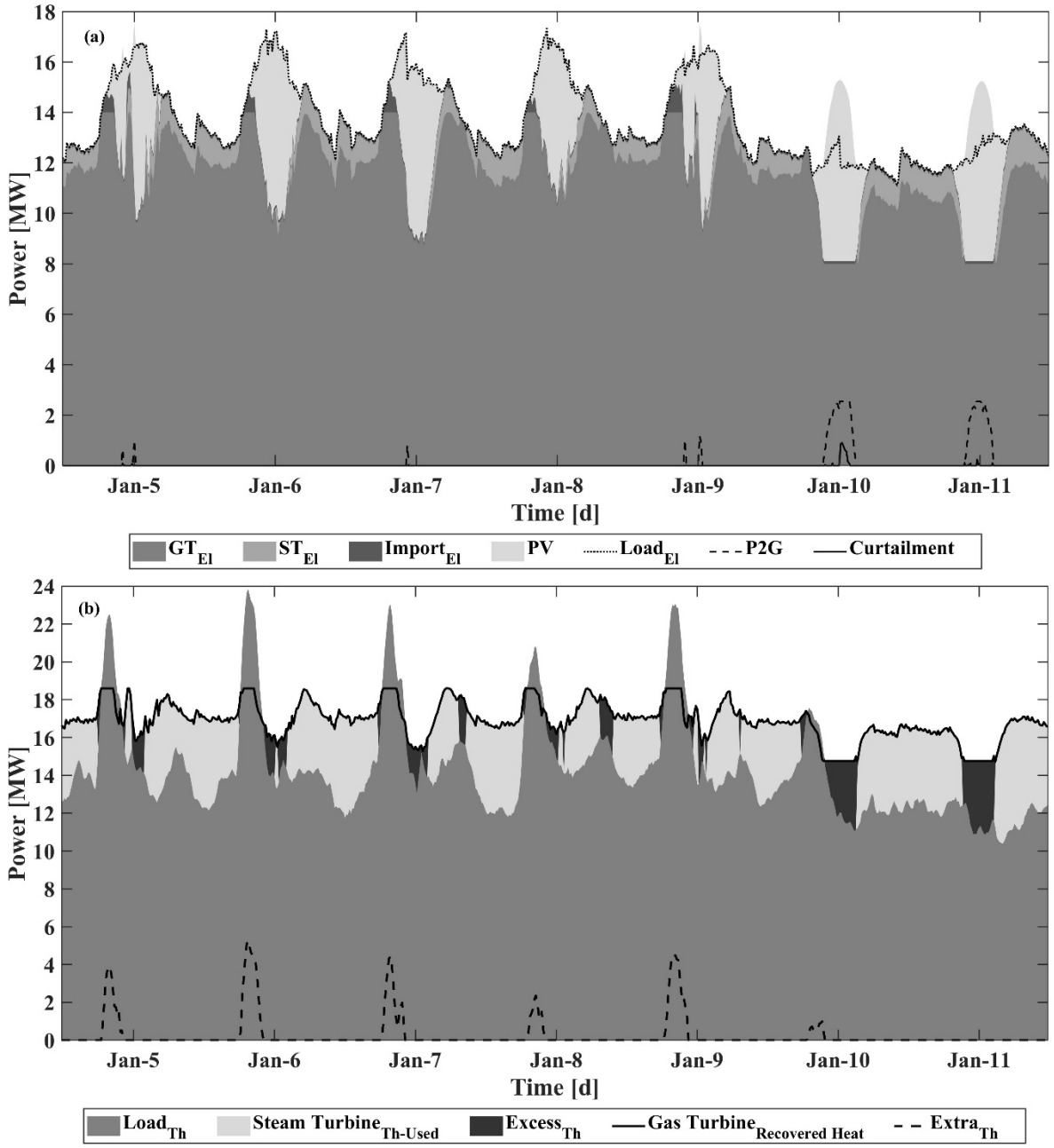

Figure 61: Microgrid-SOE dispatch simulation results in a week of January (a) electric power balance, and (b) thermal power balance with 10 MW of PV installed capacity.

The last scenario reported in Figure 62 and Figure 63 for the two chosen weeks, is the scenario corresponding to 25 MW of installed PV capacity. In this scenario the peak PV power output reaches 19 MW and during many days this value is higher than the entire campus electrical demand. This situation of excess PV generation will worsen for scenarios with higher PV capacity that are not shown here. In the represented week, every day the gas

turbine has to be turned down to the minimum operating condition while still every day massive solar excess power occurs. Electricity import is still necessary during the nights and during strong transient conditions.

According to Figure 62(a), in the represented September week, we have excess electricity that is mostly stored in the form of hydrogen via P2G electric power consumption and a portion of it is curtailed since we selected to dispatch the minimum aggregated power capacity of SOE systems required to store 80% of the annual excess electric energy. According to Figure 62(a), from September 2 to September 5, approximately all the excess electric power is stored via P2G. However, on September 6 and 7, the amount of excess electric power is relatively high which forces all the dispatched SOE units to operate at full load resulting in 8 MW of P2G power consumption. As a result, we have around 4 MW and 6 MW of peak curtailment in these two days, respectively. Also, it should be noted that in the middle of all the days, there is a huge amount of excess thermal power due to relatively low thermal demand as well as high PV power which causes the steam turbine to be turned off. Moreover, in the represented September week, there is no need for extra thermal power since again the thermal demand can be totally supplied by the gas turbine recovered heat. It can be noticed that, when the heat demand is low enough, the presence of excess electricity and heat is often simultaneous as shown in Figure 62. This fact results in supplying and utilizing the excess thermal power, which is in the form of steam (generated by recovering heat from gas turbine exhaust), as a portion of the required steam for electrolysis process. This will reduce the steam generator power consumption and consequently increase the efficiency of electrolysis system which results in higher hydrogen production in the UCI campus.

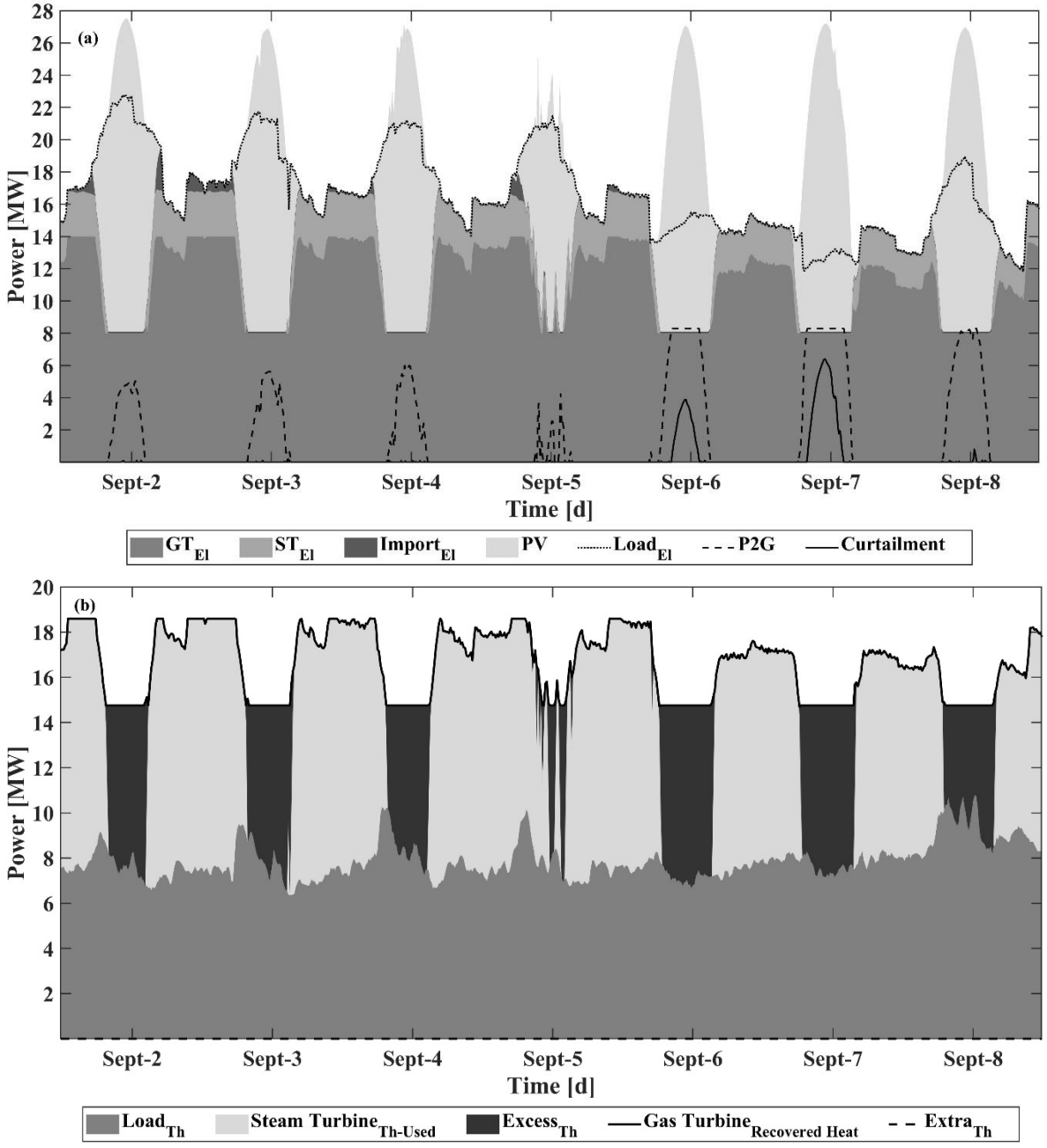

Figure 62: Microgrid-SOE dispatch simulation results in a week of September (a) electric power balance, and (b) thermal power balance with 25 MW of PV installed capacity.

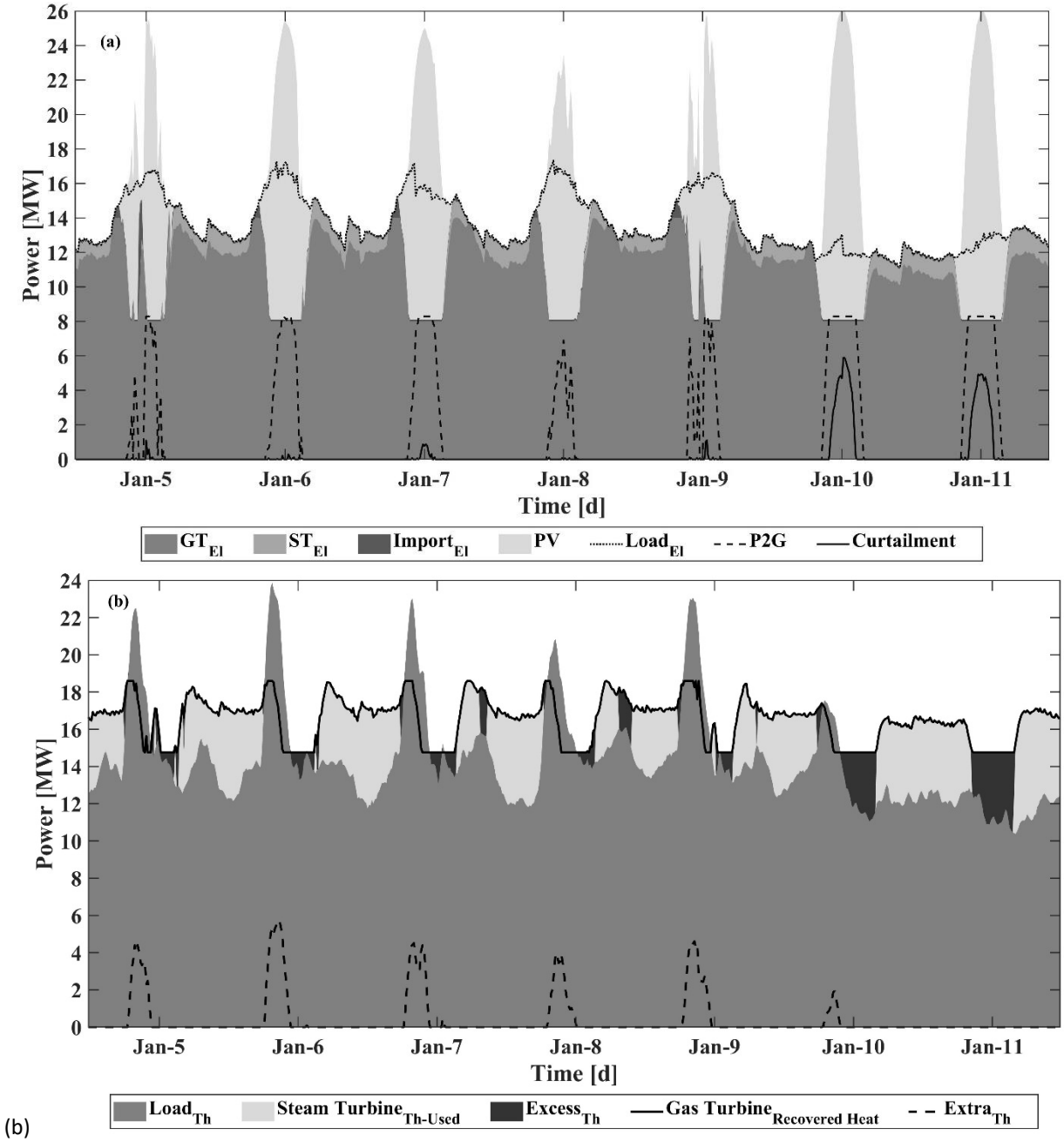

(b)

Figure 63: Microgrid-SOE dispatch simulation results in a week of January (a) electric power balance (b) thermal power balance with 25 MW of PV installed capacity.

According to Figure 63(a), in the represented January week, we have higher excess electricity compared to the September week especially from January 5 to January 8 (workdays) due to lower electric demand. However, due to higher thermal demand in January, the excess thermal power is lower and there are some hours in which extra thermal

energy is required to be supplied by additional natural gas combustion to meet the thermal demands of the campus.

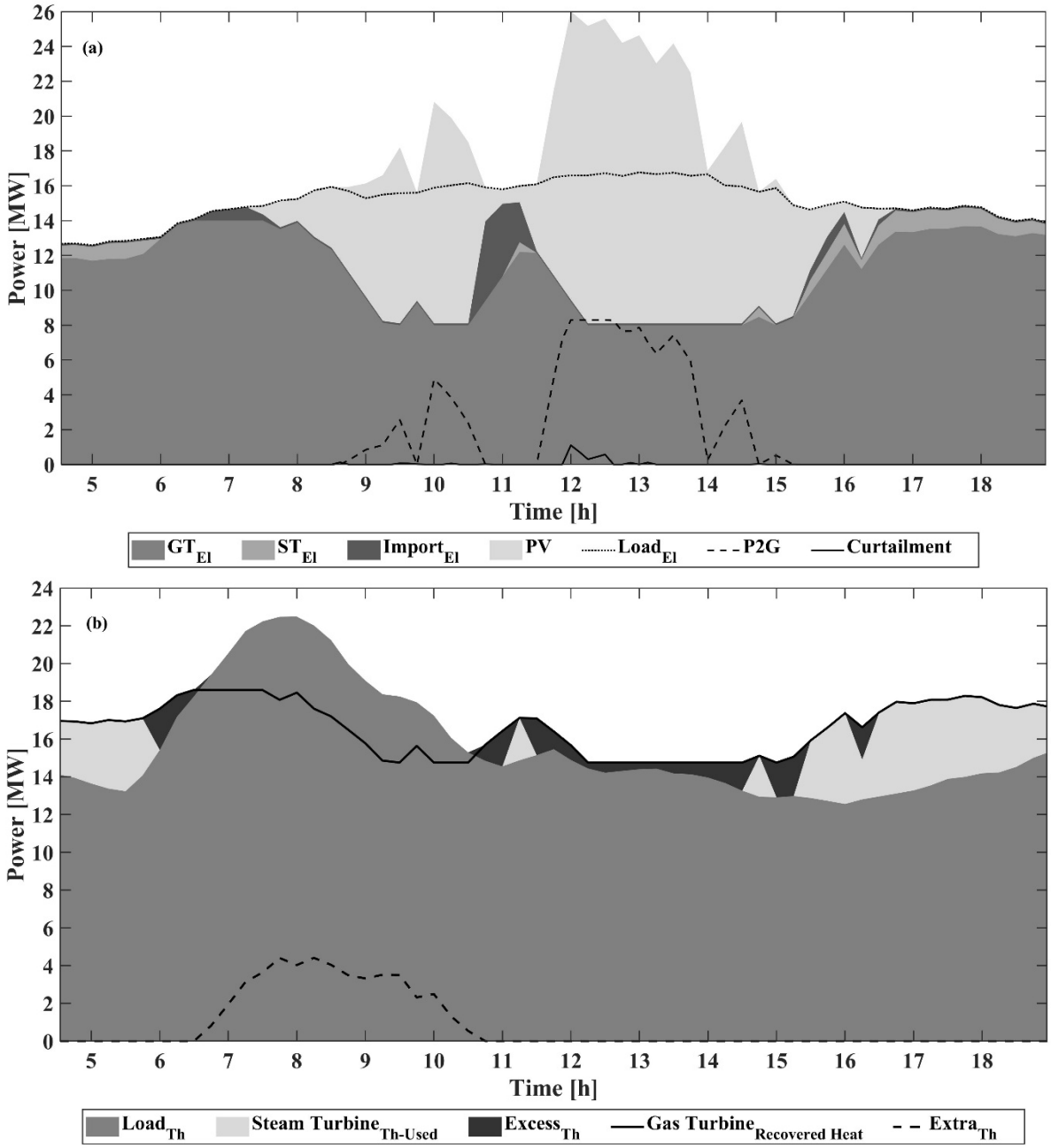

Figure 64: Details of microgrid operation during the day January 5 (a) electric power balance, and (b) thermal power balance with 25 MW of PV installed capacity.

In Figure 64, the grid operation is represented in detail for the day of September 5. During this day cloud coverage appears from 10:00 to 11:30. Consequently, PV output shows a drop

from 13 to 1.3 MW followed by an increase to 16 MW in less than 2 hours. In the same timeframe the gas turbine is not able to modulate its power output fast enough requiring electricity import to meet electrical demand from 10:30 to 11:30 during its ramp up and causing excess of electricity production during its ramp down between 11:30 and 12:15. As shown in Figure 64(a), although the gas turbine output power reaches its minimum from 12:00 to 15:00, in this timeframe there is still excess power mainly consumed via P2G, since the PV power is higher than the difference between the electric demand and the gas turbine minimum output power.

The same trends can be highlighted on a different scale looking at California net electricity demand, i.e., total electricity demand after wind and solar production, shown in Figure 65 for a day in January 2019 [352]. At the current RES capacity present in the state of California, it is clear the phenomenon known as “the duck curve”: drop of power production requested from traditional fossil fuel plants and steep ramp up required in the late afternoon when the solar production decreases and the electricity demand reaches its peak. The suggested P2G system could be integrated to the statewide electricity system in a manner like that of the UCI microgrid, enabling conversion of a portion of renewable electricity to renewable hydrogen in the middle of the day. This implementation would not only reduce the required steep ramp up rates, but also utilize the produced renewable hydrogen in the existing gas plants to lower their carbon emissions. As a result, P2G conversion using high temperature SOE systems could more generally than the specific microgrid considered herein enable penetration of high RES in many grid networks to reduce the greenhouse gas emissions.

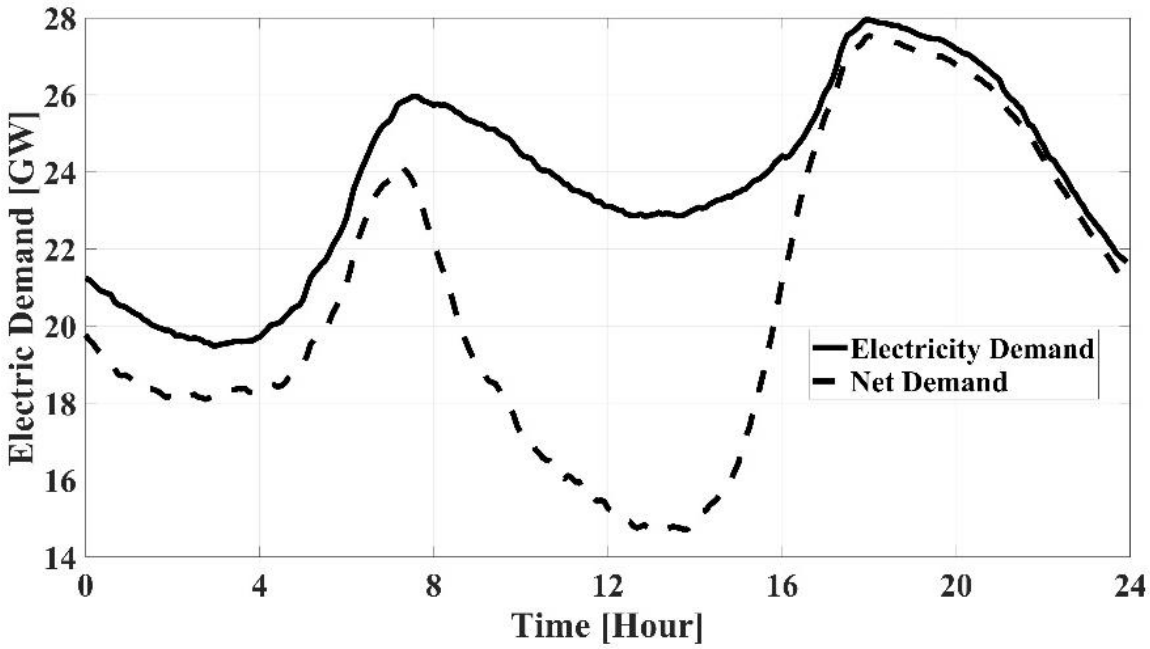

Figure 65: Statewide California electricity demand and net demand for a day in January 2019 [352].

5.6.3 Hydrogen Production

The estimations of the potential hydrogen production that could be obtained integrating high temperature SOE unit systems with the existing microgrid structure are presented in this section. Only scenarios relative to installed PV capacity higher than 10 MW are reported here because with lower capacity the electricity excess does not occur on a daily basis and the additional SOE capacity would mostly be wasted in idle mode. From the comparison of the annual hydrogen production shown in Figure 66, it can be noticed that, as previously explained, scenarios with PV capacity higher than 15 MW would result in massive excess electricity levels and this increase is reflected by the hydrogen production potential that for a doubled PV capacity, from 10 to 20 MW, shows an almost nine times increase, passing from around 22 metric tons per year to values higher than 191 tons per year.

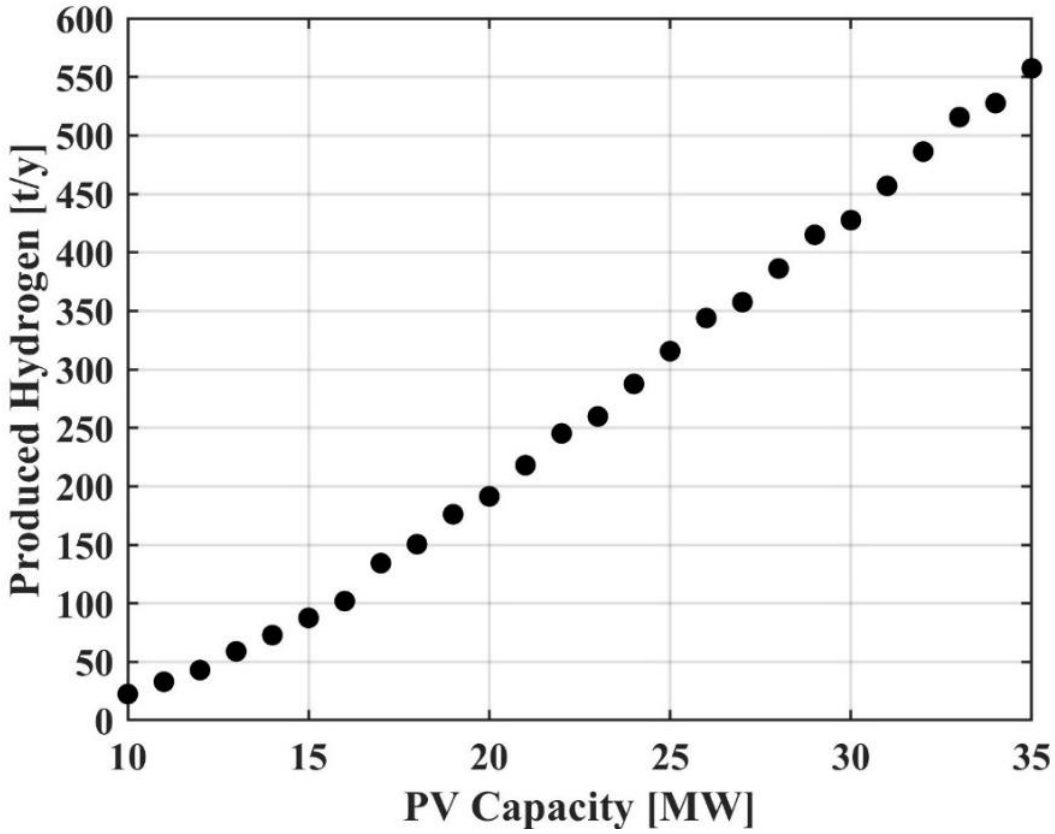

Figure 66: Annual hydrogen production for different PV installed capacity.

These results can be analyzed in terms of the average annual efficiency of the electrolysis process evaluated according to the following equation.

$$\eta_{SOEC,Average} = \frac{m_{H_2,Annual} \times LHV_{H_2}}{E_{SOEC,Annual}} \quad \text{Equation 67}$$

where $m_{H_2,Annual}$ is the amount of hydrogen produced in one year, LHV_{H_2} is lower heating value of hydrogen and $E_{SOEC,Annual}$ is the total electrical energy delivered to the SOE units over the year. The average annual efficiency of the electrolysis process is approximately 70% for all the PV installed capacities considered ranging between 10 MW to 35 MW. This nearly constant efficiency is related to the electrolysis system design strategy proposed, which is made up of individual 300kW SOE units that mostly operate at design conditions or are idle (not much part-load operation).

The simulation results show that sequential dispatch of 300 kW SOE systems into the UCI microgrid improves P2G efficiency compared to the currently available PEM electrolyzer producing hydrogen for the UCI campus. The simulated annual average efficiency of SOE systems for different PV penetration scenarios is 70% (LHV basis), which is significantly higher than the measured 50% (HHV basis) efficiency of the PEM electrolyzer that has been dynamically operated to integrate high PV use in the UCI microgrid [353].

5.6.4 On-Site Hydrogen Utilization

The P2G system is based on the assumption that, injecting hydrogen into the natural gas distribution network, the hydrogen storage does not have to be built on site taking advantage of the very large existing storage volume represented by the natural gas distribution network. The amounts of hydrogen produced has been compared with possible on-site utilization capabilities such as the local hydrogen fueling station for fuel cell electric vehicles and the direct injection of the produced hydrogen in the gas turbine inlet to reduce the natural gas consumption. The local fueling station maximum daily rated capacity is 180 kg of hydrogen and according to past years data, in 2017 were delivered 48,599 kg of hydrogen, resulting in an average daily delivery of 133 kg of hydrogen. This value more than doubled the amount of the previous year. Therefore, in the unlikely case that the local hydrogen demand for mobility does not increase in the near future, the hydrogen fueling station could consume the entire renewable hydrogen production from the microgrid excess electricity up to the scenario with 13 MW of PV capacity, in which the average daily hydrogen production is around 161 kg of hydrogen. In the case of 13 MW of PV capacity, 1.8 MW of SOE dispatched systems is required to store at least 80% of the annual excess electricity, and the annual production of the hydrogen would be around 59 metric tons.

Regarding the use of hydrogen as a fuel in the existing gas turbine, several studies have investigated the possibility of using a blend of natural gas and hydrogen to partially decarbonize the produced electricity and as a transitional solution toward future zero emissions energy systems. A reference value for the hydrogen concentration limit that does not imply structural modification or important performance changes to existing devices is around 15% volumetric [347,348]. The molar heating value of the gas mixture with the

reference hydrogen volume concentration can be estimated according to the following equation.

$$LHV_{mix} = x \times LHV_{H_2} + (1 - x) \times LHV_{NG} \quad \text{Equation 68}$$

where LHV_{H_2} and LHV_{NG} are the molar lower heating values of hydrogen and natural gas and x is the maximum volumetric hydrogen concentration. The maximum amount of hydrogen that could be injected into the gas turbine can be estimated with the following equation, if feeding the gas turbine with the mixture of hydrogen and natural gas does not affect the efficiency.

$$n_{H2,GT} = x \times \frac{E_{GT,El} / \eta_{GT,Average}}{LHV_{mix}} \quad \text{Equation 69}$$

where $E_{GT,El}$ is the annual electric energy produced by the gas turbine, $\eta_{GT,Average}$ the average electrical efficiency of the gas turbine and x the limit hydrogen volumetric concentration.

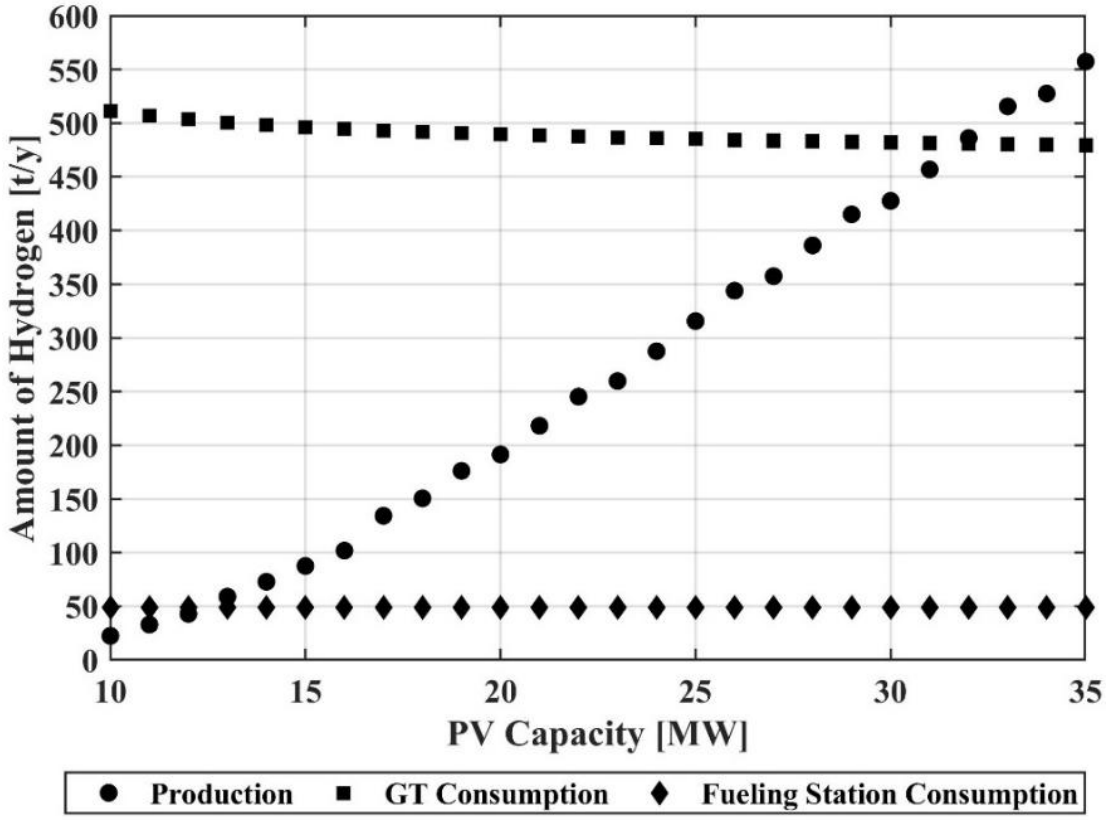

Figure 67: Hydrogen production and possible on-site consumption for different PV installed capacity.

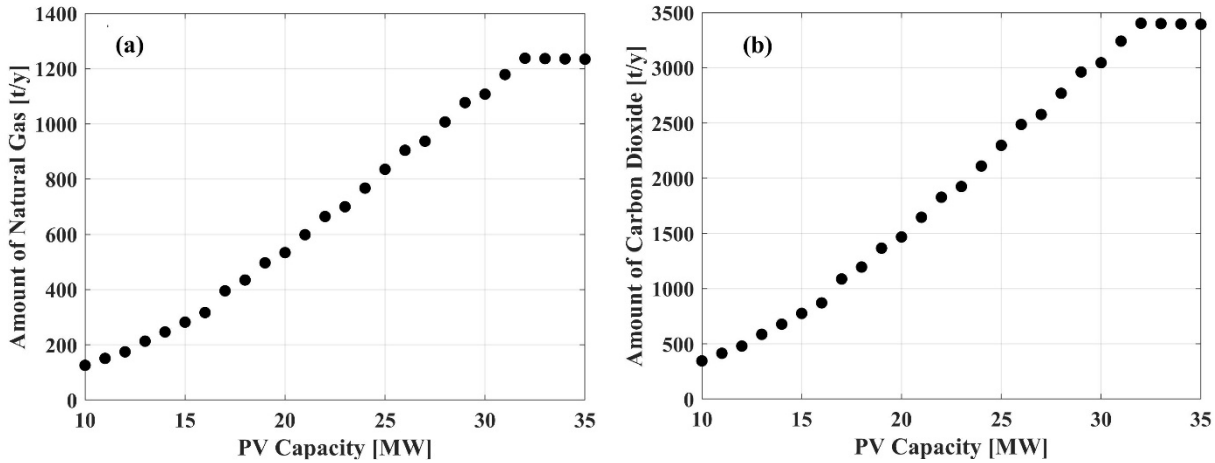

Figure 68: Yearly amount of avoided natural gas consumed by the gas turbine, and (b) yearly amount of reduction in CO_2 emission from the gas turbine for different PV installed capacity.

Figure 67 shows the yearly amount of hydrogen production, yearly amount of hydrogen consumption by the gas turbine in the case of feeding the gas turbine with a gas mixture containing 15% volumetric hydrogen and 85% natural gas, and the yearly amount of

hydrogen utilized in the local fueling station. As can be seen from Figure 67, feeding the gas turbine with a gas mixture containing 15% volumetric hydrogen would suffice to consume the hydrogen produced up to the scenario with 32 MW of PV installed capacity. Moreover, the produced hydrogen associated with all the PV capacity scenarios would be consumed in the case of using the produced hydrogen for feeding both the gas turbine and the fueling station. It is worth noting that as shown in Figure 67, the blending limit of hydrogen decreases with increasing PV capacity deployment because the electrical energy produced by the gas turbine decreases, requiring overall lower fuel consumption. Figure 68(a) shows the amount of reduced natural gas consumption in the gas turbine per year due to the 15% hydrogen blending with natural gas fed into the gas turbine. It shows that the integration of SOE systems to store 80% of surplus electricity results in saving up to about 1200 metric tons of natural gas per year for the highest PV scenario. Thanks to the injection of hydrogen in the gas turbine, the annual natural gas consumption decreases between 120 metric tons to 1200 metric tons while the PV installed capacity increases between 10 MW to 35 MW, respectively. Consequently, blending hydrogen with the natural gas feeding the gas turbine results in annual 350 to 3500 metric tons reduction in carbon dioxide emissions for 10 MW to 35 MW PV scenarios respectively as shown in Figure 68(b). On the other hand, integration of PV renewable generated electricity into the UCI microgrid also decreases the required electricity generation via gas turbine to meet the electric demand. This reduction also results in reducing natural gas consumption and carbon dioxide emissions. Microgrid simulation results show that there could be an annual 1560 to 3050 metric tons reduction in the natural gas consumption due to the increase in the PV share from the already existing 4 MW PV to 10 MW and 35 MW, respectively. Also, increasing the PV capacity from 4 MW to 10 MW and 35 MW would decrease the annual carbon dioxide emissions by 4300 to 8400 metric tons, respectively.

5.7 Summary

In this chapter, the challenges of RES penetration have been investigated in the context of the University of California, Irvine campus microgrid, simulating the existing power plant operation and examining the effects of increasing renewable installed capacity. The limits of the microgrid power plant have been identified and would result in massive excess

renewable electricity production, with no sensible increase in RES penetration in the campus electrical energy supply for renewable installed capacities higher than 15 MW, if no energy storage solution is implemented. The integration of a modular P2G system based on sequential dispatching of SOE systems into the campus microgrid has been modelled to evaluate the annual hydrogen production potential and the capability of the system to successfully absorb excess electricity from the additional renewable installations. The minimum aggregated power capacity of 300 kW dispatched SOE systems required to store at least 80% of the annual excess electricity is considered in each scenario. Utilization of the produced renewable hydrogen blended with natural gas as a fuel in UCI microgrid gas turbine, as well as the use of hydrogen in the local fueling station has been assessed. The results show that feeding the gas turbine with a gas mixture containing 15% volumetric hydrogen would suffice to consume all the hydrogen produced up to the scenario with 32 MW of PV installed capacity. Moreover, the entire renewable hydrogen production in all the PV capacity scenarios could be consumed on site considering both the feeding of the gas turbine with a gas mixture containing 15% by volume hydrogen and the delivery of hydrogen to fuel cell vehicles in the local fueling station. This would allow an increased share of renewable energy supply to the campus and accelerate decarbonization of the transportation sector of surrounding areas. In conclusion the deployment in the microgrid infrastructure of the additional PV capacity and the integration of the P2G system could reduce both natural gas consumption and carbon dioxide emissions. Up to 4250 metric tons (16%) of natural gas consumption and 11,900 tons (16%) of CO_2 emissions could be avoided.

6 Experimental Analysis of Solid Oxide Short Stack

6.1 Test Stand Set-up and Instrumentation

At the Advanced Power and Energy Program (APEP) of the University of California Irvine, there is a Short Stack Test Bench (SSTB) which is manufactured by SOLIDpower that is used for the experimental analysis in this research. The short stack has 6 cells in a co-flow flow-field arrangement (Figure 69).

Figure 69: 6-cell short stack and electric furnace to thermally manage the short stack.

The cells are made up of a thin 8 mol% Yttria (Y_2O_3) Stabilized Zirconia (YSZ) electrolyte (8 ± 2 µm) supported on a conventional porous Ni/YSZ fuel electrode (240 ± 20 µm) [354]. The air electrode (40 ± 10 µm) is comprised of a composite of metallic perovskite Sr-doped $LaMnO_3$ (LSM) and oxide-ion electrolyte YSZ. The active area of each cell is 80 cm^2. To thermally manage the 6-cell short stack which could not be self-sustained otherwise, an electric furnace is used to surround both 6-cell stack and preheating manifolds (Figure 69). The temperature is controlled by an independent temperature controller (PIXSIS ATR621) as shown in Figure 70. The maximum allowed furnace temperature is set to 900°C.

Figure 70: Independent temperature controller (PIXSIS ATR621) to control furnace temperature.

This test bench can operate in both fuel cell mode and electrolysis mode. The test bench has different inlet ports that enable feeding the stack either by the natural gas grid or by a mixture of gases, including mixtures of H_2, H_2O, CO, CO_2, N_2 and CH_4. This makes the test bench able to operate in fuel cell mode, electrolysis and co-electrolysis modes. To control flows of different gases, solenoid valves and mass flow controllers are employed as shown in Figure 71. The separate lines are then mixed and humidified with steam (If it is supplied) before being fed to the fuel electrode inlet.

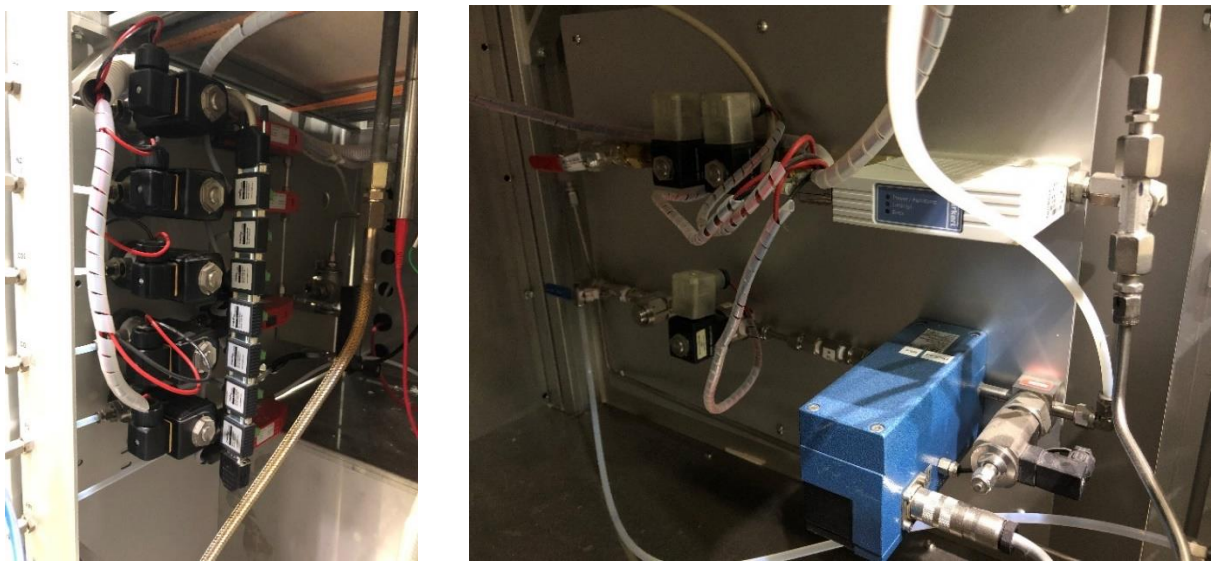

Figure 71: Solenoid valves and mass flow controllers to control flow of different gases.

The stack is electrically connected to an electronic load for fuel cell operation or a power supply for electrolysis and co-electrolysis operation as shown in the Figure 72.

To acquire and log data from different deployed thermocouples and voltage sensing cables, a data acquisition system is used as shown in Figure 73.

One of the requirements for water supply is to have deionized water fed to the stack with a conductivity of between 0.1 to 10 micro siemens per centimeter. To meet this requirement, a series of water filters is deployed to deionize the tap water as shown in Figure 74.

Upstream of the stack is a pre-reforming reactor and evaporator that is fed by the water and natural gas lines, to ensure the partial conversion of CH_4 and larger hydrocarbons as shown in Figure 75. Temperature of both evaporator and reformer is controlled by two independent temperature controllers as shown in Figure 76.

Figure 72: Electronic load and power supply.

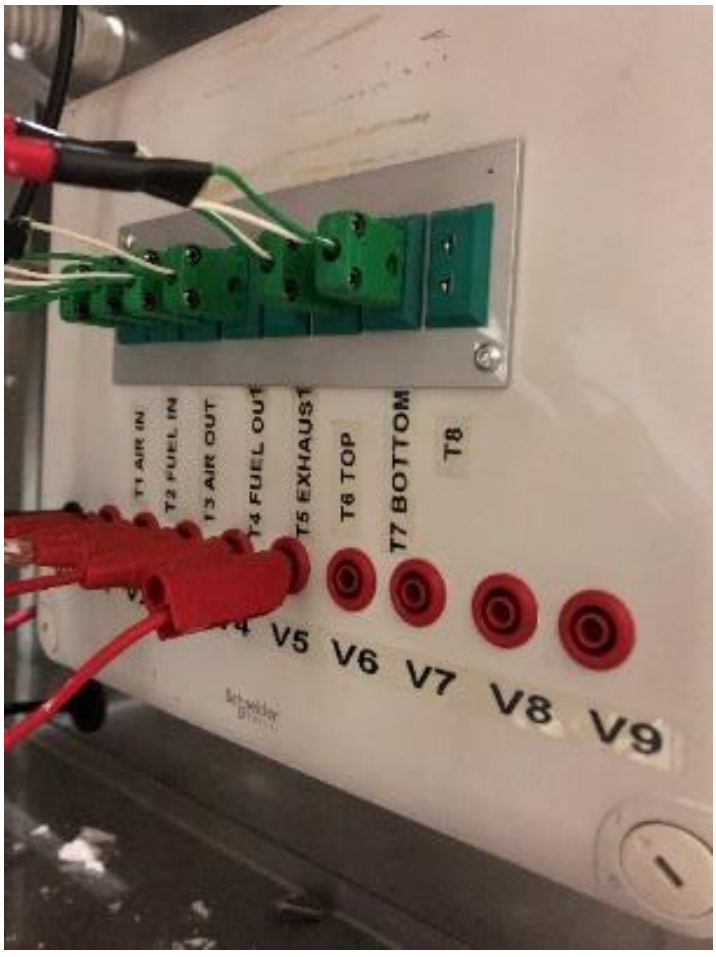

Figure 73: Data acquisition system.

Figure 74: Deionized water supply line.

Figure 75: Evaporator and reformer reactor.

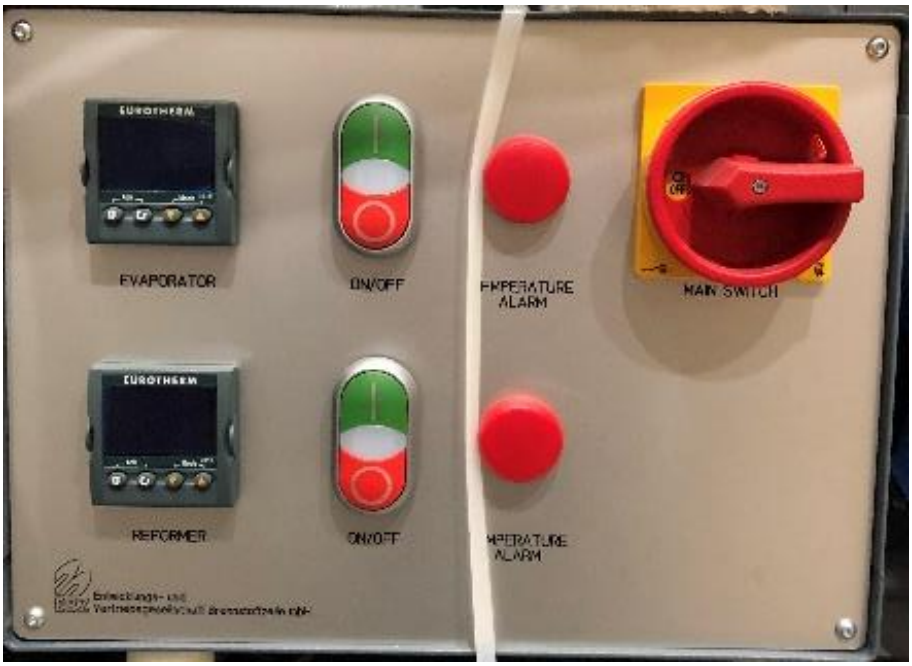

Figure 76: Evaporator and reformer reactor independent temperature controller.

The test bench is connected to a potentiostat (Figure 77) to characterize cells and the whole stack by doing different characterization tests e.g., Electrochemical Impedance Spectroscopy (EIS).

Figure 77: Princeton applied research VersaSTAT 3F potentiostat.

A schematic of the test bench process flow, including the most important instrumentation probes, is shown in Figure 78.

The actual test bench with all its connections is shown in Figure 79. The orange cables are electric power cords that connect test stand different parts to AC wall plug outlet. The test stand is comprised of two sides, right and left sides. The right side has evaporator and reformer, and the left side has short stack within the electric furnace. Two sides of the test stand are connected to each other via a composite insulation material.

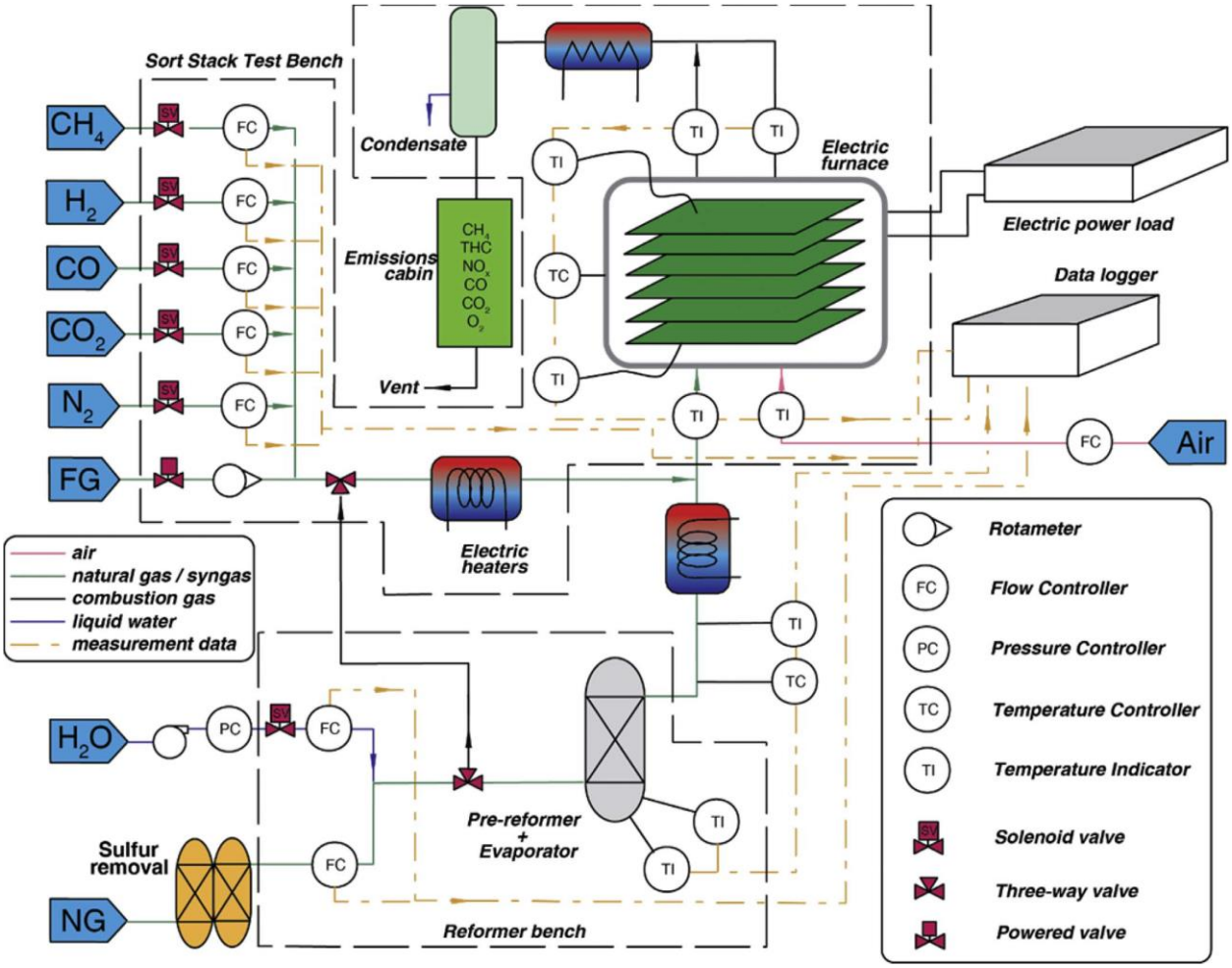

Figure 78: Schematic of test stand set-up and instrumentation [354].

Figure 79: Actual test bench and its connections.

The operation of different components can be controlled using graphic use interface installed in the embedded computer as shown in Figure 80. It enables setting different temperature and different flow rates as well as logging different parameters e.g., cells' voltage, operating current, etc.

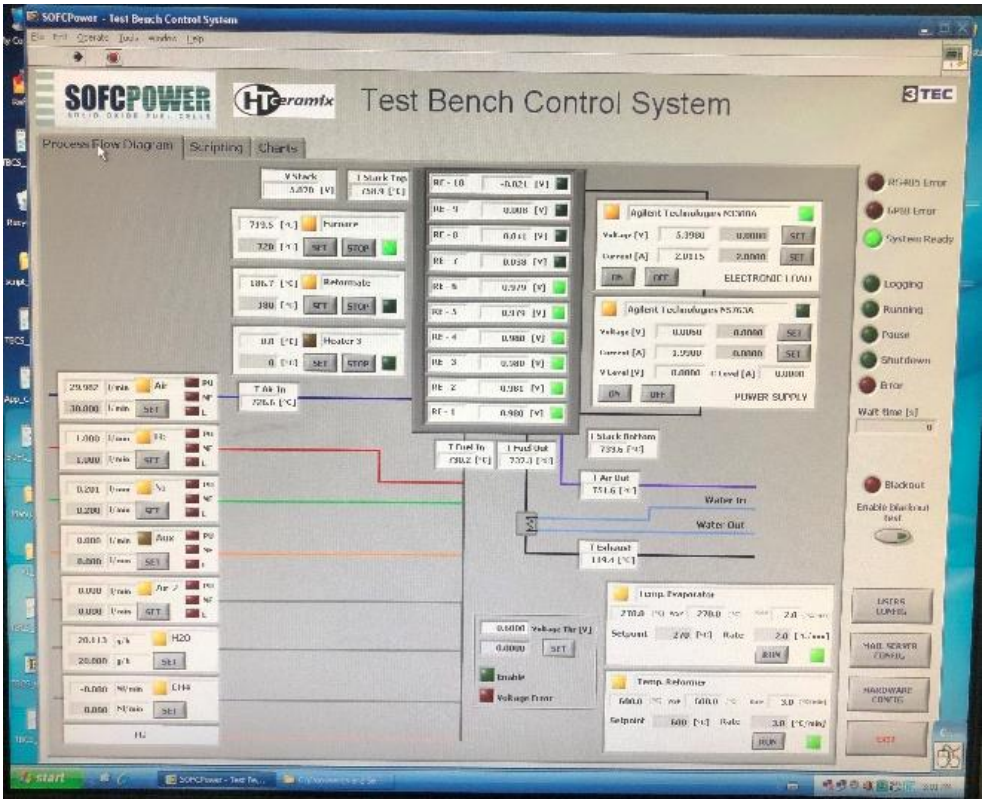

Figure 80: Graphical user interface installed in the embedded computer to control the test bench.

6.2 Experimental Results

It this research, the SOLIDpower short stack test bench was used to evaluate several short stacks of SOE cells in different modes and different operating conditions.

6.2.1 Post Process of the Experimental Data

A post-processing model has been developed in Matlab to be able to post-process the experimental data of different tests. It can statistically analyze the input experimental data while plotting different types of figures showing different operating parameters both in steady state and dynamic operating conditions.

6.2.2 Effect of Operating Temperature

To evaluate the effect of operating temperature on the V-j characteristics curve, three tests have been done at three different operating temperatures 700^{o}C, 750^{o}C and 800^{o}C. In each test, current has been changed between 0A to 60A. The mass flow rates of both fuel and air were kept constant. In the fuel electrode side, a mixture of 90% steam and 10% hydrogen was introduced. The steam flow rate was 142.47 gr/hour, and the hydrogen flow rate was 0.328 lit/min. These flow rates were determined to have 85% fuel utilization at the highest current which is 60 A. The air flow rate was 32 lit/min in all three tests. Figure 81 shows V-j curves for the mentioned three different operating temperatures. As it was expected, when the operating temperature is lower, the voltage overpotentials are higher. In 700 ^{o}C, the V-j curve is almost linear showing the ohmic overpotential is dominant overpotential in the whole operating currents. However, in 750^{o}C and 800^{o}C, the activation and concentration overpotentials are appeared at low and high current densities, respectively. Also, in these two operating temperatures, the linear profile was observed in the middle current densities which is dominated by ohmic overpotentials. It should be noted that for 700 ^{o}C, the last couple of operating point are in exothermic condition (>1.28V) while for 750 ^{o}C and 800 ^{o}C, all the operating points are in endothermic operating conditions.

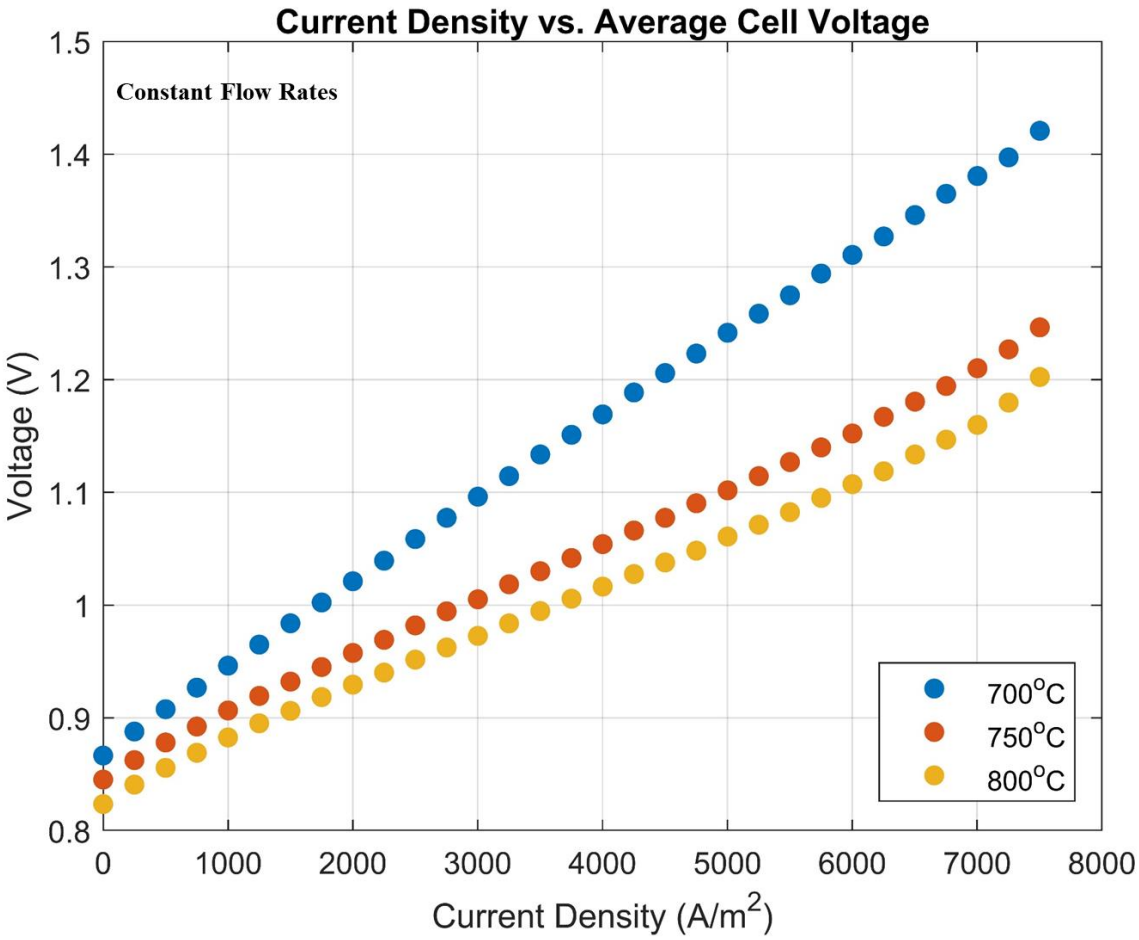

Figure 81: V-j characteristic curve for electrolysis operation at three different operating temperatures.

6.2.3 Effect of Fuel Inlet Composition

To evaluate the effect of fuel inlet composition on the V-j characteristics curve, three tests have been done at three different fuel compositions 90% H_2O-10% H_2, 75% H_2O-25% H_2 and 50% H_2O-50% H_2. In each test, current has been changed between 0A to 60A.

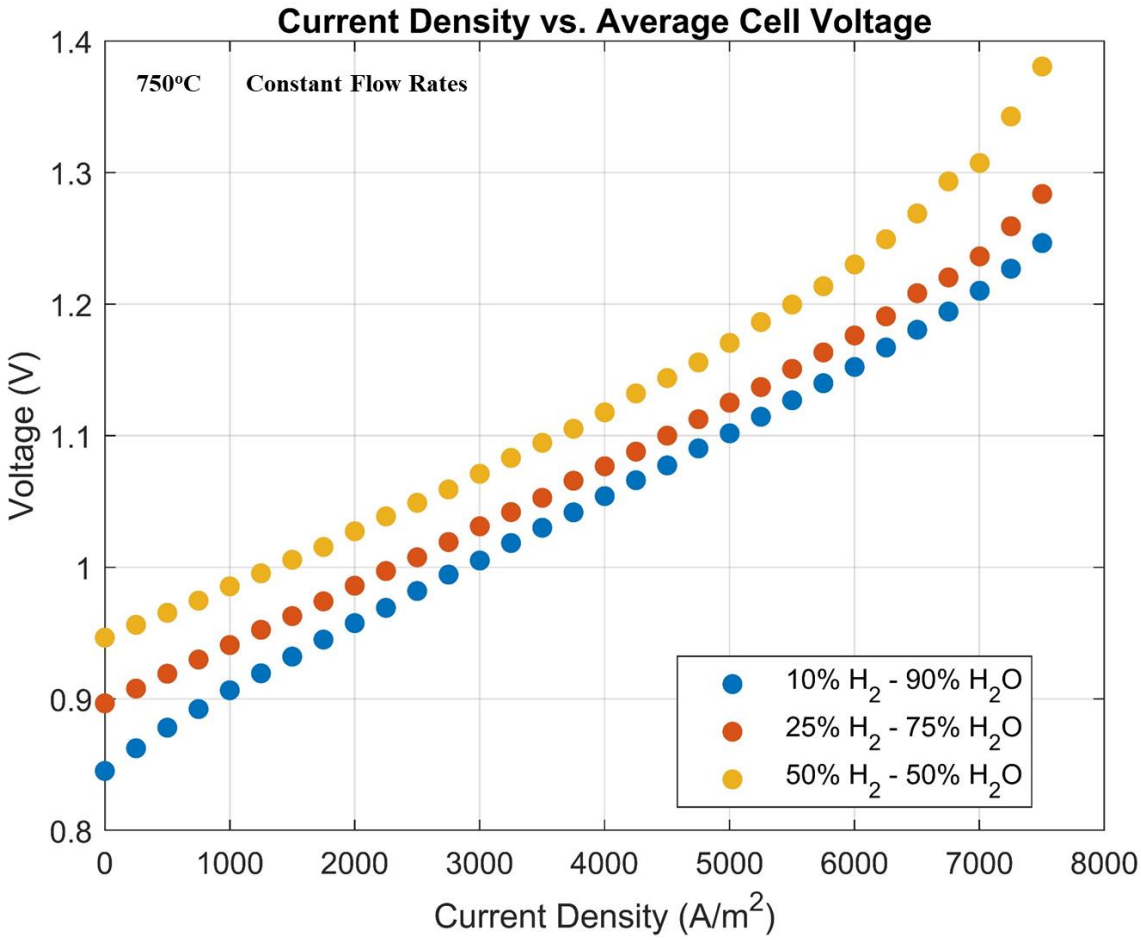

Figure 82: V-j characteristic curves for three different fuel inlet compositions showing impact of H_2 inlet percentage.

The mass flow rates of both fuel and air were kept constant during each test. In the fuel electrode side, the steam flow rate was 142.47 gr/hour while the hydrogen flow rates were 0.328 lit/min, 0.984 lit/min and 2.952 lit/min, respectively. These flow rates were determined to have 85% fuel utilization at the highest current which is 60A. The air flow rate was 32 lit/min in all three tests. Figure 82 shows V-j curves for the mentioned three different fuel compositions showing the impact of inlet hydrogen percentage. As was expected from the Nernst equation, as the percentage of hydrogen in the fuel decreases, the open circuit voltage decreases. It should be mentioned that when the hydrogen percentage increases from 10% to 50%, the open circuit voltage increases about 0.1 volts which is considerable given the fact that the higher the operating voltage is, the lower the hydrogen production efficiency will be. In 90% H_2O-10% H_2, at low current densities, activation overpotential

appears more compared to other fuel compositions. However, the concentration overpotential appears more in 50% H_2O-50% H_2 at high current densities compared to other fuel compositions. In this set of experiments, like the previous set, in the middle current densities, the linear behavior of ohmic overpotential is dominated in V-j characteristic curve. It should be noted that for 90% H_2O-10% H_2, all the operating points are in endothermic condition, while for 75% H_2O-25% H_2 the last point is at thermoneutral voltage. For 50% H_2O-50% H_2 case, the last couple of operating points are in exothermic condition.

6.2.4 Model Calibration and Validation

To calibrate and validate the stack model developed and explained in previous Chapters, the set of experimental results at different operating conditions was used. The various overpotential parameters that govern the performance characteristics of the model have been calibrated for one specific operating temperature and then validated without adjustment for predicting performance at two other operating temperatures.

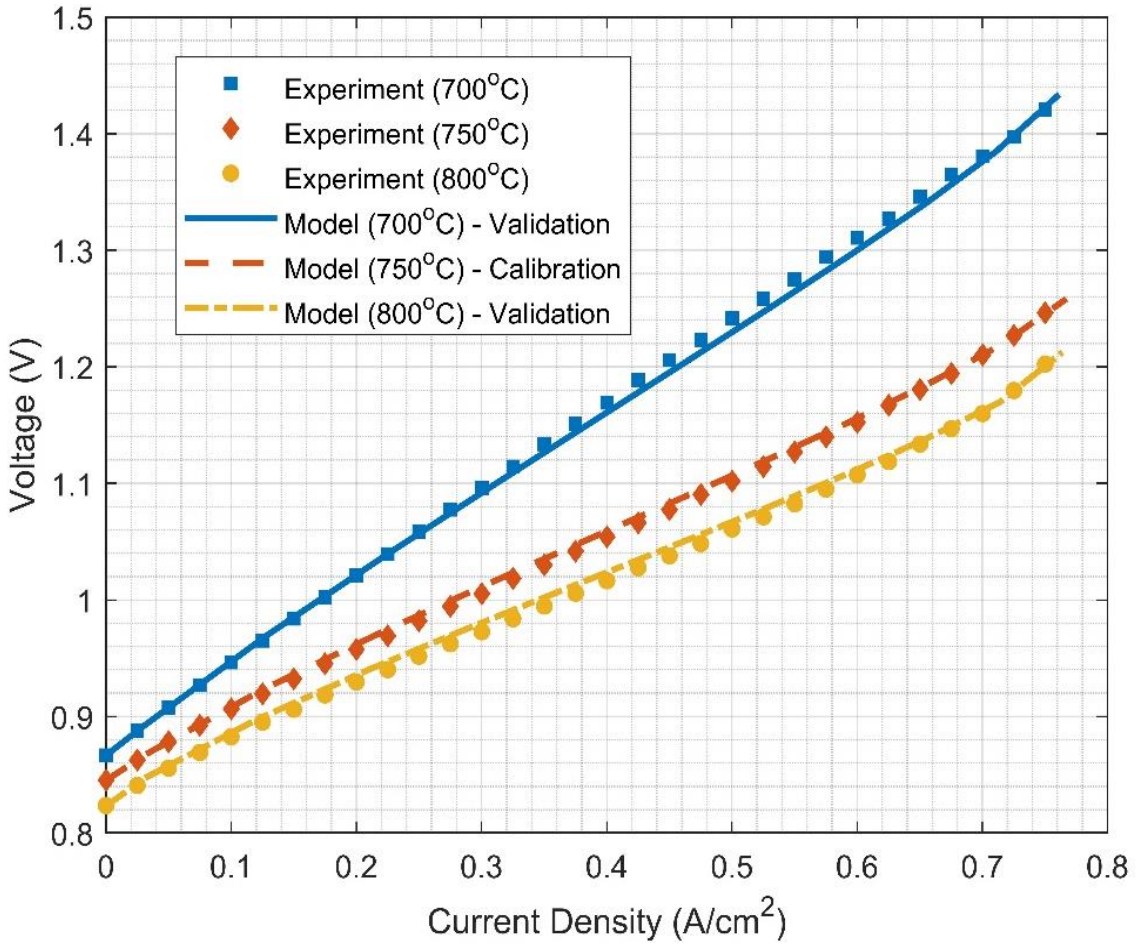

Figure 83: Model calibration and validation at different operating temperatures.

As shown in Figure 83, the model parameters were calibrated to represent the V-j curve at 750°C and then applied without adjustment to validate the model performance at 700°C and 800°C. The results show that the model accurately predicts the experimental results at different operating temperatures over the entire range of current densities investigated.

The calibrated parameters are listed in Table 2. Note that the ohmic calibrated parameters for anode, cathode, electrolyte, and interconnect are reasonable based upon the numbers reported in the literature. Activation and concentration overpotential parameters have not been reported as much as ohmic parameters in the literature. However, the obtained calibrated parameters related to the activation and concentration overpotentials are expected based upon the few numbers found in the literature.

Table 2: Calibrated parameters for the solid oxide test bench.

Parameter	Value	Unit
Geometry		
Anode thickness	4.00E-05	m
Cathode thickness	2.40E-04	m
Electrolyte thickness	8.00E-06	m
Interconnect thickness	1.28E-03	m
Fuel channel width	0.08	m
Air channel width	0.08	m
Fuel channel height	0.0025	m
Air channel height	0.0025	m
Fuel channel number	1	-
Air channel number	1	-
Ohmic Overpotential		
Pre-exponential anode	4.2017E+07	K/Ω.m
Activation Energy anode	1200	K
Pre-exponential cathode	9.5238E+07	K/Ω.m
Activation Energy cathode	1150	K
Pre-exponential electrolyte	1.023E+07	K/Ω.m
Activation Energy electrolyte	1.03E+04	K
Pre-exponential interconnect	9.3023E+06	K/Ω.m
Activation Energy interconnect	1100	K
R Contact	1.3	mΩ
Activation Overpotential		
Pre-exponential anode	4.1020E+09	A/m^2
Activation Energy anode	8.673E+04	J/mol
Pre-exponential cathode	2.6880e+10	A/m^2
Activation Energy cathode	6.673E+04	J/mol
Symmetry factor	0.5	-

Concentration Overpotential		
Porosity anode	0.3	-
Porosity cathode	0.335	-
Tortuosity anode	3.5	-
Tortuosity cathode	3.5	-
Anode pore diameter	4E-07	m
Cathode pore diameter	4E-07	m

In the second calibration and validation scenario, the set of experimental results at different fuel inlet compositions was used. As shown in Figure 84, the developed model predicts the experimental results at different fuel compositions accurately. Since it is impossible to see the details of concentration overpotentials that happen at high current densities in the performed experiments (specifically for the 50% H_2O-50% H_2 case), the calibrated and validated model is a good tool to analyze the concentration overpotential in more detail. The developed model can calculate concentrations of different species at three different levels: 1- bulk, 2- electrode surface, and 3- triple phase boundary (Figure 85). These three levels are shown in Figure 85. For the case of 90% H_2O-10% H_2, the steam concentration in the bulk and electrode surface are quite similar while reactant concentrations in the triple phase boundary region are lower (Figure 86). However, at the triple phase boundary, the steam concentration at the cell outlet is considerable which results in lower concentration overpotential. The decreasing trend in steam concentration and the increasing trend in hydrogen concentration show the hydrogen production along the cell. For the case of 75% H_2O-25% H_2, the steam concentration in the triple phase boundary region at the cell outlet gets close to zero which results in high concentration overpotential for this case (Figure 87).

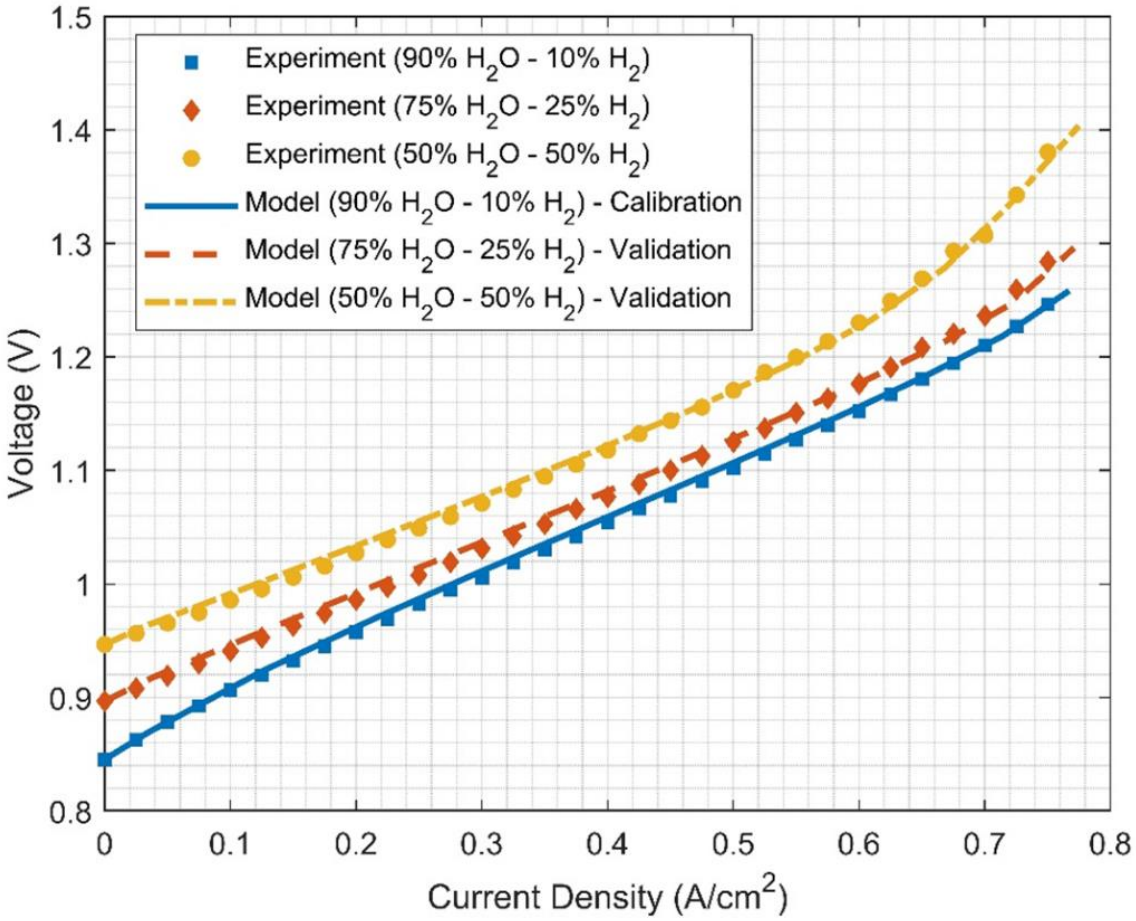

Figure 84: Model calibration and validation at different operating temperatures.

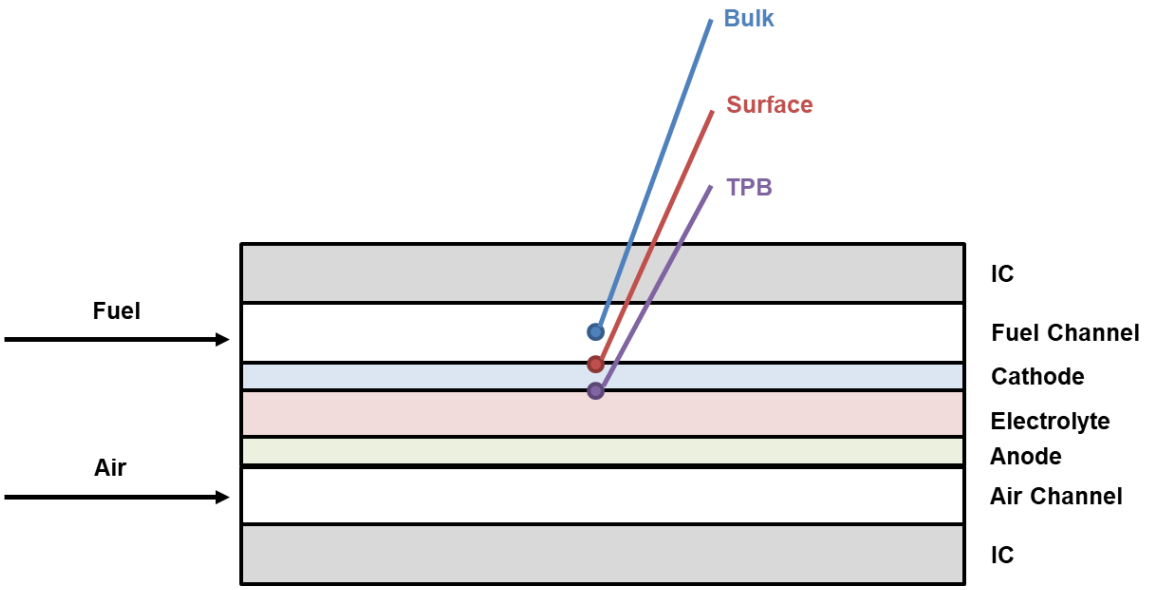

Figure 85: Schematic of solid oxide electrolysis cell showing three regions of species concentrations that are calculated in the model.

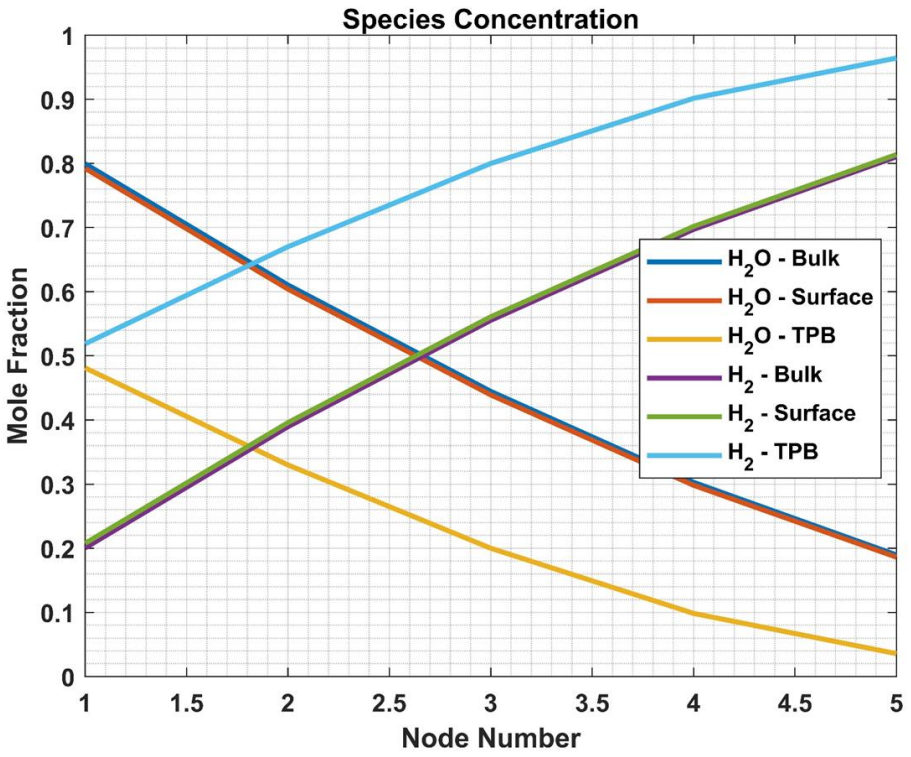

Figure 86: Species concentration at different levels for 90% H_2O-10% H_2 inlet conditions case.

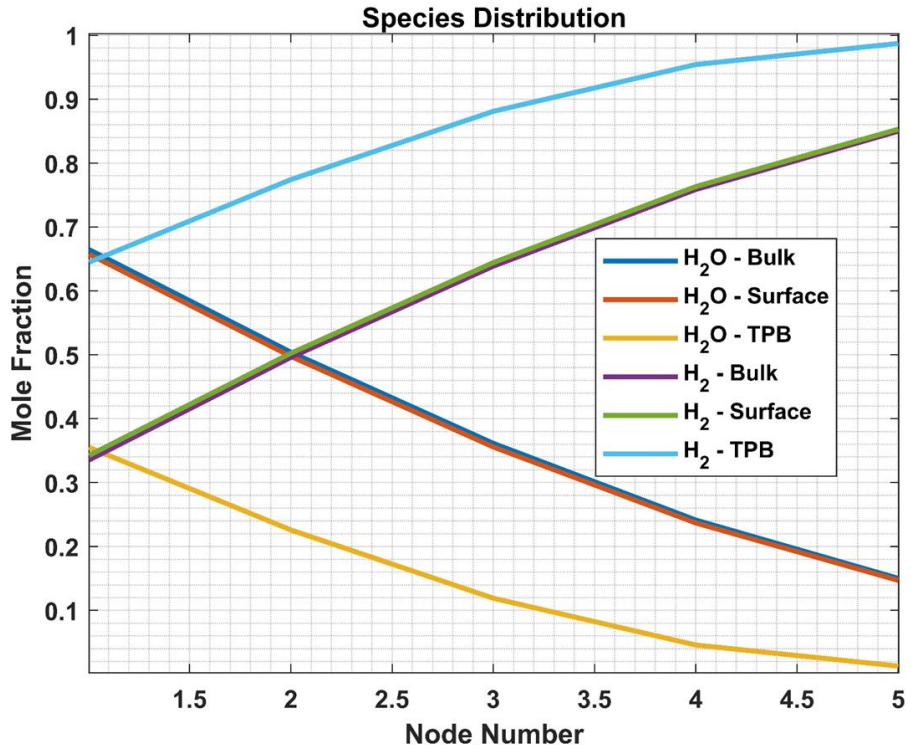

Figure 87: Species concentration at different levels for the 75% H_2O-25% H_2 inlet conditions case.

For the case of 50% H_2O-50% H_2, at triple phase boundary, the steam concentration at second half of the cell is almost zero (almost all the hydrogen is produced at the first half of the cell) which results in fuel starvation at the end of the cell and high concentration overpotential (Figure 88).

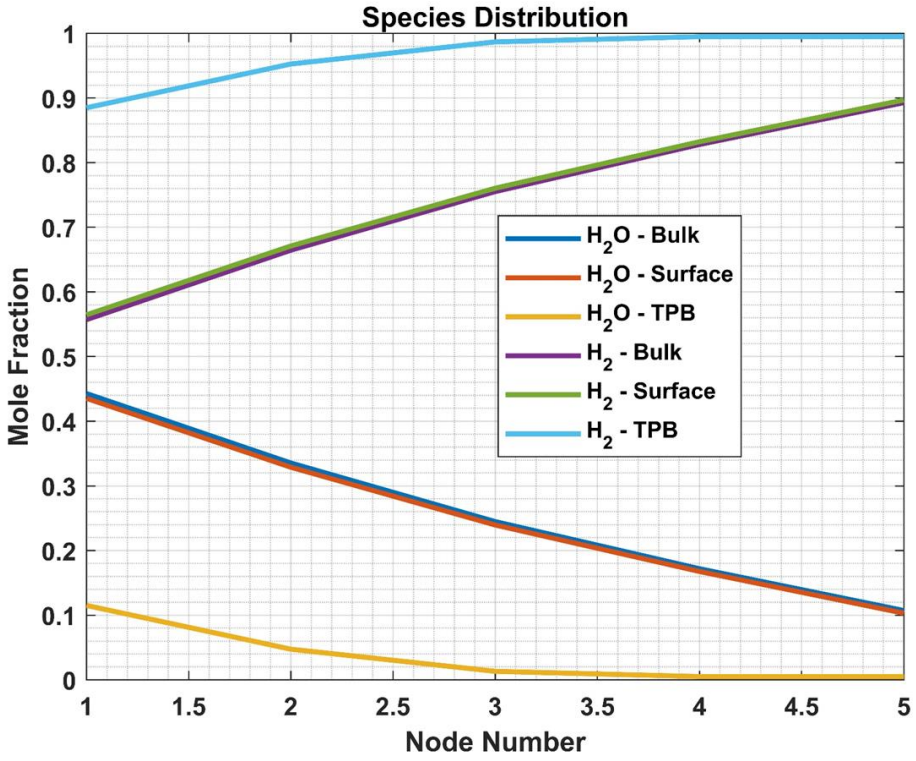

Figure 88: Species concentration at different levels for 50% H_2O-50% H_2 inlet conditions case.

6.2.5 Dynamic Step Profile

To evaluate the dynamic response and behavior of the test bench in SOEC mode, different experiments have been accomplished considering different dynamic current profiles as an input. In the first experiment, a consecutive step profile has been considered from 2500 A/m^2 to 7500 A/m^2. 90% steam and 10% hydrogen considered as fuel inlet composition. Both fuel and air flow rates have been kept constant during this experiment. To further evaluate the developed model in dynamic cases, the dynamic profile has been given to the model to evaluate the accuracy of the developed model.

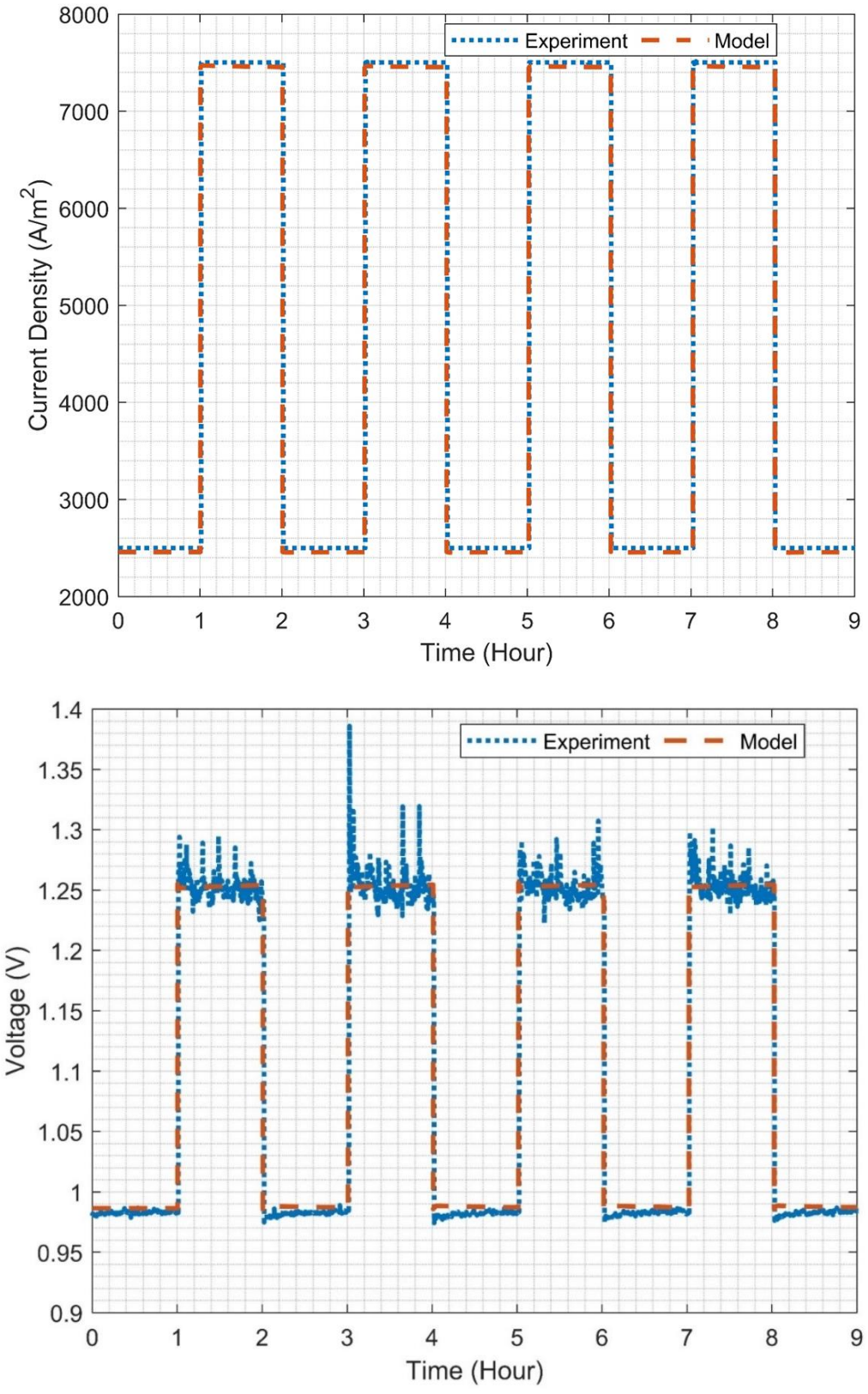

Figure 89: Dynamic response of test bench and model to the input step profile.

As discussed previously, the model input is power while the test bench output is current. However, since the manipulated parameter to control the power in the developed model is current, the model has been expected to work in the same way as test bench. The only difference is that we need to give input power to the model not the input current. To do that, the dynamic power has been calculated by multiplying the current to the sum of the cells' voltages. Figure 89 shows the behavior of current density and the average voltage of 6 cells. As shown in this figure, the current density of the model precisely follows the input current density that was set to the test bench. As a result, the voltage response in experiment has consistency with the voltage response in the model. It should be noted that the observed noise in voltage response is associated with measurement instruments. These performance curves show that during high intermittent input profiles, mainly coming from renewable resources, the SOEC system is able to respond to the variation of input power quickly which has been also predicted accurately in the developed model considering the calibrated parameters and the detailed developed thermophysical model.

6.2.6 Dynamic Solar PV (Sunny/Cloudy) and Wind Profiles

One of the applications of electrolyzers is to produce hydrogen using renewable electricity coming from solar and wind. To evaluate the dynamic response and behavior of the test bench in SOEC mode in real operating condition, the second profile is associated with PV profile in a sunny day. In this profile, the power starts from zero and goes to its highest value around noon and comes back to zero in the evening. The mentioned profile is the scaled down version of the solar PV profile from the UCI microgrid that was evaluated in the previous Chapters.

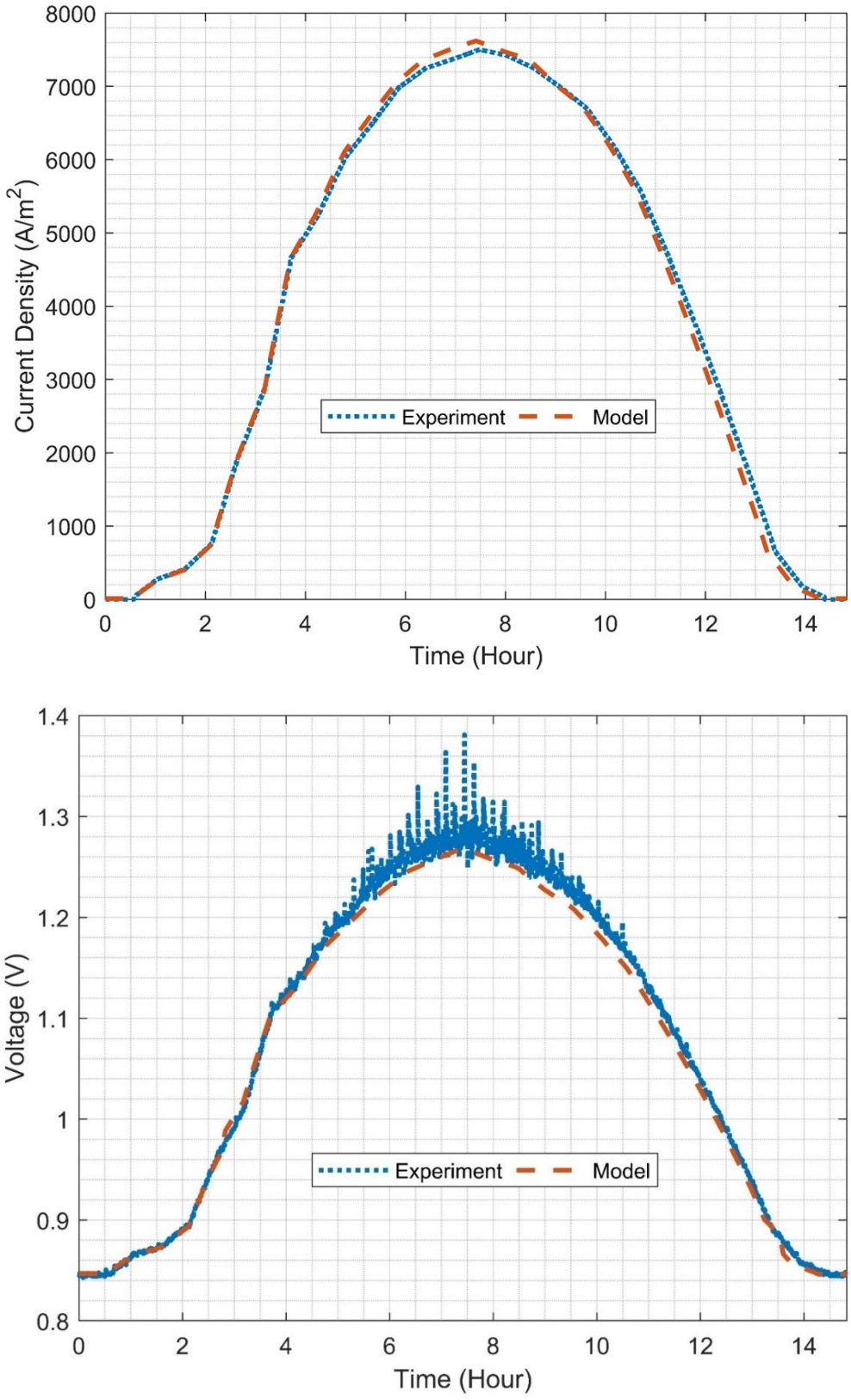

Figure 90: Dynamic response of the test bench compared to model predictions for a sunny day solar PV profile.

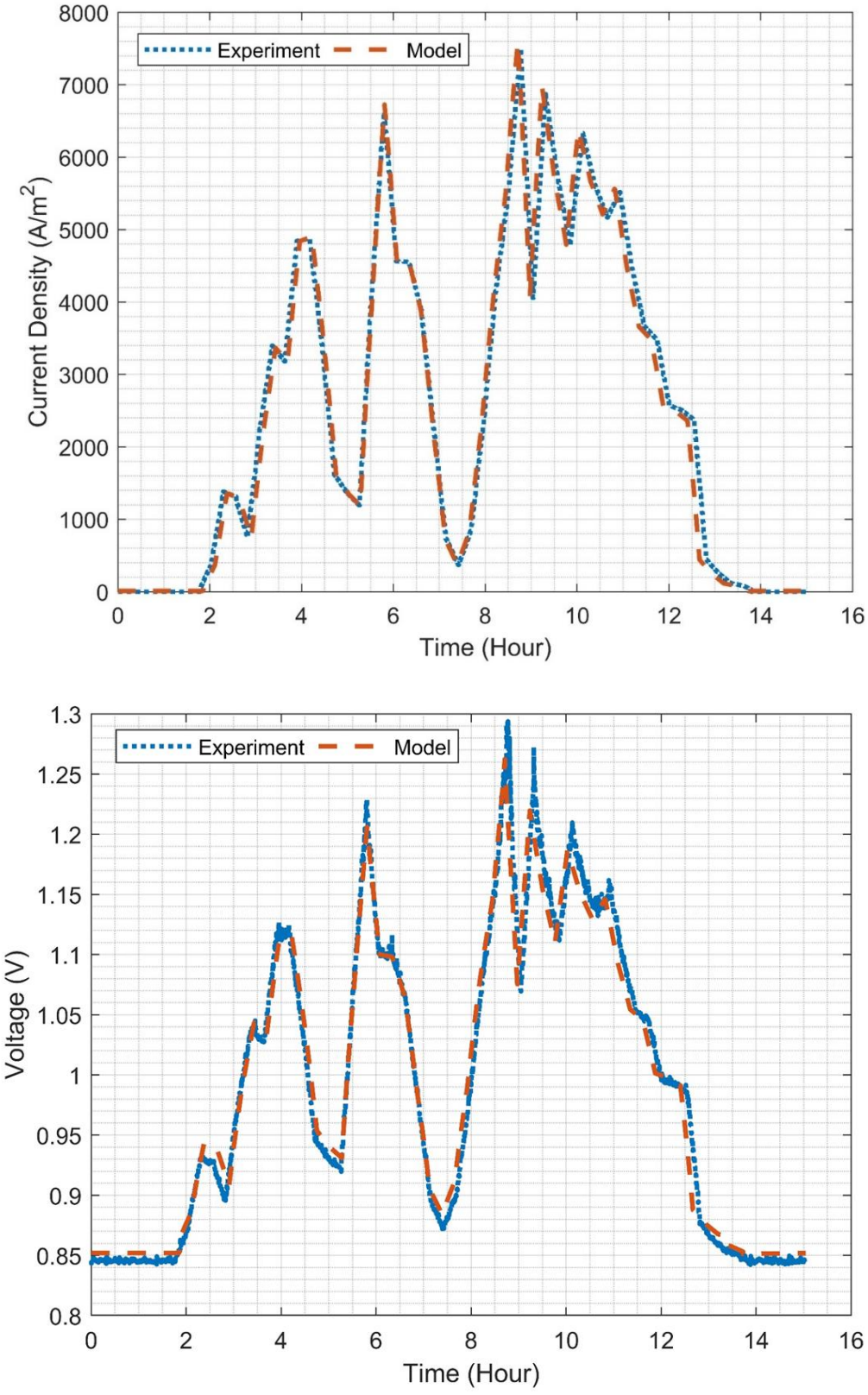

Figure 91: Dynamic response of test bench compared to model predictions for a cloudy day input solar PV profile.

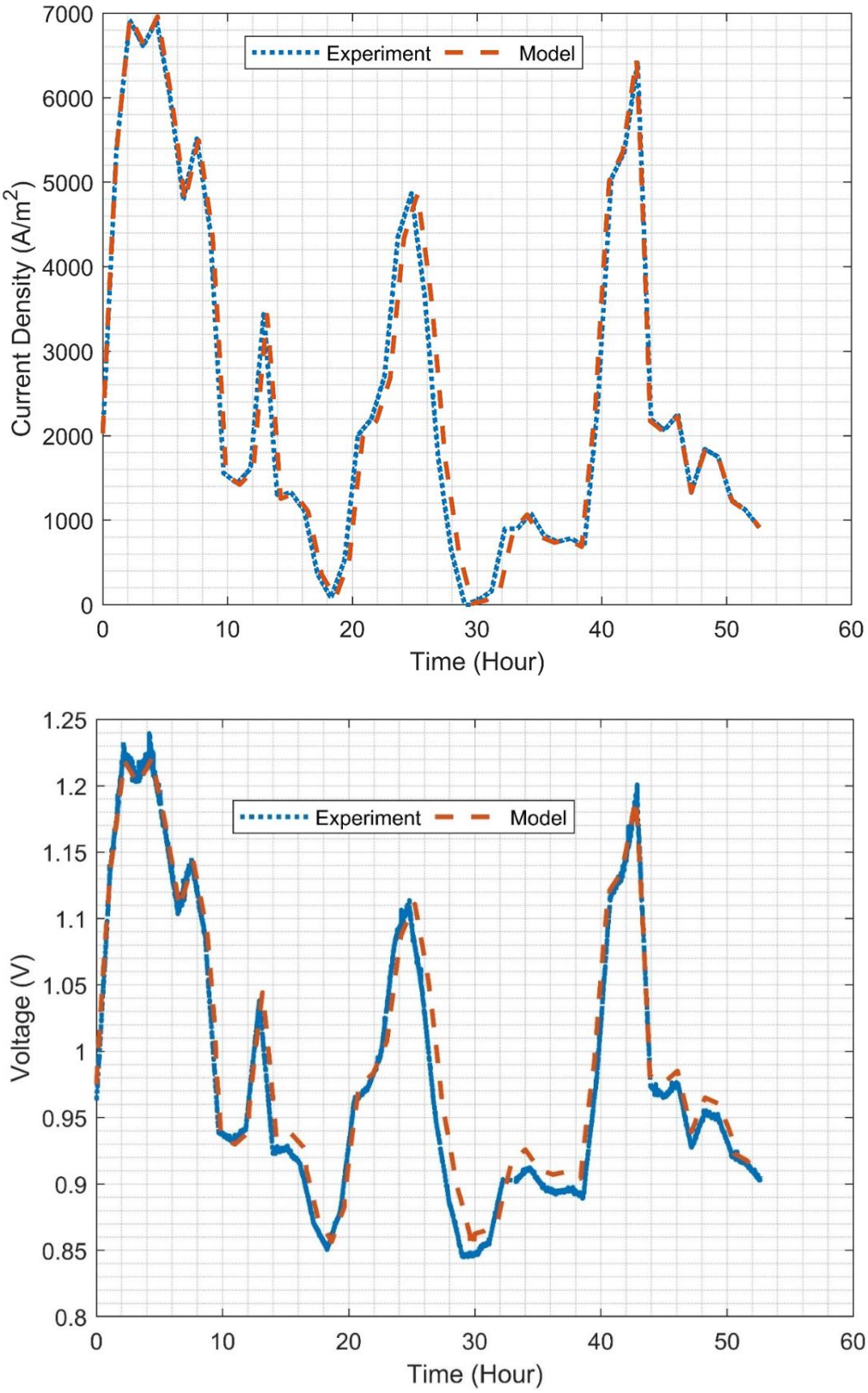

Figure 92: Dynamic response of test bench compared to model predictions for an input wind profile.

Figure 90 shows the input current given to the test bench and its voltage response as well as the current and voltage behavior of the developed model using the dynamic power of the test bench as an input power profile. As shown, the system can follow the transient PV solar profile and the developed model is able to follow the same trend as the real system. This consistency between the model and the experiment proves that the developed model considers all the different physical phenomena happing in the system.

Two other real dynamic profiles have been tested on the test bench and validated with the developed model. These two profiles include solar PV profile for a cloudy day and wind turbine profile (Figure 91 and Figure 92). According to the experimental and analytical results obtained from the discussed input profiles, SOEC systems can be integrated with highly dynamic renewable resources for long-term large-scale energy storage or for grid services.

It should be noted that all in all the dynamic results than have been shown so far, flow rates of both fuel and air were kept constant during the whole experiment. Experiments on SOEC systems can be performed in constant flow rates, constant fuel utilization, or based on lookup tables. One of the ways to get high efficiency is to keep fuel utilization constant. Running system at constant fuel utilization increase efficiency while adds instabilities to the system regarding preheating flows with variable flow rates to have flows at the stack inlet at desired temperature.

6.2.7 Durability Tests under Thermal Cycles

One of the common ways to evaluate the durability of solid oxide cells is to do thermal cycles. Thermal cycle is one of the main reasons of cell brake down and degradation. To do accelerated test, the furnace temperature varies between 700^{o}C and 800^{o}C with 100^{o}C/hour ramp-up and ramp-down rates. For the durability test, steam flow rate and hydrogen flow rate were kept constant at 142.47 gram/hour and 0.328 lit/min, respectively. These flow rates result in 90% steam and 10% hydrogen as the fuel electrode inlet composition. Air flow rate was also kept constant at 32 lit/min. The durability test was done at constant current density of 0.75 A/cm^2. In this current density state, steam utilization is 85%. 30 consecutive

thermal cycles have been executed on the furnace temperature. Figure 93 shows different temperatures during the thermal cycles. Figure 94 shows one cycle that the test bench went through. As you can see, all the furnace, air inlet and outlet, fuel inlet and outlet, and stack top and bottom temperatures have similar trends.

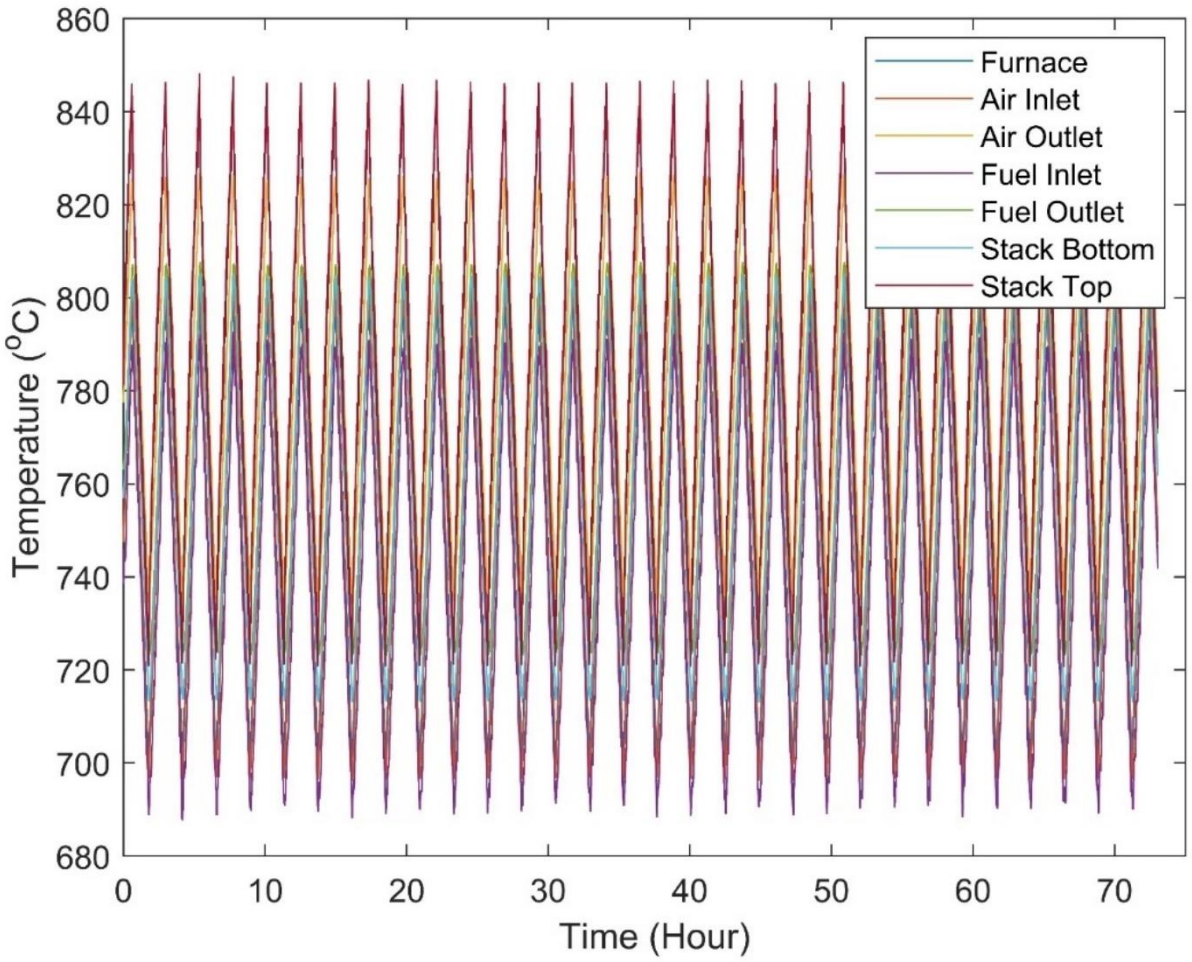

Figure 93: Temperature profiles during the durability test on the solid oxide test bench.

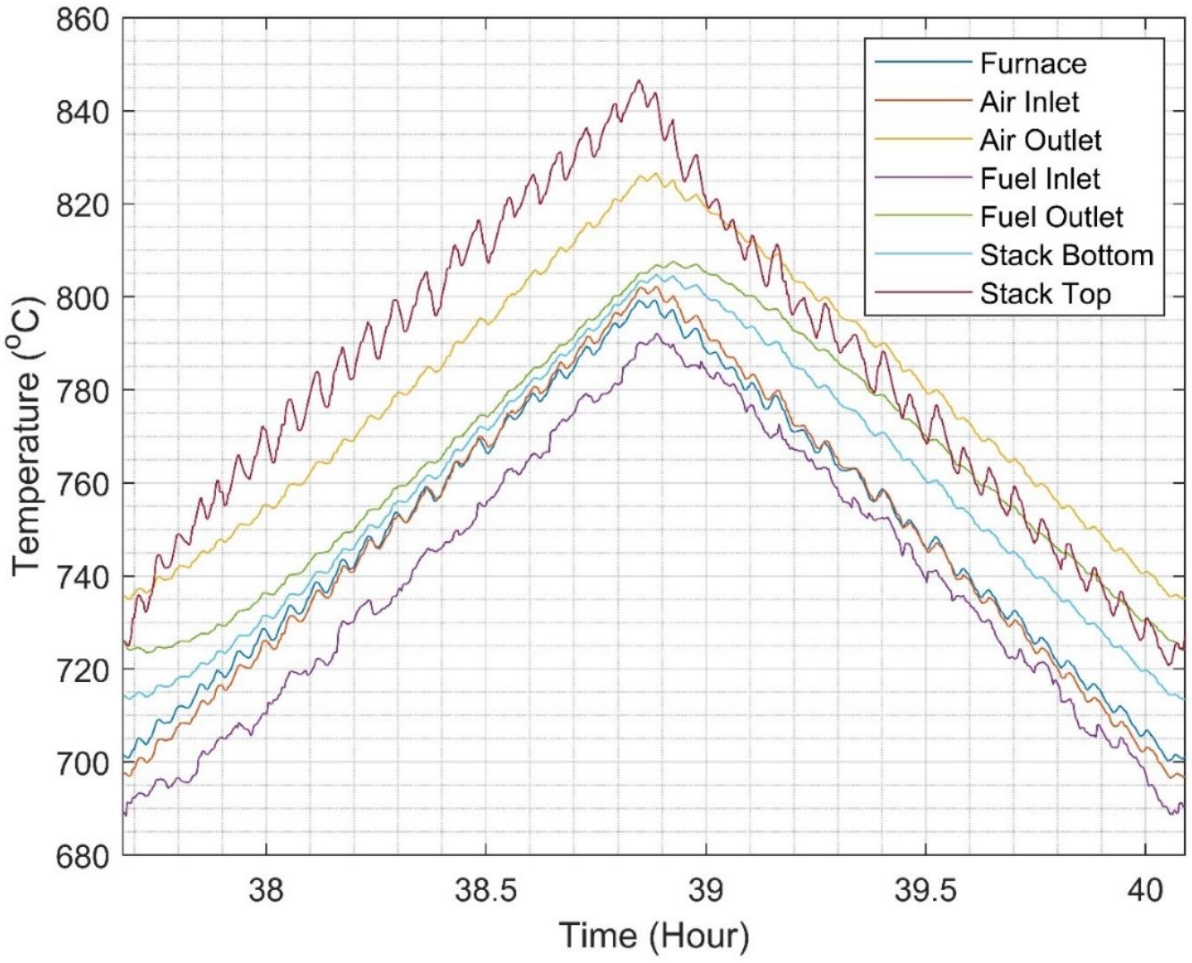

Figure 94: Temperature profiles during one cycle of the durability test on the solid oxide test bench.

Figure 95 shows the voltage change in one thermal cycle. According to this figure, during the thermal cycle, all the cells except cell number 5 cross thermoneutral voltage and switch from exothermic to endothermic and again to exothermic condition. Cell number 5 degraded more than other cells before the durability test. So, it showed different behavior compared to other cells and stayed at exothermic condition during the thermal cycle because of the higher overpotentials.

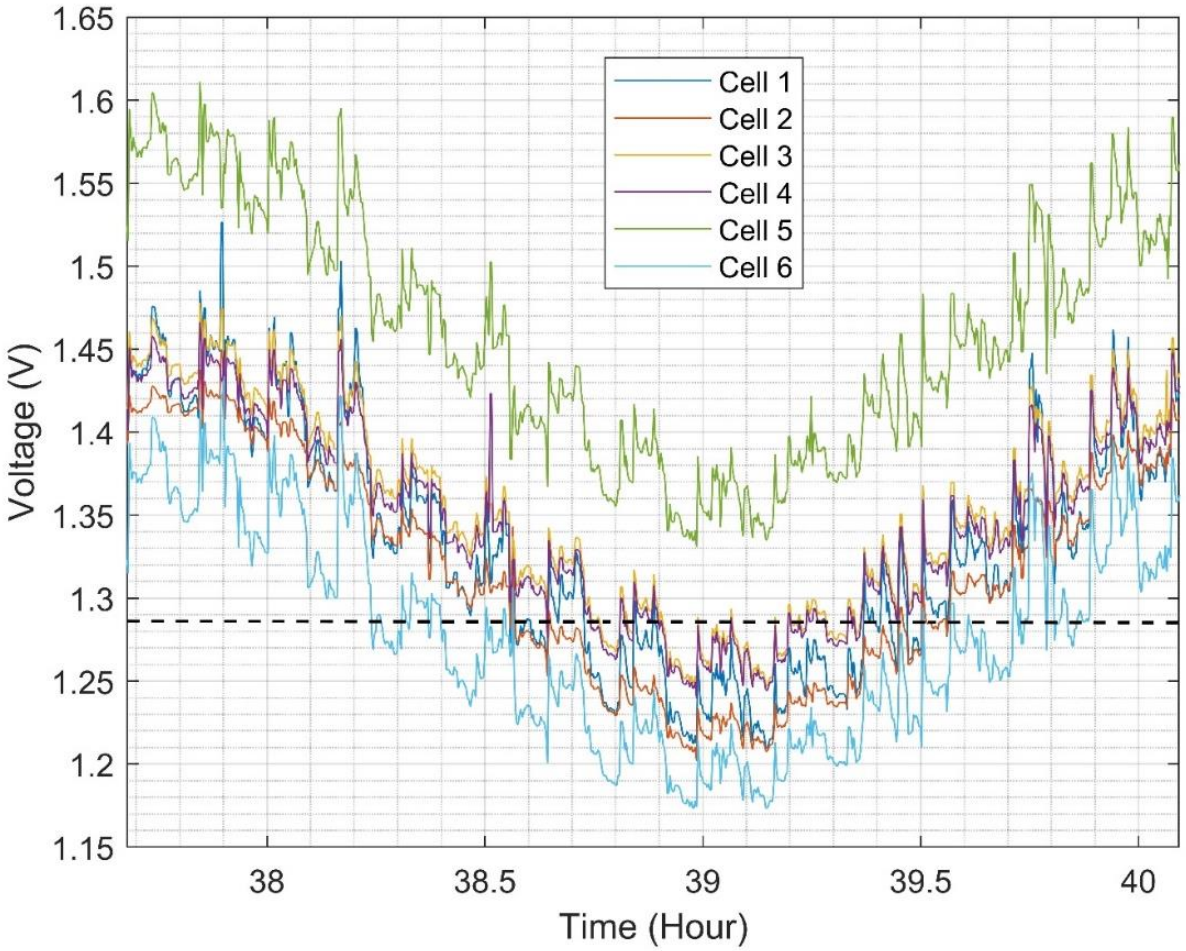

Figure 95: Voltage profiles during one cycle of the durability test on the solid oxide test bench.

To evaluate the voltage degradation of different cells during 30 thermal cycles of the durability test, the difference in the voltage before and after the durability test have been normalized with the actual voltage before the durability test to provide voltage degradation in percent. Figure 96 shows the voltage degradation percentage for all of the 6 cells. According to this figure, thermal cycles have a rather significant effect on degradation of all of the cells which proves the importance of thermal management.

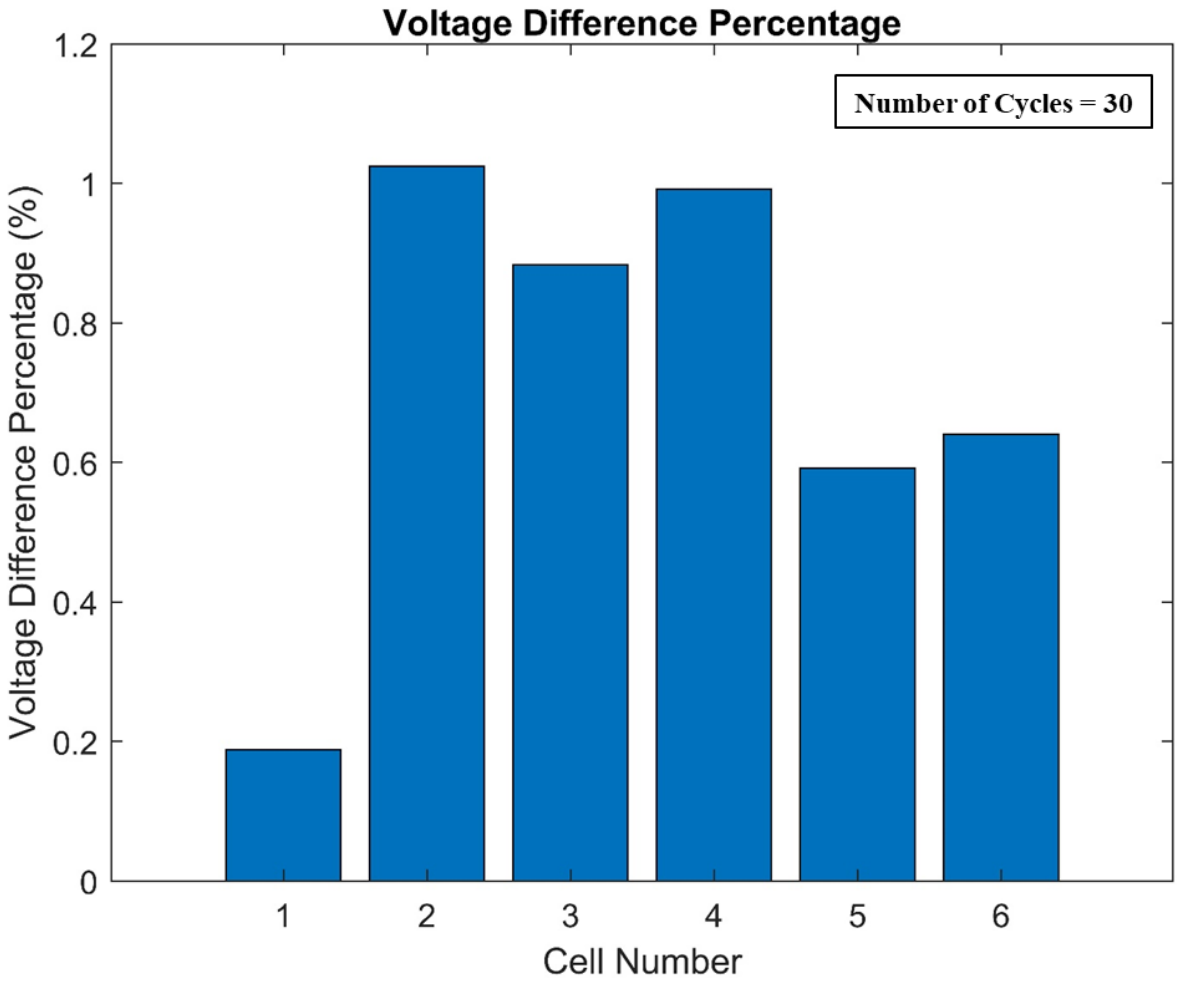

Figure 96: Voltage degradation percentage attributed to the thermal cycles imposed during the durability test.

6.2.8 Electrochemical Impedance Spectroscopy

While the V-j curve provides general quantification of fuel cell performance, a more sophisticated test is required to accurately differentiate between all the major sources of loss in a fuel cell. Electrochemical Impedance Spectroscopy (EIS) is an electrochemical technique to measure the impedance of a system in dependence of the Alternative Current (AC) frequency. EIS is a powerful non-destructive and in-operando electrochemical technique for studying electrode–electrolyte interfaces with applications in different fields such as fuel cells, electrolyzers and batteries. EIS providing useful information on transport properties, and contributions from each type of losses in SOFC operation. Within short testing times, EIS measurements provide reliable data, allowing for the prediction of the long-term

performance of different compartments. EIS measures complex electrical impedance as a function of frequency. This involves the phase sensitive measurement of current and voltage applied to a device under test while the measurement frequency is varied over the course of the measurement. Electrochemical impedance is usually measured by applying an AC potential/current (Potentiostatic/Galvanostatic) to an electrochemical cell and then measuring the current/voltage through the cell. The applied AC potential/current is a sinusoidal excitation. The response to this potential/current excitation is an AC current/potential excitation signal. Impedance is given by the ratio between a time-dependent voltage and a time-dependent current. A Nyquist diagram plots the real component of impedance versus the imaginary component of impedance (actually, the negative of the imaginary component of impedance) over a range of frequencies.

In this work, the effects of different operating conditions on the Nyquist plot are evaluated at both cell and stack level. In this study, all the EIS measurements have been done in fuel cell mode only due to issues associated with the water mass flow controller.

In the first set of EIS experiments, the cyclic EIS measurements have been performed on different cell to characterize the differences between cells' performance at the beginning of their lifetime. Figure 97 shows the V-j characterizations of all the cells which demonstrates consistent behavior among all the cells. This V-j curve has been done at 750^{o}C stack operating temperature and constant fuel flow rate with 50% volumetric hydrogen and 50% volumetric nitrogen, and constant air flow rate. It has been done at 10 different currents starting from zero with 1A step size. It shows a very small activation losses at very low current density followed by a linear behavior resulting from the ohmic losses. Figure 97 shows the Nyquist plot for all the cells that have been measured at 1A using the connected potentiostat under the galvanostatic mode. It should be noted that for each individual cell, 5 cycle EIS have been done to make sure the EIS measurements for each cell is statistically relevant. That is the reason why at each frequency for each cell, a cloud of points has been plotted. According to the Figure 97, all the cells show similar behavior including consistent ohmic loss and mass and charge transport losses. According to the obtained values on the x-axis, the ohmic area specific resistance for all the cells is around 0.3 $\Omega.\,cm^2$. The semi-circle that appears at low

frequencies is due to concentration losses along the cell of species involved in electrochemical reactions.

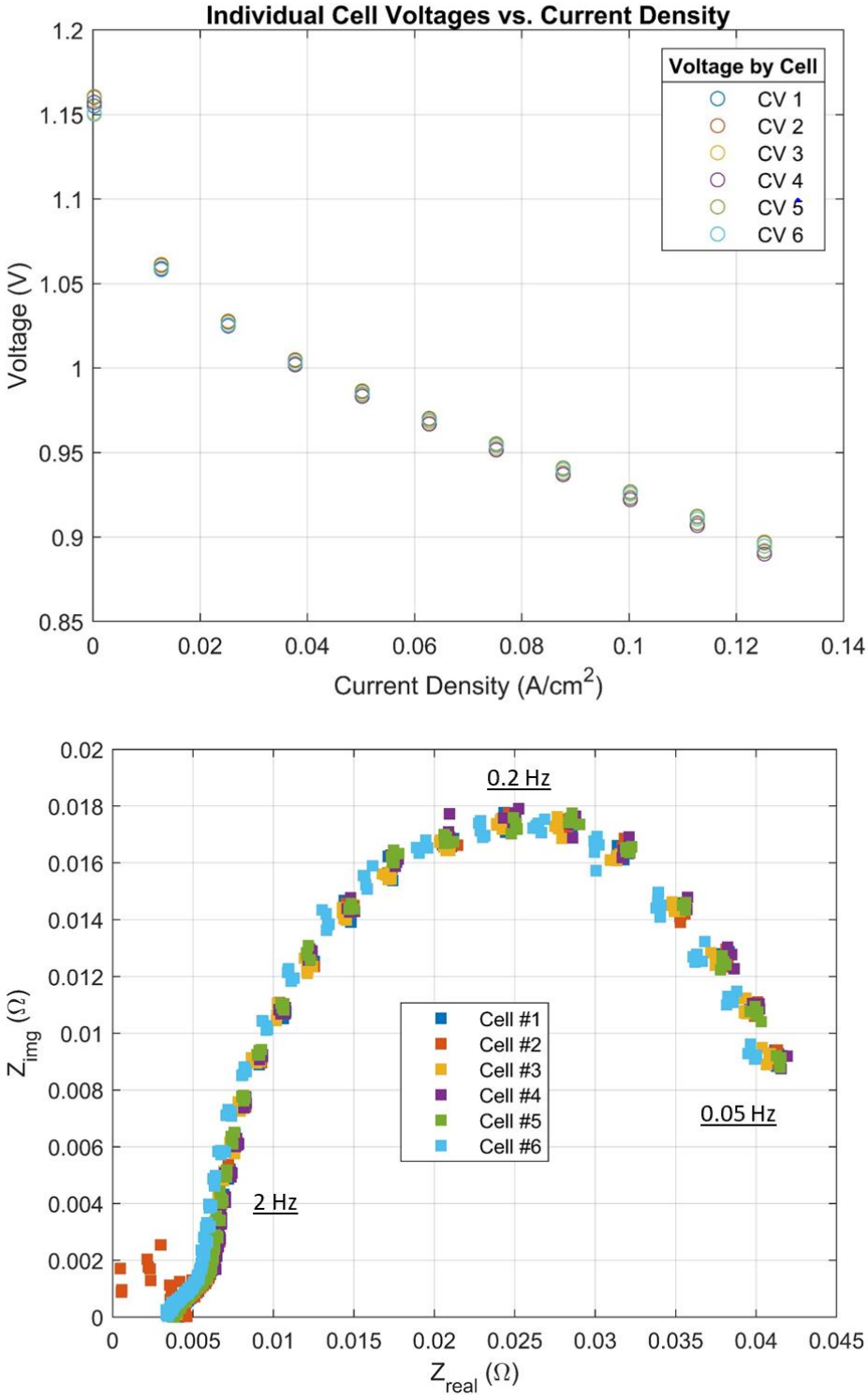

Figure 97: V-j characteristics curve and its associated cell-level EIS measurements.

It should be noted that all the EIS measurements in this study are done in a unique frequency window starting from 10^5 to 0.05 Hz.

The high frequency inductance observed for each of the single cell EIS results seems to be on the order of $1e^{-8}$ Henry, which is small and reasonable.

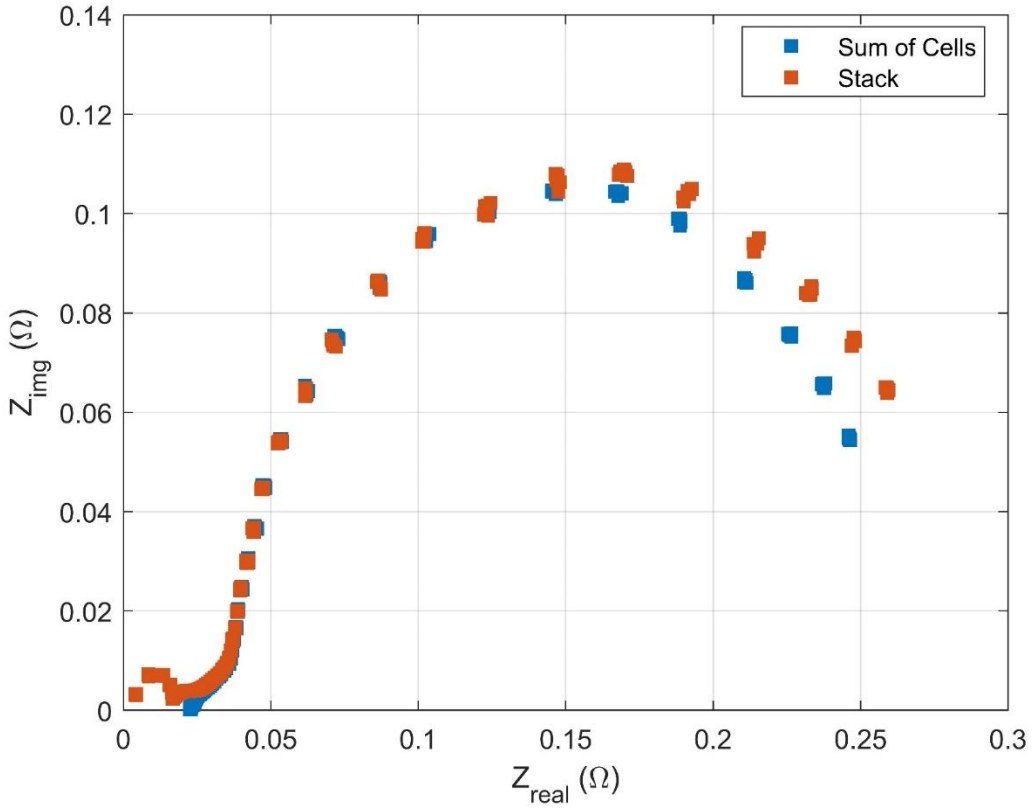

Figure 98: Stack-level and sum of the cell-level EIS measurements comparison.

The stack EIS is consistent with the sum of all 6 cells (Figure 98). The stack and summed cell results diverge on the high-frequency end, probably due to the inductance observed in individual cell EIS. Stack vs 6-cell sum EIS also diverge on the very low-frequency end. The sum of the cells EIS results show lower impedance compared to the stack EIS in this region, which could point toward an additional L//C//R (inductance, capacitance, resistance) element in the equivalent circuit for the stack (perhaps associated with the interconnects or end-plates).

In the second set of EIS measurements, the effects of operating current were evaluated on the EIS measurements of a single cell. This set of EIS measurements was performed at

operating conditions associated with the V-j characteristics curve that was shown in Figure 97. As it is shown in figure, the ohmic area specific resistance is 0.3 $\Omega.\,cm^2$ for all the operating current densities which is reasonable given the fact that it is associated with operating temperature which is constant at this set of the EIS measurements. The low frequency arch size varies significantly with operating current density (Figure 99). It decreases with increasing operating current to a certain point and increases afterwards. At 1A, the low frequency arch size is large (high impedance) due to low concentration of steam existing in the anode side. Since the operating current density is low, the molar fraction of the produced steam in the anode side is low which results in high impedance due to concentration losses. This low frequency large arch can be represented by the logarithm term in the Nernst equation. As operating current density increases, the molar fraction of the produced steam increases which results in lower low frequency impedance. The low frequency arch size decreases until the molar fraction of hydrogen gets to low amounts resulting from high operating current densities. In the case of high operating current density, the low frequency arch size gets bigger because of hydrogen concentration losses. The shifting current density for the explained case is between 6A to 10A.

In the third set of EIS measurements, the effects of operating temperature were investigated on the EIS measurements of a single cell. This set of EIS measurements was performed at two different fuel compositions including 50% hydrogen-50% nitrogen and 75% hydrogen-25% nitrogen as shown in Figure 100. As it clearly shown in Figure 100, for higher operating temperature, the ohmic loss is lower which is reasonable given the Arrhenius equation for ohmic losses. It should be noted that the ohmic resistance at different operating temperature is independent of the fuel inlet composition. The ohmic area specific resistance for 700^{o}C, 750 ^{o}C and 800 ^{o}C are 0.26 $\Omega.\,cm^2$, 0.3 $\Omega.\,cm^2$ and 0.4 $\Omega.\,cm^2$ respectively.

In the fourth set of EIS measurements, the effects of fuel inlet composition (anode side) were evaluated on the EIS measurements of a single cell. This set of EIS measurements was performed at two different operating temperature including 750 ^{o}C and 800 ^{o}C as shown in Figure 101.

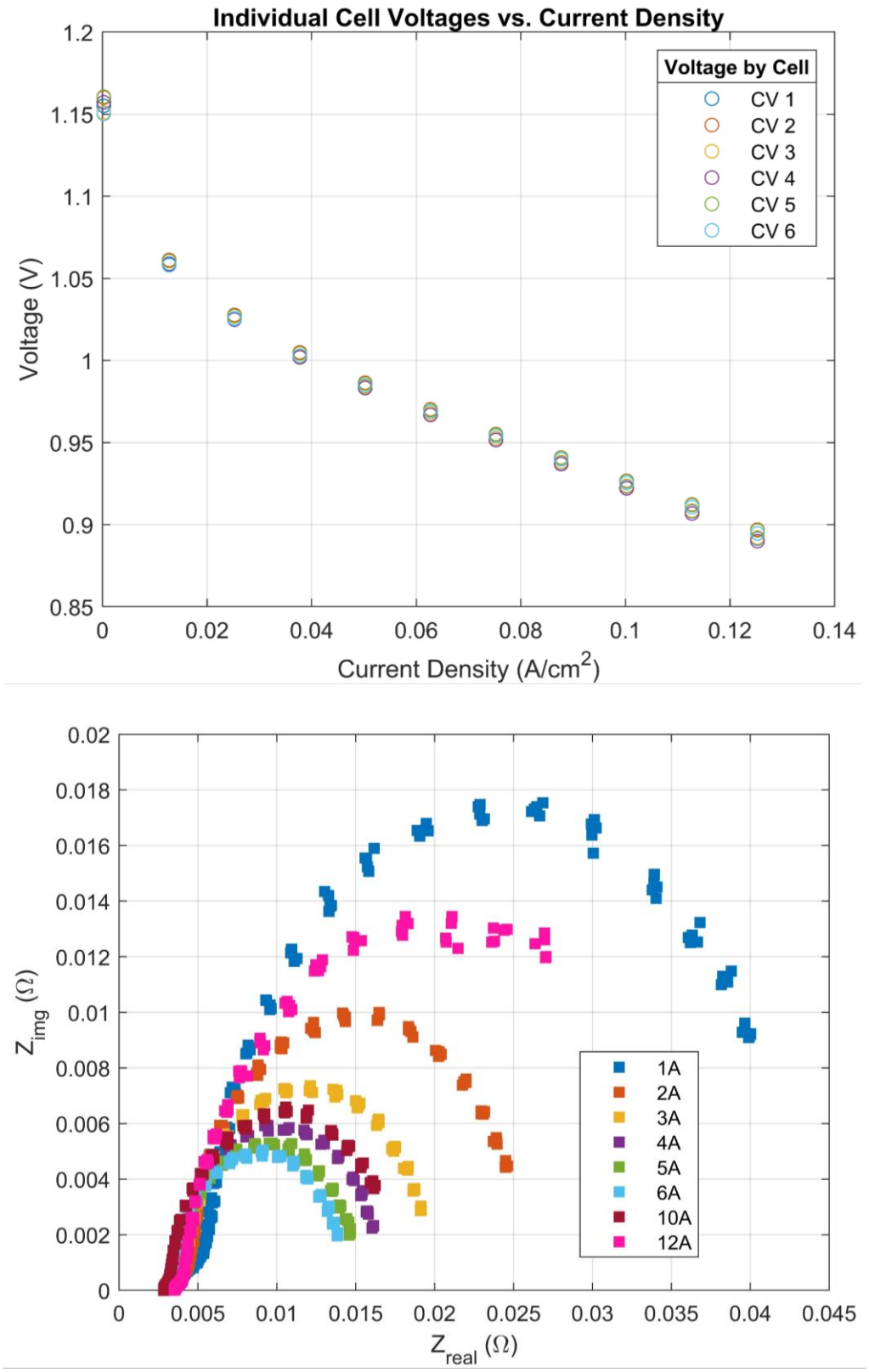

Figure 99: Effects of operating current density on the cell-level EIS measurements.

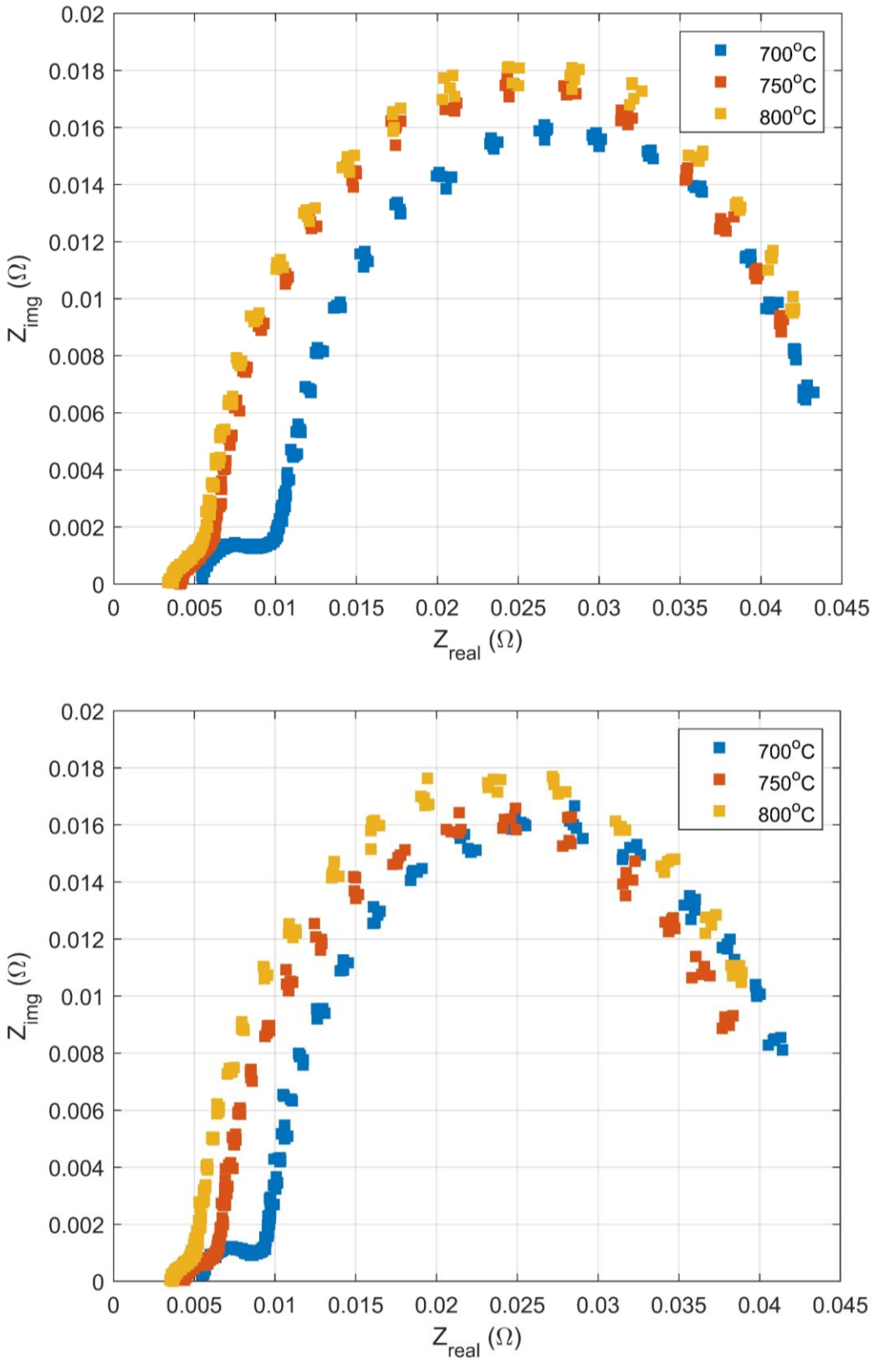

Figure 100: Effects of operating temperature on the cell-level EIS measurements.

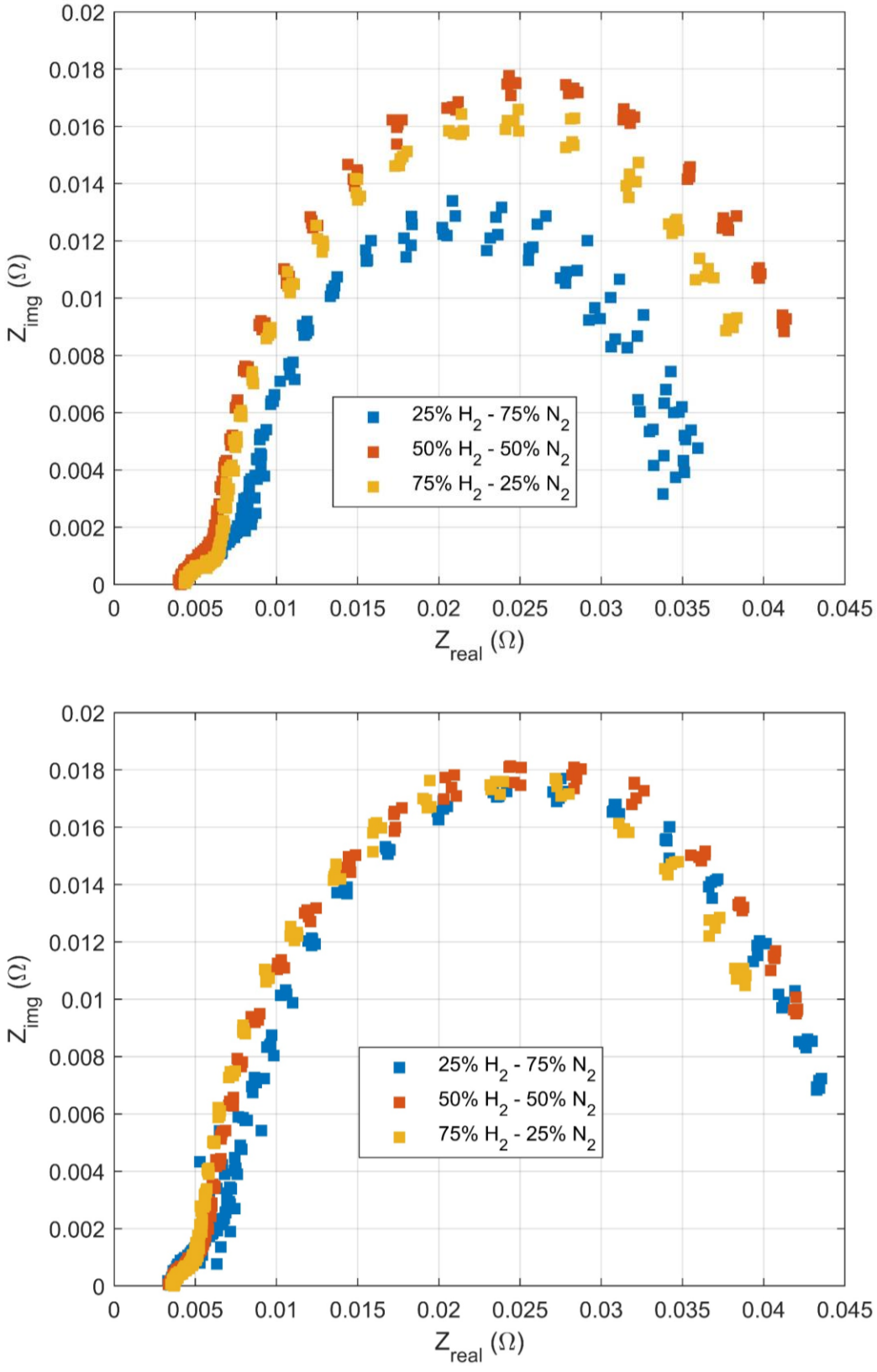

Figure 101: Effects of fuel inlet composition on the cell-level EIS measurements.

6.3 Summary

This chapter has focused on experimental investigation of solid oxide short stack operating in electrolysis mode. First, the effects of operating temperature and fuel inlet composition have been investigated regarding their impacts on the voltage-current characteristic curve. Then, the developed model in the previous chapter has been calibrated with one specific set of the obtained experimental data and validated with the remaining sets of the obtained experimental data without adjusting any model parameters. The modeled results have been consistent with the measured data for a variety of operating conditions. Second, the performance of the solid oxide short stack in the test bench has been evaluated under different dynamic input conditions e.g., step profile, solar profile, and wind profile. The calibrated model has accurately predicted different operating parameters at these dynamic conditions. Third, the solid oxide short stack has been put through durability test by thermally cycling the stack operating temperature. It has shown a considerable performance degradation after 30 full thermal cycles. Finally, the solid oxide short stack has been characterized in both cell and stack levels by electrochemical impedance spectroscopy technique. The effects of different operating conditions, i.e., temperature and fuel inlet composition as well as current density have been analyzed with electrochemical impedance spectroscopy on the Nyquist plot. The cell-level and stack-level EIS measurements have proved consistency in trend between cell and stack level EIS measurements while showing higher impedance for stack perhaps associated with the interconnects or end-plates. The ohmic area specific resistance for different temperatures, calculated based on the EIS measurements, have been consistent with the numbers reported in other studies.

7 Summary and Conclusions

7.1 Summary

The goal of this dissertation was to theoretically and experimentally develop and evaluate the advanced high-temperature solid oxide electrolysis cell (SOEC) system technology for widespread use with renewable energies. As it was shown, SOEC system can be dynamically dispatched to an electric grid or to microgrids (as a power-to-gas technology) to store inexpensive and/or otherwise curtailed renewable electricity in the form of hydrogen. Moreover, the advanced SOEC system can be integrated with renewable resources to produce a zero carbon and zero emissions fuel like hydrogen for difficult-to-electrify end-uses. The goal was accomplished by 1-conducting an extensive continuous literature review on SOEC technology in both modeling and experimental perspectives, 2-developing stack-level and system-level dynamic models and control strategies of the SOEC system that simulates physical operation of the SOEC system, 3-evaluating the dynamic operation of SOEC system in different input conditions, 4-performing theoretical analysis for integration of SOEC system into microgrids to support high renewable use, 5-developing the experimental setup to evaluate the steady state and dynamic performance characteristics of SOEC short stack and analyze experimental results and validating the developed model with different experimental results in both steady state and dynamic manners.

7.2 Conclusions

7.2.1 Solid Oxide Electrolysis System Design

The main conclusions of this section, which considered the solid oxide electrolysis system design, are as follows:

- A quasi 3D spatially and temporally resolved solid oxide electrolysis cell model was developed which was able to capture the spatial and temporal behavior of different operating parameters of the solid oxide electrolysis cell under steady-state and dynamic operation.

- A solid oxide electrolysis system and its required control strategies were advanced by developing and integrating dynamic models of different balance of plant components. The designed system could operate under endothermic, thermoneutral and exothermic modes of operation while maintaining operating conditions at the desired levels by manipulating variables within different control strategies.
- A comparative analysis of the SOEC system for a stepwise dynamic operation under two different thermal control strategies was performed by analyzing the overall system performance at different stack power loads. System simulation results showed that the PEN average temperature could be well maintained by both control strategies while operating dynamically. PEN average temperature was quite constant and invariant under the second control strategy while it varies considerably more under the first one. Operation under both control strategies, the PEN localized temperature gradient was always maintained below the maximum tolerable temperature gradient. The overall efficiency of the system was higher for the first control strategy compared to the second one while the temporal temperature variation of the PEN is lower for the second control strategy compared to the first one.

7.2.2 SOEC System Dynamic Operation

The main conclusions of this section, which focused on the dynamic operation of the SOEC system under different operating scenarios, are as follows:

- The dynamic behavior of a SOSE system without an external heat source which used transient PV generated power as an input to produce compressed (to 3 MPa) renewable hydrogen to be stored or injected directly into the natural gas network was evaluated under two different operating scenarios.
- The capability of the proposed SOSE system and its control strategies to operate dynamically to directly convert solar power to hydrogen for both sunny and cloudy days was proved.
- For the entire operating periods of both days, the stack temperature and temperature difference along the stack were maintained in a safe operating range.

- The 12.5 h operation of the SOSE system on a sunny day resulted in the production of 94 kg hydrogen by using an average of 46 kWh/kg of the produced hydrogen.
- The SOSE system operated 11 h on a cloudy day and produced 55 kg hydrogen at average system power consumption per kilogram of produced hydrogen of 48.4 kWh/kg.
- The temperature distribution and dynamics of temperature gradients (spatial and temporal) that the developed dynamic model has produced, will have a significant impact on degradation and other performance characteristics.

7.2.3 Integration of SOEC System into the UCI Microgrid to Support High Renewable Use

The main conclusions of this section, which focused on the integration of SOEC system into the UCI microgrid to support high renewable use, are as follows:

- The challenges of RES penetration have been investigated in the context of the University of California, Irvine campus microgrid, by simulating the existing power plant operation and examining the effects of increasing renewable installed capacity.
- The limits of the microgrid power plant were identified that would result in massive excess renewable electricity production, with no sensible increase in RES penetration in the campus electrical energy supply for renewable installed capacities higher than 15 MW, if no energy storage solution is implemented.
- The integration of a modular P2G system based on sequential dispatching of SOE systems into the campus microgrid was modelled to evaluate the annual hydrogen production potential and the capability of the system to successfully absorb excess electricity from the additional renewable installations. The minimum aggregated power capacity of 300 kW dispatched SOE systems required to store at least 80% of the annual excess electricity was considered in each scenario.
- Utilization of the produced renewable hydrogen blended with natural gas as a fuel in UCI microgrid gas turbine, as well as the use of hydrogen in the local fueling station was assessed.

- The results showed that feeding the gas turbine with a gas mixture containing 15% volumetric hydrogen would suffice to consume all the hydrogen produced up to the scenario with 32 MW of PV installed capacity. Moreover, the entire renewable hydrogen production in all the PV capacity scenarios could be consumed on site considering both the feeding of the gas turbine with a gas mixture containing 15% by volume hydrogen and the delivery of hydrogen to fuel cell vehicles in the local fueling station.
- The integration of SOEC system into the UCI microgrid would allow an increased share of renewable energy supply to the campus and accelerate decarbonization of the transportation sector of surrounding areas.
- The deployment in the microgrid infrastructure of the additional PV capacity and the integration of the P2G system could reduce both natural gas consumption and carbon dioxide emissions. Up to 4250 metric tons (16%) of natural gas consumption and 11,900 tons (16%) of CO_2 emissions could be avoided.

7.2.4 Experimental Analysis of Solid Oxide Short Stack

The main conclusions of this section, which focused on the experimental analysis of the solid oxide short stack, are as follows:

- The solid oxide short stack test bench manufacture by SOLIDpower and its required electrical, mechanical, and fluid/gas connections were successfully set up.
- The solid oxide test bench was able to be operated at either electrolysis mode or fuel cell mode.
- The effects of stack operating temperature and fuel inlet composition were investigated. The developed model was calibrated and validated with the experimental data on V-j characteristics curves.
- The dynamic operability of the SOEC system under various input powers e.g., step profile, PV sunny and cloudy profiles, and wind profile were evaluated. The dynamic calibrated model was validated by the experimental dynamic performance characteristics data.

- The durability of the solid oxide short stack was evaluated by putting the stack under thermal cycles. The results proved that long-term large-amplitude temperature variations will cause considerable performance degradation on the solid oxide stack.
- A potentiostat, a booster, and their connections were set up with the solid oxide short stack test bench to enable a non-destructive and in-operando electrochemical characteristics measurements in both cell and stack levels to complete the V-j characteristics measurements.
- The consistency between the EIS measurements on the cell level and stack level was examined by doing EIS on all the cells and the stack and comparing the sum of the cells' EIS measurements with the stack-level EIS measurements. The results show a good consistency over a big range of frequencies except very low frequencies.
- The effects of the operating current density, operating temperature, and fuel inlet composition on the Nyquist plot were investigated.

7.3 Future Work

7.3.1 Integration of SOEC System into the UCI Microgrid to Support High Renewable Use

In this dissertation the integration of the SOEC system together with batteries to minimize the capital costs and the operating costs was not considered. The objective function could be defined as the total costs of the installed PV, SOEC systems, storage, batteries, and inverters to find the financially optimal mix of different dispatchable storage systems for different PV installed scenarios.

7.3.2 Experimental Analysis of Solid Oxide Short Stack

In this dissertation the effects of different operating parameters on the steam/carbon dioxide co-electrolysis were not evaluated. Dynamic operation of the short stack on steam/carbon dioxide co-electrolysis mode could also be analyzed. Also, a gas chromatography analyzer could be used to analyze the concentration of different species produced from co-electrolysis of steam and carbon dioxide at different operating condition. The solid oxide test bench could also be tested under reversible operation by switching

between fuel cell and electrolysis modes. EIS measurements could be done on steam electrolysis and steam/carbon dioxide co-electrolysis to characterize the cell at different operating modes. Developing equivalent circuit model based upon EIS measurements could be useful to characterize and compare single cell level and stack level behaviors. This would characterize the effect of all compartments i.e., interconnects in the stack level performance. A machine learning and deep learning model could be developed based on degradation data of the short stack to be able to predict effects of different parameters on the degradation of the stack.

References

[1] The World Bank. Population estimates and projections | DataBank n.d.

[2] Bouman EA, Lindstad E, Rialland AI, Strømman AH. State-of-the-art technologies, measures, and potential for reducing GHG emissions from shipping – A review. Transp Res Part D Transp Environ 2017;52:408–21. doi:10.1016/j.trd.2017.03.022.

[3] Marcilio GP, Rangel JJ de A, Souza CLM de, Shimoda E, Silva FF da, Peixoto TA. Analysis of greenhouse gas emissions in the road freight transportation using simulation. J Clean Prod 2018;170:298–309. doi:10.1016/j.jclepro.2017.09.171.

[4] Saleem H, Jiandong W, Zaman K, Elsherbini Elashkar E, Mohamd Shoukry A. The impact of air-railways transportation, energy demand, bilateral aid flows, and population density on environmental degradation: Evidence from a panel of next-11 countries. Transp Res Part D Transp Environ 2018;62:152–68. doi:10.1016/j.trd.2018.02.016.

[5] Rashid Khan HU, Siddique M, Zaman K, Yousaf SU, Shoukry AM, Gani S, et al. The impact of air transportation, railways transportation, and port container traffic on energy demand, customs duty, and economic growth: Evidence from a panel of low-, middle-, and high - income countries. J Air Transp Manag 2018;70:18–35. doi:10.1016/j.jairtraman.2018.04.013.

[6] Llorca C, Molloy J, Ji J, Moeckel R. Estimation of a Long-Distance Travel Demand Model using Trip Surveys, Location-Based Big Data, and Trip Planning Services. Transp Res Rec J Transp Res Board 2018:036119811877706. doi:10.1177/0361198118777064.

[7] Wang Q, Li S, Li R. Forecasting Energy Demand in China and India: Using Single-linear, Hybrid-linear, and Non-linear Time Series Forecast Techniques. Energy 2018;161:821–31. doi:10.1016/J.ENERGY.2018.07.168.

[8] Bayomi N, Fernandez JE. Trends of energy demand in the Middle East: A sectoral level analysis. Int J Energy Res 2018;42:731–53. doi:10.1002/er.3861.

[9] Verhoef LA, Budde BW, Chockalingam C, García B, Wijk AJM Van. The e ff ect of additive manufacturing on global energy demand : An assessment using a bottom-up approach. Elsevier 2018;112:349–60. doi:10.1016/j.enpol.2017.10.034.

[10] Riva F, Tognollo A, Gardumi F, Colombo E. Long-term energy planning and demand forecast in remote areas of developing countries : Classi fi cation of case studies and insights from a modelling perspective. Energy Strateg Rev 2018;20:71–89. doi:10.1016/j.esr.2018.02.006.

[11] Mondal MAH, Bryan E, Ringler C, Mekonnen D, Rosegrant M. Ethiopian energy status and demand scenarios: Prospects to improve energy efficiency and mitigate GHG emissions. Energy 2018;149:161–72. doi:10.1016/j.energy.2018.02.067.

[12] Mason K, Duggan J, Howley E. Forecasting energy demand, wind generation and carbon dioxide emissions in Ireland using evolutionary neural networks. Energy 2018;155:705–20. doi:10.1016/j.energy.2018.04.192.

[13] Annual Energy Outlook 2017 with Projections to 2050. US Energy Inf Adm 2017.

[14] Annual Energy Outlook 2018 with Projections to 2050. US Energy Inf Adm 2018.

[15] Smil V. Energy and civilization: A history. 2017. doi:10.7551/mitpress/9780262035774.001.0001.

[16] Bock C. Forecasting energy demand by clustering smart metering time series. Commun. Comput. Inf. Sci., vol. 853, 2018, p. 431–42. doi:10.1007/978-3-319-91473-2_37.

[17] Wang X, Luo D, Zhao X, Sun Z. Estimates of energy consumption in China using a self-adaptive multi-verse optimizer-based support vector machine with rolling cross-validation. Energy 2018;152:539–48. doi:10.1016/j.energy.2018.03.120.

[18] Energy Information Administration U, Capuano L. International Energy Outlook 2018 (IEO2018). 2018.

[19] BP. Statistical Review of World Energy 2018 2018:1–53.

[20] Assareh E, Nedaei M. A metaheuristic approach to forecast the global carbon dioxide emissions. Int J Environ Stud 2018;75:99–120. doi:10.1080/00207233.2017.1374075.

[21] OECD/IEA. Global Energy & CO2 Status Report. 2018.

[22] Inventory-Us-Greenhouse-Gas-Emissions-and-Sinks @ Www.Epa.Gov n.d.

[23] Saeedmanesh A, Mac Kinnon MA, Brouwer J. Hydrogen is essential for sustainability. Curr Opin Electrochem 2018;12. doi:10.1016/j.coelec.2018.11.009.

[24] Burke MJ, Stephens JC. Political power and renewable energy futures: A critical review.

Energy Res Soc Sci 2018;35:78–93. doi:10.1016/j.erss.2017.10.018.

[25] Wagh MM, Kulkarni V V. Modeling and Optimization of Integration of Renewable Energy Resources (RER) for Minimum Energy Cost, Minimum CO2Emissions and Sustainable Development, in Recent Years: A Review. Mater Today Proc 2018;5:11–21. doi:10.1016/j.matpr.2017.11.047.

[26] Horst D, Jentsch M, Pfennig M, Mitra I, Bofinger S. Impact of renewable energies on the indian power system: Energy meteorological influences and case study of eefects on existing power fleet for rajasthan state. Energy Policy 2018;122:486–98. doi:10.1016/j.enpol.2018.07.047.

[27] Müsgens F. Equilibrium prices and investment in electricity systems with CO2-emission trading and high shares of renewable energies. Energy Econ 2018;In press. doi:10.1016/j.eneco.2018.07.028.

[28] Gómez Muñoz CQ, García Márquez FP. Future Maintenance Management in Renewable Energies. Renew. Energies, Cham: Springer International Publishing; 2018, p. 149–59. doi:10.1007/978-3-319-45364-4_10.

[29] Hoang T-H-V, Hussain Shahzad SJ, Shahbaz M, Jammazi R. Renewable Energies and Industrial Production in the USA: Does the Energy Source Matter? 2018. doi:10.2139/ssrn.3180692.

[30] Wu T, Xu D-L, Yang J-B. Multiple Criteria Performance Modelling and Impact Assessment of Renewable Energy Systems—A Literature Review. Renew. Energies, Cham: Springer International Publishing; 2018, p. 1–15. doi:10.1007/978-3-319-45364-4_1.

[31] Bosch S, Rathmann J. Deployment of Renewable Energies in Germany: Spatial Principles and their Practical Implications Based on a GIS-Tool. Adv Geosci 2018;45:115–23. doi:10.5194/adgeo-45-115-2018.

[32] Gómez-Calvet R, Martínez-Duart JM, Serrano Calle S. Present state and perspectives of variable renewable energies in Spain. Eur Phys J Plus 2018;133:126. doi:10.1140/epjp/i2018-11960-9.

[33] Konstantin P, Konstantin M. Power Generation from Renewable Energies. Power Supply Ind., Cham: Springer International Publishing; 2018, p. 89–136. doi:10.1007/978-3-319-72305-1_5.

[34] Hache E. Do renewable energies improve energy security in the long run? Int Econ 2017:1–9.

doi:10.1016/j.inteco.2018.01.005.

[35] Zong H, Cao Y, Liu Z. Energy security in Group of Seven (G7): a quantitative approach for renewable energy policy. Energy Sources, Part B Econ Plan Policy 2018;13:173–5. doi:10.1080/15567249.2017.1422053.

[36] Mkattiri S, Saad A. Analysis of the impact of the integration of renewable energies on HTA distribution networks in Morocco. 2018 19th IEEE Mediterr. Electrotech. Conf., 2018, p. 1–6. doi:10.1109/MELCON.2018.8379058.

[37] Inglesi-Lotz R, Dogan E. The role of renewable versus non-renewable energy to the level of CO2emissions a panel analysis of sub- Saharan Africa's Big 10 electricity generators. Renew Energy 2018;123:36–43. doi:10.1016/j.renene.2018.02.041.

[38] Lucas H, Pinnington S, Cabeza LF. Education and training gaps in the renewable energy sector. Sol Energy 2018;173:449–55. doi:10.1016/j.solener.2018.07.061.

[39] Maennel A, Kim H-G. Comparison of Greenhouse Gas Reduction Potential through Renewable Energy Transition in South Korea and Germany. Energies 2018;11:206. doi:10.3390/en11010206.

[40] Harrouz A, Temmam A, Abbes M. Renewable Energy in Algeria and Energy Management Systems. Int J Smart Grids 2018;2:34–9.

[41] Perea-Moreno M-A, Hernandez-Escobedo Q, Perea-Moreno A-J. Renewable Energy in Urban Areas: Worldwide Research Trends. Energies 2018;11:577. doi:10.3390/en11030577.

[42] Streicher W. Energy Efficiency and Renewable Energy: the key factors for a sustainable future. Renew Energy Sustain Dev 2018;4:1. doi:10.21622/resd.2018.04.1.001.

[43] Hentschel M, Ketter W, Collins J. Renewable energy cooperatives: Facilitating the energy transition at the Port of Rotterdam. Energy Policy 2018;121:61–9. doi:10.1016/j.enpol.2018.06.014.

[44] Nasirov S, Agostini C, Silva C, Caceres G. Renewable energy transition: a market-driven solution for the energy and environmental concerns in Chile. Clean Technol Environ Policy 2018;20:3–12. doi:10.1007/s10098-017-1434-x.

[45] Vezzoli C, Ceschin F, Osanjo L, M'Rithaa MK, Moalosi R, Nakazibwe V, et al. Distributed/Decentralised Renewable Energy Systems. Des. Sustain. Energy All, Springer;

2018, p. 23–39. doi:10.1007/978-3-319-70223-0_2.

[46] Gupta JG, De S, Gautam A, Dhar A. Introduction to Sustainable Energy , Transportation Technologies , and Policy. Energy, Environ Sustain 2018:3–7. doi:10.1007/978-981-10-7509-4_1.

[47] Geels FW, Schwanen T, Sorrell S, Jenkins K, Sovacool BK. Reducing energy demand through low carbon innovation: A sociotechnical transitions perspective and thirteen research debates. Energy Res Soc Sci 2018;40:23–35. doi:10.1016/J.ERSS.2017.11.003.

[48] Sadiqa A, Gulagi A, Breyer C. Energy transition roadmap towards 100 % renewable energy and role of storage technologies for Pakistan by 2050 Energy transition roadmap towards 100 % renewable energy and role of storage technologies for Pakistan by 2050. Energy 2018;147:518–33. doi:10.1016/j.energy.2018.01.027.

[49] Kåberger T. Progress of renewable electricity replacing fossil fuels. Glob Energy Interconnect 2018;1:48–52.

[50] Ehsan A, Yang Q. Optimal integration and planning of renewable distributed generation in the power distribution networks: A review of analytical techniques. Appl Energy 2018;210:44–59. doi:10.1016/j.apenergy.2017.10.106.

[51] Dincer I, Acar C. Smart energy systems for a sustainable future. Appl Energy 2017;194:225–35. doi:10.1016/j.apenergy.2016.12.058.

[52] Dincer I. Potential energy solutions for better sustainability. Exergetic, Energ Environ Dimens 2018:3–37. doi:10.1016/b978-0-12-813734-5.00001-9.

[53] Victor DG, Abdulla A, Auston D, Brase W, Brouwer J, Brown K, et al. Turning Paris into reality at the University of California. Nat Clim Chang 2018;8:183–5. doi:10.1038/s41558-018-0103-3.

[54] Hernández-Escobedo Q, Perea-Moreno A-J, Manzano-Aguliaro F. Wind energy research in Mexico. Renew Energy 2018;123:719–29. doi:10.1016/j.renene.2018.02.101.

[55] Rodríguez-Urrego D, Rodríguez-Urrego L. Photovoltaic energy in Colombia: Current status, inventory, policies and future prospects. Renew Sustain Energy Rev 2018;92:160–70. doi:10.1016/j.rser.2018.04.065.

[56] Kaushika ND, Mishra A, Rai AK. Solar PV System Economics. Sol. Photovoltaics, Cham:

Springer International Publishing; 2018, p. 143–54. doi:10.1007/978-3-319-72404-1_13.

[57] Honrubia-escribano A, Ramirez FJ, Gómez-lázaro E, Garcia-villaverde PM, Ruiz-ortega MJ, Parra-requena G. In fl uence of solar technology in the economic performance of PV power plants in Europe . A comprehensive analysis. Renew Sustain Energy Rev 2018;82:488–501. doi:10.1016/j.rser.2017.09.061.

[58] Stein G, Letcher TM. Integration of PV Generated Electricity into National Grids. A Compr. Guid. to Sol. Energy Syst., Elsevier; 2018, p. 321–32. doi:10.1016/b978-0-12-811479-7.00015-4.

[59] Hyder F, Sudhakar K. Solar PV tree design : A review Solar PV tree design : A review. Renew Sustain Energy Rev 2018;82:1079–96. doi:10.1016/j.rser.2017.09.025.

[60] Zhou Z, Carbajales-Dale M. Assessing the photovoltaic technology landscape: Efficiency and energy return on investment (EROI). Energy Environ Sci 2018;11:603–8. doi:10.1039/c7ee01806a.

[61] Dobrotkova Z, Surana K, Audinet P. The price of solar energy: Comparing competitive auctions for utility-scale solar PV in developing countries. Energy Policy 2018;118:133–48. doi:10.1016/j.enpol.2018.03.036.

[62] Kabir E, Kumar P, Kumar S, Adelodun AA, Kim K-HH. Solar energy: Potential and future prospects. 29 2018;82:894–900. doi:10.1016/j.rser.2017.09.094.

[63] Kaushika ND, Mishra A, Rai AK. Introduction to Solar Photovoltaic Power. Sol. Photovoltaics, Springer; 2018, p. 1–14. doi:10.1007/978-3-319-72404-1_1.

[64] Colmenar-Santos A, Perera-Perez J, Borge-Diez D, Depalacio-Rodríguez C. Offshore wind energy: A review of the current status, challenges and future development in Spain. Renew Sustain Energy Rev 2016;64:1–18. doi:10.1016/j.rser.2016.05.087.

[65] Oh K-Y, Nam W, Ryu MS, Kim J-Y, Epureanu BI. A review of foundations of offshore wind energy convertors: Current status and future perspectives. Renew Sustain Energy Rev 2018;88:16–36. doi:10.1016/j.rser.2018.02.005.

[66] Jamieson P. Innovation in wind turbine design. John Wiley & Sons; 2018. doi:10.1002/9781119975441.

[67] Serri L, Lembo E, Airoldi D, Gelli C, Beccarello M. Wind energy plants repowering potential in

Italy: technical-economic assessment. Renew Energy 2018;115:382–90. doi:10.1016/j.renene.2017.08.031.

[68] Zappa W, van den Broek M. Analysing the potential of integrating wind and solar power in Europe using spatial optimisation under various scenarios. Renew Sustain Energy Rev 2018;94:1192–216. doi:10.1016/j.rser.2018.05.071.

[69] Nurunnabi M, Roy NK, Mahmud MA. Investigating the environmental and socioeconomic impacts of grid-tied photovoltaic and on-shore wind systems in Bangladesh. IET Renew Power Gener 2018;12. doi:10.1049/iet-rpg.2017.0751.

[70] International Renewable Energy Agency (IRENA). Renewable Power Generation Costs in 2017. 2018.

[71] Zhou S, Wang Y, Zhou Y, Clarke LE, Edmonds JA. Roles of wind and solar energy in China's power sector: Implications of intermittency constraints. Appl Energy 2018;213:22–30. doi:10.1016/j.apenergy.2018.01.025.

[72] Gotzens F, Heinrichs H, Hake JF, Allelein HJ. The influence of continued reductions in renewable energy cost on the European electricity system. Energy Strateg Rev 2018;21:71–81. doi:10.1016/j.esr.2018.04.007.

[73] Renewables 2017. IEA 2017.

[74] Commission CE. California Energy Commission – Tracking Progress Energy Efficiency California Energy Commission – Tracking Progress 2017:1–21.

[75] Jiang Y, Xu J, Sun Y, Wei C, Wang J, Liao S, et al. Coordinated operation of gas-electricity integrated distribution system with multi-CCHP and distributed renewable energy sources. Appl Energy 2018;211:237–48. doi:10.1016/j.apenergy.2017.10.128.

[76] Fang J, Zeng Q, Ai X, Chen Z, Wen J. Dynamic optimal energy flow in the integrated natural gas and electrical power systems. IEEE Trans Sustain Energy 2018;9:188–98. doi:10.1109/TSTE.2017.2717600.

[77] Koraki D, Strunz K. Wind and solar power integration in electricity markets and distribution networks through service-centric virtual power plants. IEEE Trans Power Syst 2018;33:473–85. doi:10.1109/TPWRS.2017.2710481.

[78] Notton G, Nivet ML, Voyant C, Paoli C, Darras C, Motte F, et al. Intermittent and stochastic

character of renewable energy sources: Consequences, cost of intermittence and benefit of forecasting. Renew Sustain Energy Rev 2018;87:96–105. doi:10.1016/j.rser.2018.02.007.

[79] Addo K, Cakir B, Bolado-lavin R, Dijkema GPJ. SAInt – A novel quasi-dynamic model for assessing security of supply in coupled gas and electricity transmission networks. Appl Energy 2017;203:829–57. doi:10.1016/j.apenergy.2017.05.142.

[80] Zlotnik A V, Rudkevich AM, Carter R, ... Grid Architecture At the Gas-Electric Interface. Los Alamos Natl … 2017.

[81] Lewandowska-Bernat A, Desideri U. Opportunities of Power-to-Gas technology. Energy Procedia 2017;105:4569–74. doi:10.1016/j.egypro.2017.03.982.

[82] McPherson M, Harvey LDDD, Karney B. System design and operation for integrating variable renewable energy resources through a comprehensive characterization framework. Renew Energy 2017;113:1019–32. doi:10.1016/j.renene.2017.06.071.

[83] Sepulveda NA, Jenkins JD, Sisternes FJ de, Lester RK. The role of firm low-carbon electricity resources in deep decarbonization of power generation. Joule 2018;In press. doi:10.1016/j.joule.2018.08.006.

[84] ManagingOversupply @ www.caiso.com n.d.

[85] Joel W. Ager, Lapkin AA. Chemical storage of renewable energy. Science (80-) 2018;360:707–8. doi:10.1126/science.aat7918.

[86] Dostál Z, Ladányi L. Demands on energy storage for renewable power sources. J Energy Storage 2018;18:250–5. doi:10.1016/j.est.2018.05.003.

[87] Mohammadi M, Noorollahi Y, Mohammadi-Ivatloo B. Impacts of Energy Storage Technologies and Renewable Energy Sources on Energy Hub Systems. Oper. Planning, Anal. Energy Storage Syst. Smart Energy Hubs, Cham: Springer International Publishing; 2018, p. 23–52. doi:10.1007/978-3-319-75097-2_2.

[88] Jockenhöfer H, Steinmann W-DD, Bauer D. Detailed numerical investigation of a pumped thermal energy storage with low temperature heat integration. Energy 2018;145:665–76. doi:10.1016/j.energy.2017.12.087.

[89] Crotogino F, Schneider G-S, Evans DJ. Renewable energy storage in geological formations. Proc Inst Mech Eng Part A J Power Energy 2018;232:100–14.

doi:10.1177/0957650917731181.

[90] Lu B, Stocks M, Blakers A, Anderson K. Geographic information system algorithms to locate prospective sites for pumped hydro energy storage. Appl Energy 2018;222:300–12. doi:10.1016/j.apenergy.2018.03.177.

[91] Henninger S, Jaeger J. Assessing the technical performance of renewable power plants and energy storage systems from a power system perspective. J Energy Storage 2018;17:239–48. doi:10.1016/j.est.2018.03.007.

[92] Moghaddam IN, Chowdhury BH, Mohajeryami S. Predictive Operation and Optimal Sizing of Battery Energy Storage With High Wind Energy Penetration. IEEE Trans Ind Electron 2018;65:6686–95. doi:10.1109/TIE.2017.2774732.

[93] Sedghi M, Ahmadian A, Elkamel A, Golkar MA, Fowler M. Battery energy storage planning. Power Syst., 2018, p. 185–214. doi:10.1007/978-981-10-7056-3_7.

[94] Wang Z, Gu C, Li F. Flexible operation of shared energy storage at households to facilitate PV penetration. Renew Energy 2018;116:438–46. doi:10.1016/j.renene.2017.10.005.

[95] Caldera U, Breyer C. The role that battery and water storage play in Saudi Arabia's transition to an integrated 100% renewable energy power system. J Energy Storage 2018;17:299–310. doi:10.1016/j.est.2018.03.009.

[96] Zohuri B. Reliable Renewables with Cryogenic Energy Storage. Hybrid Energy Syst., Cham: Springer International Publishing; 2018, p. 89–103. doi:10.1007/978-3-319-70721-1_3.

[97] McPherson M, Tahseen S. Deploying storage assets to facilitate variable renewable energy integration: The impacts of grid flexibility, renewable penetration, and market structure. Energy 2018;145:856–70. doi:10.1016/j.energy.2018.01.002.

[98] Acar C. A comprehensive evaluation of energy storage options for better sustainability. Int J Energy Res 2018;42:3732–46. doi:10.1002/er.4102.

[99] Aghahosseini A, Bogdanov D, Ghorbani N, Breyer C. Analysis of 100% renewable energy for Iran in 2030: integrating solar PV, wind energy and storage. Int J Environ Sci Technol 2018;15:17–36. doi:10.1007/s13762-017-1373-4.

[100] Gür TM. Review of electrical energy storage technologies, materials and systems: challenges and prospects for large-scale grid storage. Energy Environ Sci 2018.

doi:10.1039/C8EE01419A.

[101] Branco H, Castro R, Setas Lopes A. Battery energy storage systems as a way to integrate renewable energy in small isolated power systems. Energy Sustain Dev 2018;43:90–9. doi:10.1016/j.esd.2018.01.003.

[102] Yang Y, Bremner S, Menictas C, Kay M. Battery energy storage system size determination in renewable energy systems: A review. Renew Sustain Energy Rev 2018;91:109–25. doi:10.1016/j.rser.2018.03.047.

[103] Buonomano A, Calise F, d'Accadia MD, Vicidomini M. A hybrid renewable system based on wind and solar energy coupled with an electrical storage: Dynamic simulation and economic assessment. Energy 2018;155:174–89. doi:10.1016/j.energy.2018.05.006.

[104] Helbig C, Bradshaw AM, Wietschel L, Thorenz A, Tuma A. Supply risks associated with lithium-ion battery materials. J Clean Prod 2018;172:274–86. doi:10.1016/j.jclepro.2017.10.122.

[105] Olivetti EA, Ceder G, Gaustad GG, Fu X. Lithium-Ion Battery Supply Chain Considerations: Analysis of Potential Bottlenecks in Critical Metals. Joule 2017;1:229–43. doi:10.1016/j.joule.2017.08.019.

[106] Vikström H, Davidsson S, Höök M. Lithium availability and future production outlooks. Appl Energy 2013;110:252–66. doi:10.1016/j.apenergy.2013.04.005.

[107] Kushnir D, Sandén BA. The time dimension and lithium resource constraints for electric vehicles. Resour Policy 2012;37:93–103. doi:10.1016/j.resourpol.2011.11.003.

[108] Seong WM, Park KY, Lee MH, Moon S, Oh K, Park H, et al. Abnormal self-discharge in lithium-ion batteries. Energy Environ Sci 2018;11:970–8. doi:10.1039/c8ee00186c.

[109] An F, Zhao H, Li P. Self-discharge rates in cells have a critical effect on the cycle life of parallel lithium-ion batteries. RSC Adv 2018;8:30802–12. doi:10.1039/C8RA05403G.

[110] Choi SH, Kim J, Yoon YS. Self-discharge analysis of licoo2 for lithium batteries. J Power Sources 2004;138:283–7. doi:10.1016/j.jpowsour.2004.06.047.

[111] Utsunomiya T, Hatozaki O, Yoshimoto N, Egashira M, Morita M. Self-discharge behavior and its temperature dependence of carbon electrodes in lithium-ion batteries. J Power Sources 2011;196:8598–603. doi:10.1016/j.jpowsour.2011.05.066.

[112] Utsunomiya T, Hatozaki O, Yoshimoto N, Egashira M, Morita M. Influence of particle size on the self-discharge behavior of graphite electrodes in lithium-ion batteries. J Power Sources 2011;196:8675–82. doi:10.1016/j.jpowsour.2011.06.070.

[113] Zeng X, Li J, Liu L. Solving spent lithium-ion battery problems in China: Opportunities and challenges. Renew Sustain Energy Rev 2015;52:1759–67. doi:10.1016/j.rser.2015.08.014.

[114] Richa K, Babbitt CW, Gaustad G, Wang X. A future perspective on lithium-ion battery waste flows from electric vehicles. Resour Conserv Recycl 2014;83:63–76. doi:10.1016/j.resconrec.2013.11.008.

[115] Winslow KM, Laux SJ, Townsend TG. A review on the growing concern and potential management strategies of waste lithium-ion batteries. Resour Conserv Recycl 2018;129:263–77. doi:10.1016/j.resconrec.2017.11.001.

[116] Zeng X, Li J, Singh N. Recycling of spent lithium-ion battery: a critical review. Crit Rev Environ Sci Technol 2014;44:1129–65. doi:10.1080/10643389.2013.763578.

[117] Scrosati B, Hassoun J, Sun Y-K. Lithium-ion batteries. A look into the future. Energy Environ Sci 2011;4:3287. doi:10.1039/c1ee01388b.

[118] Zu C-X, Li H. Thermodynamic analysis on energy densities of batteries. Energy Environ Sci 2011;4:2614. doi:10.1039/c0ee00777c.

[119] Thackeray MM, Wolverton C, Isaacs ED. Electrical energy storage for transportation - Approaching the limits of, and going beyond, lithium-ion batteries. Energy Environ Sci 2012;5:7854–63. doi:10.1039/c2ee21892e.

[120] McDonagh S, Wall DM, Deane P, Murphy JD. The effect of electricity markets, and renewable electricity penetration, on the levelised cost of energy of an advanced electro-fuel system incorporating carbon capture and utilisation. Renew Energy 2019;131:364–71. doi:10.1016/j.renene.2018.07.058.

[121] Mazza A, Bompard E, Chicco G. Applications of power to gas technologies in emerging electrical systems. Renew Sustain Energy Rev 2018;92:794–806. doi:10.1016/j.rser.2018.04.072.

[122] Lewandowska-Bernat A, Desideri U. Opportunities of power-to-gas technology in different energy systems architectures. Appl Energy 2018;228:57–67.

doi:10.1016/j.apenergy.2018.06.001.

[123] Leonard MD, Michaelides EE, Michaelides DN. Substitution of coal power plants with renewable energy sources–Shift of the power demand and energy storage. Energy Convers Manag 2018;164:27–35. doi:10.1016/j.enconman.2018.02.083.

[124] Bailera M, Lisbona P. Energy storage in Spain: Forecasting electricity excess and assessment of power-to-gas potential up to 2050. Energy 2018;143:900–10. doi:10.1016/j.energy.2017.11.069.

[125] Orhan MF, Kahraman H, Babu BS. Approaches for integrated hydrogen production based on nuclear and renewable energy sources: Energy and exergy assessments of nuclear and solar energy sources in the United Arab Emirates. Int J Hydrogen Energy 2017;42:2601–16. doi:10.1016/j.ijhydene.2016.05.044.

[126] Blanco H, Faaij A. A review at the role of storage in energy systems with a focus on Power to Gas and long-term storage. Renew Sustain Energy Rev 2018;81:1049–86. doi:10.1016/j.rser.2017.07.062.

[127] Kavadias KA, Apostolou D, Kaldellis JK. Modelling and optimisation of a hydrogen-based energy storage system in an autonomous electrical network. Appl Energy 2018:574–86. doi:10.1016/j.apenergy.2017.08.050.

[128] Bennoua S, Le Duigou A, Quéméré MM, Dautremont S. Role of hydrogen in resolving electricity grid issues. Int J Hydrogen Energy 2015;40:7231–45. doi:10.1016/j.ijhydene.2015.03.137.

[129] Ali M, Ekström J, Lehtonen M. Sizing hydrogen energy storage in consideration of demand response in highly renewable generation power systems. Energies 2018;11:1–11. doi:10.3390/en11051113.

[130] Rau GH, Willauer HD, Ren ZJ. The global potential for converting renewable electricity to negative-CO2-emissions hydrogen. Nat Clim Chang 2018;8:621–5. doi:10.1038/s41558-018-0203-0.

[131] Won W, Kwon H, Han J-HH, Kim J. Design and operation of renewable energy sources based hydrogen supply system: Technology integration and optimization. Renew Energy 2017;103:226–38. doi:10.1016/j.renene.2016.11.038.

[132] Li Z, Guo P, Han R, Sun H. Current status and development trend of wind power generation-based hydrogen production technology. Energy Explor Exploit 2018:0144598718787294. doi:10.1177/0144598718787294.

[133] Ardo S, Fernandez Rivas D, Modestino MA, Schulze Greiving V, Abdi FF, Alarcon Llado E, et al. Pathways to electrochemical solar-hydrogen technologies. Energy Environ Sci 2018. doi:10.1039/C7EE03639F.

[134] Burhan M, Oh SJ, Chua KJE, Ng KC. Solar to hydrogen: Compact and cost effective CPV field for rooftop operation and hydrogen production. Appl Energy 2017;194:255–66. doi:10.1016/j.apenergy.2016.11.062.

[135] Schiebahn S, Grube T, Robinius M, Tietze V, Kumar B, Stolten D. Power to gas: Technological overview, systems analysis and economic assessment for a case study in Germany. Int J Hydrogen Energy 2015;40:4285–94. doi:10.1016/j.ijhydene.2015.01.123.

[136] Walker SB, Mukherjee U, Fowler M, Elkamel A. Benchmarking and selection of Power-to-Gas utilizing electrolytic hydrogen as an energy storage alternative. Int J Hydrogen Energy 2016;41:7717–31. doi:10.1016/j.ijhydene.2015.09.008.

[137] Guandalini G, Robinius M, Grube T, Campanari S, Stolten D. Long-term power-to-gas potential from wind and solar power: A country analysis for Italy. Int J Hydrogen Energy 2017;42:13389–406. doi:10.1016/j.ijhydene.2017.03.081.

[138] Marchenko O V., Solomin S V. Modeling of hydrogen and electrical energy storages in wind/PV energy system on the Lake Baikal coast. Int J Hydrogen Energy 2017;42:9361–70. doi:10.1016/j.ijhydene.2017.02.076.

[139] Dincer I, Acar C. Smart energy solutions with hydrogen options. Int J Hydrogen Energy 2018;43:8579–99. doi:10.1016/j.ijhydene.2018.03.120.

[140] Vivas FJ, De las Heras A, Segura F, Andújar JM. A review of energy management strategies for renewable hybrid energy systems with hydrogen backup. Renew Sustain Energy Rev 2018;82:126–55. doi:10.1016/j.rser.2017.09.014.

[141] Dahbi S, Aziz A, Messaoudi A, Mazozi I, Kassmi K, Benazzi N. Management of excess energy in a photovoltaic/grid system by production of clean hydrogen. Int J Hydrogen Energy 2018;43:5283–99. doi:10.1016/j.ijhydene.2017.11.022.

[142] Eriksson ELV, Gray EM. Optimization and integration of hybrid renewable energy hydrogen fuel cell energy systems – A critical review. Appl Energy 2017;202:348–64. doi:10.1016/j.apenergy.2017.03.132.

[143] Fischer D, Kaufmann F, Selinger-Lutz O, Voglstätter C. Power-to-gas in a smart city context – Influence of network restrictions and possible solutions using on-site storage and model predictive controls. Int J Hydrogen Energy 2018;43:9483–94. doi:10.1016/j.ijhydene.2018.04.034.

[144] Rahmouni S, Negrou B, Settou N, Dominguez J, Gouareh A. Prospects of hydrogen production potential from renewable resources in Algeria. Int J Hydrogen Energy 2017;42:1383–95. doi:10.1016/j.ijhydene.2016.07.214.

[145] Mohsin M, Rasheed AK, Saidur R. Economic viability and production capacity of wind generated renewable hydrogen. Int J Hydrogen Energy 2018;43:2621–30. doi:10.1016/j.ijhydene.2017.12.113.

[146] Fereidooni M, Mostafaeipour A, Kalantar V, Goudarzi H. A comprehensive evaluation of hydrogen production from photovoltaic power station. Renew Sustain Energy Rev 2018;82:415–23. doi:10.1016/j.rser.2017.09.060.

[147] Apak S, Atay E, Tuncer G. Renewable hydrogen energy and energy efficiency in Turkey in the 21st century. Int J Hydrogen Energy 2017;42:2446–52. doi:10.1016/j.ijhydene.2016.05.043.

[148] da Silva Veras T, Mozer TS, da Costa Rubim Messeder dos Santos D, da Silva César A. Hydrogen: Trends, production and characterization of the main process worldwide. Int J Hydrogen Energy 2017;42:2018–33. doi:10.1016/j.ijhydene.2016.08.219.

[149] Lisbona P, Frate GF, Bailera M, Desideri U. Power-to-Gas: Analysis of potential decarbonization of Spanish electrical system in long-term prospective. Energy 2018;159:656–68. doi:10.1016/j.energy.2018.06.115.

[150] Parra D, Zhang X, Bauer C, Patel MK. An integrated techno-economic and life cycle environmental assessment of power-to-gas systems. Appl Energy 2017;193:440–54. doi:10.1016/j.apenergy.2017.02.063.

[151] Olateju B, Kumar A, Secanell M. A techno-economic assessment of large scale wind-hydrogen production with energy storage in Western Canada. Int J Hydrogen Energy 2016;41:8755–76. doi:10.1016/j.ijhydene.2016.03.177.

[152] Qolipour M, Mostafaeipour A, Tousi OM. Techno-economic feasibility of a photovoltaic-wind power plant construction for electric and hydrogen production: A case study. Renew Sustain Energy Rev 2017;78:113–23. doi:10.1016/j.rser.2017.04.088.

[153] Khosravi A, Koury RNN, Machado L, Pabon JJG. Energy, exergy and economic analysis of a hybrid renewable energy with hydrogen storage system. Energy 2018;148:1087–102. doi:10.1016/j.energy.2018.02.008.

[154] Hanley ES, Deane J, Gallachóir BÓ. The role of hydrogen in low carbon energy futures – A review of existing perspectives. Renew Sustain Energy Rev 2018;82:3027–45. doi:10.1016/j.rser.2017.10.034.

[155] Penev M, Rustagi N, Hunter C, Eichman J. Energy Storage: Days of Service Sensitivity Analysis 2019.

[156] Hart EK, Jacobson MZ. The carbon abatement potential of high penetration intermittent renewables. Energy Environ Sci 2012;5:6592–601. doi:10.1039/c2ee03490e.

[157] Jacobson MZ, Delucchi MA, Bauer ZAF, Goodman SC, Chapman WE, Cameron MA, et al. 100% clean and renewable wind, water, and sunlight all-sector energy roadmaps for 139 countries of the world. Joule 2017;1:108–21. doi:10.1016/j.joule.2017.07.005.

[158] Jacobson MZ, Delucchi MA, Bazouin G, Bauer ZAF, Heavey CC, Fisher E, et al. 100% clean and renewable wind, water, and sunlight (WWS) all-sector energy roadmaps for the 50 United States. Energy Environ Sci 2015;8:2093–117. doi:10.1039/c5ee01283j.

[159] García-Olivares A, Solé J, Osychenko O. Transportation in a 100% renewable energy system. Energy Convers Manag 2018;158:266–85. doi:10.1016/j.enconman.2017.12.053.

[160] Miller M. Electrification: Its Role in Deeply Decarbonized Energy Systems [Guest Editorial]. IEEE Power Energy Mag 2018;16:20–3. doi:10.1109/mpe.2018.2824099.

[161] Mahone A, Subin Z, Orans R, Miller M, Regan L, Calviou M, et al. On the Path to Decarbonization: Electrification and Renewables in California and the Northeast United States. IEEE Power Energy Mag 2018;16:58–68. doi:10.1109/mpe.2018.2822865.

[162] Ebrahimi S, Mac Kinnon M, Brouwer J. California end-use electrification impacts on carbon neutrality and clean air. Appl Energy 2018;213:435–49. doi:10.1016/j.apenergy.2018.01.050.

[163] Deason J, Wei M, Leventis G, Smith S, Schwartz L. Electrification of buildings and industry in the United States 2018. doi:10.2172/1430688.

[164] Mai T, Jadun P, Logan J, Mcmillan C, Muratori M, Steinberg D, et al. Electrification Futures Study : Scenarios of Electric Technology Adoption and Power Consumption for the United States Electrification Futures Study : Scenarios of Electric Technology Adoption and Power Consumption for the United States. National Renewable Energy Lab.(NREL), Golden, CO (United States); 2018. doi:NREL/TP-6A20-71500.

[165] Mai TT. The Electrification Futures Study: Demand-Side Scenarios. National Renewable Energy Lab.(NREL), Golden, CO (United States); 2018.

[166] Moraga JL, Mulder M. Electrification of Heating and Transport - A scenario analysis of the Netherlands up to 2050 2018.

[167] Fowler R, Elmhirst O, Richards J. Electrification in the United Kingdom: A case study based on future energy scenarios. IEEE Power Energy Mag 2018;16:48–57. doi:10.1109/MPE.2018.2822864.

[168] Mai T, Steinberg D, Logan J, Bielen D, Eurek K, McMillan C. An electrified future: Initial scenarios and future research for U.S. Energy and electricity systems. IEEE Power Energy Mag 2018;16:34–47. doi:10.1109/MPE.2018.2820445.

[169] Jones R, Haley B, Kwok G, Hargreaves J, Williams J. Electrification and the future of electricity markets: Transitioning to a low-carbon energy system. IEEE Power Energy Mag 2018;16:79–89. doi:10.1109/MPE.2018.2823479.

[170] Jadun P, McMillan C, Steinberg D, Muratori M, Vimmerstedt L, Mai T. Electrification Futures Study : End-Use Electric Technology Cost and Performance Projections through 2050. Natl Renew Energy Lab 2017:94. doi:NREL/TP-6A20-70485.

[171] Jones PB, Levy J, Bosco J, Howat J, Alst JW Van, Schwartz L, et al. The Future of Transportation Electrification: Utility, Industry and Consumer Perspectives. FEUR Rep No 10 2018. doi:10.2172/1464173.

[172] Gohlke D, Zhou Y. Impacts of Electrification of Light-Duty Vehicles in the United States, 2010-2017. Office of Scientific and Technical Information ({OSTI}); 2018. doi:10.2172/1418278.

[173] Koj JC, Wulf C, Linssen J, Schreiber A, Zapp P. Utilisation of excess electricity in different

Power-to-Transport chains and their environmental assessment. Transp Res Part D Transp Environ 2018. doi:10.1016/j.trd.2018.01.016.

[174] Levesque A, Pietzcker RC, Baumstark L, De Stercke S, Grübler A, Luderer G. How much energy will buildings consume in 2100? A global perspective within a scenario framework. Energy 2018;148:514–27. doi:10.1016/j.energy.2018.01.139.

[175] Tarroja B, Chiang F, AghaKouchak A, Samuelsen S, Raghavan S V., Wei M, et al. Translating climate change and heating system electrification impacts on building energy use to future greenhouse gas emissions and electric grid capacity requirements in California. Appl Energy 2018;225:522–34. doi:10.1016/j.apenergy.2018.05.003.

[176] Heinen S, Mancarella P, O'Dwyer C, O'Malley M. Heat electrification: The latest research in Europe. IEEE Power Energy Mag 2018;16:69–78. doi:10.1109/MPE.2018.2822867.

[177] Jo JH, Aldeman M, Lee HS, Ahn YH. Parametric analysis for cost-optimal renewable energy integration into residential buildings: Techno-economic model. Renew Energy 2018;125:907–14. doi:10.1016/j.renene.2018.03.025.

[178] Ebrahimi S, Mac Kinnon M, Leong K, Brouwer J. GHG Emission Benefits and Air Quality Impacts of California Renewable Integration and Electrification. 2016.

[179] Schüwer D, Schneider C. Electrification of industrial process heat: long-term applications, potentials and impacts 2018.

[180] Wiertzema H, Harvey S, Åhman M. Bottom-up methodology for assessing electrification options for deep decarbonisation of industrial processes. Eur. Counc. an Energy Effic. Econ., 2018, p. 389–97.

[181] Vine D, Ye J. Decarbonizing Us Industry. Cent Clim Energy Solut 2018.

[182] Cooper SJG, Hammond GP. 'Decarbonising'UK industry: towards a cleaner economy. Proc Inst Civ Eng 2018:1–25. doi:10.1680/jener.18.00007.

[183] The City of Palo Alto. Palo Alto Electrification Final Report. 2016.

[184] Keith DW, Holmes G, St. Angelo D, Heidel K. A Process for Capturing CO2 from the Atmosphere. Joule 2018;2:1573–94. doi:10.1016/J.JOULE.2018.05.006.

[185] Vaillancourt K, Bahn O, Frenette E, Sigvaldason O. Exploring deep decarbonization pathways

to 2050 for Canada using an optimization energy model framework. Appl Energy 2017;195:774–85. doi:10.1016/j.apenergy.2017.03.104.

[186] Olcay H, Malina R, Upadhye AA, Hileman JI, Huber GW, Barrett SRH. Techno-economic and environmental evaluation of producing chemicals and drop-in aviation biofuels via aqueous phase processing. Energy Environ Sci 2018;11:2085--2101. doi:10.1039/C7EE03557H.

[187] Ericsson K. Biogenic carbon dioxide as feedstock for production of chemicals and fuels:A techno-economic assessment with a European perspective. 2017.

[188] Davis SJ, Lewis NS, Shaner M, Aggarwal S, Arent D, Azevedo IL, et al. Net-zero emissions energy systems. Science (80-) 2018;360:eaas9793. doi:10.1126/science.aas9793.

[189] Hon S. Reconstructing the Ethanol Production Pathway of Thermoanaerobacterium saccharolyticum in Clostridium thermocellum. 2018.

[190] Woolf D, Lehmann J. Pathways to Carbon-Negative Liquid Biofuels. AGU Fall Meet Abstr 2017.

[191] Demirbas A. Future hydrogen economy and policy. Energy Sources, Part B Econ Planning, Policy 2017;12:172–81. doi:10.1080/15567249.2014.950394.

[192] Baykara SZ. Hydrogen: A brief overview on its sources, production and environmental impact. Int J Hydrogen Energy 2018;43:10605–14. doi:10.1016/j.ijhydene.2018.02.022.

[193] Pivovar B, Rustagi N, Satyapal S. Hydrogen at Scale (H2@Scale): Key to a Clean, Economic, and Sustainable Energy System. Electrochem Soc Interface 2018;27:47–52. doi:10.1149/2.F04181if.

[194] Gondal IA, Masood SA, Khan R. Green hydrogen production potential for developing a hydrogen economy in Pakistan. Int J Hydrogen Energy 2018;43:6011–39. doi:10.1016/j.ijhydene.2018.01.113.

[195] Hosseini SE, Wahid MA. Hydrogen production from renewable and sustainable energy resources: Promising green energy carrier for clean development. Renew Sustain Energy Rev 2016;57:850–66. doi:10.1016/j.rser.2015.12.112.

[196] Abdalla MA, Hossaina S, Nisfindya OB, Azadd AT, Mohamed Dawood, Azada AK. Hydrogen production, storage, transportation and key challenges with applications: A review. Energy Convers Manag 2018;165:602–27. doi:10.1016/j.enconman.2018.03.088.

[197] Bailera M, Lisbona P, Romeo LM, Espatolero S. Power to Gas projects review: Lab, pilot and demo plants for storing renewable energy and CO2. Renew Sustain Energy Rev 2017;69:292–312. doi:10.1016/j.rser.2016.11.130.

[198] Loisel R, Baranger L, Chemouri N, Spinu S, Pardo S. Economic evaluation of hybrid off-shore wind power and hydrogen storage system. Int J Hydrogen Energy 2015;40:6727–39. doi:10.1016/j.ijhydene.2015.03.117.

[199] McDonagh S, O'Shea R, Wall DM, Deane JP, Murphy JD. Modelling of a power-to-gas system to predict the levelised cost of energy of an advanced renewable gaseous transport fuel. Appl Energy 2018;215:444–56. doi:10.1016/j.apenergy.2018.02.019.

[200] Koponen K, Hannula I. GHG emission balances and prospects of hydrogen enhanced synthetic biofuels from solid biomass in the European context. Appl Energy 2017;200:106–18. doi:10.1016/j.apenergy.2017.05.014.

[201] Likkasit C, Maroufmashat A, Elkamel A, Ku H, Fowler M. Solar-aided hydrogen production methods for the integration of renewable energies into oil & gas industries. Energy Convers Manag 2018;168:395–406. doi:10.1016/j.enconman.2018.04.057.

[202] Weidner S, Faltenbacher M, François I, Thomas D, Skùlason JB, Maggi C. Feasibility study of large scale hydrogen power-to-gas applications and cost of the systems evolving with scaling up in Germany, Belgium and Iceland. Int J Hydrogen Energy 2018;43:15625–38. doi:10.1016/j.ijhydene.2018.06.167.

[203] Welder L, Ryberg DS, Kotzur L, Grube T, Robinius M, Stolten D. Spatio-temporal optimization of a future energy system for power-to-hydrogen applications in Germany. Energy 2018;158:1130–49. doi:10.1016/j.energy.2018.05.059.

[204] Burkhardt J, Patyk A, Tanguy P, Retzke C. Hydrogen mobility from wind energy–A life cycle assessment focusing on the fuel supply. Appl Energy 2016;181:54–64. doi:10.1016/j.apenergy.2016.07.104.

[205] Kurtz J, Peters M, Muratori M, Gearhart C. Renewable Hydrogen-Economically Viable: Integration into the U.S. Transportation Sector. IEEE Electrif Mag 2018;6:8–18. doi:10.1109/MELE.2017.2784631.

[206] Uyar TS, Beşikci D. Integration of hydrogen energy systems into renewable energy systems for better design of 100% renewable energy communities. Int J Hydrogen Energy

2017;42:2453–6. doi:10.1016/j.ijhydene.2016.09.086.

[207] Schoenung SM, Keller JO. Commercial potential for renewable hydrogen in California. Int J Hydrogen Energy 2017;42:13321–8. doi:10.1016/j.ijhydene.2017.01.005.

[208] Sinigaglia T, Lewiski F, Santos Martins ME, Mairesse Siluk JC. Production, storage, fuel stations of hydrogen and its utilization in automotive applications-a review. Int J Hydrogen Energy 2017;42:24597–611. doi:10.1016/j.ijhydene.2017.08.063.

[209] Colbertaldo P, Guandalini G, Campanari S. Modelling the integrated power and transport energy system: The role of power-to-gas and hydrogen in long-term scenarios for Italy. Energy 2018;154:592–601. doi:10.1016/j.energy.2018.04.089.

[210] Llera E, Romeo LLM, Bailera M, Osorio JL. Exploring the integration of the power to gas technologies and the sustainable transport. Int J Energy Prod Manag 2018;3:1–9. doi:10.2495/EQ-V3-N1-1-9.

[211] Monaco F, Lanzini A, Santarelli M. Making synthetic fuels for the road transportation sector via solid oxide electrolysis and catalytic upgrade using recovered carbon dioxide and residual biomass. J Clean Prod 2018;170:160–73. doi:10.1016/j.jclepro.2017.09.141.

[212] Mesfun S, Sanchez DL, Leduc S, Wetterlund E, Lundgren J, Biberacher M, et al. Power-to-gas and power-to-liquid for managing renewable electricity intermittency in the Alpine Region. Renew Energy 2017;107:361–72. doi:10.1016/j.renene.2017.02.020.

[213] Luo Y, Wu X yu, Shi Y, Ghoniem AF, Cai N. Exergy analysis of an integrated solid oxide electrolysis cell-methanation reactor for renewable energy storage. Appl Energy 2018;215:371–83. doi:10.1016/j.apenergy.2018.02.022.

[214] Wang L, Pérez-Fortes M, Madi H, Diethelm S, herle J Van, Maréchal F. Optimal design of solid-oxide electrolyzer based power-to-methane systems: A comprehensive comparison between steam electrolysis and co-electrolysis. Appl Energy 2018;211:1060–79. doi:10.1016/j.apenergy.2017.11.050.

[215] Nakaten N, Chabab E, Kempka T, Kühn M. Excess renewable energy flexibilisation by integration of geological storage. Geophys Res Abstr 2018;20.

[216] Götz M, Lefebvre J, Mörs F, McDaniel Koch A, Graf F, Bajohr S, et al. Renewable Power-to-Gas: A technological and economic review. Renew Energy 2016;85:1371–90.

doi:10.1016/j.renene.2015.07.066.

[217] Uusitalo V, Väisänen S, Inkeri E, Soukka R. Potential for greenhouse gas emission reductions using surplus electricity in hydrogen, methane and methanol production via electrolysis. Energy Convers Manag 2017;134:125–34. doi:10.1016/j.enconman.2016.12.031.

[218] Ghaib K, Ben-Fares FZ. Power-to-Methane: A state-of-the-art review. Renew Sustain Energy Rev 2018;81:433–46. doi:10.1016/j.rser.2017.08.004.

[219] Zhang X, Bauer C, Mutel CL, Volkart K. Life Cycle Assessment of Power-to-Gas: Approaches, system variations and their environmental implications. Appl Energy 2017;190:326–38. doi:10.1016/j.apenergy.2016.12.098.

[220] Estermann T, Newborough M, Sterner M. Power-to-gas systems for absorbing excess solar power in electricity distribution networks. Int J Hydrogen Energy 2016;41:13950–9. doi:10.1016/j.ijhydene.2016.05.278.

[221] Simonis B, Newborough M. Sizing and operating power-to-gas systems to absorb excess renewable electricity. Int J Hydrogen Energy 2017;42:21635–47. doi:10.1016/j.ijhydene.2017.07.121.

[222] Prieto-Prado I, Del Río-Gamero B, Gómez-Gotor A, Pérez-Báez SO. Water and energy self-supply in isolated areas through renewable energies using hydrogen and water as a double storage system. Desalination 2018;430:1–14. doi:10.1016/j.desal.2017.12.022.

[223] Al-Sharafi A, Sahin AZ, Ayar T, Yilbas BS. Techno-economic analysis and optimization of solar and wind energy systems for power generation and hydrogen production in Saudi Arabia. Renew Sustain Energy Rev 2017;69:33–49. doi:10.1016/j.rser.2016.11.157.

[224] Sorgulu F, Dincer I. A renewable source based hydrogen energy system for residential applications. Int J Hydrogen Energy 2018;43:5842–51. doi:10.1016/j.ijhydene.2017.10.101.

[225] Stern AG. A new sustainable hydrogen clean energy paradigm. Int J Hydrogen Energy 2018;43:4244–55. doi:10.1016/j.ijhydene.2017.12.180.

[226] Ishaq H, Dincer I, Naterer GF. Performance investigation of an integrated wind energy system for co-generation of power and hydrogen. Int J Hydrogen Energy 2018;43:9153–64. doi:10.1016/j.ijhydene.2018.03.139.

[227] Schmidt Rivera XC, Topriska E, Kolokotroni M, Azapagic A. Environmental sustainability of

renewable hydrogen in comparison with conventional cooking fuels. J Clean Prod 2018;196:863–79. doi:10.1016/j.jclepro.2018.06.033.

[228] IRENA. Hydrogen: a renewable energy perspective. 2019.

[229] Safari F, Dincer I. A review and comparative evaluation of thermochemical water splitting cycles for hydrogen production. Energy Convers Manag 2020;205:112182. doi:10.1016/j.enconman.2019.112182.

[230] Demir ME, Dincer I. Cost assessment and evaluation of various hydrogen delivery scenarios. Int J Hydrogen Energy 2018;43:10420–30. doi:10.1016/j.ijhydene.2017.08.002.

[231] Aakko-Saksa PT, Cook C, Kiviaho J, Repo T. Liquid organic hydrogen carriers for transportation and storing of renewable energy – Review and discussion. J Power Sources 2018;396:803–23. doi:10.1016/j.jpowsour.2018.04.011.

[232] Nagpal M, Kakkar R. An evolving energy solution: Intermediate hydrogen storage. Int J Hydrogen Energy 2018;43:12168–88. doi:10.1016/j.ijhydene.2018.04.103.

[233] Le Duigou A, Bader AG, Lanoix JC, Nadau L. Relevance and costs of large scale underground hydrogen storage in France. Int J Hydrogen Energy 2017;42:22987–3003. doi:10.1016/j.ijhydene.2017.06.239.

[234] Reuß M, Grube T, Robinius M, Preuster P, Wasserscheid P, Stolten D. Seasonal storage and alternative carriers: A flexible hydrogen supply chain model. Appl Energy 2017;200:290–302. doi:10.1016/j.apenergy.2017.05.050.

[235] Melaina MW, Antonia O, Penev M. Blending Hydrogen into Natural Gas Pipeline Networks. A Review of Key Issues. 2013. doi:10.2172/1219920.

[236] Clegg S, Mancarella P. Storing renewables in the gas network: modelling of power-to-gas seasonal storage flexibility in low-carbon power systems. IET Gener Transm Distrib 2016;10:566–75. doi:10.1049/iet-gtd.2015.0439.

[237] Kouchachvili L, Entchev E. Power to gas and H 2 /NG blend in SMART energy networks concept. Renew Energy 2018;125:456–64. doi:10.1016/j.renene.2018.02.088.

[238] Qadrdan M, Ameli H, Strbac G, Jenkins N. Efficacy of options to address balancing challenges: Integrated gas and electricity perspectives. Appl Energy 2017;190:181–90. doi:10.1016/j.apenergy.2016.11.119.

[239] Speirs J, Balcombe P, Johnson E, Martin J, Brandon N, Hawkes A. A greener gas grid: What are the options. Energy Policy 2018;118:291–7. doi:10.1016/j.enpol.2018.03.069.

[240] Chaczykowski M. Simulation of natural gas quality distribution for pipeline systems. Energy 2017;134:681–98. doi:10.1016/j.energy.2017.06.020.

[241] Ogden J, Jaffe AM, Scheitrum D, McDonald Z, Miller M. Natural gas as a bridge to hydrogen transportation fuel: Insights from the literature. Energy Policy 2018;115:317–29. doi:10.1016/j.enpol.2017.12.049.

[242] Hernández-Gómez R, Tuma D, Gómez-Hernández A, Chamorro CR. Accurate Experimental (p , ρ, T) Data for the Introduction of Hydrogen into the Natural Gas Grid: Thermodynamic Characterization of the Nitrogen–Hydrogen Binary System from 240 to 350 K and Pressures up to 20 MPa. J Chem Eng Data 2017;62:4310–26. doi:10.1021/acs.jced.7b00694.

[243] Wang B, Liang Y, Zheng J, Qiu R, Yuan M, Zhang H. An MILP model for the reformation of natural gas pipeline networks with hydrogen injection. Int J Hydrogen Energy 2018;43:16141–53. doi:10.1016/j.ijhydene.2018.06.161.

[244] Guandalini G, Colbertaldo P, Campanari S. Dynamic modeling of natural gas quality within transport pipelines in presence of hydrogen injections. Appl Energy 2017;185:1712–23. doi:10.1016/j.apenergy.2016.03.006.

[245] Heydarzadeh Z, McVay D, Flores R, Thai C, Brouwer J. Dynamic Modeling of California Grid-Scale Hydrogen Energy Storage. Electrochem Soc 2018;86:245–58. doi:10.1149/08613.0245ecst.

[246] Momirlan M, Veziroglu TN. The properties of hydrogen as fuel tomorrow in sustainable energy system for a cleaner planet. Int J Hydrogen Energy 2005;30:795–802. doi:10.1016/j.ijhydene.2004.10.011.

[247] Quarton CJ, Samsatli S. Power-to-gas for injection into the gas grid: What can we learn from real-life projects, economic assessments and systems modelling? Renew Sustain Energy Rev 2018;98:302–16. doi:10.1016/j.rser.2018.09.007.

[248] Qadrdan M, Abeysekera M, Chaudry M, Wu J, Jenkins N. Role of power-to-gas in an integrated gas and electricity system in Great Britain. Int J Hydrogen Energy 2015;40:5763–75. doi:10.1016/j.ijhydene.2015.03.004.

[249] Mukherjee U, Elsholkami M, Walker S, Fowler M, Elkamel A, Hajimiragha A. Optimal sizing of an electrolytic hydrogen production system using an existing natural gas infrastructure. Int J Hydrogen Energy 2015;40:9760–72. doi:10.1016/j.ijhydene.2015.05.102.

[250] Jun C, Yu H. Water electrolysis based on renewable energy for hydrogen production. Chinese J Catal 2018;39:390–4. doi:10.1016/S1872.

[251] Luo Y, Shi Y, Li W, Cai N. Synchronous enhancement of H2O/CO2co-electrolysis and methanation for efficient one-step power-to-methane. Energy Convers Manag 2018;165:127–36. doi:10.1016/j.enconman.2018.03.028.

[252] AlZahrani AA, Dincer I. Modeling and performance optimization of a solid oxide electrolysis system for hydrogen production. Appl Energy 2018;225:471–85. doi:10.1016/j.apenergy.2018.04.124.

[253] Im-orb K, Visitdumrongkul N, Saebea D, Patcharavorachot Y, Arpornwichanop A. Flowsheet-based model and exergy analysis of solid oxide electrolysis cells for clean hydrogen production. J Clean Prod 2018;170:1–13. doi:10.1016/j.jclepro.2017.09.127.

[254] AlZahrani AA, Dincer I. Thermodynamic and electrochemical analyses of a solid oxide electrolyzer for hydrogen production. Int J Hydrogen Energy 2017;42:21404–13. doi:10.1016/j.ijhydene.2017.03.186.

[255] Lin M, Haussener S. Techno-economic modeling and optimization of solar-driven high-temperature electrolysis systems. Sol Energy 2017;155:1389–402. doi:10.1016/j.solener.2017.07.077.

[256] Seitz M, von Storch H, Nechache A, Bauer D. Techno economic design of a solid oxide electrolysis system with solar thermal steam supply and thermal energy storage for the generation of renewable hydrogen. Int J Hydrogen Energy 2017;42:26192–202. doi:10.1016/j.ijhydene.2017.08.192.

[257] Kim JS, Boardman RD, Bragg-Sitton SM. Dynamic performance analysis of a high-temperature steam electrolysis plant integrated within nuclear-renewable hybrid energy systems. Appl Energy 2018;228:2090–110. doi:10.1016/j.apenergy.2018.07.060.

[258] Zhang JH, Lei L Bin, Liu D, Zhao FY, Chen F, Wang HQ. Numerical investigation of solid oxide electrolysis cells for hydrogen production applied with different continuity expressions. Energy Convers Manag 2017;149:646–59. doi:10.1016/j.enconman.2017.07.013.

[259] Kim J, Jun A, Gwon O, Yoo S, Liu M, Shin J, et al. Hybrid-solid oxide electrolysis cell: A new strategy for efficient hydrogen production. Nano Energy 2018;44:121–6. doi:10.1016/j.nanoen.2017.11.074.

[260] Hu B, Aphale AN, Reisert M, Belko S, Marina OA, Stevenson JW, et al. Solid Oxide Electrolysis for Hydrogen Production: From Oxygen Ion to Proton Conducting Cells. ECS Trans 2018;85:13–20. doi:10.1149/08510.0013ecst.

[261] Graves C, Ebbesen SD, Mogensen M, Lackner KS. Sustainable hydrocarbon fuels by recycling CO2 and H 2O with renewable or nuclear energy. Renew Sustain Energy Rev 2011;15:1–23. doi:10.1016/j.rser.2010.07.014.

[262] Jensen SH, Larsen PH, Mogensen M. Hydrogen and synthetic fuel production from renewable energy sources. Int J Hydrogen Energy 2007;32:3253–7. doi:10.1016/j.ijhydene.2007.04.042.

[263] Pandiyan A, Uthayakumar A, Subrayan R, Cha SW, Krishna Moorthy SB. Review of solid oxide electrolysis cells: a clean energy strategy for hydrogen generation. Nanomater Energy 2019;8:2–22. doi:10.1680/jnaen.18.00009.

[264] Wendel CH, Kazempoor P, Braun RJ. A thermodynamic approach for selecting operating conditions in the design of reversible solid oxide cell energy systems. J Power Sources 2016;301:93–104. doi:10.1016/j.jpowsour.2015.09.093.

[265] Graves C, Ebbesen SD, Mogensen M. Co-electrolysis of CO2 and H2O in solid oxide cells: Performance and durability. Solid State Ionics 2011;192:398–403. doi:10.1016/j.ssi.2010.06.014.

[266] Ebbesen SD, Mogensen M. Electrolysis of carbon dioxide in Solid Oxide Electrolysis Cells. J Power Sources 2009;193:349–58. doi:10.1016/j.jpowsour.2009.02.093.

[267] Ebbesen SD, Graves C, Mogensen M. Production of synthetic fuels by co-electrolysis of steam and carbon dioxide. Int J Green Energy 2009;6:646–60. doi:10.1080/15435070903372577.

[268] Ni M, Leung MKH, Leung DYC. A modeling study on concentration overpotentials of a reversible solid oxide fuel cell. J Power Sources 2006;163:460–6. doi:10.1016/j.jpowsour.2006.09.024.

[269] Ni M, Leung MKH, Leung DYC. An electrochemical model of a solid oxide steam electrolyzer

for hydrogen production. Chem Eng Technol 2006;29:636–42. doi:10.1002/ceat.200500378.

[270] Ni M, Leung MKH, Leung DYC. Parametric study of solid oxide steam electrolyzer for hydrogen production. Int J Hydrogen Energy 2007;32:2305–13. doi:10.1016/j.ijhydene.2007.03.001.

[271] Zahadat P, Milewski J. Modeling electrical behavior of solid oxide electrolyzer cells by using artificial neural network. Int J Hydrogen Energy 2015;40:7246–51. doi:10.1016/j.ijhydene.2015.04.042.

[272] Udagawa J, Aguiar P, Brandon NP. Hydrogen production through steam electrolysis: Model-based steady state performance of a cathode-supported intermediate temperature solid oxide electrolysis cell. J Power Sources 2007;166:127–36. doi:10.1016/j.jpowsour.2006.12.081.

[273] Udagawa J, Aguiar P, Brandon NP. Hydrogen production through steam electrolysis: Control strategies for a cathode-supported intermediate temperature solid oxide electrolysis cell. J Power Sources 2008;180:354–64. doi:10.1016/j.jpowsour.2008.01.069.

[274] Nieminen J, Dincer I, Naterer G. Comparative performance analysis of PEM and solid oxide steam electrolyzers. Int J Hydrogen Energy 2010;35:10842–50. doi:10.1016/j.ijhydene.2010.06.005.

[275] Ni M. Modeling of a solid oxide electrolysis cell for carbon dioxide electrolysis. Chem Eng J 2010;164:246–54. doi:10.1016/j.cej.2010.08.032.

[276] Xie Y, Xue X. Modeling of solid oxide electrolysis cell for syngas generation with detailed surface chemistry. Solid State Ionics 2012;224:64–73. doi:10.1016/j.ssi.2012.07.015.

[277] Luo Y, Shi Y, Li W, Ni M, Cai N. Elementary reaction modeling and experimental characterization of solid oxide fuel-assisted steam electrolysis cells. Int J Hydrogen Energy 2014;39:10359–73. doi:10.1016/j.ijhydene.2014.05.018.

[278] Kazempoor P, Braun RJ. Model validation and performance analysis of regenerative solid oxide cells: Electrolytic operation. Int J Hydrogen Energy 2014;39:2669–84. doi:10.1016/j.ijhydene.2013.12.010.

[279] Menon V, Fu Q, Janardhanan VM, Deutschmann O. A model-based understanding of solid-oxide electrolysis cells (SOECs) for syngas production by H2O/CO2 co-electrolysis. J Power

Sources 2015;274:768–81. doi:10.1016/j.jpowsour.2014.09.158.

[280] Luo Y, Shi Y, Li W, Cai N. Dynamic electro-thermal modeling of co-electrolysis of steam and carbon dioxide in a tubular solid oxide electrolysis cell. Energy 2015;89:637–47. doi:10.1016/j.energy.2015.05.150.

[281] Duhn JD, Jensen AD, Wedel S, Wix C. Optimization of a new flow design for solid oxide cells using computational fluid dynamics modelling. J Power Sources 2016;336:261–71. doi:10.1016/j.jpowsour.2016.10.060.

[282] Tanaka Y, Hoerlein MP, Schiller G. Numerical simulation of steam electrolysis with a solid oxide cell for proper evaluation of cell performances. Int J Hydrogen Energy 2016;41:752–63. doi:10.1016/j.ijhydene.2015.11.048.

[283] Xu H, Chen B, Irvine J, Ni M. Modeling of CH4-assisted SOEC for H2O/CO2 co-electrolysis. Int J Hydrogen Energy 2016;41:21839–49. doi:10.1016/j.ijhydene.2016.10.026.

[284] Ni M. Computational fluid dynamics modeling of a solid oxide electrolyzer cell for hydrogen production. Int J Hydrogen Energy 2009;34:7795–806. doi:10.1016/j.ijhydene.2009.07.080.

[285] Grondin D, Deseure J, Brisse A, Zahid M, Ozil P. Simulation of a high temperature electrolyzer. J Appl Electrochem 2010;40:933–41. doi:10.1007/s10800-009-0030-0.

[286] Jin X, Xue X. Computational fluid dynamics analysis of solid oxide electrolysis cells with delaminations. Int J Hydrogen Energy 2010;35:7321–8. doi:10.1016/j.ijhydene.2010.04.158.

[287] Laurencin J, Kane D, Delette G, Deseure J, Lefebvre-Joud F. Modelling of solid oxide steam electrolyzer: Impact of the operating conditions on hydrogen production. J Power Sources 2011;196:2080–93. doi:10.1016/j.jpowsour.2010.09.054.

[288] Ni M. 2D thermal modeling of a solid oxide electrolyzer cell (SOEC) for syngas production by H2O/CO2 co-electrolysis. Int J Hydrogen Energy 2012;37:6389–99. doi:10.1016/j.ijhydene.2012.01.072.

[289] Hawkes G, O'Brien J, Stoots C, Hawkes B. 3D CFD model of a multi-cell high-temperature electrolysis stack. Int J Hydrogen Energy 2009;34:4189–97. doi:10.1016/j.ijhydene.2008.11.068.

[290] Ni M, Leung MKH, Leung DYC. Energy and exergy analysis of hydrogen production by solid oxide steam electrolyzer plant. Int J Hydrogen Energy 2007;32:4648–60.

doi:10.1016/j.ijhydene.2007.08.005.

[291] Sigurvinsson J, Mansilla C, Lovera P, Werkoff F. Can high temperature steam electrolysis function with geothermal heat? Int J Hydrogen Energy 2007;32:1174–82. doi:10.1016/j.ijhydene.2006.11.026.

[292] Gopalan S, Mosleh M, Hartvigsen JJ, McConnell RD. Analysis of self-sustaining recuperative solid oxide electrolysis systems. J Power Sources 2008;185:1328–33. doi:10.1016/j.jpowsour.2008.09.027.

[293] Stoots C, O'Brien J, Hartvigsen J. Results of recent high temperature coelectrolysis studies at the Idaho National Laboratory. Int J Hydrogen Energy 2009;34:4208–15. doi:10.1016/j.ijhydene.2008.08.029.

[294] O'Brien JE, McKellar MG, Stoots CM, Herring JS, Hawkes GL. Parametric study of large-scale production of syngas via high-temperature co-electrolysis. Int J Hydrogen Energy 2009;34:4216–26. doi:10.1016/j.ijhydene.2008.12.021.

[295] Wang Z, Mori M, Araki T. Steam electrolysis performance of intermediate-temperature solid oxide electrolysis cell and efficiency of hydrogen production system at 300 Nm3 h-1. Int J Hydrogen Energy 2010;35:4451–8. doi:10.1016/j.ijhydene.2010.02.058.

[296] Stoots CM, O'Brien JE, Condie KG, Hartvigsen JJ. High-temperature electrolysis for large-scale hydrogen production from nuclear energy - Experimental investigations. Int J Hydrogen Energy 2010;35:4861–70. doi:10.1016/j.ijhydene.2009.10.045.

[297] Jensen SH, Sun X, Ebbesen SD, Knibbe R, Mogensen M. Hydrogen and synthetic fuel production using pressurized solid oxide electrolysis cells. Int J Hydrogen Energy 2010;35:9544–9. doi:10.1016/j.ijhydene.2010.06.065.

[298] Zhang H, Lin G, Chen J. Evaluation and calculation on the efficiency of a water electrolysis system for hydrogen production. Int J Hydrogen Energy 2010;35:10851–8. doi:10.1016/j.ijhydene.2010.07.088.

[299] Ebbesen SD, Høgh J, Nielsen KA, Nielsen JU, Mogensen M. Durable SOC stacks for production of hydrogen and synthesis gas by high temperature electrolysis. Int J Hydrogen Energy 2011;36:7363–73. doi:10.1016/j.ijhydene.2011.03.130.

[300] Mougin J, Chatroux A, Couturier K, Petitjean M, Reytier M, Gousseau G, et al. High

temperature steam electrolysis stack with enhanced performance and durability. Energy Procedia 2012;29:445–54. doi:10.1016/j.egypro.2012.09.052.

[301] Brisse A, Schefold J. High temperature electrolysis at EIFER, main achievements at cell and stack level. Energy Procedia 2012;29:53–63. doi:10.1016/j.egypro.2012.09.008.

[302] Dillig M, Karl J. Thermal management of high temperature solid oxide electrolyser cell/fuel cell systems. Energy Procedia 2012;28:37–47. doi:10.1016/j.egypro.2012.08.038.

[303] Kim SD, Yu JH, Seo DW, Han IS, Woo SK. Hydrogen production performance of 3-cell flat-tubular solid oxide electrolysis stack. Int J Hydrogen Energy 2012;37:78–83. doi:10.1016/j.ijhydene.2011.09.079.

[304] Kim J, Ji H Il, Dasari HP, Shin D, Song H, Lee JH, et al. Degradation mechanism of electrolyte and air electrode in solid oxide electrolysis cells operating at high polarization. Int J Hydrogen Energy 2013;38:1225–35. doi:10.1016/j.ijhydene.2012.10.113.

[305] Petipas F, Brisse A, Bouallou C. Model-based behaviour of a high temperature electrolyser system operated at various loads. J Power Sources 2013;239:584–95. doi:10.1016/j.jpowsour.2013.03.027.

[306] Diethelm S, Herle J Van, Montinaro D, Bucheli O. Electrolysis and Co-electrolysis performance of SOE short stacks. Fuel Cells 2013;13:631–7. doi:10.1002/fuce.201200178.

[307] Ferrero D, Lanzini A, Santarelli M, Leone P. A comparative assessment on hydrogen production from low- and high-temperature electrolysis. Int J Hydrogen Energy 2013;38:3523–36. doi:10.1016/j.ijhydene.2013.01.065.

[308] Petipas F, Fu Q, Brisse A, Bouallou C. Transient operation of a solid oxide electrolysis cell. Int J Hydrogen Energy 2013;38:2957–64. doi:10.1016/j.ijhydene.2012.12.086.

[309] A. Momma, K. Takano, Y. Tanaka TK and AY. Experimental Investigation of the Effect of Operating Pressure on the Performance of SOFC and SOEC 2013;57:699–708.

[310] Zhang X, O'Brien JE, O'Brien RC, Housley GK. Durability evaluation of reversible solid oxide cells. J Power Sources 2013;242:566–74. doi:10.1016/j.jpowsour.2013.05.134.

[311] Li W, Wang H, Shi Y, Cai N. Performance and methane production characteristics of H2O- CO2 co-electrolysis in solid oxide electrolysis cells. Int J Hydrogen Energy 2013;38:11104–9. doi:10.1016/j.ijhydene.2013.01.008.

[312] Li W, Shi Y, Luo Y, Cai N. Elementary reaction modeling of CO2/H2O co-electrolysis cell considering effects of cathode thickness. J Power Sources 2013;243:118–30. doi:10.1016/j.jpowsour.2013.05.119.

[313] Dasari HP, Park SY, Kim J, Lee JH, Kim BK, Je HJ, et al. Electrochemical characterization of Ni-yttria stabilized zirconia electrode for hydrogen production in solid oxide electrolysis cells. J Power Sources 2013;240:721–8. doi:10.1016/j.jpowsour.2013.05.033.

[314] Lay-Grindler E, Laurencin J, Delette G, Aicart J, Petitjean M, Dessemond L. Micro modelling of solid oxide electrolysis cell: From performance to durability. Int J Hydrogen Energy 2013;38:6917–29. doi:10.1016/j.ijhydene.2013.03.162.

[315] Ozturk M, Dincer I. Thermodynamic analysis of a solar-based multi-generation system with hydrogen production. Appl Therm Eng 2013;51:1235–44. doi:10.1016/j.applthermaleng.2012.11.042.

[316] Klotz D, Leonide A, Weber A, Ivers-Tiffée E. Electrochemical model for SOFC and SOEC mode predicting performance and efficiency. Int J Hydrogen Energy 2014;39:20844–9. doi:10.1016/j.ijhydene.2014.08.139.

[317] Sanz-Bermejo J, Gallardo-Natividad V, González-Aguilar J, Romero M. Coupling of a solid-oxide cell unit and a linear fresnel reflector field for grid management. Energy Procedia 2014;57:706–15. doi:10.1016/j.egypro.2014.10.226.

[318] Stempien JP, Ni M, Sun Q, Chan SH. Thermodynamic analysis of combined solid oxide electrolyzer and fischer-tropsch processes. Energy 2015;81:682–90. doi:10.1016/j.energy.2015.01.013.

[319] Stempien JP, Ni M, Sun Q, Chan SH. Production of sustainable methane from renewable energy and captured carbon dioxide with the use of Solid Oxide Electrolyzer: Athermodynamic assessment. Energy 2015;82:714–21. doi:10.1016/j.energy.2015.01.081.

[320] Reytier M, Di Iorio S, Chatroux A, Petitjean M, Cren J, De Saint Jean M, et al. Stack performances in high temperature steam electrolysis and co-electrolysis. Int J Hydrogen Energy 2015;40:11370–7. doi:10.1016/j.ijhydene.2015.04.085.

[321] Bernadet L, Gousseau G, Chatroux A, Laurencin J, Mauvy F, Reytier M. Influence of pressure on solid oxide electrolysis cells investigated by experimental and modeling approach. Int J Hydrogen Energy 2015;40:12918–28. doi:10.1016/j.ijhydene.2015.07.099.

[322] Aicart J, Petitjean M, Laurencin J, Tallobre L, Dessemond L. Accurate predictions of H2O and CO2 co-electrolysis outlet compositions in operation. Int J Hydrogen Energy 2015;40:3134–48. doi:10.1016/j.ijhydene.2015.01.031.

[323] Pozzo M, Lanzini A, Santarelli M. Enhanced biomass-to-liquid (BTL) conversion process through high temperature co-electrolysis in a solid oxide electrolysis cell (SOEC). Fuel 2015;145:39–49. doi:10.1016/j.fuel.2014.12.066.

[324] Peters R, Deja R, Blum L, Nguyen VN, Fang Q, Stolten D. Influence of operating parameters on overall system efficiencies using solid oxide electrolysis technology. Int J Hydrogen Energy 2015;40:7103–13. doi:10.1016/j.ijhydene.2015.04.011.

[325] Cacciuttolo Q, Vulliet J, Lair V, Cassir M, Ringuedé A. Effect of pressure on high temperature steam electrolysis: Model and experimental tests. Int J Hydrogen Energy 2015;40:11378–84. doi:10.1016/j.ijhydene.2015.04.034.

[326] Zhang X, O'Brien JE, Tao G, Zhou C, Housley GK. Experimental design, operation, and results of a 4 kW high temperature steam electrolysis experiment. J Power Sources 2015;297:90–7. doi:10.1016/j.jpowsour.2015.07.098.

[327] Sanz-Bermejo J, Muñoz-Antón J, Gonzalez-Aguilar J, Romero M. Part load operation of a solid oxide electrolysis system for integration with renewable energy sources. Int J Hydrogen Energy 2015;40:8291–303. doi:10.1016/j.ijhydene.2015.04.059.

[328] Joneydi Shariatzadeh O, Refahi AH, Abolhassani SS, Rahmani M. Modeling and optimization of a novel solar chimney cogeneration power plant combined with solid oxide electrolysis/fuel cell. Energy Convers Manag 2015;105:423–32. doi:10.1016/j.enconman.2015.07.054.

[329] Buttler A, Koltun R, Wolf R, Spliethoff H. A detailed techno-economic analysis of heat integration in high temperature electrolysis for efficient hydrogen production. Int J Hydrogen Energy 2015;40:38–50. doi:10.1016/j.ijhydene.2014.10.048.

[330] Visitdumrongkul N, Tippawan P, Authayanun S, Assabumrungrat S, Arpornwichanop A. Enhanced performance of solid oxide electrolysis cells by integration with a partial oxidation reactor: Energy and exergy analyses. Energy Convers Manag 2016;129:189–99. doi:10.1016/j.enconman.2016.10.023.

[331] Cinti G, Bidini G, Hemmes K. An experimental investigation of fuel assisted electrolysis as a

function of fuel and reactant utilization. Int J Hydrogen Energy 2016;41:11857–67. doi:10.1016/j.ijhydene.2016.05.205.

[332] Zhang W, Yu B, Wang X, Chen J. Thermodynamic analysis of the efficiency of high temperature co-electrolysis system for syngas production. Int J Hydrogen Energy 2016;41:15960–9. doi:10.1016/j.ijhydene.2016.04.223.

[333] Seitz M, von Storch H, Nechache A, Bauer D. Techno economic design of a solid oxide electrolysis system with solar thermal steam supply and thermal energy storage for the generation of renewable hydrogen. Int J Hydrogen Energy 2017;42:26192–202. doi:10.1016/j.ijhydene.2017.08.192.

[334] Kupecki J, Motylinski K, Jagielski S, Wierzbicki M, Brouwer J, Naumovich Y, et al. Energy analysis of a 10 kW-class power-to-gas system based on a solid oxide electrolyzer (SOE). Energy Convers Manag 2019;199. doi:10.1016/j.enconman.2019.111934.

[335] Schiller G, Lang M, Szabo P, Monnerie N, von Storch H, Reinhold J, et al. Solar heat integrated solid oxide steam electrolysis for highly efficient hydrogen production. J Power Sources 2019;416:72–8. doi:10.1016/j.jpowsour.2019.01.059.

[336] Mastropasqua L, Pecenati I, Giostri A, Campanari S. Solar hydrogen production: Techno-economic analysis of a parabolic dish-supported high-temperature electrolysis system. Appl Energy 2020;261:114392. doi:10.1016/j.apenergy.2019.114392.

[337] Chen B, Xu H, Ni M. Modelling of SOEC-FT reactor: Pressure effects on methanation process. Appl Energy 2017;185:814–24. doi:10.1016/j.apenergy.2016.10.095.

[338] Posdziech O, Schwarze K, Brabandt J. Efficient hydrogen production for industry and electricity storage via high-temperature electrolysis. Int J Hydrogen Energy 2019:19089–101. doi:10.1016/j.ijhydene.2018.05.169.

[339] Roeb M, Monnerie N, Houaijia A, Sattler C, Sanz-Bermejo J, Romero M, et al. Coupling Heat and Electricity Sources to Intermediate Temperature Steam Electrolysis. J Energy Power Eng 2013;7:2068–77.

[340] McLarty D, Brouwer J, Samuelsen S. A spatially resolved physical model for transient system analysis of high temperature fuel cells. Int J Hydrogen Energy 2013;38:7935–46. doi:10.1016/j.ijhydene.2013.04.087.

[341] Saeedmanesh A, Colombo P, McLarty D, Brouwer J. Dynamic Behavior of a Solid Oxide Steam Electrolyzer System Using Transient Photovoltaic Generated Power for Renewable Hydrogen Production. J Electrochem Energy Convers Storage 2019;16:041008. doi:10.1115/1.4043340.

[342] Petipas F, Brisse A, Bouallou C. Model-based behaviour of a high temperature electrolyser system operated at various loads. J Power Sources 2013;239:584–95. doi:10.1016/j.jpowsour.2013.03.027.

[343] Colombo P, Saeedmanesh A, Santarelli M, Brouwer J. Dynamic dispatch of solid oxide electrolysis system for high renewable energy penetration in a microgrid. Energy Convers Manag 2020;204:112322. doi:10.1016/j.enconman.2019.112322.

[344] Samuelsen S, Mueller F, Eichman J, Tarroja B. Piloting the integration and use of renewables to achieve a flexible and secure energy infrastructure. Calif Energy Comm PIR-08-13 2013.

[345] McLarty D, Civit Sabate C, Brouwer J, Jabbari F. Micro-grid energy dispatch optimization and predictive control algorithms; A UC Irvine case study. Int J Electr Power Energy Syst 2015;65:179–90. doi:10.1016/j.ijepes.2014.09.039.

[346] Chandan V, Do A, Jin B, Jabbari F, Brouwer J, Akrotirianakis I, et al. Modeling and optimization of a combined cooling, heating and power plant system. 2012 Am. Control Conf., 2012, p. 3069–74. doi:10.1109/ACC.2012.6315606.

[347] Shaffer B, Tarroja B, Samuelsen S. Advancing Toward Sustainability Goals at the University of California, Irvine. Proc. ASME 2014 8th Int. Conf. Energy Sustain., Boston, Massachusetts: 2014, p. 1–14. doi:10.1115/ES2014-6453.

[348] Do A-TV. Performance and Controls of Gas Turbine-Driven Combined Cooling Heating and Power Systems for Economic Dispatch. University of California, Irvine, 2013.

[349] YII Prous R. Dynamic dispatch and control of hydrogen energy storage from solar power in microgrids. University of California, Irvine, 2015.

[350] Hoeschele M, Weitzel E. Hot Water Distribution System Model Enhancements Alliance for Residential Building Innovation (ARBI). 2012.

[351] Petipas F, Brisse A, Bouallou C. Modelled behaviour of a high temperature electrolyser system coupled with a solar farm. Chem Eng Trans 2015;45. doi:10.3303/CET1545170.

[352] California ISO - Todays Outlook n.d. http://www.caiso.com/TodaysOutlook/Pages/default.aspx.

[353] Stansberry J, Hormaza Mejia A, Zhao L, Brouwer J. Experimental analysis of photovoltaic integration with a proton exchange membrane electrolysis system for power-to-gas. Int J Hydrogen Energy 2017;42:30569–83. doi:10.1016/j.ijhydene.2017.10.170.

[354] Mastropasqua L, Campanari S, Brouwer J. Solid Oxide Fuel Cell short stack performance testing - part B: Operation in carbon capture applications and degradation issues. J Power Sources 2017;371:238–48. doi:10.1016/j.jpowsour.2017.10.014.